Lehrstuhl für Feststoff- und Grenzflächenverfahrenstechnik der
Technischen Universität München

Optimal Operation of Batch Cooling Crystallizers

Michael Löffelmann

Vollständiger Abdruck der von der Fakultät für Maschinenwesen der
Technischen Universität München zur Erlangung des akademischen Grades eines

Doktor-Ingenieurs

genehmigten Dissertation.

Vorsitzender: Univ.-Prof. Dr.-Ing., Dr.-Ing. habil. R. Schilling
Prüfer der Dissertation: 1. Univ.-Prof. Dr.-Ing. A. Mersmann, emeritiert
2. Univ.-Prof. Dr.-Ing., Dr.-Ing. habil. J. Stichlmair

Die Dissertation wurde am 17.04.2002 bei der Technischen Universität München eingereicht und durch die Fakultät für Maschinenwesen am 12.07.2002 angenommen.

Die vorliegende Arbeit entstand während meiner Tätigkeit als wissenschaftlicher Angestellter am Lehrstuhl für Feststoff- und Grenzflächenverfahrenstechnik – ehemals Lehrstuhl B für Verfahrenstechnik – der Technischen Universität München in den Jahren 1997 bis 2001.

Mein besonderer Dank gilt meinem hochverehrten Lehrer, Prof. Dr.-Ing. Alfons Mersmann, für die große und unermüdliche Unterstützung, das in mich gesetzte Vertrauen und den stets großzügig gewährten Freiraum.

Herrn Prof. Dr.-Ing., Dr.-Ing. habil. J. Stichlmair danke ich für die Übernahme des Korreferates und Herrn Prof. Dr.-Ing., Dr.-Ing. habil. R. Schilling für die Führung des Prüfungsvorsitzes.

Weiterhin möchte ich mich bei den Mitarbeitern des Fraunhofer Institutes für Zuverlässigkeit und Mikrointegration Dr. Drost, Dr. Leidl, Dr. Endres und Dr. Langer für die fruchtbare und unkomplizierte Kooperation bedanken. Herrn Prof. Dr. techn. R. Müller danke ich für die Diskussionsbereitschaft und Anregungen.

Bei allen Mitarbeitern des Lehrstuhls möchte ich mich auf das herzlichste für die gewährleistete Unterstützung und das äußerst angenehme und offene Arbeitsklima bedanken.
Markus Kühberger und Harald Schubert danke ich für die Unterstützung zu Beginn meiner Arbeit und den täglichen Telefonkonferenzen, die eine große Bereicherung des Universitätsalltages darstellten. Christiane Heyer, Björn Braun, Axel Eble und Klaus Bartosch danke ich für die angenehme und spaßgeladene Atmosphäre innerhalb unserer Arbeitsgruppe. Lars Frye, Lutz Vogel und ganz besonders Carsten Mehler schulde ich für manch unvergessenen Abend ebenso Dank.
Bedanken möchte ich mich ebenso bei meinen drei ehemaligen Bürokollegen Holger Kajszika, Johannes Wittmann und Hans-Christoph Schwarzer für Ihre Toleranz und Geduld beim Ertragen meiner manchmal etwas unkonventionellen Art.
Wolfgang Lützenburg und seiner Werkstatt bin ich nicht nur wegen seiner Fähigkeit aus meinen unleserlichen Skizzen funktionstüchtige Versuchsaufbauten zu zaubern auf Ewigkeit zu Dank verpflichtet.
Frau Baumann, Frau Stellmacher und ganz besonders Ralf Hübner danke ich für die Abnahme manch lästiger administrativer Arbeit.

Am meisten möchte ich mich jedoch bei meinen Eltern, Klaus und Edeltraud Löffelmann, bedanken. Sie haben mir diese Ausbildung ermöglicht und dabei gleichzeitig jede Menge Geduld bewiesen.

München, im November 2002 Michael Löffelmann

Für meine Eltern

“Eine gute wissenschaftliche Theorie sollte einer Bardame erklärbar sein.”
(“A good scientific theory should be explicable to a barmaid.”)

Ernest Rutherford (1871-1937)

1 Introduction 1

2 Fundamentals 4

2.1 The Driving Force: Chemical Potential and Supersaturation 4

2.2 Nucleation: The Birth of a Crystal 10

2.2.1 Homogeneous Nucleation 11

2.2.2 Heterogeneous Nucleation 14

2.2.3 Surface or Secondary Nucleation 20

2.2.4 Attrition induced Nucleation 21

2.3 Crystal Growth: From Nucleus to Crystal 27

2.3.1 Diffusion Controlled Growth 28

2.3.2 Integration Controlled Growth 29

2.3.3 General Characterization of Crystal Growth Rates 31

2.4 Metastable Zone and Induction Time: What we still cannot see! 32

2.5 Agglomeration – How Particles stick together 37

3 Operational Modes and Control of Cooling Crystallizers 40

4 Optimal Process Management 53

4.1 Cooling or Evaporation Crystallization? 53

4.2 Optimal Supersaturation for Coarse Crystalline Products 57

5 Innovative Supersaturation Measuring System 64

5.1 Measurement Method 64

5.2 Sensor 68

5.2.1 Interdigital Transducer (IDT) 68

5.2.2 Surface Acoustic Wave (SAW) 69

5.2.3 Peltier Element 70

5.2.4 Sensor Setup 71

6 Experiments 82

6.1 Measurement Signals 82

6.2 Beaker Glass Experiments 87

6.3 Crystallizer Experiments 94

6.4 Further Experiments with other Systems 102

7 Theoretical Approach 108

7.1 Model of Metastability 108

7.2 Simplified Criteria for the Estimation of the Field of Application 117

8 Conclusion 125

9 Notation 127

10 References 132

11 Appendix 141

11.1 Comparison of the Dependence of the pre-exponential Factor on Supersaturation S 141

11.2 Conversion of the Rate B_{het} of heterogeneous Nucleation into the Rate B_{hom} of homogeneous nucleation for the Models of Schubert and Heyer 142

11.3 System properties 144

11.4 Experimental results 145

11.5 Calculated heterogeneous nucleation rates B_{het} 152

11.6 Calculation of σ_{met} for primary heterogeneous nucleation 153

11.7 Further possibilities for improvement and additional sensor concepts 154

- 11.7.1 Design improvement of the existing sensor 154
- 11.7.2 Sensor for systems with flat solubility curves 155
- 11.7.3 Equilibrium state sensor 158

1 Introduction

In the early stages of chemical engineering the major aim was to find an adequate process for every desired product. These days, the objective of chemical engineering has changed. In order to enable competitiveness it is not sufficient to manufacture a product, but also to provide the desired product properties with respect to an economic production. Therefore, the dream of every process engineer is the possibility of the adjustment or the control of a process in order to optimize profitability, efficiency and product quality.

Nowadays, crystallization from solution is world-wide a common process for separation or purification of substances. The field of application comprises nearly every industry branch, like pharmaceuticals, pigments, food, plastics etc.. Despite the frequent implementation of crystallization in industrial processes and the knowledge of the positive influence of process control on economics and product quality, most crystallizers lack an efficient process control. The most important parameter for the control of a crystallization process is the supersaturation ΔC as the thermodynamic driving force.

For every substance, crystallizer and parameters describing the product quality, like

- median crystal size
- crystal purity,
- crystal size distribution,
- specific surface area, and
- crystal morphology,

an optimal supersaturation ΔC_{opt} exits. Only the control of the crystallization with respect to the optimal supersaturation allows an economic operation.

Plotting revenues and costs of a crystallization process versus the supersaturation ΔC, Figure 1-1 is obtained.

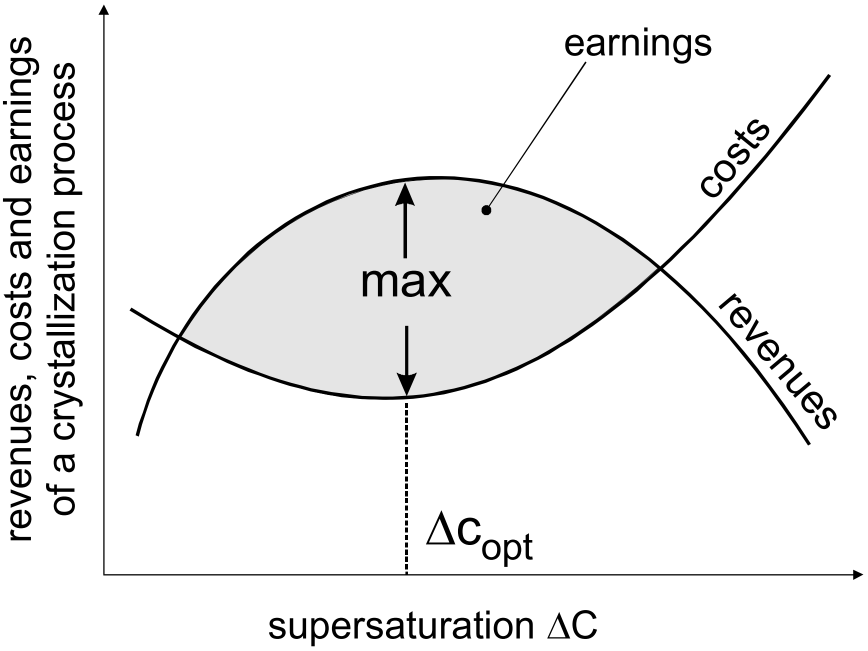

Figure 1-1: Optimal supersaturation ΔC_{opt} *with respect to the maximization of the earnings [Kind89]*

As can be seen, profit or earnings can only be maximized if the process is operated at the optimal supersaturation ΔC_{opt}. If the supersaturation is too low, the time of operation increases, thus raising operating costs. Further, the production rate is reduced and a higher percentage of the resources remain in the mother liquor. As a consequence the profit declines. Increasing supersaturation drastically causes higher incrustation of crystallizer installations, especially heat exchanger surfaces, and blockage of pipelines. This leads to a lower operating time, since more time for maintenance and cleaning is required. The drop of the median crystal size caused by spontaneous nucleation at higher supersaturations can result in faulty production, thus making it necessary to dissolve the crystals again, because desired product requirements (e. g. crystals size) could not be fulfilled. A higher energy consumption during downstream processing, like drying, is another consequence of the generation of smaller crystal sizes by uncontrolled crystallization.

This shows the urgent need of a control of the crystallization process, which is only possible when the driving force of the process – the supersaturation ΔC – can be measured quantitatively. Up to now many different supersaturation measurement techniques have been found, but none of them is able to measure the supersaturation directly. Instead, concentration dependent physical properties of a solution are used as measurands to obtain the current concentration. A subsequent estimation of the supersaturation on the basis of solubility data provides only a vague way of supersaturation measurement, since the influence of small impurities on the crystallization kinetics and solubility can not be measured.

In addition, none of the existing supersaturation measurement methods became widely accepted because of a restricted applicability considering the substances, high investment costs, low reliability or high instrumental expenses.

The aim of this work is the design, construction and testing of an innovative supersaturation sensor in a co-operation with Grimm Aerosol Technik GmbH and the Fraunhofer Institute for Reliability and Microintegration. Since this measurement method incorporates the crystallization process, it should be possible to measure the driving force of the crystallization process, i. e. the supersaturation, directly and quantitatively, thus enabling an optimal operation of crystallizers.

2 Fundamentals

Crystallization can be described as the response of a system to non-equilibrium between the solid and liquid phase. In this chapter the different expressions for the degree of deviation from equilibrium and its calculation will be explained. Next the processes caused by the effort of the system to reach equilibrium, i.e. nucleation and growth , will be described.

2.1 The Driving Force: Chemical Potential and Supersaturation

Assuming constant pressure and temperature, the thermodynamic driving force of a crystallization process can be described as the difference in the chemical potentials μ_i of one component i in the liquid (index L) and solid (index S) phases:

$$\Delta\mu_i = \mu_{i,L} - \mu_{i,S} \qquad (2\text{-}1)$$

Whereas a solution saturated with component i implies an equilibrium between the dissolved molecules in the liquid phase and the crystallized molecules in the solid phase. In this case the chemical potentials in both phases are equal:

$$\mu_{i,S} = \mu_{i,L}^{*} \qquad (2\text{-}2)$$

The chemical potential $\mu_{i,S}$ in the solid phase is very difficult to determine. An easier possibility for obtaining the difference of the chemical potential is to combine equations (2-1) and (2-2):

$$\Delta\mu_i = \mu_{i,L} - \mu_{i,L}^{*} \qquad (2\text{-}3)$$

The actual chemical potential of a component i in a single phase is defined by

$$\mu_i = \mu_{i,0} + \Re T \ln a_i \qquad (2\text{-}4)$$

where $\mu_{i,0}$ is the chemical potential at standard state, $\Re$ the ideal gas constant, T the absolute temperature, and a_i the activity. Using the two equations (2-3) and (2-4) the general expression for the difference of the chemical potentials between supersaturated (non-equilibrium) and saturated (equilibrium) state for a entirely dissociated system can be written as:

$$\Delta\mu_i = \nu\,\Re\,T\left(\ln a_i - \ln a_i^*\right) = \nu\,\Re\,T \ln\left(\frac{a_i}{a_i^*}\right) \tag{2-5}$$

ν represents the number of ions emerging from a decomposing molecule. Defining the ratio of the activities as the supersaturation S_a

$$S_a = \frac{a_i}{a_i^*} \tag{2-6}$$

equation (2-5) can be written dimensionless as:

$$\frac{\Delta\mu_i}{\Re\,T} = \nu\ \ln S_a \tag{2-7}$$

It can easily be seen that the actual driving force of a crystallization process is the ratio of a_i / a_i^*, the supersaturation S_a. Reaching the state of equilibrium means attaining the same value for a_i and a_i^*, which leads to a supersaturation $S_a = 1$ and a difference of the chemical potentials $\Delta\mu_i = 0$. Another possibility of expressing the difference of the chemical potentials $\Delta\mu_i$ is to use the heat of crystallization ΔH^*_{CL}, which is given by:

$$\Delta H_{CL}^* = -\left(\Re\left(\frac{d \ln a_i}{d(1/T)}\right)\right) = -\Re\,T\frac{d \ln a_i}{d \ln T} \tag{2-8}$$

and

$$\Delta\mu_i = \Delta H_{CL}^* \frac{\Delta T}{T} \tag{2-9}$$

The parameter ΔT represents the subcooling of the solution and the index C denotes the crystalline state.

There are many possibilities of expressing the concentration of one component in a mixture. The most common concentration scales can be found in equation (2-10). In the case of the mole fraction x_i the amount of substance n_i is based on the total amount of substances n of the system. The molarity C_i can be calculated by dividing the amount of substance n_i by the total volume V of the system.

$$x_i = \frac{n_i}{n} \quad ; \quad C_i = \frac{n_i}{V} \tag{2-10}$$

For a non-ideal solution the activity a_i can be obtained with the help of the activity coefficient. The activity can be expressed on different bases and therefore the corresponding activity coefficient has to be chosen for the following calculation (see equation (2-11)). Assuming an ideal behaviour of the solution or at infinite dilution the activity coefficient equals one.

$$a_i = \gamma_i \, x_i = f_i \, C_i \tag{2-11}$$

As can be seen, the activity coefficient γ_i is based on mole fractions x_i and f_i is based on molarity C_i. In reality ions of only one species (negative or positive) cannot be found without their corresponding species (positive or negative), which means that ions in a solution appear only in pairs and therefore only an activity coefficient considering both ions can be determined by experiments. Furthermore, dissociated ions are interacting with their corresponding activities . Thus it is reasonable to introduce an average activity coefficient $\gamma_\pm$:

$$\gamma_\pm = \left(\gamma_+^{\nu+} \gamma_-^{\nu-}\right)^{1/\nu} \tag{2-12}$$

The stoichiometric coefficient ν specifies the number of ions emerging from one totally dissociated molecule.

$$\nu = \nu_+ + \nu_- \tag{2-13}$$

In the case of crystallization from solution the degree of dissociation α has to be taken into account in addition to the stoichiometric coefficient ν. Most electrolytes dissociate incompletely and therefore the concentration-dependent degree of dissociation α is introduced as the ratio of dissociated molecules $n_{i,dis}$ and total amount of molecules n_i of one component.

$$\alpha = \frac{n_{i,dis}}{n_i} \qquad (2\text{-}14)$$

According to [Robi55] the degree of dissociation α can be derived from the mole fraction based dissociation constant K_x which is given by the ratio of undissociated and dissociated molecules. This constant is dependent on pressure and temperature and is analogically defined according to the law of mass action of thermodynamics.

$$K_x = \frac{x_+^{\nu+}\, x_-^{\nu-}}{x} \frac{\gamma_+^{\nu+}\, \gamma_-^{\nu-}}{\gamma} \qquad (2\text{-}15)$$

or

$$K_x = x \frac{\alpha^2}{1-\alpha} \gamma_\pm^2 \qquad (2\text{-}16)$$

Inserting the average activity coefficient $\gamma_\pm$ and the degree of dissociation α in equation (2-5) the difference of the chemical potentials can be formulated dimensionless as follows:

$$\frac{\Delta\mu_i}{\Re T} = \nu \ln\left(\frac{\alpha\, \gamma_\pm\, x_i}{\alpha^*\, \gamma_\pm^*\, x_i^*} \right) \qquad (2\text{-}17)$$

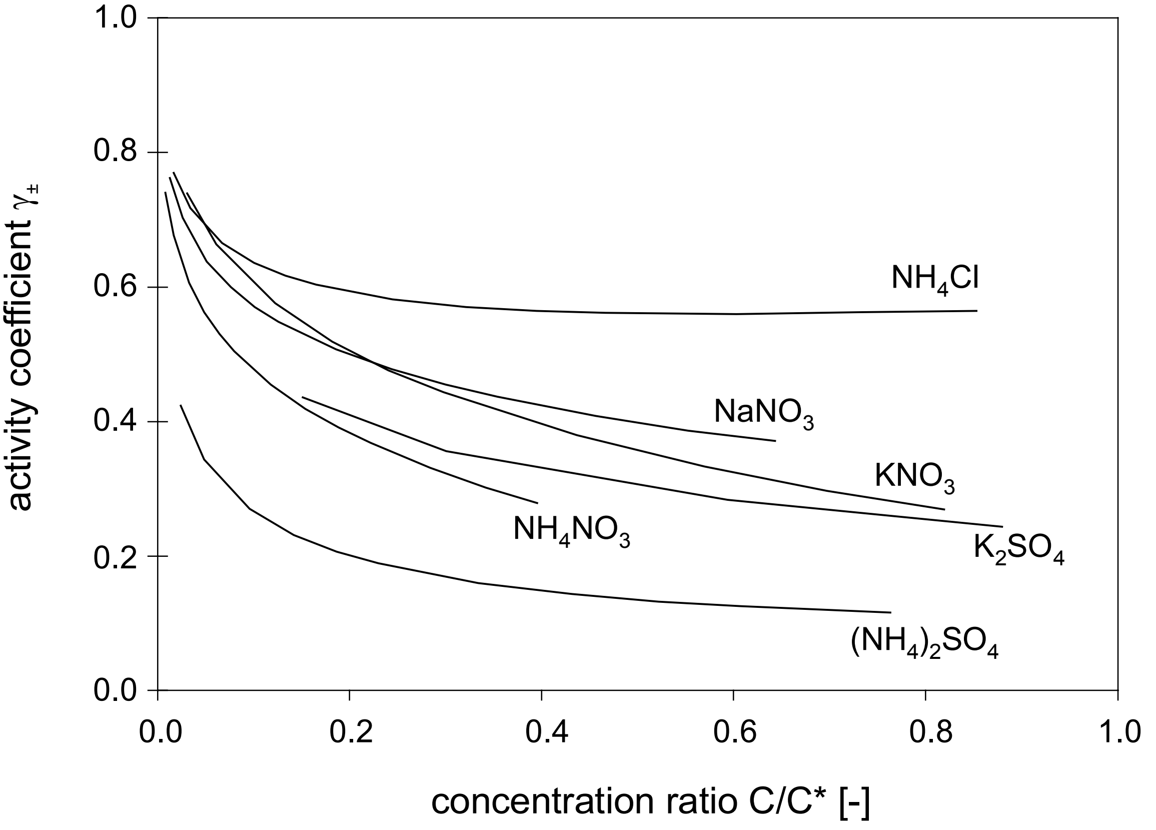

Figure 2-1: Activity coefficients $\gamma_\pm$ of various inorganic systems

Figure 2-1 shows the dependence of the activity coefficient $\gamma_\pm$ on the concentration [Mull93]. Here the concentration is given as a ratio of actual concentration C and equilibrium concentration C* at 25 °C. It is obvious, that in the range of $C/C^* < 0.2$ the concentration-dependency is strong, whereas in the range of $C/C^* \approx 1$ the activity coefficient hardly changes. At lower concentrations or in diluted solutions the activity coefficient experiences the highest fluctuations of its value. In most cases the deviation of the activity coefficient $\gamma_\pm$ of a real system from an activity coefficient ($\gamma_\pm = 1$) of an ideal system reaches its maximum at the maximum concentration, the saturation concentration C*. In crystallization from solution of highly soluble systems only low supersaturations ($\sigma < 0.1$) can be achieved. Although in the range between $C/C^* = 1$ and $C/C^* = 1.1$ we have the maximum deviation from ideal state, we also have the smallest fluctuations, that means an almost constant activity coefficient $\gamma_\pm$. Therefore it is possible to use the same value for $\gamma_\pm$ and $\gamma_\pm^*$. This simplifying assumption makes it possible to use concentrations scales which we can easily access in order to determine the driving force, i. e. the supersaturation. As already mentioned, this step is only reasonable for small differences between $\gamma_\pm$ and $\gamma_\pm^*$, i. e. correspondingly low supersaturations. In precipitation, however, very high supersaturations ($S > 1000$) are reached. There it is necessary to calculate the supersaturation with the help of the activity coefficient since the accuracy of the driving force would otherwise be very low [Schu98].

Implementing the above described simplification in equation (2-6), the supersaturation S is given by:

$$S = \frac{C}{C^*} \tag{2-18}$$

The relative supersaturation σ with $\sigma \equiv S-1$ can be calculated in the following way:

$$\sigma = \nu \ln(S) = \nu \ln\left(\frac{C}{C^*}\right) \tag{2-19}$$

for low supersaturations ($\sigma < 0.1$) equation (2-19) can be simplified with an error less than 5%:

$$\sigma = \nu\left(\frac{C - C^*}{C^*}\right) \tag{2-20}$$

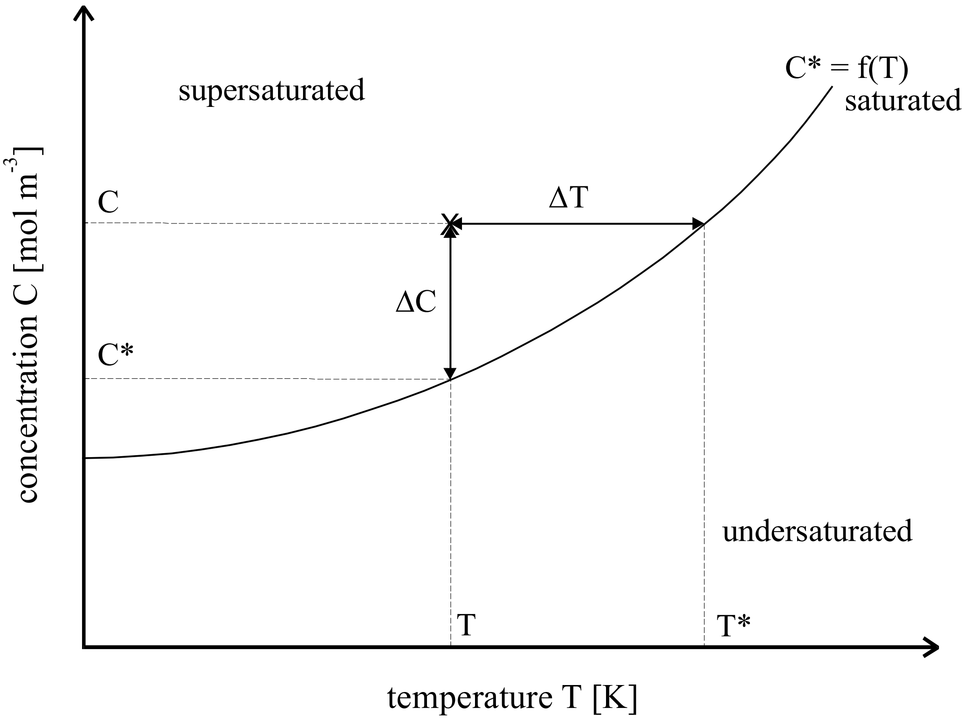

Figure 2-2: Solubility diagram

In the solubility diagram in Figure 2-2 the equilibrium or saturation concentration C* is plotted versus temperature. As can be seen in this plot, the supersaturation can be expressed as a concentration difference ΔC

$$\Delta C = C - C^* \tag{2-21}$$

or as a subcooling (temperature difference) ΔT

$$\Delta T = T^* - T \tag{2-22}$$

where T is the actual temperature of the solution and T* the saturation temperature for a solution with the concentration C.
If a rather constant slope of the solubility curve is given in the relevant temperature range, a simplified conversion of supersaturation into subcooling is possible:

$$\Delta C = \left(\frac{dC^*}{dT}\right)\Delta T \tag{2-23}$$

2.2 Nucleation: The Birth of a Crystal

Generally speaking the nucleation rate B is defined by the variation with time of the number of particles N per Volume V:

$$B = \frac{dN}{dt\ V} \tag{2-24}$$

The nucleation can be caused by various mechanisms. In the case of a crystal free solution which contains no foreign particles, nuclei are formed by homogeneous nucleation. If nucleation takes place on the surface of foreign particles in a crystal-free solution heterogeneous nucleation is the decisive mechanism. The third possible kind of activated nucleation is surface or secondary activated nucleation which only happens in the presence of own crystals. Non-activated nucleation is induced by attrition or breakage and will be briefly discussed at the end of this section.
Figure 2-3 gives an overview of the different types of nucleation mechanisms.

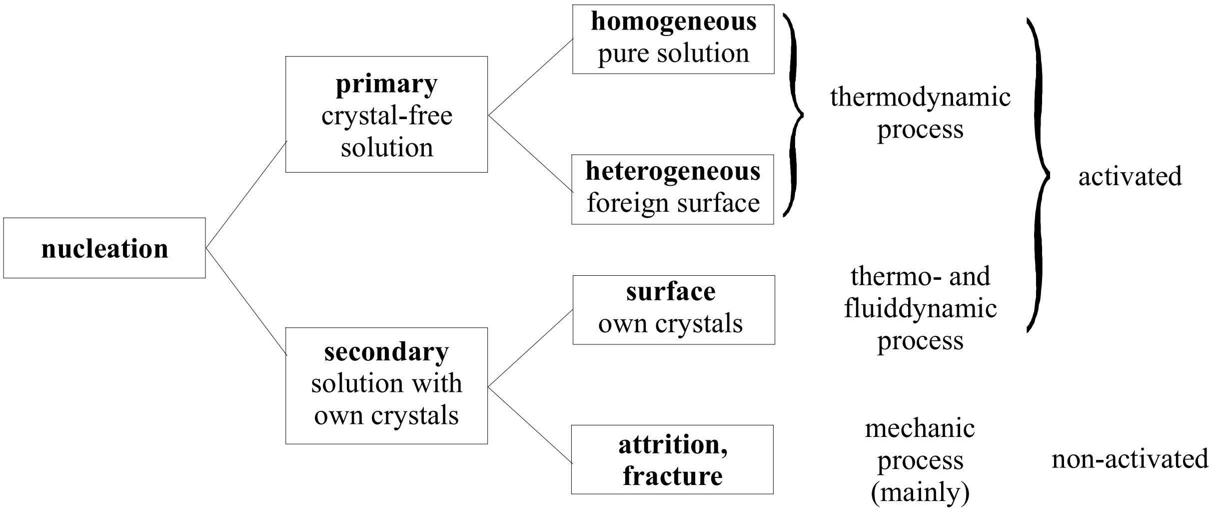

Figure 2-3: Different kinds of nucleation

2.2.1 Homogeneous Nucleation

The classical nucleation theory according to Volmer and Weber [Volm26, Volm39] is the basis for the modelling of nucleation rates.

In a supersaturated solution collisions of single molecules occur stochastically, thus leading to a formation of clusters. The higher the supersaturation, the higher the probability of such collisions and cluster formation. Further collisions of such a cluster with monomers lead to the growth of the cluster. If the cluster reaches a critical size L_c, it becomes thermodynamically stable. In the case of a spherical nucleus, assuming complete dissociation ($\alpha = 1$) and the number of ions $\nu = 1$, the critical size L_c can be calculated with the following equation:

$$L_c = \frac{4\gamma_{CL}}{k\,T\ln S} V_m \qquad (2\text{-}25)$$

where γ_{CL} is the interfacial tension, k the Boltzmann constant and V_m the volume of a unit (molecule). Only clusters with a size $L > L_c$ will continue to grow, whereas clusters smaller than L_c will disintegrate. It is obvious that with an increasing supersaturation S the critical size L_c of a nucleus decreases.

γ_{CL}, i. e. the interfacial tension between crystal and liquid phase, can be estimated based on theoretical considerations given in [Mers90]:

$$\gamma_{CL} = K\,k\,T\left(C_C N_A\right)^{2/3} \ln\left(\frac{C_C}{C^*}\right) \qquad (2\text{-}26)$$

with C_C as the molar crystal density and N_A as Avogadro's number. Unfortunately there is an uncertainty regarding the factor K for which data between K = 0.414 and K = 0.31 were published. The first value has been derived from an estimation of the interfacial geometry in [Mers90], whereas the second value origins from a comparison with experimental results [Mers95]. The influence of the factor K on the calculation of nucleation rates will be shown later.
The free nucleation enthalpy ΔG_c of a critical cluster can be calculated by:

$$\Delta G_c = \frac{1}{3} A_c \gamma_{CL} \qquad (2\text{-}27)$$

where A_c is the interface area between nuclei and solution.

When the impact frequency of monomers [Kind83], the surface area A_c of a critical nucleus, the Zeldovich factor Z [Zeld42], and the concentration of critical clusters are taken into account, the homogeneous nucleation rate B_{hom} can be written as:

$$B_{hom} = 1.5\, D_{AB} \left(C\, N_A\right)^{7/3} \sqrt{\frac{\gamma_{CL}}{kT}}\, \frac{1}{C_C\, N_A} \cdot \exp\left[-\frac{16}{3}\pi \left(\frac{\gamma_{CL}}{kT}\right)^3 \left(\frac{1}{C_C\, N_A}\right)^2 \frac{1}{(\nu \ln S)^2}\right] \qquad (2\text{-}28)$$

According to Heyer [Heye01] the dependence of the pre-exponential factor on the supersaturation S is $S^2 \cdot \ln S$ instead of S^2, however, for S > 3 the differences are negligible, see Figure 11-1 in the appendix 11.1.
The binary diffusion coefficient D_{AB} can be estimated using the Stokes-Einstein equation [Eins22]:

$$D_{AB} = \frac{kT}{3\pi \eta d_m} \qquad (2\text{-}29)$$

with the dynamic viscosity η and the molecule diameter d_m, which is given by

$$d_m \approx \left(\frac{\tilde{M}}{\rho_c\, N_A}\right)^{1/3} = V_m^{1/3} \qquad (2\text{-}30)$$

Here $\tilde{M}$ is the molar mass and ρ_S the density of the solid.

In Figure 2-4 and Figure 2-5 the homogeneous nucleation rate B_{hom} has been calculated for different values of the parameter C^*/C_C, i.e. different systems, as a function of the relative supersaturation σ. It is remarkable that for highly soluble systems ($C^*/C_C > 0.1$), which are commonly used in crystallization from solutions, a high dependency on the supersaturation can be observed. Because of that fact high supersaturations should be avoided during the crystallization from solution if large and pure crystals are to be generated.

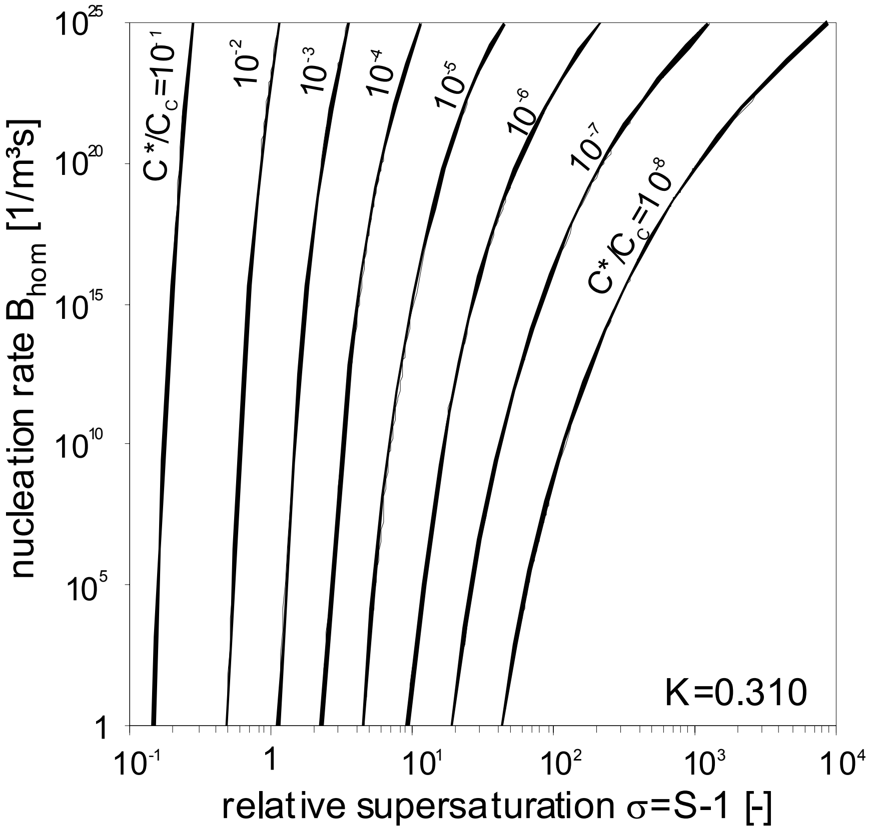

Figure 2-4: Homogeneous nucleation rates as a function of the relative supersaturation σ for different dimensionless solubilities C^*/C_C. Calculated for $D_{AB} = 1.5 \cdot 10^{-9}\ m^2 s^{-1}$, $\nu = 2$, $T = 293$ K, and $K = 0.310$

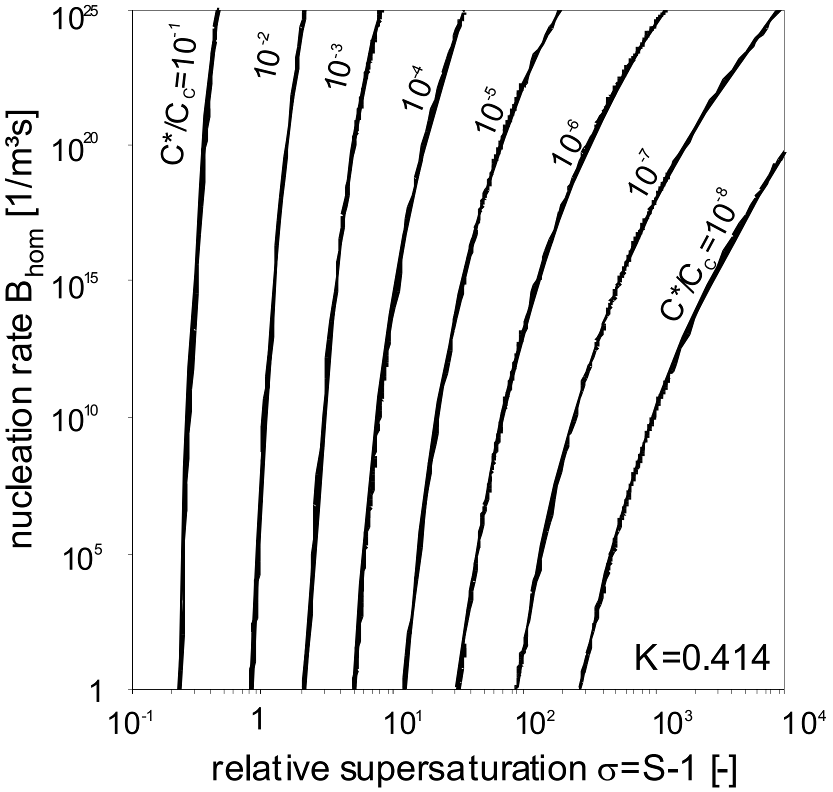

Figure 2-5: Homogeneous nucleation rates as a function of the relative supersaturation σ for different dimensionless solubilities C^*/C_C. Calculated for $D_{AB} = 1.5 \cdot 10^{-9}\ m^2 s^{-1}$, $\nu = 2$, $T = 293$ K, and $K = 0.414$

A comparison between Figure 2-4 and Figure 2-5 shows the influence of the factor K in equation (2-26), which is used to determine the interfacial tension γ_{CL}. This evokes the crucial question of how to determine the exact value of the interfacial tension. Unfortunately no other way to obtain a more precise value for the interfacial tension has yet been found. Therefore the influence of the factor K should always be kept in mind when interfacial tensions or nucleation rates are calculated.

2.2.2 Heterogeneous Nucleation

Dealing with the operation of batch crystallizers makes it necessary to have a closer look at the determination of the heterogeneous nucleation rate. Homogeneous nucleation can hardly be found in industrial crystallizers because the major premise for that nucleation mechanism – a pure and foreign particle- / surface-free solution – is not fulfilled. It is very difficult to obtain homogeneous nucleation even in laboratory experiments [Schu98]. In almost every batch crystallizer stirrers are installed to mix the solution in order to establish or maintain a homogeneous supersaturation and temperature profile. Suspending the generated crystals is another important function of the stirrer. As a consequence the stirrer, the cooling jacket, the wall of the crystallizer, and foreign particles (e.g. dirt or impurities) provide a huge amount of foreign surface for heterogeneous nucleation. The reason for the occurrence of heterogeneous nucleation at lower supersaturation than homogenous nucleation is the reduced free - nucleation enthalpy $\Delta G_{c,het}$.

$$\Delta G_{c,het} = f\, \Delta G_{c,hom} \qquad (2\text{-}31)$$

with f $(0 < f < 1)$ as the geometric correction factor dependent on the contact or wetting angle θ as illustrated in Figure 2-6.

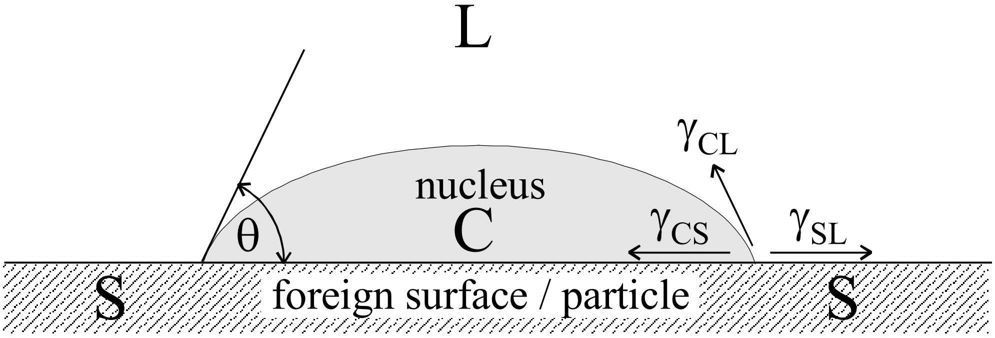

Figure 2-6: Nucleation on a foreign surface

According to that definition the factor f can be determined by:

$$f = \frac{(2+\cos\theta)(1-\cos\theta)^2}{4} \qquad (2\text{-}32)$$

Young [Youn55] defines the contact angle θ as the ratio of the interfacial tensions between solid (foreign), liquid, and crystal phase:

$$\cos\theta = \frac{\gamma_{SL} - \gamma_{CS}}{\gamma_{CL}} \qquad (2\text{-}33)$$

This reduction of the total free nucleation enthalpy by the factor f results in the following equation for the calculation of B_{het} of the heterogeneous nucleation rate:

$$B_{het} = 1.5\, D_{AB} \left(C\, N_A\right)^{7/3} \sqrt{f \frac{\gamma_{CL}}{k\,T} \frac{1}{C_C\, N_A}} \cdot \exp\left[-f \frac{16}{3} \pi \left(\frac{\gamma_{CL}}{k\,T}\right)^3 \left(\frac{1}{C_C\, N_A}\right)^2 \frac{1}{(\nu \ln S)^2} \right] \qquad (2\text{-}34)$$

As already mentioned heterogeneous nucleation takes place on foreign surfaces, thus it seems to be obvious that there should be a dependence on the foreign surface area provided in the solution. Equation (2-34) neglects this correlation, i. e. for different volumetric surface areas a_{for} we would obtain identical heterogeneous nucleation rates. Schubert [Schu98] suggested a model describing B_{het} as a product of the volumetric surface a_{for} and the heterogeneous nucleation rate based on the surface of foreign particles $B_{het,surf}$:

$$B_{het} = a_{for}\, B_{het,surf} \qquad (2\text{-}35)$$

$$B_{het} = \frac{1}{2\pi} a_{for}\, d_m\, He_{ad} \left(C\, N_A\right)^{7/3} \sqrt{\frac{\gamma_{CL}}{k\,T} \frac{1}{C_C\, N_A}} \left[\frac{D_{surf} \sin\theta}{r_c} \left(He_{ad}\, d_m\right)^{3/2} \left(C\, N_A\right)^{1/6} + \frac{3}{2} \pi D_{AB} (1 - \cos\theta) \right] \cdot \exp\left[-f \frac{16}{3} \pi \left(\frac{\gamma_{CL}}{k\,T}\right)^3 \left(\frac{1}{C_C\, N_A}\right)^2 \frac{1}{(\nu \ln S)^2} \right] \qquad (2\text{-}36)$$

Here He_{ad} is the adsorption constant, r_c is the radius of a critical nucleus

$$r_c = \frac{2\, \gamma_{CL}\, \tilde{M}}{\rho_c\, \Re\, T\, \nu \ln S} \qquad (2\text{-}37)$$

and D_{surf} is the surface–diffusion coefficient according to Suzuki [Suzu90] and Schubert [Schu98].

$$D_{surf} = \frac{1}{4\, He_{ad}\, d_m^2\, C\, N_A} \sqrt{\frac{\pi\, k\, T\, N_A}{2 \tilde{M}}} \qquad (2\text{-}38)$$

This equation (2-38) should be handled with care because it forecasts physically impossible values for $He_{ad} \to 0$. Rauls and Beckmann [Raul90] obtained values for the surface-diffusion coefficient D_{surf} in the range of $0.5 \cdot 10^{-12} - 15 \cdot 10^{-12}$ m^2 s^{-1} by experiments.

It should be mentioned, that in equation (2-36), derived by Schubert [Schu98], the factor f is missing in the pre-exponential term, although it has to be taken into account with $f^{-1/2}$ in the case of a rigorous derivation of the Zeldovich factor for the assumed geometry, like it is shown in equation (2-39) by Heyer [Heye01].

When comparing the rate B_{het} of heterogeneous nucleation in equation (2-36) with the rate B_{hom} of homogeneous nucleation in equation (2-28) it can be seen that the following additional parameters influence B_{het}:

- a_{for} - volumetric surface area of foreign particles
  Please note that only the volumetric surface area and not the number of particles is important for the heterogeneous nucleation rate. In case of $a_{for} < 10^4$ m^2 m^{-3} attention should be paid to the basic level of SiO_2 particles , which are even present in ultrapure water ($a_{for} \approx 2500$ m^2 m^{-3}) [Schu98].
- He_{ad} – adsorption constant
  Up to now it is not possible to predict or calculate this parameter. In further calculations we will take the value 10^{-9} which has been found by Schubert [Schu98]
- θ – contact angle (f – factor)
  Unfortunately we are not able to measure this decisive parameter, but some experiments have shown that θ is frequently within the range $40° < \theta < 53°$, i. e. $0.038 < f < 0.1$.
- D_{surf} – surface diffusion coefficient
  Equation (2-38) makes it possible to estimate D_{surf}. Nevertheless the influence of D_{surf} on the calculation of heterogeneous nucleation rates is very small, as will be shown later.

In order to decide which nucleation mechanism is dominant or relevant for the actual process, it is useful to have a closer look at the ratio B_{het}/B_{hom}. In Figure 2-7 this ratio is plotted as a function of the dimensionless supersaturation $\Delta C/C_C$ and the dimensionless solubility C^*/C_C for two different dissociation numbers $\nu = 1$ and $\nu = 2$ [Mers01]. It can be seen that for molecular substances ($\nu = 1$) higher supersaturations have to be established if an equality of nucleation rates between homogenous and heterogeneous nucleation is desired as in case of dissociated systems. The higher difficulty of controlling a crystallization process with dissociated systems ($\nu = 2$) lies in the smaller range of change between heterogeneous and homogeneous dominated nucleation. Of course all these calculations are strongly dependent on the properties of the material, the supersaturation, and the prevailing process conditions.

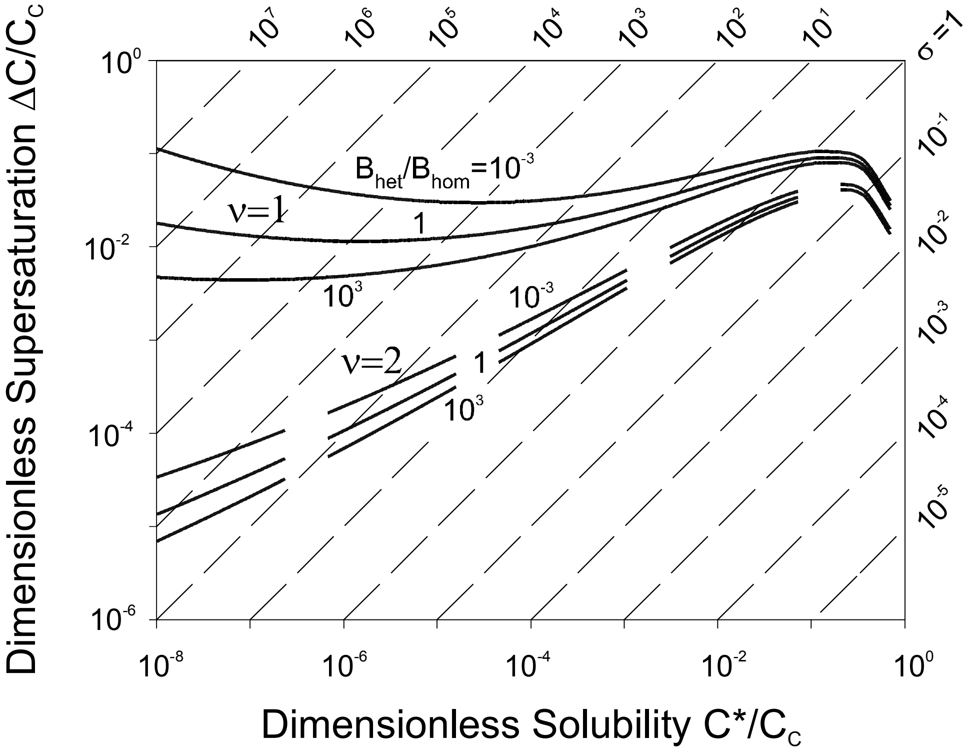

Figure 2-7: Ratio of heterogeneous to homogeneous nucleation rate (valid for: $D_{AB} = 10^{-9}\ m^2\ s^{-1}$*,* $d_m = 5 \cdot 10^{-10}\ m$*,* $K = 0.414$*,* $a_{for} = 10^5\ m^2\ m^{-3}$*,* $He_{ad} = 10^{-9}$*,* $f = 0.1$*)*

The basis of the model proposed by Schubert [Schu98] (see equation (2-36)) is the assumption of a flat or platelike foreign particle as shown in Figure 2-8. His model is appropriate for small nuclei on large particles, whereas in the case of large nuclei on very small foreign particles the surface area and the circumference of the nucleus are dependent on the shape of the foreign particle. Heyer [Heye01] extended Schuberts model to nucleation on small foreign particles, assuming spherical particles and clusters (see Figure 2-9).

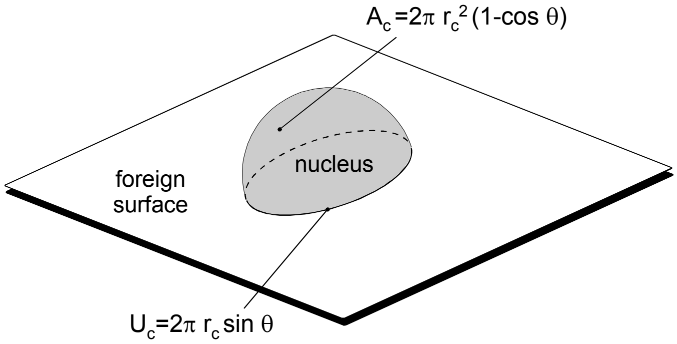

Figure 2-8: Model for heterogeneous nucleation according to Schubert [Schu98]

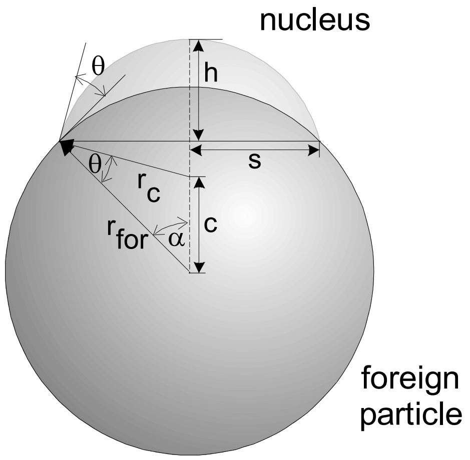

Figure 2-9: Model for heterogeneous nucleation according to Heyer [Heye01]

The model derived by Heyer is presented in equation (2-39).

$$B_{het} = 2\,a_{for}\,d_m\,He_{ad}\left(C\,N_A\right)\sqrt{\frac{\gamma_{CL}}{f\,k\,T}}\,\frac{1}{\left(C_C\,N_A\right)L_c}$$
$$\left[\frac{x\,\sin\theta}{m}\,\frac{D_{surf}}{2\,\pi}\left(He_{ad}\,d_m C\,N_A\right)^{3/2}+D_{AB}C\,N_A\left(1-\frac{1-x\cos\theta}{m}\right)\right]$$
$$\cdot\exp\left[-f\,\frac{16}{3}\,\pi\left(\frac{\gamma_{CL}}{k\,T}\right)^3\left(\frac{1}{C_C\,N_A}\right)^2\frac{1}{\left(\nu\ln S\right)^2}\right] \qquad (2\text{-}39)$$

where

$$x=\frac{r_{for}}{r_c} \qquad (2\text{-}40)$$

is the ratio of the sizes of foreign particle to critical nucleus, and m is given by:

$$m=\sqrt{1+x^2-2\,x\cos\theta} \qquad (2\text{-}41)$$

In the special case of homogeneous nucleation the following assumptions are valid:

- $\theta = 180°$; $\sin\theta = 0$; $\cos\theta = -1$
- $f = 1$ (see equation (2-32))
- $a_{for} \cdot d_m = 1$
- $He_{ad} = 1$
- $x \rightarrow 0$
- $m = 1$

With these specifications the rate of heterogeneous nucleation B_{het} suggested by Schubert (equation (2-36)) can be converted into the rate of homogeneous nucleation B_{hom} (equation (2-28)) as shown in the appendix 11.2.
Whereas B_{het} calculated with the model proposed by Heyer (equation (2-39)) equals 0 for the assumptions made for homogeneous nucleation.
As a consequence Schuberts model can be used for both cases, heterogeneous and homogeneous nucleation, whereas Heyers model is only valid for heterogeneous nucleation on very small foreign particles.

2.2.3 Surface or Secondary Nucleation

The third activated nucleation mechanism is the secondary or surface nucleation. In contrast to both primary nucleation mechanisms, homogeneous and heterogeneous, the presence of own crystals is a precondition for secondary nucleation. Nuclei are formed in the vicinity of own crystals (same substance) or on their surface by dendritic growth and coarsening [Denk70, Kind89]. According to [Niels81] and [Dirk91] the surface nucleation rate B_s can be written as, after the introduction of equation (2-26):

$$B_s = \frac{D_{AB}}{d_m^4} \exp\left\{ -\pi \frac{\left[K \ln\left(\frac{C_C}{C^*} \right) \right]^2}{\nu \ln S} \right\} \tag{2-42}$$

The pre-exponential factor D_{AB} / d_m is probably not correct, however, in the case of high solubilities (C^* / C_C > 0.01) the difference of data regarding the factor of equations (2-42) and (2-28) is not significant.
In order to convert the surface nuclei into volume nuclei it is necessary to remove them from the surface and place them into the solution. This demands a relation between the volumetric crystal surface a_C, the detachment probability of surface nuclei

or efficiency factor E (0 < E < 1) and the surface nucleation rate B_s as follows [Mers96]:

$$B_{surf} = E \cdot B_s \cdot a_C \tag{2-43}$$

An efficiency factor of 1 connotes that all surface nuclei will be detached from the crystal surface and become volume nuclei. Whereas an efficiency factor of 0 results in $B_{surf} = 0$ and in this case B_s would only contribute to the growth of the crystals.
Introducing the Sauter mean diameter of crystals, L_{32}, and the crystal hold-up φ_T equation (2-43) can be converted into:

$$B_{surf} = E \frac{6 \varphi_T}{L_{32}} B_s \tag{2-44}$$

2.2.4 Attrition induced Nucleation

In almost every crystallizer installations for solution circulation and suspending crystals, e.g. a stirrer or a pump, can be found. These mixing devices evoke crystal – crystal or crystal – installation collisions, thus producing small attrition fragments. These can act like new nuclei. The amount of produced attrition fragments or nuclei is dependent on the properties of the material and on the operating conditions of the crystallizer. Although attrition induced nucleation is a non-activated process, it is in most batch-cooling crystallizations the dominant nucleation mechanism, because these crystallizers are usually operated at very low supersaturations ($\sigma < 0.1$), where the rates of activated nucleation are extremely low, see Figure 2-4 and Figure 2-5. Therefore this mechanism is very crucial for an optimum operation of a crystallizer. Many experiments have shown that a huge number $N_{a,tot}$ of attrition fragments is produced in industrial crystallizers but only a small part of them has the ability to grow at these low supersaturations. Many authors have measured the size distribution of attrition fragments resulting from parent crystals which are suspended in a stirred vessel [Sang91, Heds94, Chia96, Gahn97]. In Figure 2-10 the number density and the cumulative number distribution of KNO_3 attrition fragments are plotted against the attrition fragment size L_a according to Gahn [Gahn97].

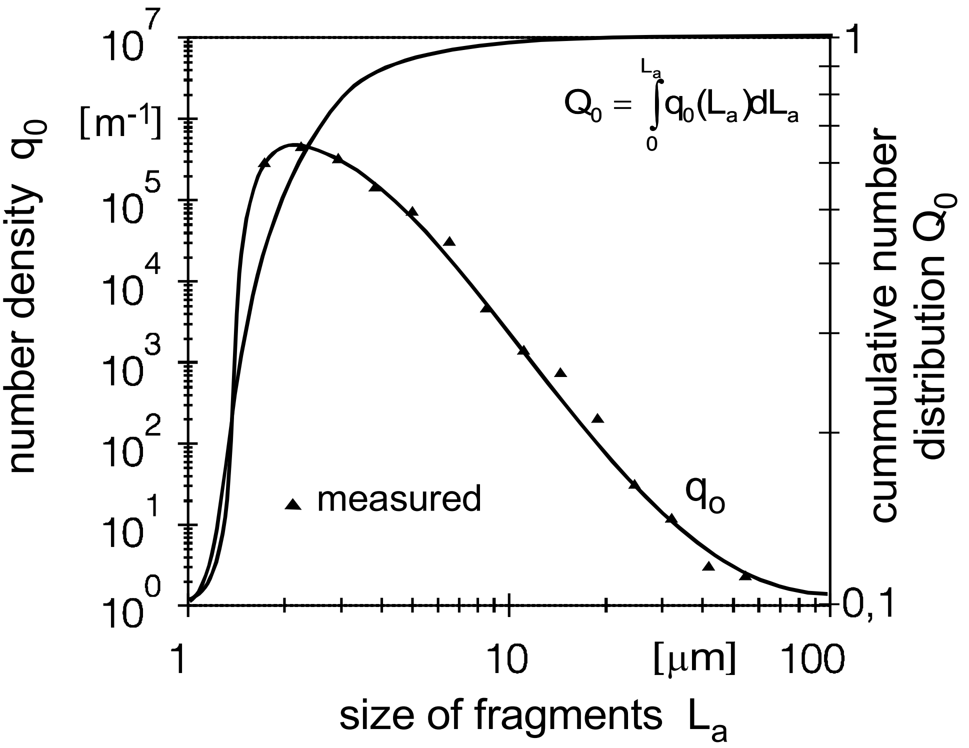

Figure 2-10:Number density and cumulative number distribution of KNO_3 attrition fragments [Gahn97]

It is somewhat surprising that only attrition fragments in the size range between 2 µm and 200 µm have been measured for stirrer tip speeds below 5 m/s. According to Gahn [Gahn97] the minimum size $L_{a,min}$ is given by

$$L_{a,min} = 9{,}4 \frac{\mu}{H_v^2}\left(\frac{\Gamma}{K_r}\right) \qquad (2\text{-}45)$$

and the maximum size $L_{a,max}$ can be calculated from

$$L_{a,max} = 0{,}5 \frac{H_v^{2/9}}{\mu^{1/3}}\left(\frac{K_r}{\Gamma}\right)^{1/3} W_{col}^{4/9} \qquad (2\text{-}46)$$

In these equations H_v is the Vickers Hardness, µ is the shear modulus, Γ is the fracture resistance, K_r is an efficiency factor and W_{col} is the collision energy which increases with the square of the collision velocity w_{col} according to

$$W_{col} = \alpha L_{par}^3 \rho_C \frac{w_{col}^2}{2} \qquad (2\text{-}47)$$

Here L_{par} is the size of the parent crystal and ρ_C is its density.
Theoretical considerations as well as many experimental results lead to the following equation for the total number $N_{a,tot}$ of attrition fragments resulting from one parent crystal which takes up the collision energy W_{col}:

$$N_{a,tot} = 7 \cdot 10^{-4} \frac{H_V^5}{\alpha \mu^3} \left(\frac{K_r}{\Gamma} \right)^3 W_{col} = 7 \cdot 10^{-4} \frac{H_V^5}{\mu^3} \left(\frac{K_r}{\Gamma} \right)^3 \alpha L_{par}^3 \frac{\rho_C w_{col}^2}{2} \qquad (2\text{-}48)$$

It is important to note that nearly all small attrition fragments possess an increased chemical potential (elevated solubility) due to deformation and do not grow at a low supersaturation [Heij92, Zach95]. Therefore the number $N_{a,eff}$ of effective attrition fragments is decisive for the rate of secondary nucleation. The effectiveness of KNO_3 attrition fragments has been determined by Wang [Wang92], see Figure 2-11. Here the growth rate of 356 KNO_3 fragments has been measured in growth cells.

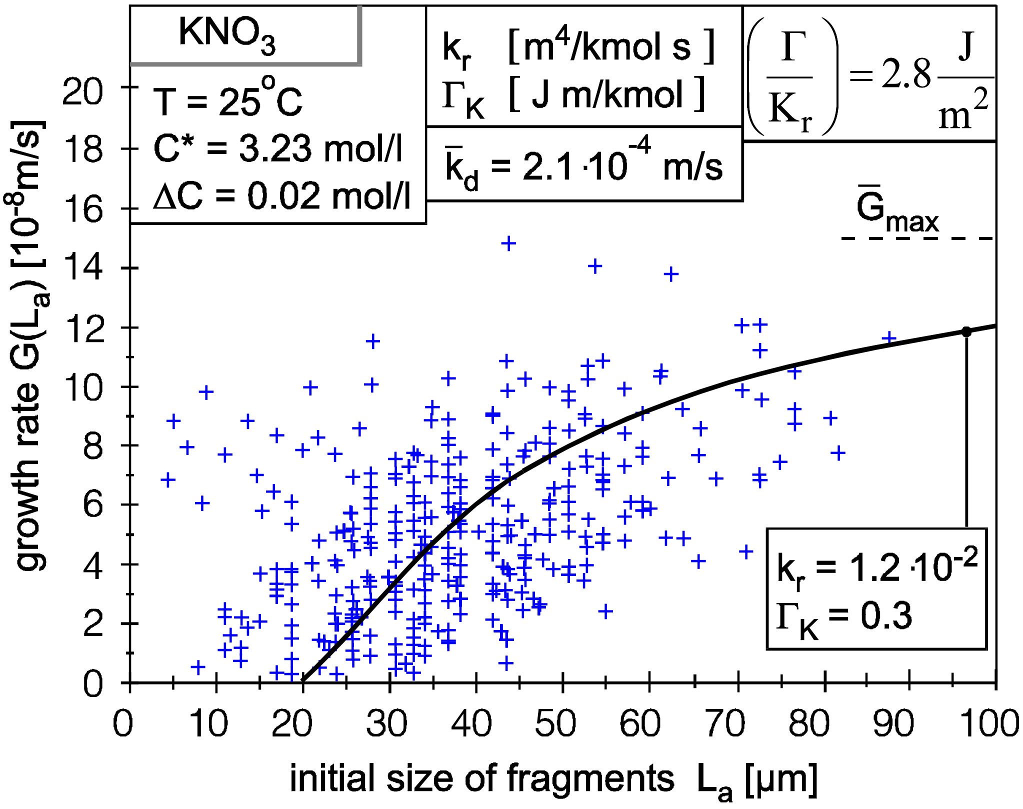

Figure 2-11: Growth rate of 356 KNO_3 attrition fragments [Wang92]

As can be seen only fragments larger than $L_{a,eff} = 25$ µm contribute significantly to growth $\left(G(L_a) > 0{,}1\,\overline{G}_{max}\right)$. In Figure 2-10 and Figure 2-12 the ratio $\frac{N_{a,eff}}{N_{a,tot}}$ according to

$$\frac{N_{a,eff}}{N_{a,tot}} = \int_{25\mu m}^{\infty} q_0(L_a)dL_a = 1 - \int_{0}^{25\mu m} q_0(L_a)dL_a \qquad (2\text{-}49)$$

is $\frac{N_{a,eff}}{N_{a,tot}} \approx 0.017$.

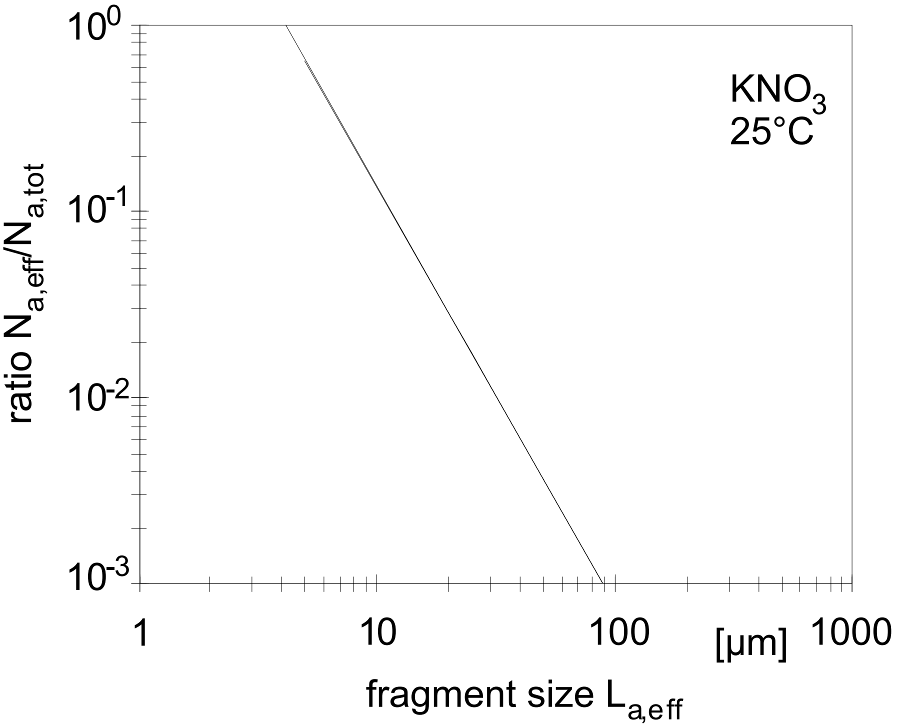

Figure 2-12: Ratio $N_{a,eff}/N_{a,tot}$ as a function of the size $L_{a,eff}$ of effective attrition fragments according to equation (2-49)

In the following a very simplified model will be presented in order to show how it is possible to give an estimation of the effective rate of attrition controlled secondary nucleation, $B_{0,eff}$. The purpose of this crude estimation is to clarify the importance of the material properties H_v, μ and $\left(\frac{\Gamma}{K_r}\right)$ which are described in more detail in [Mers01].

The mean specific power input, $\bar{\varepsilon}$, can be expressed by the Newton number Ne, the stirrer diameter d and the stirrer tip speed $u_{tip} = d\,\pi\,s$:

$$\bar{\varepsilon} = \frac{Ne}{\pi^3} \frac{u_{tip}^3 d^2}{V_{Susp}} \tag{2-50}$$

Here V_{susp} is the volume of the suspension. The collision velocity, w_{col}, is smaller than the tip speed:

$$w_{col} = \eta_w \, u_{tip} \tag{2-51}$$

and the frequency of contacts, f_c, of a parent crystal with the rotor is smaller than the speed s:

$$f_c \approx \eta_f \eta_w \frac{\dot{V}}{V_{Susp}} = \eta_f \eta_w \frac{N_v n d^3}{V_{Susp}} \tag{2-52}$$

with $\eta_f = \eta_{geo}$ (for propeller) ≈ 0.03.

A combination of the equations (2-48), (2-50), (2-51) and (2-52) leads to

$$\frac{f_c N_{a,tot}}{V_{Susp}} = 7 \cdot 10^{-4} \frac{H_v^5}{\mu^3} \left(\frac{K_r}{\Gamma} \right)^3 \frac{\pi^2 \rho_c \bar{\varepsilon} N_v}{2Ne} \frac{L_{par}^3}{V_{Susp}} \eta_w^3 \eta_f \tag{2-53}$$

The right hand side of this equation has to be multiplied by the factor $\frac{N_{a,eff}}{N_{a,tot}}$ and by the total number of parent crystals which amounts to $\frac{V_{Susp}\,\varphi}{(\alpha L_{par})^3}$ in the case of monodispersed parent crystals. This leads to the effective rate of secondary nucleation based on the volumetric crystal hold-up:

$$\frac{B_{0,eff}}{\varphi} = 7 \cdot 10^{-4} \frac{H_v^5}{\mu^3} \left(\frac{K_r}{\Gamma} \right)^3 \frac{\pi^2 \rho_c \bar{\varepsilon} N_v}{2\alpha^3 Ne} \frac{N_{a,eff}}{N_{a,tot}} \eta_w^3 \eta_f \tag{2-54}$$

All these four nucleation mechanisms, which were briefly explained during the previous pages, contribute to the entire nucleation rate B_0 in the following way:

$$B_0 = B_{hom} + B_{het} + B_{surf} + B_{att} \tag{2-55}$$

Depending on the operating conditions of a crystallizer one of these nucleation mechanisms will be dominant. Generally speaking at very high supersaturations heterogeneous nucleation B_{het} outmatches surface or attrition induced nucleation. Since we consider only batch crystallization processes, homogeneous nucleation can be neglected as it plays only a major part in precipitation where very high supersaturations are achieved (S > 100). In the case of low supersaturations and a high mean specific power input $\bar{\varepsilon}$, B_{att} is the decisive nucleation mechanism.

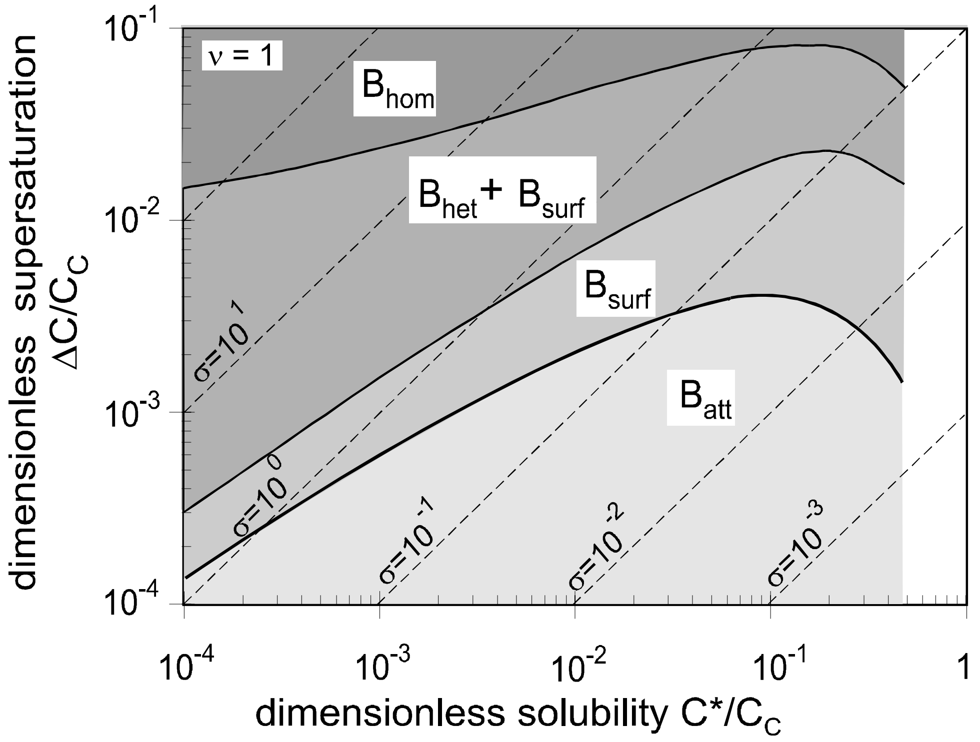

Figure 2-13: Regions for the different nucleation mechanisms plotted as a function of the dimensionless solubility and the dimensionless supersaturation [Mers96]

Figure 2-13 shows lines of constant nucleation rates valid for $B_{hom} = 10^{18}$ m^{-3} s^{-1} and $B_{surf} = 1$ m^{-3} s^{-1}. B_{het} was calculated with the assumption of f = 0.1. It can be seen that in the case of low supersaturations ($\sigma < 0.1$) B_{att} is dominant. In order to produce large crystals this region should be chosen for the operation of the crystallizer since it prevents activated nucleation and the generation of many small particles.

2.3 Crystal Growth: From Nucleus to Crystal

In the previous section the various mechanisms of nucleation have been briefly explained. In the following the complex mechanisms of crystal growth will be introduced.

The general definition of a growth rate G is the change of size L of a crystal within time t:

$$G = \frac{dL}{dt} \tag{2-56}$$

The growth of a crystal requires many subsequent processes until a growth unit is incorporated into the crystal lattice. Mullin [Mull93] distinguishes between seven different steps. In order to reduce the high complexity of the growth mechanism the various steps can be summarized and divided into a transportation step by diffusion and / or convection and an integration reaction step. In the case of a slow diffusion step which is compared to the integration step the growth mechanism can be characterised as diffusion-controlled, whereas an integration controlled growth implies a very slow integration reaction.

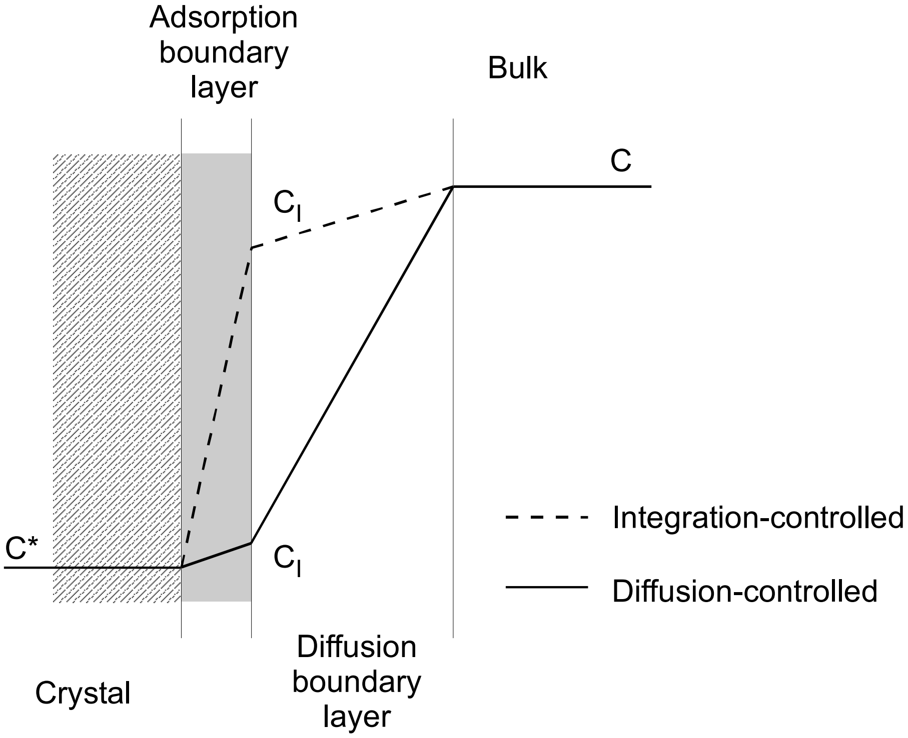

Figure 2-14: Concentration profiles for diffusion- and integration-controlled growth

With reference to Figure 2-14 the driving force or concentration gradient $\Delta C = C - C^*$ can be seen as the sum of a diffusive - convective term, $C - C_I$, and an integration reaction term, $C_I - C^*$. For an integration – controlled growth $C_I - C^* \gg C - C_I$ is valid, whereas for diffusion – controlled growth $C_I - C^* \ll C - C_I$ is obtained. The mass flux density, $\dot{m}$ with direction towards the crystal surface is defined by:

$$\dot{m} = \tilde{M}\,k_d(C - C_I) = \tilde{M}\,k_r(C_I - C^*)^r \qquad (2\text{-}57)$$

Here, k_d is the mass transfer coefficient, k_r the reaction rate constant, and r the order of the integration reaction.

Another way of describing crystal growth is via a displacement rate, v, of a crystal surface which corresponds to equation (2-56). The coherence of the growth rate G, the mass flux density $\dot{m}$, and the displacement rate v is shown in equation (2-58).

$$G = \frac{\dot{m}\,\beta}{3\,\alpha\,\rho_C} = 2\,v \qquad (2\text{-}58)$$

Where the volume shape factor α and the surface shape factor β are defined by

$$\alpha = \frac{V_P}{L^3} \qquad (2\text{-}59)$$

and

$$\beta = \frac{A_P}{L^2} \qquad (2\text{-}60)$$

Here V_P is the volume of the particle and A_P is the surface area of the particle.

2.3.1 Diffusion Controlled Growth

If the diffusion step is slow compared to the integration step the crystal growth is dominated by the diffusive – convective transport of growth units. The diffusion – controlled growth rate can be calculated by

$$G = \frac{\beta}{3\alpha}\,k_d\,\frac{\Delta C}{C_C} \qquad (2\text{-}61)$$

For spherical particles (β / 3α = 2) and pure molecular diffusion the following equation is valid:

$$k_d = 2\frac{D_{AB}}{L} \qquad (2\text{-}62)$$

The analogy between the mass transfer coefficient and the Sherwood number Sh

$$Sh = k_d \frac{L}{D_{AB}} \qquad (2\text{-}63)$$

reveals the dependence on fluid dynamics, particle size, diffusivity, and viscosity. In order to choose a correct model among the existing ones for the determination of $k_{d,}$ it should always be paid attention to the prevailing boundary conditions. In addition, it also has to be mentioned that growth rates obtained by equation (2-61) always represent the maximum possible growth rate, because no growth unit may be integrated into the crystal lattice that has not been first transported through the bulk solution.

2.3.2 Integration Controlled Growth

A fast diffusive – convective transport of growth units ($k_d \rightarrow \infty$) and / or a very slow integration reaction into the crystal lattice ($k_r \rightarrow 0$) implies an integration – controlled growth mechanism. Due to the complexity of this integration step different models have been developed in order to predict growth rates. In the following a short overview of the major models will be given.

In the model of Burton, Cabrera and Frank [Fran49, Burt51], also known as the BCF model, steps on the crystal surface are created by dislocations, thus creating imperfections as favourable integration sites for growth units. In the case of low supersaturations these spiral steps offer the only location for the integration of growth units since the crystal surface is rather smooth, thus leading to further growing spiral steps on the crystal surface. Equation (2-64) shows the result of the deliberations of Burton, Cabrera and Frank:

$$v_{BCF} = K_{BCF}\, T\left(\frac{\Delta C}{C*}\right)^2 \tanh\left(\frac{K'_{BCF}}{T}\frac{C*}{\Delta C}\right) \qquad (2\text{-}64)$$

The parameters K_{BCF} and K'_{BCF} are difficult to determine, for further information see [Burt51, Benn69, Benn73, Benn76]. It can be seen in equation (2-64) that in the case of low supersaturations the linear growth rate v_{BCF} is proportional to the second power of the supersaturation as it depends on the density of steps and kinks on the crystal surface.

$$v_{BCF} \sim \sigma^2 \qquad (2\text{-}65)$$

For high supersaturations a linear correlation between the growth rate v_{BCF} and the supersaturation σ is valid:

$$v_{BCF} \sim \sigma \qquad (2\text{-}66)$$

In the case of even higher supersaturations, the collision of growth unit clusters on the crystal surface, which leads to the forming of two-dimensional nuclei spreading over the crystal surface, has to be taken into account, too. This is done in the Birth and Spread (B+S) model [Ohar73, Hill66, Niel81]. The linear growth rate v_{B+S} is given by

$$v_{B+S} = K_{B+S}\left(\frac{\Delta C}{C^*}\right)^{5/6} \exp\left(\frac{-K'_{B+S}}{T}\frac{C^*}{\Delta C}\right) \qquad (2\text{-}67)$$

and demands an exponential dependence on supersaturation.
The size of a critical nucleus decreases with increasing supersaturation (see equation (2-37)). As a consequence this critical size approximates to the average size of a growth unit. The two assumptions of a small spreading rate and of the only possible completion of a surface layer by nuclei formation leads to the polynuclear (PN) growth model [Dirk91], which shows a very strong dependence on supersaturation. With equation (2-26) we obtain:

$$v_{PN} = \frac{D_{AB}}{3\,d_m}\left(\frac{\Delta C}{C_C}\right)^{2/3} \exp\left(-\pi\frac{\left[K\ln\left(\frac{C_C}{C^*}\right)\right]^2}{\nu \ln S}\right) \qquad (2\text{-}68)$$

2.3.3 General Characterization of Crystal Growth Rates

Of course all integration–controlled growth rates (BCF, B+S, and PN) occur simultaneously when a crystal is growing. The answer to the question which mechanism plays the major role depends on the prevailing supersaturation. Integration–controlled crystal growth is a competition between the three different mechanisms, dominated by one of them. In Figure 2-15 the different mechanisms are plotted as a function of the supersaturation.

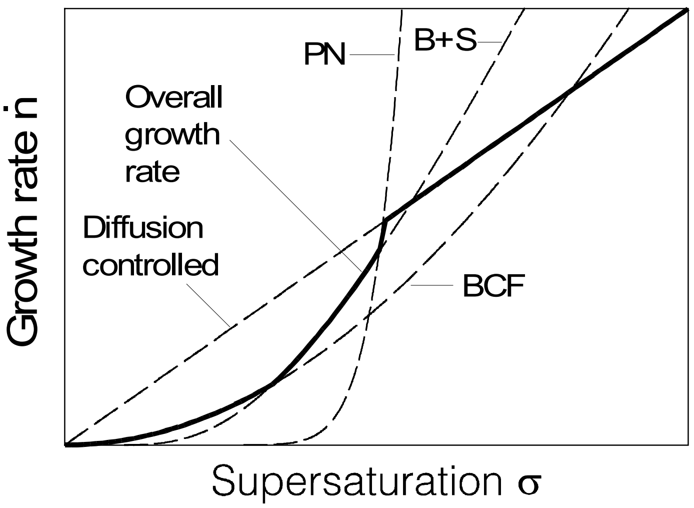

Figure 2-15: Competing growth mechanisms as a function of supersaturation σ

Crystal growth which is solely controlled by either diffusion or integration is hardly found, in most cases both steps play a limiting role. Therefore a model considering the diffusion and the integration step was derived by Mersmann [Mers95]. With the help of this model mean crystal growth rates $\bar{v}$ for crystal collectives in industrial crystallizers can be calculated according to

$$\frac{\bar{v}}{k_d} \equiv \frac{G}{2k_d} = \frac{\Delta C}{C_C} + \frac{k_d}{2k_g'}\left(\frac{C^*}{C_C}\right)^2 - \sqrt{\left(\frac{k_d}{2k_g'}\right)^2\left(\frac{C^*}{C_C}\right)^4 + \frac{k_d}{k_g'}\left(\frac{C^*}{C_C}\right)^2\frac{\Delta C}{C_C}} \qquad (2\text{-}69)$$

with the growth rate constant k_g'

$$k_g' = 2.25 \cdot 10^{-3} \nu^2 \frac{D_{AB}}{d_m} \frac{\left(C^*/C_C\right)^{4/3}}{\ln\left(C_C/C^*\right)} \qquad (2\text{-}70)$$

The value 2.25 · 10^{-3} was determined by experiments at 25°C, as a consequence equation (2-70) should only be used for calculations in the same temperature range, otherwise a correction factor has to be added. Figure 2-16 shows lines of crystal growth rates calculated with equation (2-69) for various systems according to the parameter C^*/C_C. The growth rates are plotted as a function of supersaturation σ and the regions indicating the dominant growth mechanism are shown.

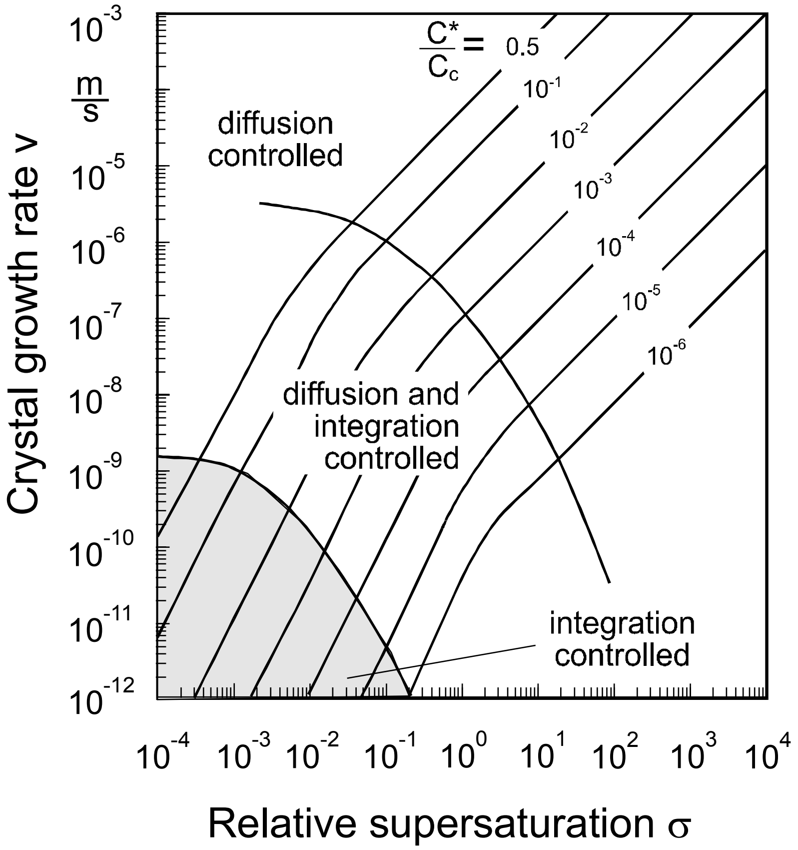

Figure 2-16: Crystal growth rate v *as a function of supersaturation* σ *(valid for* $k_d = 10^{-4}\ m\ s^{-1}$ *and* $D_{AB} = 10^{-9}\ m^2\ s^{-1}$*)*

2.4 Metastable Zone and Induction Time: What we still cannot see!

To express it in very simple terms, the metastable zone is one of the last frontiers in crystallization. The knowledge about that phenomenon is very little in comparison to nucleation and growth. But due to the topic of this thesis it is inevitable to describe it in more details since it plays a very important role in the operation of crystallizers. In general terms of thermodynamics, the difference between a stable and a metastable state is that a small perturbation does not affect the stable state as it soon returns to its

initial state, whereas a metastable state becomes instable which leads to irreversible changes.
The idea of the metastable zone was first introduced by Ostwald [Ostw97]. He mentioned the terms stable, metastable and unstable (labile) in context with the solubility plot. He defined the border between the metastable and the stable region in the solubility plot by the onset of an uncontrolled, spontaneous and detectable nucleation (nuclei shower, avalanche effect). This implies that there is an individual metastable zone for each activated nucleation mechanism, which can be seen in Figure 2-17.

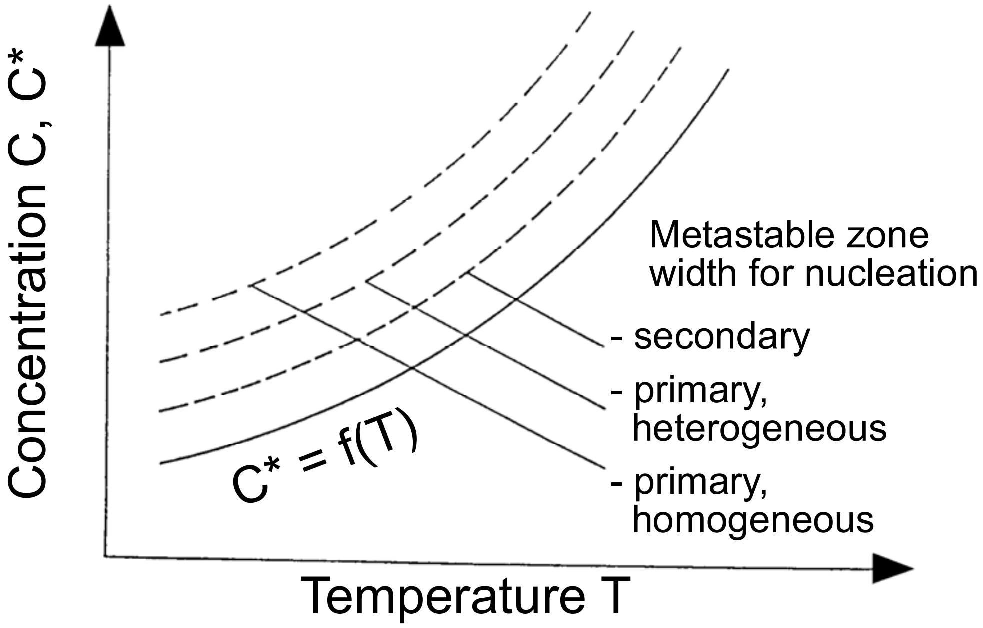

Figure 2-17: Metastable supersaturations for different nucleation mechanisms

Miers [Miers07] tried to explain that phenomenon by the introduction of the supersolubility curve which is almost parallel to the solubility curve. As a consequence the following zones and border lines can be defined according to the solubility plot.

- stable zone (undersaturated):
  no crystallization possible
- solubility or equilibrium curve (saturated):
  border line between undersaturated and supersaturated state
- metastable zone (supersaturated):
  crystallization possible, but no spontaneous nucleation
- supersolubility curve (supersaturated):
  border line between metastable and unstable zone
- unstable (labile) zone (supersaturated):
  spontaneous and uncontrolled nucleation

Unfortunately the metastable zone, also called the Ostwald-Miers-Zone, cannot be predicted with the help of physical or thermodynamic properties of a solute – solvent system. It is therefore necessary to determine the metastable zone width for each system experimentally. According to Figure 2-2 the metastable zone width can be expressed by the supersaturation ΔC_{met} or the subcooling ΔT_{met} at which spontaneous nucleation occurs. Unfortunately it is not possible to derive empirical correlations from experiments which are universally valid for the metastable zone width of one specific system since the metastable zone width depends on various parameters:

- temperature
- rate of supersaturation generation (cooling or evaporation rate)
- agitation
- thermal history of the solution
- presence of seed crystals
- presence of impurities
- method of detection
- definition of the "nuclei shower"

The dependence of the metastable zone width on the presence of seed crystals is shown in Figure 2-18, where experiments with an $(NH_4)_2SO_4$-solution were conducted. The different slopes indicate different nucleation mechanisms.

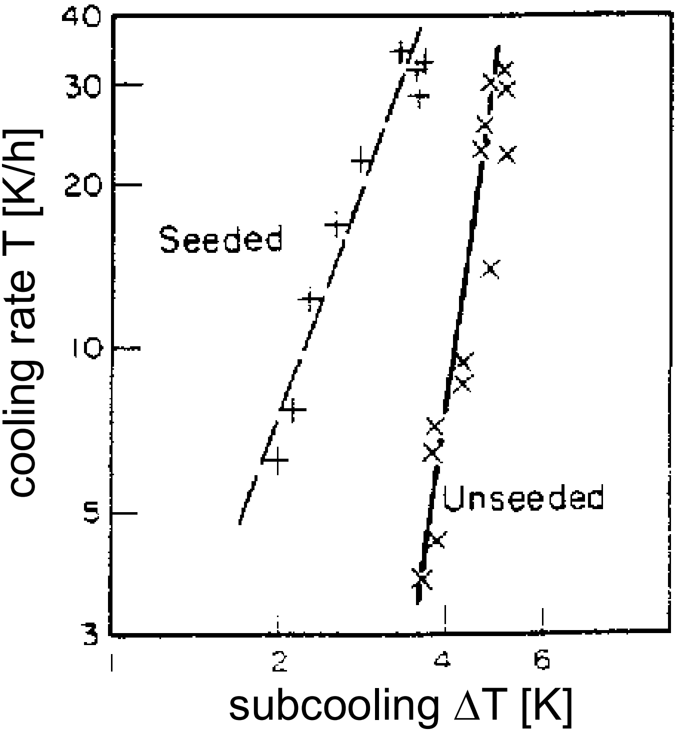

Figure 2-18: Metastable subcoolings ΔT_{met} for seeded and unseeded ammonium sulphate solutions as a function of the cooling rate [Mull70]

Extremely crucial is the detection of the onset of the nucleation as this could be defined for instance by a nucleation rate $B = 1\ m^{-3}\ s^{-1}$ or by a "noticeable" nucleation rate $B = 10^{30}\ m^{-3}\ s^{-1}$. In addition to the definition of the required nucleation rate the detection device or the detectable size L_{det} of the nuclei is also decisive, since nuclei are hardly detectable at their moment of creation. This means that the subsequent growth of the nuclei to the detectable size L_{det} is also influencing the metastable zone width.

There are two different ways to measure the metastable zone:

- polythermal method ($T, \sigma \neq$ const.)

  The solution is cooled with a constant cooling rate $\dot{T}$ from an undersaturated state until the detection of a nuclei shower. The difference of the saturation temperature T^* and the temperature T reached at the moment of detection of nucleation determines the metastable zone width ΔT_{met}.
- isothermal method (T, σ = const.)

  A well defined supersaturation is established and the induction time t_{ind} until the start of the detectable nucleation is measured. By plotting the induction time t_{ind} as a function of the supersaturation or subcooling, as indicated in Figure 2-19, the metastable zone width is obtained.

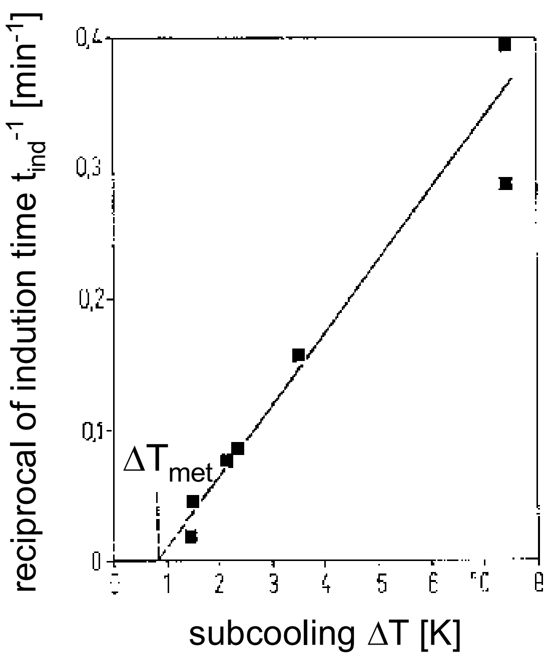

Figure 2-19: Determination of the metastable zone width for a KCl – solution by plotting the reciprocal induction time as a function of the subcooling [Seife76]

Different measurement methods are given in [Kind89, Mull79, Mull93, Nyvl70, Seife76].

Nyvlt [Nyvl70] discovered a higher reproducibility for the determination of the metastable zone width for anhydrates than for hydrates. This is in agreement with the model of nucleation, where clusters have to be formed by stochastic collisions. He also states a higher metastable zone width for sparingly soluble systems in comparison to high soluble systems. His explanation is that a higher concentration, as is the case for high soluble systems, leads to a smaller inter-molecular distance, thus promoting the probability of collisions in order to form a cluster or nucleus.

The already mentioned induction time t_{ind} is defined by the time period elapsed between the achievement of supersaturation and the onset of nucleation. In case of a polythermal measurement method the relationship between metastable zone width ΔT_{met} and induction time t_{ind} is the following:

$$\Delta T_{met} = t_{ind} \dot{T} \qquad (2\text{-}71)$$

Therefore the induction time t_{ind} shows the same dependence on various process parameters as the metastable zone width. Mullin [Mull93] defines induction time t_{ind} as the sum of relaxation time t_r, nucleation time t_n, and growth time t_g.

$$t_{ind} = t_r + t_n + t_g \qquad (2\text{-}72)$$

The relaxation time t_r is the time required by the system to establish a quasi-steady-state distribution of molecular clusters, the nucleation time t_n represents the time for the formation of a stable nucleus, and the growth time t_g is needed for the growth of a nucleus to a detectable size L_{det}. Unfortunately its nearly impossible to distinguish between these three time periods.

Although the best way for a determination of the metastable zone width is to conduct time consuming experiments, which are also extremely dependent on various parameters, it is a good guideline for the adjustment of the operating supersaturation during the crystallization process [Mers98, Mull93, Tava95]. The measurement of a metastable zone for an unseeded solution $\Delta C_{met,prim}$ has a very low industrial relevance, since secondary nucleation is the dominating mechanism in most crystallizations from solution. Thus the smallest metastable zone width for a seeded solution $\Delta C_{met,sec}$ can be regarded as the maximum supersaturation that can be adjusted during the crystallization process, since nuclei shower should be avoided.

Mersmann [Mers98, Mers00] proposed a model for the estimation of metastable zone widths. This model, which is only valid for seeded solutions, considers the growth of crystals to a detectable size L_{det} as the relevant step. It will be discussed in more details in chapter 4.2 since it can also be used for the estimation of the optimal supersaturation for cooling as well as for evaporation crystallization.

2.5 Agglomeration – How Particles stick together

In most cases of crystallization from solutions high median crystal sizes are desired. In this range agglomeration plays only a minor role. Whereas in precipitation, where particles in the size range of nanometers are generated, agglomeration can be a very decisive mechanism since it has a strong influence on the particle size distribution. Nevertheless a short introduction to agglomeration will be given in the next paragraphs.

It is nearly impossible to compare theoretically predicted agglomeration with experimental results because it is very hard to separate or distinguish between the different mechanisms of nucleation, growth and agglomeration. Furthermore the population balance equation (PBE), which must be often used in crystallization in addition to mass and energy balance, is a integro partial differential equation and in most cases not analytically solvable. Considering a volume V, the PBE describes the change of the number density n by growth G, the in- and outflow of the volume $\dot{V}_i$ with the number density n_i and agglomeration [Rand88].

$$\frac{\partial n}{\partial t} + \frac{\partial (G\,n)}{\partial L} + D_{agg} - B_{agg} + \sum_k \frac{\dot{V}_i n_i}{V} = 0 \tag{2-73}$$

$$D_{agg}(L,\lambda) = n(L)\int_0^{\infty} \beta(L,\lambda)\,n(\lambda)\,d\lambda \tag{2-74}$$

$$B_{agg}(L,\lambda) = \frac{1}{2}\int_0^{L} \beta(L,L-\lambda)\,n(\lambda)\;n(L-\lambda)\,d\lambda \tag{2-75}$$

In order to solve the equations (2-74) and (2-75) an expression for the agglomeration kernel β(L, λ) is required. Considering only collisions between two particles the agglomeration rate can generally be described by:

$$-\frac{dN}{dt} = \beta\,N^2 \tag{2-76}$$

The theory of von Smoluchowski [Smol17] basically distinguishes between ortho- and perikinetic agglomeration. In the case of perikinetic agglomeration collisions of particles are caused by Brownian motion and lead to an agglomeration rate proportional to the second power of the particle number N.

Generally speaking the agglomeration kernel β consists of two parts, one part depending on particle size with the particle radii r_1 and r_2 and the other part describing hydrodynamics and particle interaction. According to von Smoluchowski the following equation is valid for perikinetic agglomeration:

$$\beta = \frac{2\,k\,T}{3\,\eta\,W}\left(r_1 + r_2\right)\left(\frac{1}{r_1} + \frac{1}{r_2}\right) \qquad (2\text{-}77)$$

where W is an efficiency factor which takes into account the particle interaction that is influenced by many parameters, like particle size, pH, and ionic strength [Mers01].

External force fields and forces by fluid play a major role in orthokinetic agglomeration, which is dominant in the case of particle sizes larger than 1 µm, where Brownian motion becomes negligible. If collisions are caused by different settling velocities in a solution at rest, the following equation is valid for the agglomeration kernel β:

$$\beta = \pi\,g\left(r_1 + r_2\right)^2\left(1 - \frac{\rho_F}{\rho_C}\right)\left|\tau_1 - \tau_2\right| \qquad (2\text{-}78)$$

$$\tau_i = \frac{2\,r_i^2\,\rho_C}{9\,\eta} \quad \text{with}\; i = 1,2 \qquad (2\text{-}79)$$

Here the agglomeration kernel β is a function of the ratio of the densities of fluid and solid ρ_F / ρ_C. If the particles have the same size the relaxation times τ_i have also the same values, thus the agglomeration kernel β is zero, which means that no collisions take place.

A general mathematic description of agglomeration in a flow field is given by:

$$-\frac{d\,N}{d\,t} = \alpha\,\beta_{coll}\,N^2 \qquad (2\text{-}80)$$

The efficiency factor α takes the collisions contributing to agglomeration into account. Unfortunately it is very complex to predict α theoretically [Brau02]. For the collision kernel β_{coll} various expressions for laminar and turbulent flow can be found in literature [Abra75, Camp43, Krui97, Kubo72, Saff56, Smol17]. The influencing parameters are the local specific power input ε and the supersaturation S. The influence of supersaturation S on the agglomeration kernel β through the efficiency factor α is described in [Hart86a, Hart86b, Marc88, Mumt97, Mumt00]. Breakage and attrition caused by particle – apparatus or particle – particle collisions has to be considered if a certain power input is exceeded.

In order to calculate agglomeration it is inevitable to know the actual fluid dynamics and all forces affecting the particles, otherwise it is not possible to choose the right agglomeration kernel.

3 Operational Modes and Control of Cooling Crystallizers

In this chapter it will be shown how cooling crystallization is realised in industrial scale apparatuses. Furthermore, additional aspects of the necessity and the implementation of process control will be discussed. To put it into simple words, it will be shown how a crystallizer is turned into a 'good' crystallizer.

At first the question of the difference between cooling crystallization and other crystallization processes should be answered. Cooling crystallization is only one of various crystallization processes applied in industry and can generally be categorized according to the method of supersaturation generation (see Table 3-1).

Table 3-1: Crystallization processes for $d\,C^* / d\,T \geq 0$

process	supersaturation established by
cooling crystallization	change of temperature
evaporation crystallization	removal of solvent
vacuum crystallization	removal of solvent & change of temperature
precipitation	chemical reaction
drowning-out	change of solubility

The field of application for cooling crystallization is therefore limited to substances with solubilities which have a positive dependence on temperature ($d\,C^* / d\,T >> 0$). The minimum slope of the solubility curve required for an economic cooling crystallization will be discussed in Chapter 4.

The possible operational modes of cooling crystallization are:

- batch
- semi-continuous
- continuous

In the following only batch and continuos cooling crystallization will be considered since semi-continuos operation is a mixture of the two other operational modes.

Different control methods and strategies have been developed but all of them have the same objective: the improvement or adjustment of product quality.

The major parameters characterising a crystalline product are:

- crystal median size L_{50}
- crystal size distribution (CSD)
- specific surface area
- shape
- purity
- morphology

Generally speaking, there are three major process parameters used for control strategies in cooling crystallization:

- mean specific power input $\bar{\varepsilon}$
- residence time τ
- supersaturation σ

It is assumed that the geometry (diameter of the impeller etc.) and the fluid dynamics (speed, tip speed etc.) are optimized and, therefore, the flow conditions can be characterized by the mean specific power input ε.

These parameters, however, cannot be implemented independently in a control strategy since they interact with each other.

Classified product removal and fines destruction represent additional possibilities to influence the CSD of the product. Since the latter methods only eliminate crystals of undesired size, which emerged from an uncontrolled process, it will only be introduced briefly at the end of this chapter.

Batch crystallizers are often employed for the manufacture of small to medium tonnage products, especially with changing compositions or production sequences and well-defined product requirements or quality. Flexibility of the process, simplicity of the equipment and low encrustation due to easy cleaning of the heat exchanger surfaces after each crystallization make batch crystallization attractive. Lower operating costs and less complicated supersaturation control are advantages of continuously operated crystallizers. They are suitable for large tonnage products, provided that the demanded product quality can be fulfilled.

Considering batch cooling crystallization and control of supersaturation there are three different cooling strategies applicable:

natural cooling:

The cooling jacket of the crystallizer is provided with a coolant of a constant temperature ϑ_{cool}. According to Newtons-law the temperature of the solution as function of time t $\vartheta(t)$ can be calculated by [Dave00]:

$$\vartheta(t) = \vartheta_\omega + \exp\left(\frac{-t}{\tau_B}\right)(\vartheta_\alpha - \vartheta_\omega) \tag{3-1}$$

with the initial temperature ϑ_α, the final temperature ϑ_ω and the batch time constant τ_B:

$$\tau_B = \frac{M_{sol}\, c_p}{h\, A_{cool}} \tag{3-2}$$

M_{sol} is the mass of the solution with the specific heat capacity c_p, h the overall heat transfer coefficient and A_{cool} the heat transfer area.

linear cooling:

The temperature of the coolant is adjusted to a linear decrease of the solution temperature ϑ_{sol} defined by a constant cooling rate $\dot{T}$:

$$\vartheta(t) = \vartheta_\alpha - \dot{T}\, t \tag{3-3}$$

controlled cooling:

Neglecting size dependent crystal growth and attrition, a cooling rate guaranteeing a constant nucleation and crystal growth rate is chosen. Although this strategy is probably the best solution, two major problems come along with controlled cooling: The determination of the optimal supersaturation (see chapter 4 for more details) and the time consuming precalculation of the cooling curve. Various authors have developed complex models [Jone73, Jone74, Mayr88, Mull71] for the evaluation of the cooling curve. A simplified estimation of a controlled cooling curve was given by Mullin and Nyvlt [Mull71]:

$$\vartheta(t) = \vartheta_\alpha - \left(\frac{t}{\tau_B}\right)^n (\vartheta_\alpha - \vartheta_\varpi) \tag{3-4}$$

where τ_B is the batch time, the exponent n equals 4 for unseeded crystallization and 3 in case of a seeded crystallization. Considering all the different existing models, they are subjected to the condition of a constant supersaturation which is smaller than the metastable supersaturation $\sigma < \sigma_{met}$:

$$\frac{d\sigma}{dt} = \text{const.} \tag{3-5}$$

A comparison of the three different cooling strategies is shown in Figure 3-1. Natural cooling results in high initial cooling rates, thus creating a very high supersaturation which might exceed the metastable zone and lead to an undesired nuclei shower. Additionally high crystal growth rates cause incorporation of impurities. At the end, a low and therefore uneconomic cooling rate can be observed. Linear cooling reduces these problems since the initial cooling rates are lower. Nevertheless it is far from being an optimum cooling strategy as the possibility of crossing the metastable limit at the beginning of the crystallization is still very high. Only a controlled or in this case precalculated cooling curve is able to avoid uncontrolled crystallization by keeping the supersaturation at an optimum level below the metastable limit.

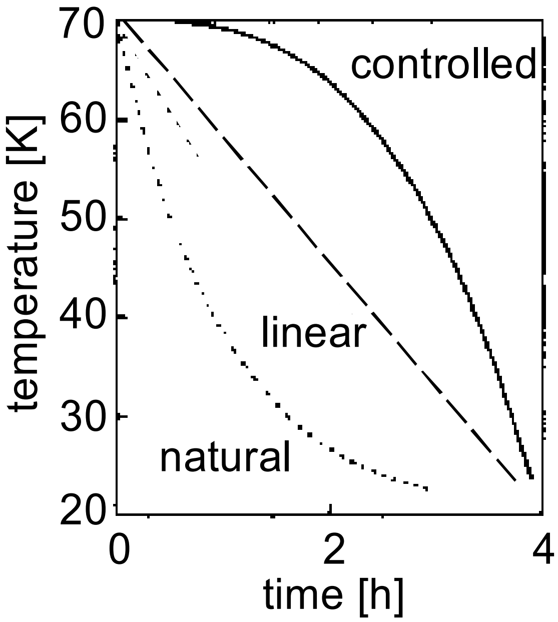

Figure 3-1: Natural, linear and controlled cooling

It can be seen that the controlled cooling curve is nearly the mirror image of the natural cooling curve as it ensures low initial cooling rates increasing with batch time. In this way supersaturation is kept within the metastable zone keeping activated nucleation and growth rates at a low level. In the final stages of batch crystallization the cooling rate is increased because the huge amount of crystals already produced provides a large surface area for the reduction of supersaturation by growth.

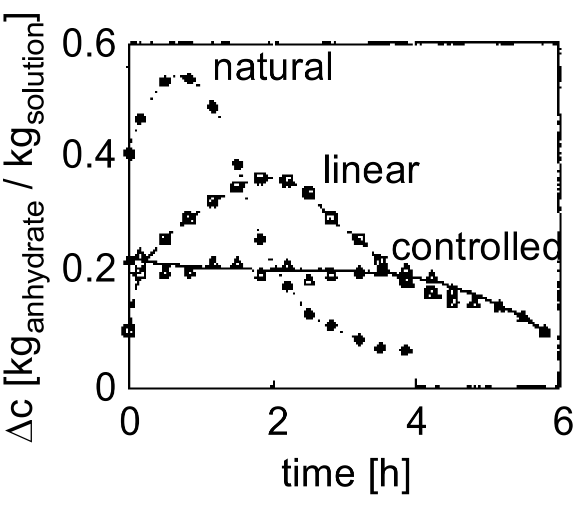

Figure 3-2: Course of supersaturation during batch crystallization of K_2SO_4 [Dave00]

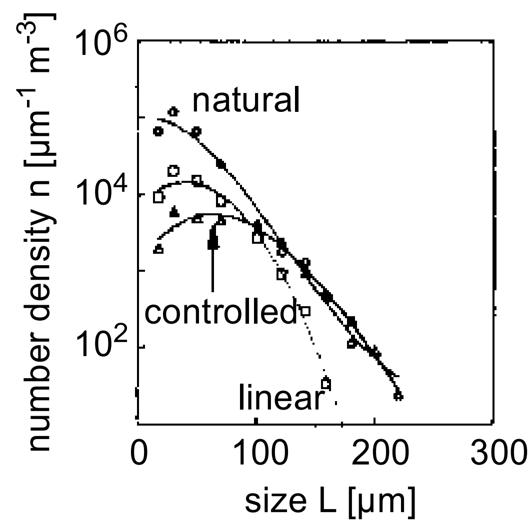

Figure 3-3: Influence of the cooling strategies on the number density n of K_2SO_4 crystals [Dave00]

Figure 3-2 depicts the high initial supersaturation peaks occurring in the cases of natural or linear cooling and the almost constant level of supersaturation provided by controlled crystallization. The obvious minimization of the small particle fraction by a controlled cooling strategy and thus the rising of the median crystal size L_{50} is shown in Figure 3-3.

Seeding is another technique to prevent a high supersaturation peak at the beginning of a crystallization process leading to uncontrolled nucleation. Adding crystals to a solution at the moment when the equilibrium state is left, i. e. supersaturation is created, leads to a reduction of supersaturation by growth of the seed crystals and surface nucleation which takes place at lower supersaturations than heterogeneous nucleation. It is, however, very important to determine the exact moment of seeding. Adding the seed crystals too early, when the solution is still undersaturated, would lead to the dissolution of the seed crystals, whereas late seeding diminishes the advantage of the seeding technique since high supersaturations have already been established. The required mass of seed crystals M_S of a median size L_S can be estimated according to [Gutw94]:

$$M_S = -\frac{2\alpha_S}{\beta_S}\left(\frac{dW^*}{dT}\right) M_{Solv} \frac{\dot{T} L_S}{G_{met}} \left(1 + \frac{1}{2}\frac{G_{met}\,\Delta T_{met}}{\dot{T} L_S}\right)^{-2} \qquad (3\text{-}6)$$

where M_{Solv} is the mass of the solvent, d W* / d T is the slope of the solubility curve and W* the solubility in $kg_{solute}/kg_{solvent}$.

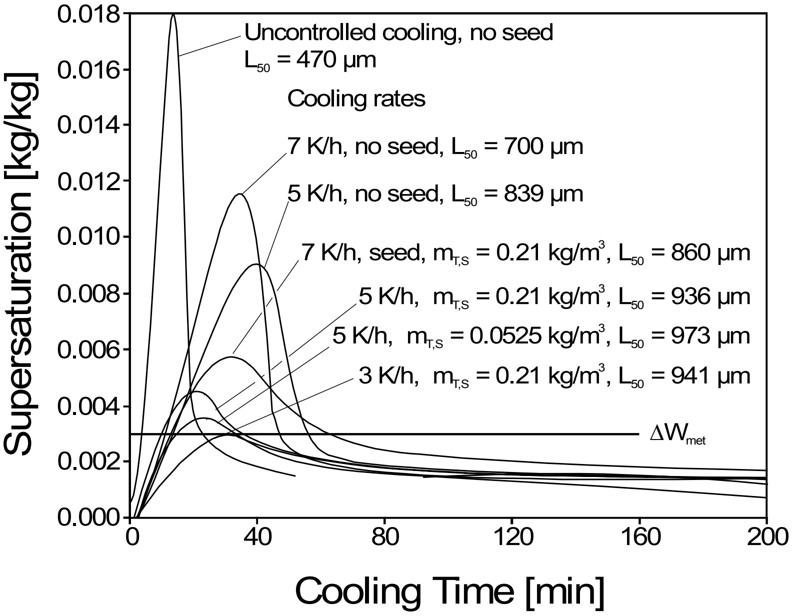

Figure 3-4: Supersaturation versus time for seeded and unseeded crystallization of $(NH_4)_2SO_4$ *[Mers01]*

The positive influence of seeding with a specific crystal mass $m_{T,S}$ on the maximum supersaturation which is achieved during a batch crystallization is proven in Figure 3-4.

In order to maximize the amount of crystal surface available for growth, to provide each crystal with supersaturated solution and to prevent them from settling (except for the case of a classified product removal) it is necessary to suspend all crystals. Therefore in nearly all crystallizers pumps and / or stirrers are installed. Unfortunately the power input of these installations causes secondary or attrition induced nucleation which plays another major role in the operation of crystallizers as it restricts the maximum obtainable crystal size. Once crystals are formed in the solution secondary nucleation can be observed and more and more nuclei with increasing suspension density are created. As a consequence the CSD is broadened with proceeding batch time by attrition fragments and secondary nuclei. Therefore it is inevitable to reduce the mean specific power input (e.g. stirrer speed) if large crystals with a narrow distribution are to be produced.

Crystal – crystal and crystal – apparatus collisions cause attrition of crystals at an attrition rate G_a. In general G_a is proportional to the square of the crystal size L_{par}. A detailed model for the estimation of the attrition rate G_a can be found in [Mers01]. As a consequence an effective growth rate G_{eff} can be formulated:

$$G_{eff} = G - G_a \tag{3-7}$$

The possible maximum size of a crystal is reached when the kinetic growth rate G equals the attrition rate G_a. A graphic interpretation of equation (3-7) is plotted in Figure 3-5.

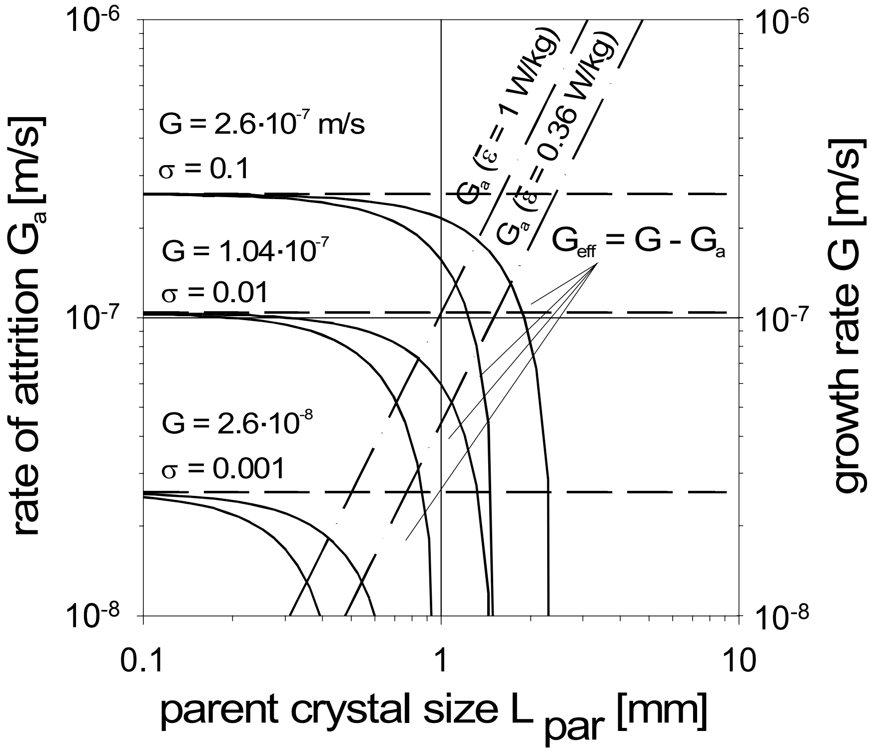

Figure 3-5: Rates of growth and attrition valid for KNO_3 [Pohl87]

Neglecting nucleation and attrition and assuming a constant growth rate G the development in time of the suspension density m_T of a seeded batch crystallizer is given by:

$$m_T(t) = m_S\left(\frac{G\,t}{L_S} + 1\right)^3 \qquad (3\text{-}8)$$

If supersaturation is kept constant, a high mean specific power input $\bar{\varepsilon}$ leads to the generation of additional crystal surface which leads to a drastic increase of the suspension density m_T. In order to avoid a reduction of the supersaturation caused by the growth of attrition fragments it is necessary to increase the cooling rate of the crystallizer. As a result the batch time will be shortened. Gutwald and Mersmann [Gutw91, Mers01] proposed a model for the estimation of the suspension density m_T for a seeded batch crystallization taking attrition into account:

$$\frac{m_T(t)}{m_{T,S}} = A \cosh t^* + \left(\frac{1}{2}\sqrt{\frac{\alpha_S}{\beta_S}}(A-1)^{3/2} + \frac{1}{4}\sqrt{\frac{\beta_S}{\alpha_S}}(A-1)^{1/4} \right) \sinh t^*$$
$$+ (1-A)\cos\ t^* + \left(\frac{1}{2}\sqrt{\frac{\alpha_S}{\beta_S}}(A-1)^{3/2} + \frac{1}{4}\sqrt{\frac{\beta_S}{\alpha_S}}(A-1)^{1/4} \right) \sin\ t^* \qquad (3\text{-}9)$$

with the attrition parameter A

$$A = 1 + \alpha_S \left(\frac{\beta_S G}{(\alpha_S L_S)^4 \cdot {}^{B_{0,\mathrm{eff}}}\!/\!_{\varphi_T}} \right)^{1/2} \qquad (3\text{-}10)$$

Figure 3-6 and Figure 3-7 show the increase of the suspension density as the ratio of $m_T(t)$ / m_S for a seeded batch crystallizer with and without attrition. The comparison of an attrition-free and an attrition-controlled crystallization shows the tremendous influence of attrition on the production rate as well as the suspension density. Attrition creates secondary nuclei (additional crystal surface) causing the faster increase of suspension density, if a constant growth rate G is provided.

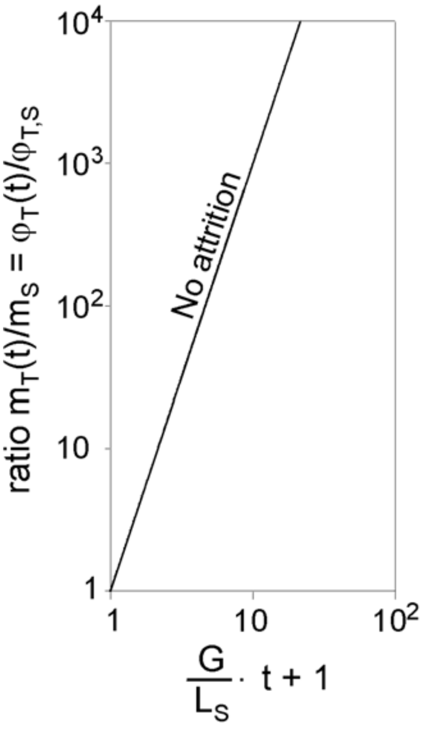

Figure 3-6:Dimensionless volumetric hold-up for batch crystallization without attrition (equation (3-8))

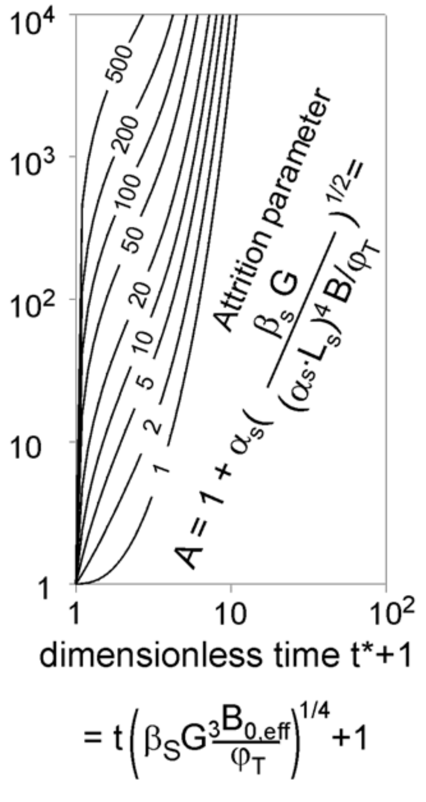

Figure 3-7: Dimensionless volumetric hold-up for batch crystallization with attrition (equation (3-9))

It is important to mention that the assumptions of constant supersaturation and constant power input are the basis of the Gutwald model [Gutw91] resulting in a constant nucleation rate $B_{0,\mathrm{eff}}$ and growth rate G. In order to verify the impact of an increase in the power input on the production rate during a crystallization process it is misleading to evaluate another curve with the newly calculated parameter A in the same diagram, since this parameter curve represents a crystallizer with a totally different previous history. Instead, the current value for $\varphi_T(t)/\varphi_{T,S}$ has to be set to the initial value of 1 and a new calculation has to be started.

The interaction of $B_{0,\mathrm{eff}}$ and G can be seen in Figure 3-8. It is obvious that it is not possible to change the rate of secondary nucleation $B_{0,\mathrm{eff}}$ without affecting the growth rate G. This diagram shows the crystallization of ammonium sulphate and potassium aluminium sulphate in a stirred (STR) and a fluidized bed (FB) crystallizer for different mean specific power inputs. The advantage of the lower power input in the case of the fluidized bed crystallizer results in higher crystal sizes, but higher investment costs have to be accepted. The technical relevant range of $B_{0,\mathrm{eff}} / \varphi_T$ and G for coarse products with $L_{50} > 0.1$ mm can be taken from Figure 3-8 since crystallizers with low (FB) and high (STR) mean specific input are represented:

$$10^{6}\ \mathrm{m^{-3}\ s^{-1}} < B_{0,\mathrm{eff}}/\ \varphi_T < 10^{10}\ \mathrm{m^{-3}\ s^{-1}}$$
$$10^{-8}\ \mathrm{m\ s^{-1}} < G < 2\cdot 10^{-7}\ \mathrm{m\ s^{-1}}$$

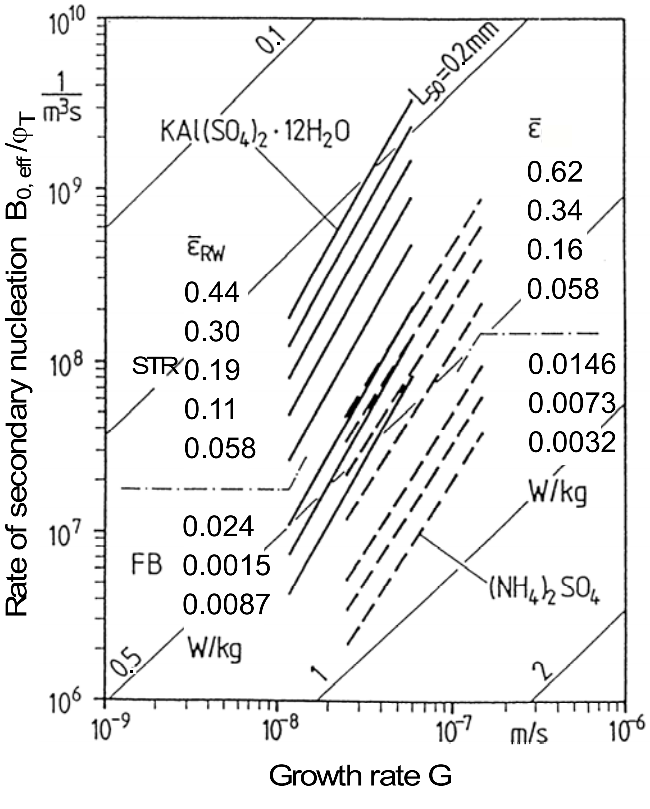

Figure 3-8: Rate of secondary nucleation based on φ_T versus the mean growth rate for $KAl(SO_4)_2$ and $(NH_4)_2SO_4$ in stirred and fluidized bed crystallizers [Gutw91].

Continuously operated crystallizers can be exposed to an oscillating supersaturation and CSD (L_{50}). The reasons for this unsteady-state behaviour are the changes in feed rates, compositions and temperatures. Even if the operating conditions are kept constant, fluctuations in supersaturation and crystal size are observed. Product removal and especially classified product removal leads to a decrease in crystal surface. As a result less crystal surface is available for the degradation of supersaturation by growth, followed by an increase in supersaturation which causes a higher nucleation rate. The new nuclei shift the median crystal size L_{50} to smaller particle sizes. The previously high supersaturation is now reduced by nucleation and so on.

Most continuous crystallizers tend to stabilize after multiples of residence time τ. This process can last from several hours up to a few days. Only under worst operating conditions stabilization does not take place at all, see Figure 3-9. Generally speaking, classified product removal promotes unsteady-state behaviour, whereas clear liquor overflow reduces oscillations of supersaturation and CSD.

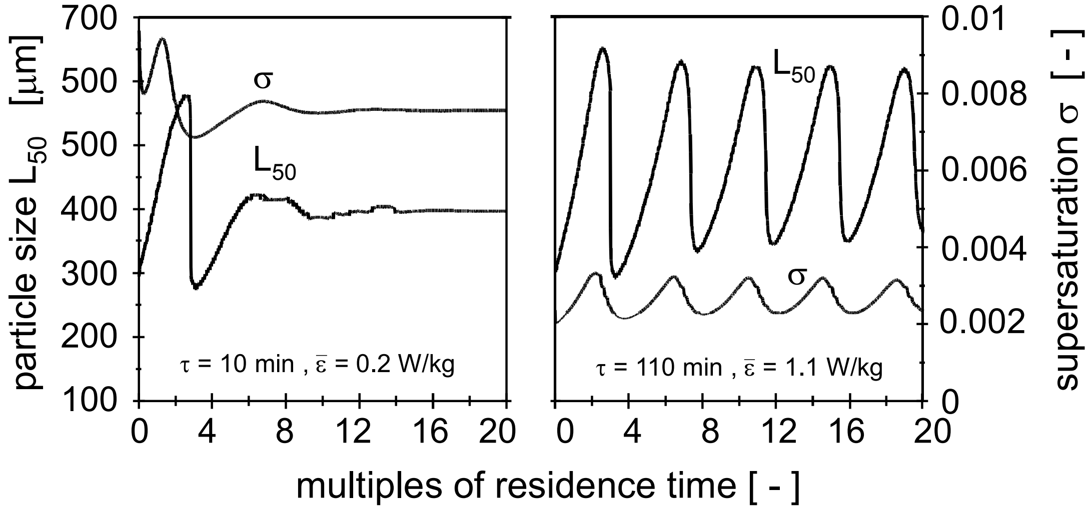

Figure 3-9: Calculated cycling behaviour of stirred continuos crystallizers for potassium nitrate [Gahn97]

Models for the prediction or the control of the unsteady behaviour of continuously operated crystallizers can be found in [Eek95a, Gers98, Roha86, Rous82, Yu75]. These models and the previously mentioned models for an optimal batch crystallization are only model-predictive control strategies with no chance of responding to process disturbances. Feedback control strategies offer the possibility of counteracting unexpected offset due to disturbances. Classifying feedback control strategies according to their measurand, a big variety of such control strategies have been developed. A survey is given in Table 3-2.

Table 3-2: Feedback control methods for batch and continuous crystallizers

Measurand	Reference
calorimetry	[Fevo96a, Fevo96b]
concentration (ATR FTIR)	[Dunu97]
concentration (conductivity)	[Hloz92]
concentration (refractometry)	[Helt77, Mess72]
density (radiometry)	[Aust85, Hemp87]
density (temperature float method)	[Wang89]
density (ultrasonic)	[Omar99a, Omar99b]
density, temperature of solution	[Redm95, Rieb90, Roha87]
dry substance content (high-frequency measurement)	[Ehre97]
particle size and CSD	[Eek95b, Kara, Roha86, Zeve98]
slurry density (turbidity of fines loop)	[Roha86, Roha90]

Most of these methods described are tailored for specific processes and systems. Therefore it is impossible to specify a general or universal method for supersaturation measurement in order to control crystallization. In addition, supersaturation is measured with the help of the concentration dependent physical properties of the solution and refers to the solubility curve of the corresponding pure two component system. As a consequence, impurities or small changes in the composition of the solution cause the wrong determination of the current supersaturation.

Although these control methods lead to high improvement in product control, they are not capable of guaranteeing an operation of a crystallizer at optimum supersaturation during the whole process.

Classified product removal and fines dissolution represent other possibilities of obtaining a crystalline product of a defined CSD. In contrast to the previously mentioned control strategies the whole process is not dedicated to the control of supersaturation. Contrary to this, crystals of an undesired size ($L < L_{fine}$) are dissolved in a heated bypass (fines removal and dissolution) and crystals of desired size ($L > L_{prod}$) are removed from the crystallizer (classified product removal).

Figure 3-10 shows a schematic illustration of such a crystallizer.

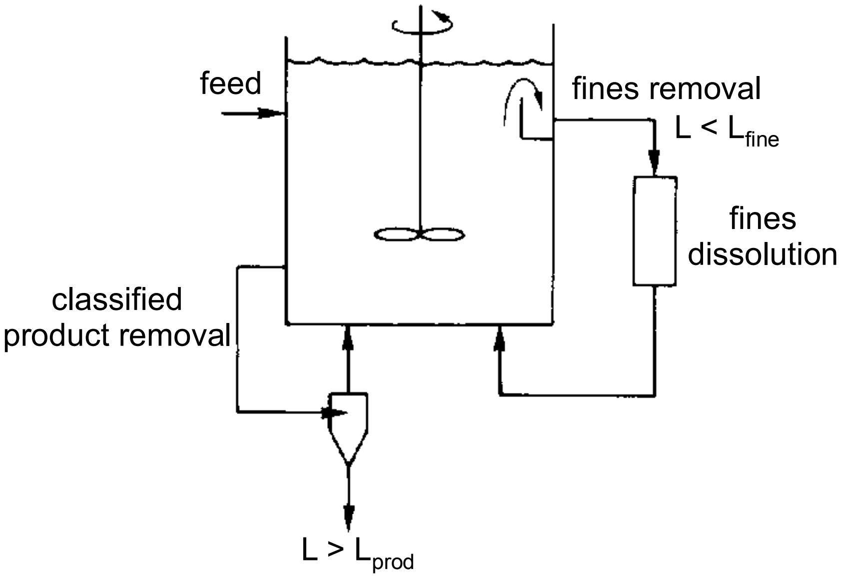

Figure 3-10: Mixed suspension crystallizer with fines destruction and classified product removal

The classified product removal can be realized with the help of a hydrocyclone or a settling zone in the crystallizer.

The positive impact on the CSD caused by fines dissolution, where nuclei obtained by an uncontrolled nucleation are dissolved, can be seen in Figure 3-11.

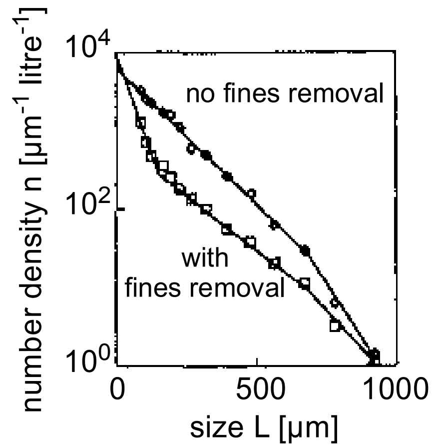

Figure 3-11: Number density of a crystallization with and without fines removal of potassium nitrate [Juza77]

Here the required product quality (a narrow CSD) is achieved by a final quality control, since classified product removal and fines dissolution represent no active supersaturation control.

The overall impact of the supersaturation ΔC and the mean specific power input $\bar{\varepsilon}$ on production rate, the batch time τ and the maximum crystal size L_{max} is shown in Figure 3-12. Here the ratio $m_T(t)/m_{T,S}$ for different batch crystallizations is plotted versus batch time τ. Gutwald model (equation (3-9)) was used for the calculation of the nucleation rate $B_{0,eff}$ / φ_T. The maximum obtainable crystal size L_{max} was determined by neglecting the negative growth rate G_a caused by attrition. The higher supersaturation and mean specific power input, the higher the increase of suspension density. As a consequence the batch time τ is shortened and the maximum crystal size L_{max} is reduced.

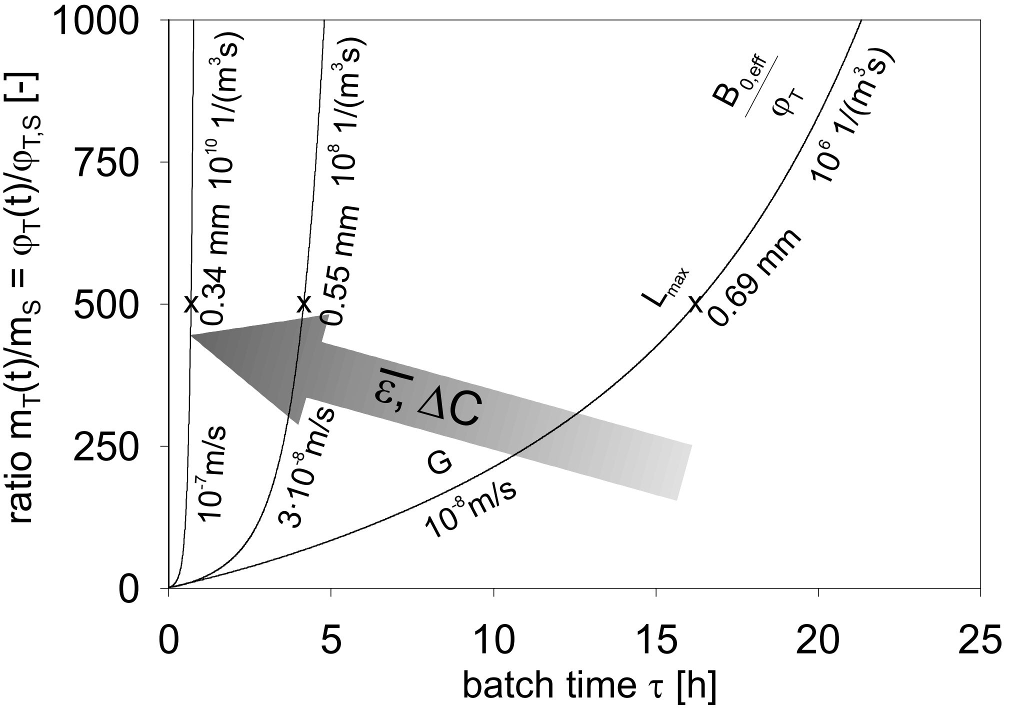

Figure 3-12: Influence of supersaturation and mean specific power input on batch time (valid for KNO_3,, prone to attrition)

In general, if large crystals are desired, low supersaturation and low mean specific power input are required throughout the process. In the case of a short batch time and low product quality requirements, high supersaturation and high mean specific power input are the right choice. This relationship is less pronounced in the case of attrition resistant crystals.

Independent from this choice of adequate control strategy, one important question has to be answered before each crystallization process: what is the optimal supersaturation?

4 Optimal Process Management

This chapter will answer two questions which arose during the design of a crystallization process from solutions:

- Which way of supersaturation generation, cooling or evaporation, or both (pressure and temperature change) should be chosen?
- What is the optimal supersaturation for an arbitrary system?

4.1 Cooling or Evaporation Crystallization?

Before focussing on cooling crystallization a general criterion should be formulated which helps to decide whether cooling or evaporation crystallization should be applied.
Neglecting the product quality, the profitability of a crystallization process is influenced by two decisive aspects:

- product yield or suspension density at the end of the process and
- energy consumption.

The supersaturation Δc established during a cooling crystallization can be calculated by:

$$\Delta c = \frac{d\,c^*}{d\,T}\Delta T \qquad (4\text{-}1)$$

where d c* / d T is the slope of the solubility curve and ΔT the temperature difference between the temperature T of the operation and the equilibrium temperature T* of the solution with the concentration c. Strictly speaking this equation is only valid for linear solubility curves c* ~ T. For evaporation crystallization the total desupersaturation range $\Delta c_{tot}=c_\alpha - c_\omega$ is given by (see Figure 4-1):

$$\Delta c_{tot} \approx c^*\left(\frac{V_\alpha}{V_\alpha - \Delta V} - 1\right) \qquad (4\text{-}2)$$

With V_α as the volume of the solution at the beginning of the evaporation and ΔV as the volume of evaporated solvent in the liquid state. In this equation changes in the density of the solution due to changes in the concentration are neglected.

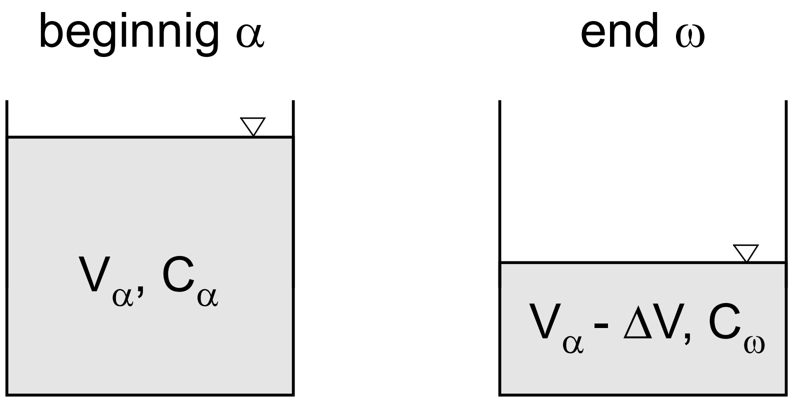

Figure 4-1 : Batch evaporation crystallization

Assuming a total desupersaturation at the end, the suspension density $m_{T,C}$ of the cooling crystallization and the suspension density for evaporation crystallization $m_{T,V}$ equals the supersaturation:

$$m_{T,C} = \Delta c_{tot} \tag{4-3}$$

and

$$m_{T,E} = \Delta c_{tot} \tag{4-4}$$

The following assumptions allow an easy estimation of the energy consumed during the crystallization:

- linear solubility curve,
- energy losses are neglected,
- heat of crystallization is neglected and
- a heating-up of the solution before evaporation is not necessary.

The total energy required for cooling crystallization Q_C and for evaporation crystallization Q_E can then be calculated by:

$$Q_C = V_\alpha \, \rho_{sol} \, c_{p,sol} \, \Delta T_{tot} \tag{4-5}$$

with ΔT_{tot} as the total temperature range and

$$Q_E = \rho_{solv}\, \Delta h_{LV}\, \Delta V_{tot} \tag{4-6}$$

with ΔV_{tot} as the total volume of evaporated liquid solvent.
Combining the equations (4-1) to (4-6) we obtain:

$$\frac{m_{T,E} / Q_E}{m_{T,C} / Q_C} = \frac{\rho_{sol}\, c_{p,sol}}{\rho_{solv}\, \Delta h_{LV}} \frac{c^*}{dc^* / dT} \left(\frac{\Delta c_{tot}}{c^*} + 1 \right) \tag{4-7}$$

If the total desupersaturation range Δc_{tot} is small compared to the solubility c*, equation (4-7) can be simplified to equation (4-8), see Figure 4-2.

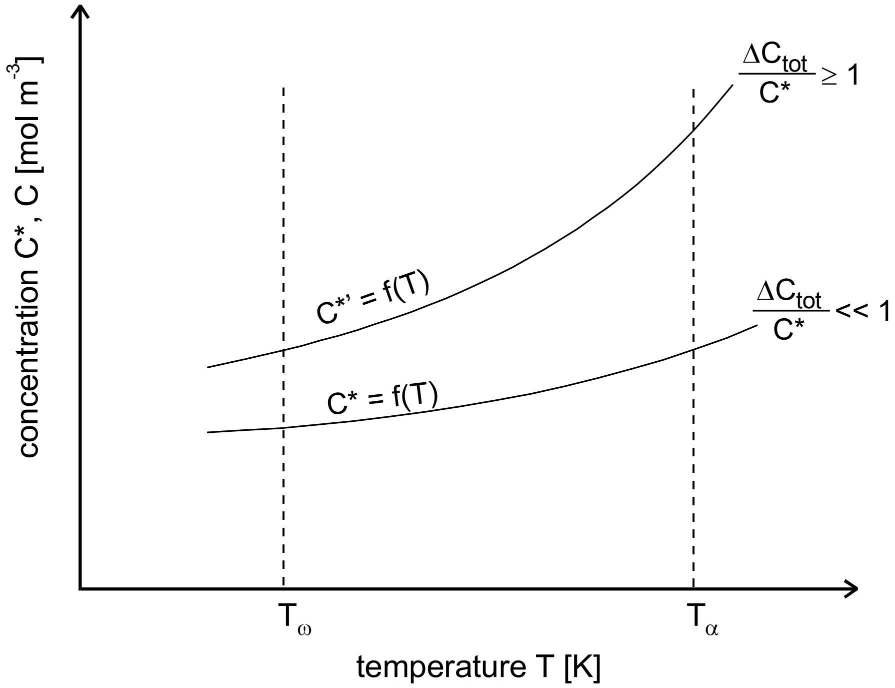

Figure 4-2: Ratio of desupersaturation span Δc_{tot} and c for different solubilities*

$$\frac{m_{T,C} / Q_C}{m_{T,E} / Q_E} = \frac{\rho_{solv}\, \Delta h_{LV}}{\rho_{sol}\, c_{p,sol}} \frac{dc^*}{c^* dT} \tag{4-8}$$

This equation can be interpreted as follows:

- the higher the term $(m_{T,C}/Q_C)/(m_{T,E}/Q_E)$ (the ratio of suspension densities based on transported energy for cooling and evaporation) the higher the efficiency in case of cooling crystallization,
- a steep slope dc*/dT demands cooling crystallization,
- a high solubility makes evaporation crystallization more applicable, and
- if $(m_{T,C}/Q_C)/(m_{T,E}/Q_E)$ equals 1, both processes, i. e. cooling and evaporation, have the same efficiency.

Figure 4-3 shows the efficiency $(m_{T,C}/Q_C)/(m_{T,V}/Q_V)$ plotted versus dc*/(c*dT) according to equation (4-7) and (4-8).

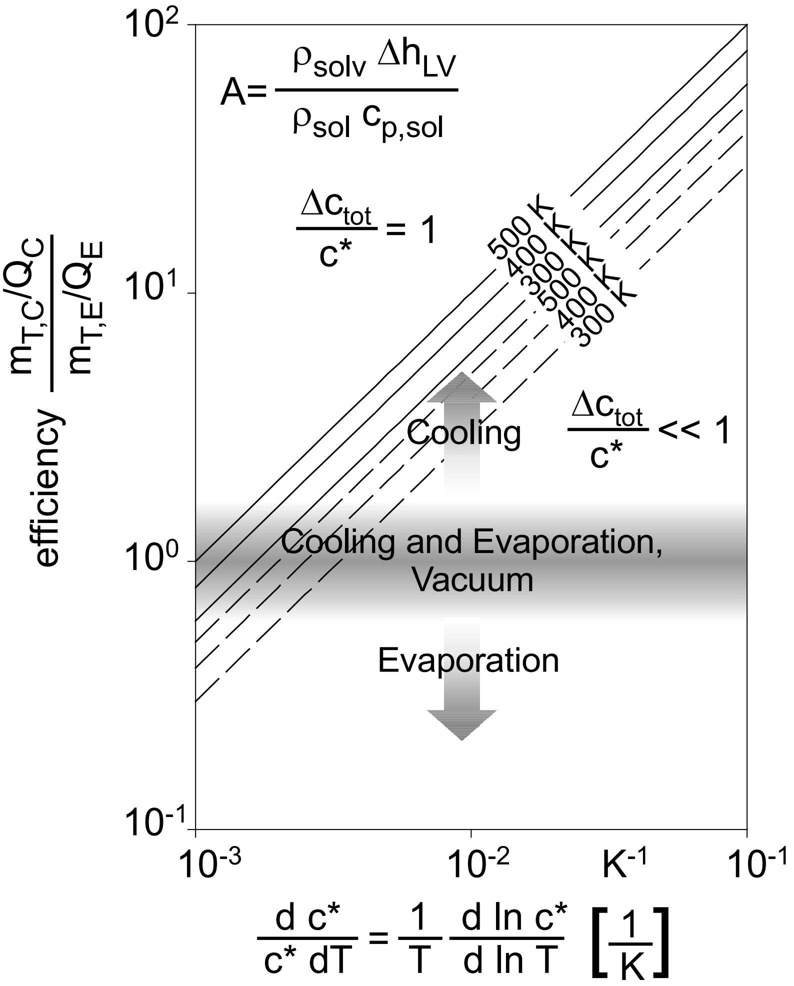

Figure 4-3: Efficiency $(m_{T,C}/Q_C)/(m_{T,E}/Q_E)$ as a function of the slope dc / (c* dT) = 1/T d(ln c*)/d(ln T) of the solubility curve*

Due to the simplifying assumptions that were made this criterion gives only an estimation. In addition vacuum crystallization as a mixture of cooling and evaporation crystallization can also be taken into account.

4.2 Optimal Supersaturation for Coarse Crystalline Products

Although the various possibilities of controlling crystallization have been shown in the previous chapter, one major question has not been answered yet: what is the optimum supersaturation, especially for batch or fed batch crystallization?

In most cases the properties or the quality of the product are adjusted by controlling the supersaturation. Considering product quality and economic efficiency an individual optimal supersaturation σ_{opt} exists for every system. This supersaturation lies within the metastable zone.

At first we should call to mind the interaction of supersaturation, nucleation, growth, product quality and economic aspects of the process. The 2x2 matrix in Figure 4-4 shows these interactions schematically.

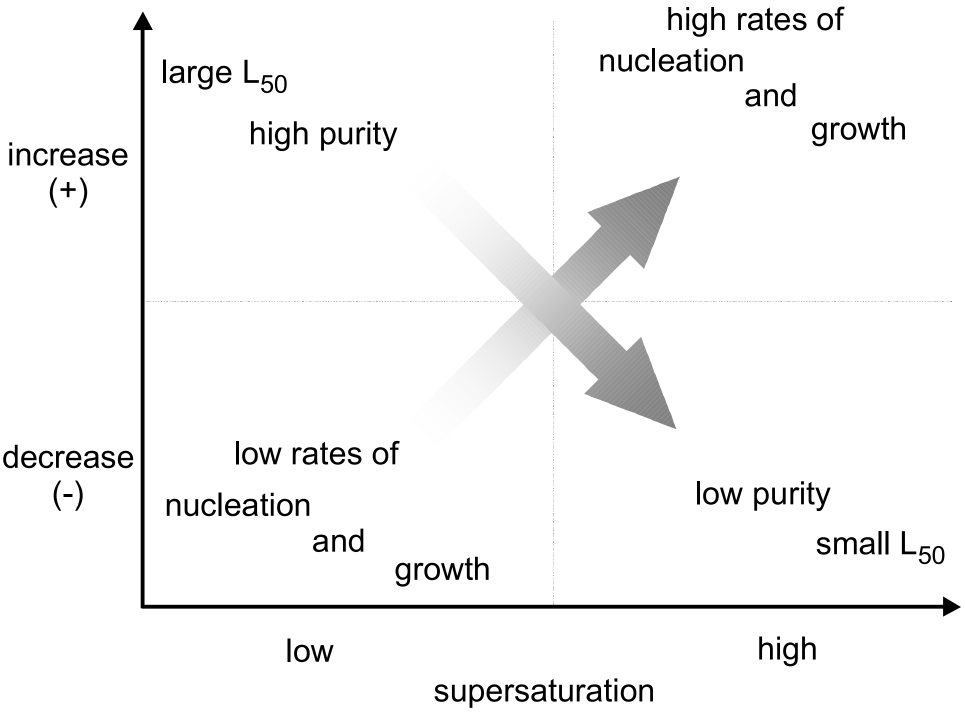

Figure 4-4: Scheme of interactions between nucleation, growth, batch time and product quality (valid for the optimal specific power input, ε_{opt}, necessary for suspension and mixing)

The rates of nucleation and crystal growth increase with supersaturation, resulting in a shorter batch time τ as in comparison with a low level of supersaturation. A short batch time means economic production since less time is needed to obtain the same suspension density or product. Independent of batch time, almost the same amount of energy is consumed. But accelerating the process by increasing supersaturation, i. e. higher cooling rates, increasing nucleation and growth rates lead to a deterioration of product quality. Due to the high nucleation rate the median crystal size L_{50} drops and the CSD is broadened. In addition the high growth rate causes the incorporation of solvent and impurities in the crystals.

Generally speaking, activated nucleation should be avoided during the whole batch crystallization as it influences the median crystal size L_{50} and the CSD in an undesired way. As a consequence supersaturations exceeding the metastable limit $\sigma_{met,sec}$ have to be avoided. Mersmann [Mers98] and Hofmann [Hofm91] proposed the optimal supersaturation σ_{opt} to be half the metastable supersaturation σ_{met}. The difficulty of characterizing or measuring the metastable zone width can be reduced by a simplified model for the estimation of the metastable zone width proposed by Mersmann [Mers98, Mers00].

As mentioned in the chapter dealing with metastable zones, there are three major parameters influencing the experimental results for measurements of metastable zone widths:

- the definition of the number of required nuclei or nucleation rate
- the definition of the detectable size L_{det} of crystals
- the rate of supersaturation generation

The model of Mersmann is based on the following assumptions:

- seed crystals are present in the solution,
- the solution is cooled with a constant cooling rate $\dot{T}$,
- the growth of crystals is the decisive or limiting step for the occurrence of a visible shower of nuclei,
- the growth of the small nuclei is controlled by the integration step and
- the metastable zone width is observed when the nuclei have grown to a mean detectable size L_{det} and the volumetric crystal hold-up is at least $\varphi = 10^{-4}$.

According to the model [Mers98] the metastable zone width for cooling crystallization is given by:

$$\sigma_{met} = 12 \cdot \left[\frac{d(\ln C^*)}{d(\ln T)} \cdot \frac{\dot{T}}{T} \cdot \left(\frac{\rho_C}{c^*} \right)^{\frac{4}{3}} \cdot \ln\left(\frac{\rho_C}{c^*} \right) \cdot \frac{d_m \cdot L_{det}}{D_{AB}} \right]^{\frac{1}{3}} \qquad (4\text{-}9)$$

or

$$\frac{\Delta c_{met}}{\rho_C} = 12 \cdot \left[\frac{d(\ln C^*)}{d(\ln T)} \cdot \frac{\dot{T}}{T} \cdot \left(\frac{c^*}{\rho_C} \right)^{\frac{5}{3}} \cdot \ln\left(\frac{\rho_C}{c^*} \right) \cdot \frac{d_m \cdot L_{det}}{D_{AB}} \right]^{\frac{1}{3}} \qquad (4\text{-}10)$$

Calculations have shown that it is possible to predict the metastable zone widths which are published in the literature by assuming $L_{det} = 10\mu m$ and $D_{AB} = 5 \cdot 10^{-10}$ m^2/s for low viscous solutions. In this case the expression $\frac{d_m \cdot L_{det}}{D_{AB}}$ is 10^{-5} s for the molecule diameter $d_m = 5 \cdot 10^{-10}$ m.

Cooling crystallization is only economical for relatively steep solubility curves with $\frac{d(\ln C^*)}{d(\ln T)} > 8$, compare Figure 4-5. With cooling rates between 1 - 20 K/h ($2.8 \cdot 10^{-4}$ – $5.6 \cdot 10^{-3}$ K/s) the cooling parameter $\dot{P}_{cool}$

$$\dot{P}_{cool} = \frac{d(\ln C^*)}{d(\ln T)} \cdot \frac{\dot{T}}{T} \qquad (4\text{-}11)$$

is approximately in the range between 10^{-5} s^{-1} and $2 \cdot 10^{-4}$ s^{-1} for T = 313 K. In Figure 4-5 the optimal relative supersaturation σ_{opt} is shown as a function of the dimensionless solubility $\frac{c^*}{\rho_C}$ and the cooling rate $\frac{d(\ln C^*)}{d(\ln T)} \cdot \frac{\dot{T}}{T}$ as parameter. It is necessary to operate the crystallizer at a supersaturation $\sigma_{opt} < \sigma_{met}$ in order to avoid activated nucleation. The curve shown in Figure 4-5 is valid for $\sigma_{opt} = 0{,}5\ \sigma_{met}$. It is important to note that this diagram indicates optimal supersaturation if

- the dissolved molecules do not dissociate ($\nu = 1$),
- the solution is low viscous ($\eta_L < \approx 10$ m Pa s) and
- only one component is crystallizing in a pure solution.

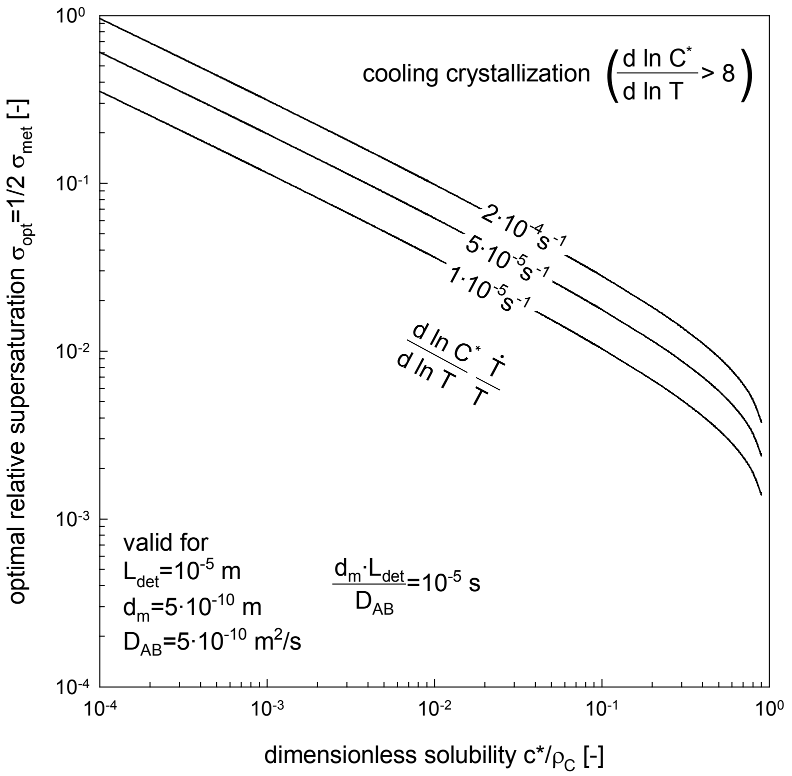

Figure 4-5: Metastable and optimal supersaturation versus the dimensionless solubility for various cooling rates $\frac{d(\ln C^*)}{d(\ln T)} \cdot \frac{\dot{T}}{T}$ *of cooling crystallization*

Trying to apply this model to evaporation crystallization, the following assumptions have been made:

- the solution is ideally mixed,
- seed crystals are present in the solution,
- the solvent is evaporated with a constant evaporation rate $\Delta\dot{L}^0$,
- the growth of crystals is the decisive or limiting step for the occurrence of a visible shower of nuclei,
- the growth of the small nuclei is controlled by the integration step
- the metastable zone width is observed when the nuclei have grown to a mean detectable size L_{det} and
- no change in the density of the solution.

The metastable zone width is then obtained by [Mers00]:

$$\sigma_{met} = 12 \cdot \left[\frac{\Delta \dot{L}^{\circ}}{V_{\alpha}\, \rho_{solv}} \cdot \left(\frac{\rho_C}{c^*} \right)^{\frac{4}{3}} \ln\left(\frac{\rho_C}{c^*} \right) \cdot \frac{d_m \cdot L_{det}}{D_{AB}} \right]^{\frac{1}{3}} \qquad (4\text{-}12)$$

or

$$\frac{\Delta c_{met}}{\rho_C} = 12 \cdot \left[\frac{\Delta \dot{L}^{\circ}}{V_{\alpha}\, \rho_{solv}} \cdot \left(\frac{c^*}{\rho_C} \right)^{\frac{5}{3}} \ln\left(\frac{\rho_C}{c^*} \right) \cdot \frac{d_m \cdot L_{det}}{D_{AB}} \right]^{\frac{1}{3}} \qquad (4\text{-}13)$$

where V_{α} is the starting volume of the solution.
These equations show that the metastable supersaturation at which the shower of nuclei occurs is high when the evaporation rate $\dot{P}_{evap} = \frac{\Delta \dot{L}^{o}}{V_{\alpha} \cdot \rho_{solv}}$ is high for large values of c^* and L_{det}. In Figure 4-6 the optimal supersaturation σ_{opt} (the optimal value according to $\sigma_{opt} = 0.5\ \sigma_{met}$) is plotted against the dimensionless solubility $\frac{c^*}{\rho_C}$ with the evaporation rate $\dot{P}_{evap} = \frac{\Delta \dot{L}^{o}}{V_{\alpha} \cdot \rho_{solv}} \approx \frac{\Delta \dot{L}^{o}}{L^{o}_{\alpha}}$ as parameter. Figure 4-6 is only valid for a completely mixed solution which is subject to the same pressure everywhere such as is the case with a film evaporator with a thin liquid layer (< 1 mm) and a short film length.

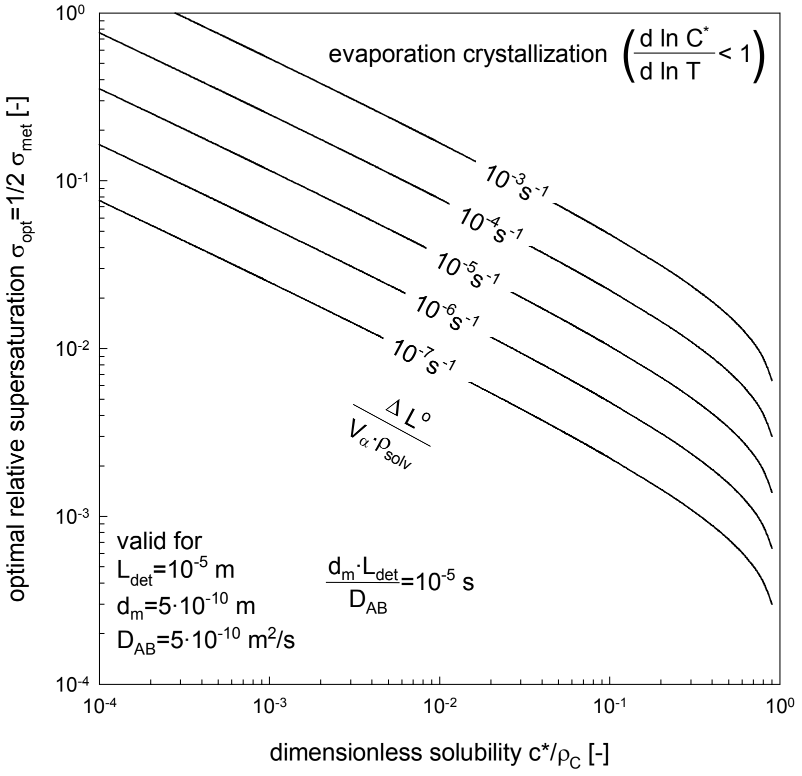

Figure 4-6: Metastable and optimal supersaturation versus the dimensionless solubility for various evaporation rates $\frac{\Delta \dot{L}^o}{V_\alpha \cdot \rho_{solv}}$ *of evaporation crystallization*

When dealing with evaporative or flash crystallizers evaporation occurs in a relatively thin layer under the boiling surface. The relative thickness $\frac{\Delta w}{w}$ of a stagnant layer containing supersaturated solution can be calculated by

$$\frac{\Delta w}{w} \approx \frac{1}{\sigma} \frac{\Delta m_{solv}}{m_L} \left(1 + X^*\right) \qquad (4\text{-}14)$$

Here Δm_{solv} is the mass of the evaporated solvent, m_L the total mass of the solution and X^* the equilibrium mass ratio of solute and solvent.

Unfortunately this estimation is only valid for several simplified assumptions:

- the change of concentration due to evaporation takes place only in the surface layer of the solution with the thickness Δw
- there is no diffusion and convection in the solution
- the solution is at rest

- there is no smoothing-out of concentration between the bulk and the layer (bulk concentration remains constant).

According to equation (4-14) $\frac{\Delta w}{w}$ is proportional to the mass of evaporated solvent and inversely proportional to the relative supersaturation σ. In reality the density of the supersaturated solution with its suspension density is greater than the density of the solution below. Therefore a natural convection takes place perhaps supported by a forced convection which is induced by a mechanical mixing device (stirrer, pump). Due to a low turbulence and sedimentation of particles the suspension density is low in the surface layer. It is very difficult to predict the field of supersaturation.
A few experiments carried out in a crystallizing dish showed that the relative thickness $\frac{\Delta w}{w}$ varies in the range of 0.02 and 0.2 depending on the evaporation rate. Therefore it is useful to introduce the active volume reduction factor $\frac{\Delta w}{w}$ in the equations (4-12) and (4-13) in order to maintain the validity of the model. Reducing the considered volume V_α with $\frac{\Delta w}{w}$ we obtain:

$$\sigma_{met} = 12 \cdot \left[\frac{\Delta \dot{L}^{\circ}}{\frac{\Delta w}{w} V_\alpha \, \rho_{solv}} \cdot \left(\frac{\rho_C}{c^*} \right)^{\frac{4}{3}} \ln\left(\frac{\rho_C}{c^*} \right) \cdot \frac{d_m \cdot L_{det}}{D_{AB}} \right]^{\frac{1}{3}} \qquad (4\text{-}15)$$

and

$$\frac{\Delta c_{met}}{\rho_C} = 12 \cdot \left[\frac{\Delta \dot{L}^{\circ}}{\frac{\Delta w}{w} V_\alpha \, \rho_{solv}} \cdot \left(\frac{c^*}{\rho_C} \right)^{\frac{5}{3}} \ln\left(\frac{\rho_C}{c^*} \right) \cdot \frac{d_m \cdot L_{det}}{D_{AB}} \right]^{\frac{1}{3}} \qquad (4\text{-}16)$$

Now the question arises: How can we measure and maintain the optimal supersaturation? The next chapter is devoted to this problem.

5 Innovative Supersaturation Measuring System

Having explained the possibilities of calculating and retaining optimal supersaturation during a cooling crystallization, one important question has not been discussed yet: How can we measure supersaturation in order to control its optimum level?
An answer to this question will be given in this chapter and the difference between the existing and the new measurement method will be explained. The technical implementation of the innovative supersaturation measuring system will be described at the end of this chapter.

5.1 Measurement Method

Up to now different methods have been developed to measure supersaturation. A short overview of the existing supersaturation measurement methods is given in Table 5-1.

Table 5-1: Supersaturation measurement methods [Prof87]

measurement technique	measurement method	measurand
particle analysis	particle analyser	size distribution, particle density
gravimetry	densimeter	density
acoustics	ultra sonic	sonic speed, phase shift
shear stress	viscometer, quartz-crystal oscillator	viscosity
conductometry	Kohlrausch-cell, inductive measurements	electrolytic conductivity
potentiometry	ionspecific electrodes, ionspecific membranes	ionic conductivity
spectroscopy	spectrophotometry, infrared spectroscopy	absorption spectra
radiometry	nuclear radiation	absorption spectra
optics	refractometry, interferometry, polarimetry, turbidimetry	refraction index, interference, rotation of polarization plane, turbidity
thermic	calorimetry	heat of crystallization
chemistry	titration, indicators	concentration, tinct

In Table 5-1 each method described has restrictions regarding its applicability, such as certain ranges of temperature, turbidity, physical properties as viscosity and solution density, or suspension density. As can be seen, a lot of different measurands for determining supersaturation are available, but all of them use physical properties (such as density, viscosity or electric conductivity) which show a dependence on concentration in order to obtain the actual level of supersaturation with the help of solubility data. Therefore, all existing measurement methods are more or less concentration measurements which are only applicable in pure systems. The actual extent of the driving force of crystallization, the supersaturation, cannot be quantified directly. Additionally, these concentration-dependent measurement methods require a solubility diagram of the system which is valid for the actual composition including all impurities. In case of changing or alternating compositions of the mother liquor this requirement is very hard to fulfill. A schematic measuring procedure can be seen in Figure 5-1.

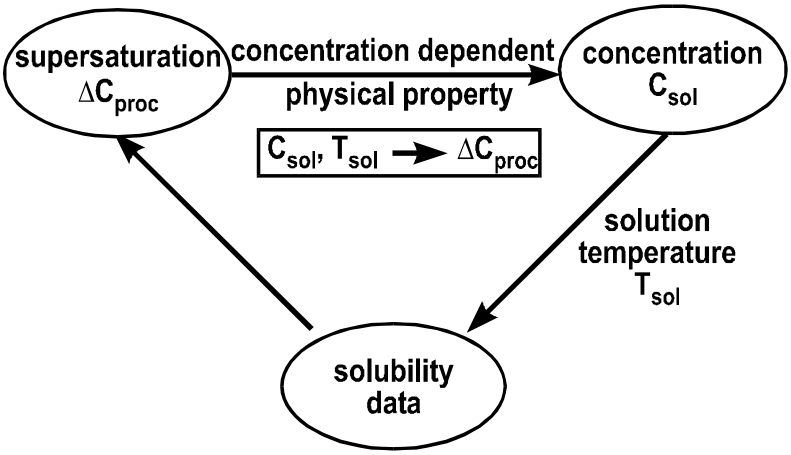

- measurement of a concentration dependent physical property of the solution
- solubility data required
- influence on the process caused by impurities is not detectable

Figure 5-1: Scheme of conventional supersaturation measuring methods.

The crystallization process itself is not considered in the various measurement methods. In the case of alternating compositions or changing impurities of the mother liquor, solubility data for each possible composition or impurity would be required if the effective supersaturation should be determined by the way described above.

If impurities (e. g. foreign particles) or other process disturbances exist, the measuring of supersaturation with the help of physical properties of the solution still results in the same value as before. However, it is well known that such impurities influence the metastable zone width and the kinetics of nucleation and crystal growth [Raul00]. As a consequence, the crystallization performance changes without any chance of reacting in adequate time to avoid a reduction of the product quality.

In order to gather the complete information of all parameters which influence the crystallization processes, including the supersaturation, it is necessary to induce a crystallization either in the suspension or on the surface of the sensor [Pate95, Pate95a]. In the case of a surface sensor it is necessary to observe the development in time of the first deposition of solid matter which finally leads to incrustation. Therefore, the basic idea of the new measurement method is to generate an additional supersaturation and to conduct an accelerated crystallization in accordance with the current process and to observe it. The main idea is illustrated in Figure 5-2, see also Figure 5-3.

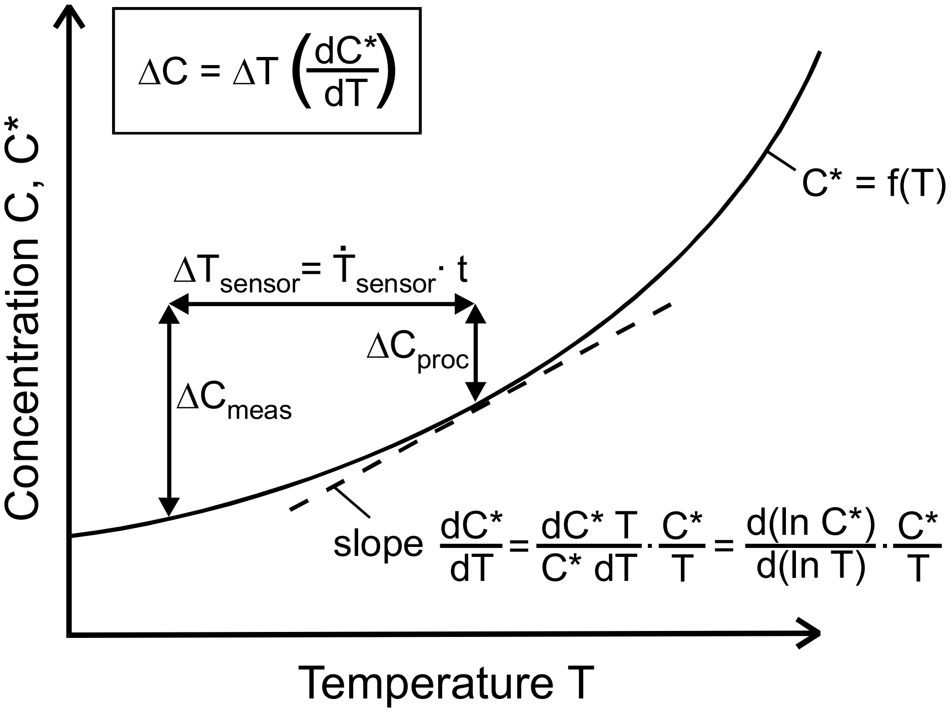

Figure 5-2: The solubility C^* is plotted against the temperature T. The supersaturation ΔC_{meas} is composed of two contributions according to equation (5-1).

If a solution with unknown supersaturation ΔC_{proc} comes into contact with a cooled surface, the incrustation will start there first, since this is the location with the highest supersaturation. Consequently, the crystallization on the sensor surface will be accelerated by generating an additional supersaturation ΔC_{sensor}. The measurement supersaturation ΔC_{meas} is then made up of the prevailing process supersaturation ΔC_{proc} and the supersaturation ΔC_{sensor} which is established by cooling of the sensor surface:

$$\Delta C_{meas} = \Delta C_{proc} + \Delta C_{sensor} = \Delta C_{proc} + \dot{T}_{sensor} \cdot t \cdot \frac{dC^*}{dT} \qquad (5\text{-}1)$$

In the case of a constant cooling rate $\dot{T}_{sensor}$ and a high supersaturated solution the incrustation on the cold sensor surface will start after a very short period of time, whereas in the case of a saturated or unsaturated solution the incrustation starts later because additional supersaturation has to be established. So, as shown in Figure 5-3, the starting point of the incrustation, i. e. the time t_{start} which elapsed from the beginning of the cooling until the detection of the incrustation, is the decisive measurement signal.

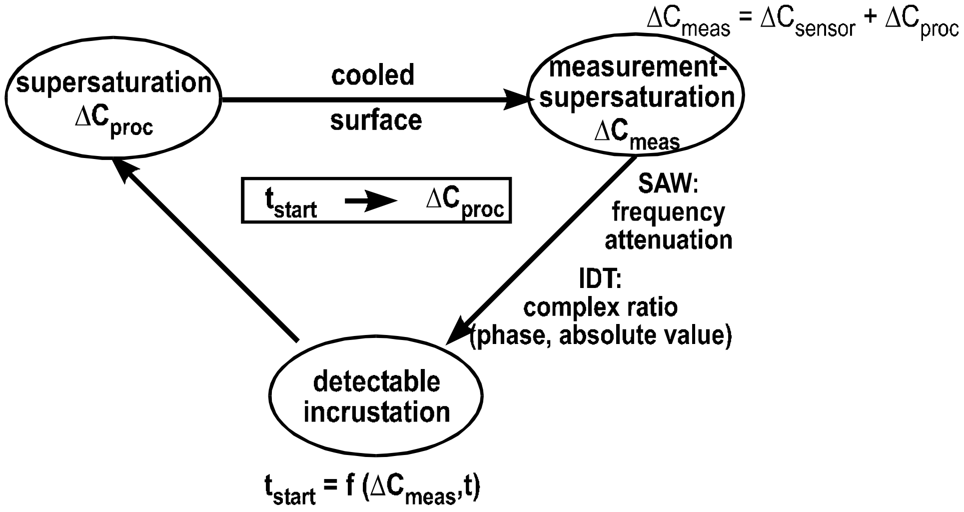

- measurement of an accelerated local crystallization according to the current process
- no solubility data required
- influence on the process caused by impurities is detectable

Figure 5-3: Scheme of the innovative supersaturation measurement method

By using and providing constant settings and conditions for each measurement (e. g. cooling rate, sensor surface properties) the incrustation of the sensor surface is then only dependent on time and supersaturation.

The influence of impurities or admixtures in the solution on solubility and metastable zone width can now be measured since the incrustation on the sensor surface is influenced in the same way.

5.2 Sensor

In the first functional prototype two different devices for the detection of the onset of incrustation were integrated: the interdigital transducer (IDT) and the surface acoustic wave sensor (SAW). Both sensors were provided by the Fraunhofer Institute for Microelectronic Circuits and Systems in Munich. The following brief description of the sensors might help to understand their mode of operation. For more details see [Drob93, Leid97, Leid98].

5.2.1 Interdigital Transducer (IDT)

A planar capacitor is formed by affixing comb-like electrodes in an interlocked way with the help of thin-film technology on a dielectric substrate, see Figure 5-4. The impedance Z of this capacitor depends on the properties of the substrate material and on the adjacent solution. Thus, a change of the electric conductivity and / or the relative permittivity could be specified by the impedance Z. The penetration of the electric field into the solution, which could be seen as the range of the measurement in the solution, depends on the distance of the electrodes and averages in our case up to 50 µm. The whole surface is passivated with a SiC-layer (500 nm) ensuring mechanical and chemical resistivity. This sensor is able to measure the electric conductivity κ and the relative permittivity ε_r in a rather thin liquid layer adjacent to the sensor surface (ca. 10µm). This device is therefore suitable for detecting incrustations

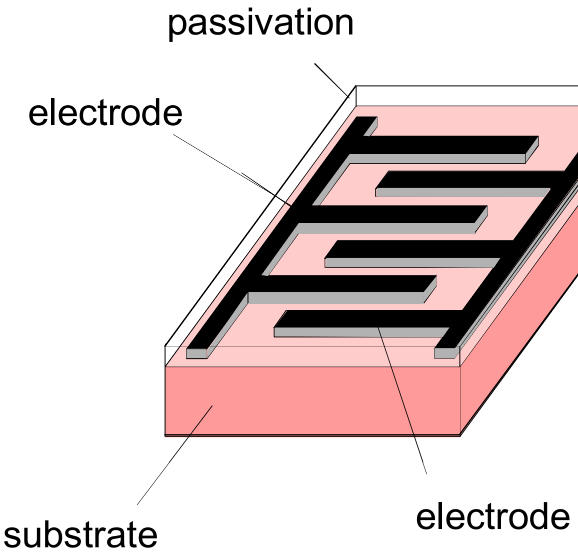

Figure 5-4: Interdigital transducer (IDT)

5.2.2 Surface Acoustic Wave (SAW)

In Figure 5-5 two IDTs are acting as a emitter and receiver of electroacoustic waves. The resonance frequency of the emitter is determined by its geometry variables and the properties of the substrate. Applying an electric high frequency signal electroacoustic waves with a frequency from 50 MHz up to 150 MHz will be emitted. The propagation conditions for such waves depend on the properties of the solution between the IDTs. The effective range of the SAW in the solution is about 300 nm and has a very low mass detection limit, which is in the magnitude of ng / cm². The sensitive zone lies between the emitter and receiver of the waves. This type of sensor is also passivated with SiC. For liquid sensing surface-localized shear waves (Bleustein-Gulyaev-Waves) are used. These waves exhibit a high sensitivity of wave velocity and attenuation in case of alternating physical boundary conditions on the interface substrate/solution. The electric field of the wave is shielded from the solution (skineffect) by the metallization of the sensitive zone. Thus, only the mechanical properties (density, viscosity) of the solution influence the propagation properties of the wave.

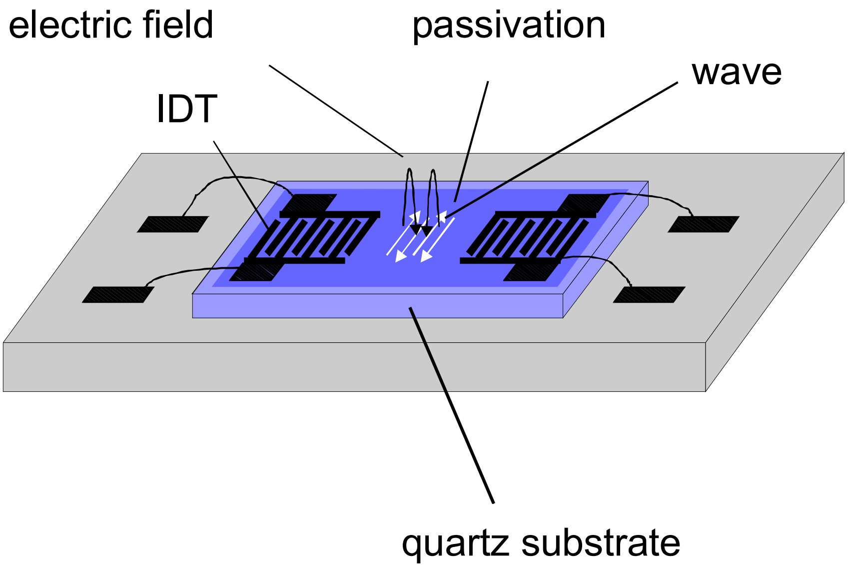

Figure 5-5: Surface acoustic wave sensor (SAW)

5.2.3 Peltier Element

In order to generate the additional supersaturation ΔC_{sensor} the sensor surface has to be cooled. For an evaluation of the measurements a controllable and reproducible cooling is necessary. Therefore a peltier element was implemented.

As current flows the temperature of the contact of the two different conductors changes according to the direction of the current. This effect is named after its discoverer, the physicist J. Peltier, in 1834. Generally speaking, the peltier effect is caused by the energy transport of charge carriers. Its utilization for technical applications was only possible with the introduction of semiconductor materials, since the peltier effect is very small for conventional conductors (metals).

A peltier element consists of two semiconductor limbs, one n- and one p-doped semiconductor. These semiconductor limbs are linked with a contact bridge, see Figure 5-6. When direct current is applied, one side of the element cools down, thus absorbing heat from the surrounding. The heat absorbed by the cold side of the peltier element is released to the other side of the element, the warm side. By this way the peltier element “pumps” heat from the cold side to the warm side. A reversion of polarity of the direct current leads to a change in the direction of the heat flow, this means the cold side heats up and the warm side cools down.

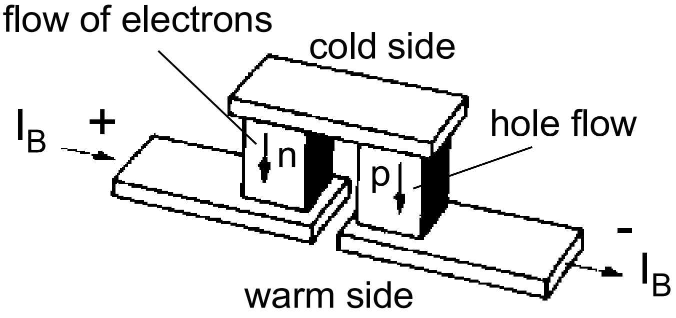

Figure 5-6: Peltier element (schematic)

In order to increase the cooling power, peltier elements are combined to a peltier cooling block as can be seen in Figure 5-7.

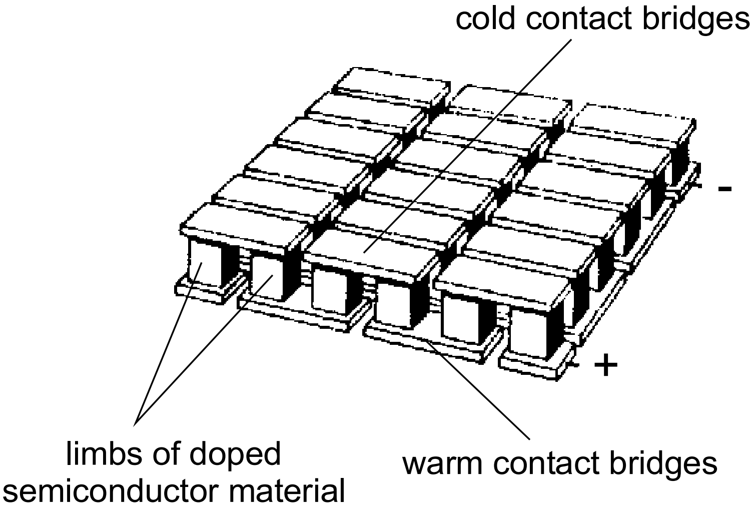

Figure 5-7: Peltier cooling block

The cooling power Q_{cool} of a peltier element or cooling block is reduced by Joule's heat loss due to the electric resistance of the semiconductors and by the heat flow from the warm contact bridges to the cold ones caused by the heat conductivity of the semiconductor limbs. Further descriptions for the layout and the design of peltier elements can be found in [Alte09, Just53, Gold54, Müll63, Müll91, Neum92, Sage62]. For this work a peltier element provided by EuroQuant GmbH with the specifications shown in Table 5-2 was used:

Table 5-2: Specifications of the peltier element

type	I_{max} [A]	Q_{max} [W]	U_{max} [V]	ΔT_{max} [K]	length [mm]	width [mm]	height [mm]
TB-63-1,4-1,5	6.1	29.7	7.9	70.0	20.0	40.0	3.9

5.2.4 Sensor Setup

Both sensors (IDT and SAW) are cooled by a peltier element positioned on its back. This guarantees the highest supersaturation in the solution on the sensor surface, thus promoting incrustation or crystallization to start on the sensor surface first. As can be seen in Figure 5-9 the IDT detects the generated crystal mass by a change of the impedance, whereas the SAW (see Figure 5-8) measures the incrustation by different propagation properties of the electroacoustic wave.

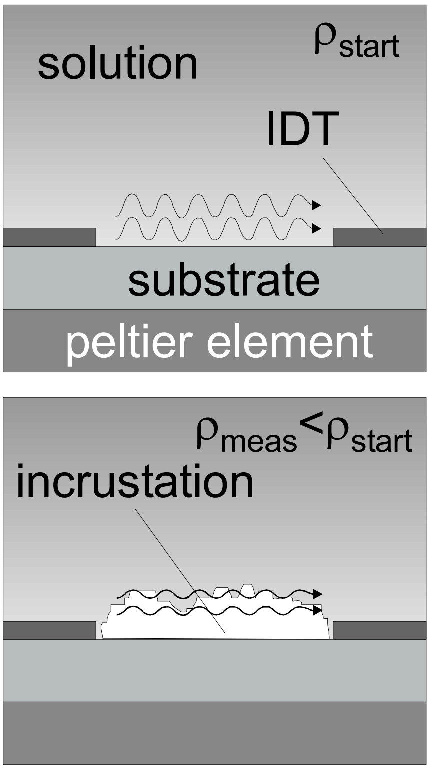

Figure 5-8: Detection of the incrustation with the SAW

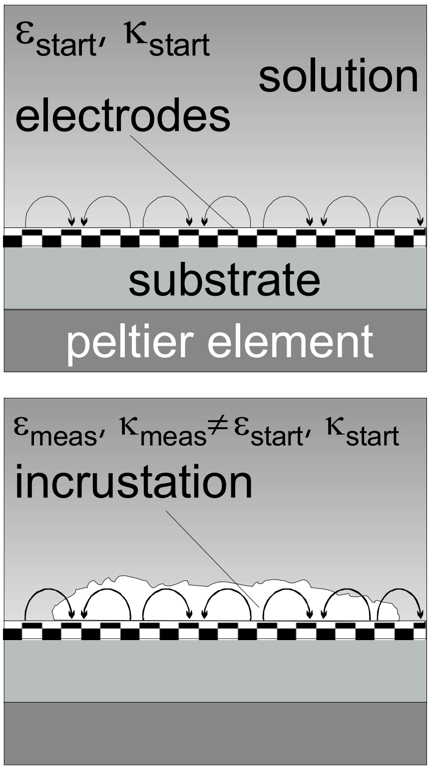

Figure 5-9: Detection of the incrustation with the IDT

Each sensor records two measurement signals:

IDT

- phase
- absolute value

SAW

- frequency
- attenuation

In general it can be said that the IDT measures a change of the electric properties of the media adjacent to the sensor surface, whereas the SAW detects alternating mechanic properties.

The complex impedance $\underline{Z}$ of the IDT is given by:

$$\underline{Z} = \frac{\underline{U}}{\underline{I}} = \frac{\hat{U} e^{j\varphi_u}}{\hat{I} e^{j\varphi_i}} = \frac{\hat{U}}{\hat{I}} e^{j(\varphi_u - \varphi_i)} \qquad (5\text{-}2)$$

or in exponential expression

$$\underline{Z} = Z e^{j\varphi} \qquad (5\text{-}3)$$

with

$$Z = \sqrt{R^2 + X^2} \qquad (5\text{-}4)$$

Where X is the reactive part of impedance, R is the resistance and φ is phase angle describing the phaseshift of the voltage against the current.

The frequency change Δf of the SAW is dependent on the properties (viscosity η, density ρ) of the media between emitter and receiver of the electroacoustic wave and can be described by [Leid97]

$$\Delta f \sim \sqrt{\eta \rho} \qquad (5\text{-}5)$$

In order to provide reproducible conditions for each measurement, the incrustation has to be removed from the sensor surface before a new measurement can be started. This can be realised by flushing the surface with an unsaturated solution and / or by heating the sensor surface with the help of the peltier element by changing the direction of the direct current. Thus the measurement is conducted as a quasi-continuous process with sequences of one to two minutes duration. One measurement consists of three steps:

1. Generating additional supersaturation by cooling with the peltier element
2. Solid formation or deposition and incrustation of the sensor surface
3. Removing the crystal layer by heating or flushing

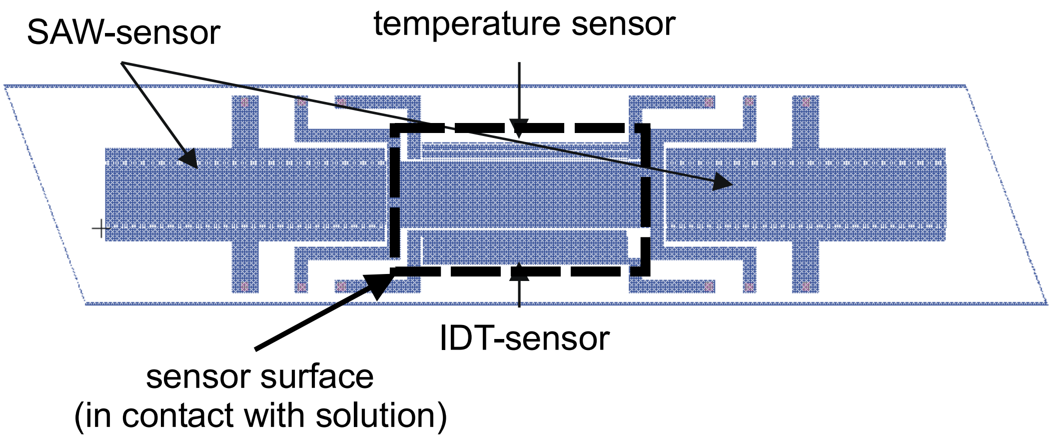

Figure 5-10: Design of the sensor chip

Figure 5-10 illustrates the design of the sensor chip placed on the cold side of the peltier element. Both sensors, IDT and SAW, and a gold resistance thermometer are integrated. The dashed rectangle marks the active sensor surface which is in contact with the solution. This sensor surface has a size of 8 mm x 5 mm. A silicone sealing protects the receiver and emitter of the SAW from the solution. Otherwise the dielectric stress caused by the solution would lead to a drastic degradation of the electroacoustic wave excitation, resulting in a SAW-oscillation-failure.
The casing of the sensor shown in Figure 5-11 and Figure 5-12 is made of V4A-steel. This material has a high resistance to corrosion and a good heat conductivity, which is necessary to provide a good heat removal from the warm side of the peltier element. In order to guarantee a high cooling power of the peltier element the heat removal is increased by cooling fins which are attached on the back of the casing.
The sensor chip placed on a peltier element is located in the middle of the casing. For high leakproofness the casing is filled with silicone and the casing cover made of PTFE (Teflon) is fixed with screws. The whole sensor device has a diameter of 9 cm and a height of 3 cm.

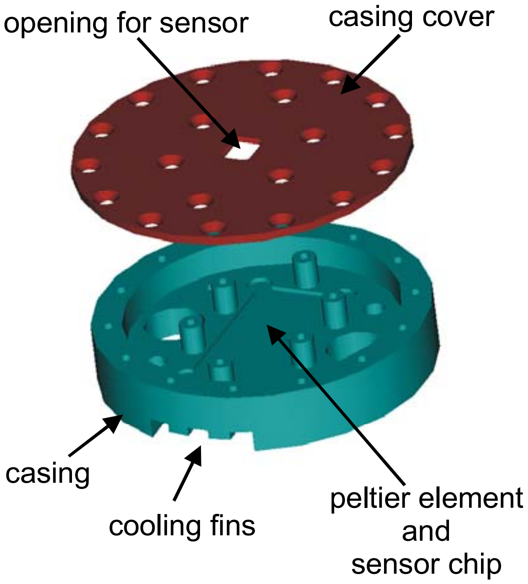

Figure 5-11: Sensor setup

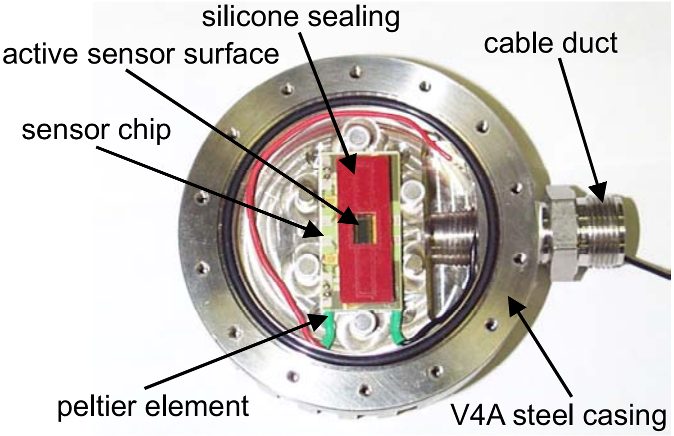

Figure 5-12: Inner life of the sensor

An additional temperature sensor measuring the temperature of the solution is placed on the cover (see Figure 5-13). The active sensor surface is located in a dent.

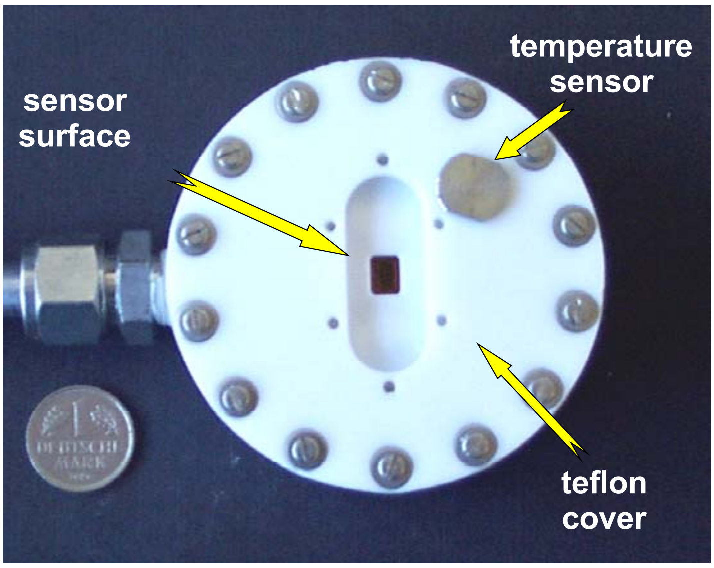

Figure 5-13: Top view of the assembled sensor

This sensor was tested in beaker glasses with undersaturated and therefore crystal-free solutions. The intention of the first experiments was to prove the applicability of the sensor and to test the reproducibility of the measurements. Thus it was necessary to provide constant conditions for these experiments. For this reason the experiments were performed in beakers without stirring (no fluid flow) containing KNO_3-solutions of various degrees of undersaturation. The major advantage of measuring in undersaturated solutions lies in the constant solution composition. Supersaturated solutions are not stable because nucleation and growth would cause an unknown shift in the concentration as well as in the saturation temperature. Of course, all concentrations of the solutions investigated have been chosen in such a way that supersaturation after cooling was obtained. The only difference between measurements conducted in under- and supersaturated solutions is the required cooling power to induce incrustation on the sensor surface. The results of these experiments are presented in chapter 6.2.

Switching from beaker glasses to crystallizers generates additional problems. This is explained in Figure 5-14 to Figure 5-19, where a schematic comparison of the three major steps during a measurement in a beaker glass and a crystallizer is made.

Step I – cooling

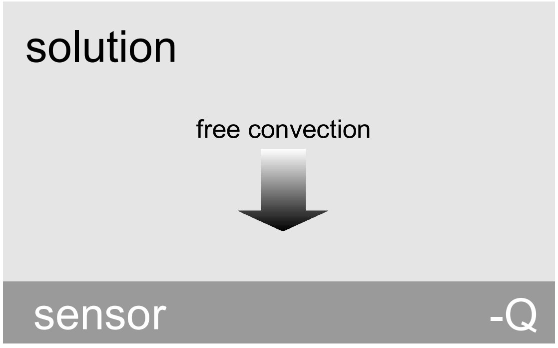

Figure 5-14: Generating additional supersaturation ΔC_{sensor} by cooling (beaker glass)

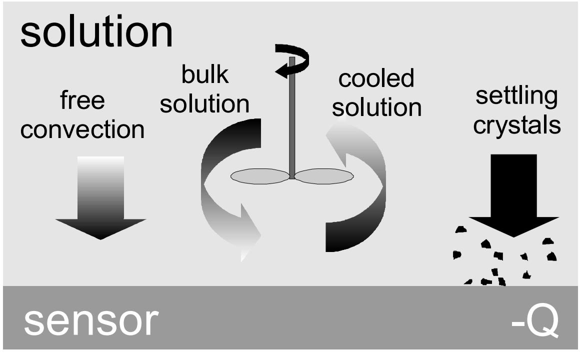

Figure 5-15: Generating additional supersaturation ΔC_{sensor} by cooling (crystallizer)

Cooling the solution in order to establish the additional supersaturation ΔC_{sensor}, required for the incrustation of the sensor surface, can lead to a free convection of the solution since the cooled fluid has a higher density. This is the case if the walls or the ceiling of the measurement chamber are cooled instead of the bottom. As shown in Figure 5-14, the solution is quiescent above the sensor surface. In the case of the unstirred and crystal-free solution in the beaker glasses, a temperature profile in the solution with the lowest temperature on the sensor surface and the highest temperatue in the bulk phase is created, without natural convection. In crystallizers stirrers for the suspension of the crystals are installed, thus generating a forced convection, see Figure 5-15. By this means, already cooled fluid is removed from the sensor surface and is replaced by warm fluid from the bulk phase. This leads to fluctuations and perturbations in the temperature profile of the solution adjacent to the sensor surface, depending on the power input (e. g. revolutions per minute of the stirrer). Since the measurement signals of the SAW are dependent on the mechanic properties of the solution (viscosity η and density ρ) and therefore temperature-dependent, the signals get noisy and become unreproducible. The start of the incrustation is then unreproducibly delayed since cooled fluid is removed and warm fluid from the bulk has to be cooled again. This demands that even in unstrirred solutions the only possible position for the sensor is horizontal with an upwards facing sensor surface. Otherwise free convection would transport cooled fluid from the sensor surface to the bulk.

Another problem arises through suspended crystals which might settle on the sensor surface and influence the measurement signals, making it nearly impossible to detect the starting point of the incrustation.

Step II - incrustation

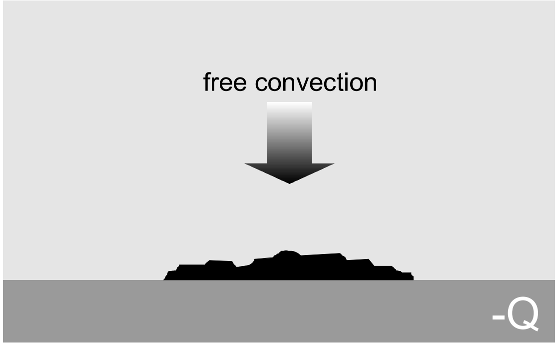

Figure 5-16: Incrustation of the sensor (beaker glass)

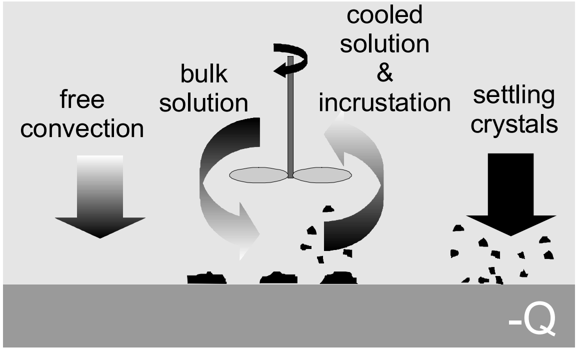

Figure 5-17: Incrustation of the sensor (crystallizer)

As shown in Figure 5-16, free convection due to local temperature differences would be the only force that affects the crystal layer on the sensor surface during the incrustation phase in beaker glasses. Due to the fact that free convection is orientated towards the sensor surface, the incrustation remains stable on the sensor. Whereas in crystallizers (see Figure 5-17), forced convection might tear off crystal layer fragments, thus influencing the measurement signals. This influence is primarily dependent on the power input and represents another dependency of the measurement signals on turbulence. The aspect of random crystal settling on the sensor surface and the resulting loss in reproducibility is present during the incrustation phase, too.

Step III – removal of incrustation

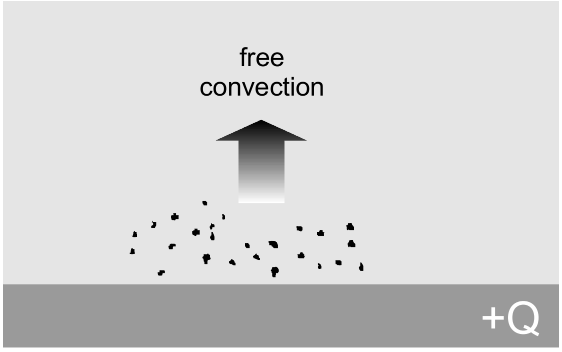

Figure 5-18: Removal of incrustation (beaker glass)

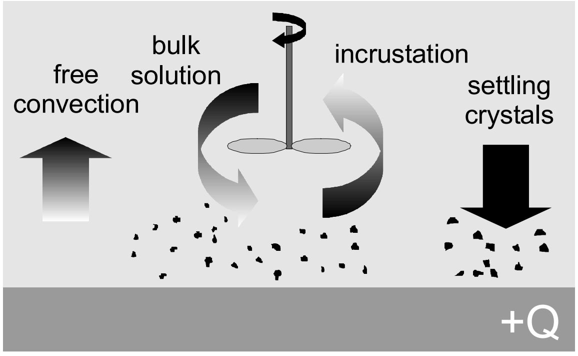

Figure 5-19: Removal of incrustation (crystallizer)

Reversing the polarity of direct current of the peltier element leads to the heating of the sensor surface. Since the solubility increases with temperature for systems with $\frac{dC^*}{dT} > 0$, the crystal layer on the sensor surface dissolves and a clean sensor surface for the next measurement is obtained (see Figure 5-18). The dissolution, however, leads to high increase of concentration of the solution adjacent to the sensor surface. Observations and calculations have shown that this accumulated concentration can be twice as high as the bulk concentration. Since free convection is the only transport mechanism in beaker glasses, mixing times are quite high. If the heating of the peltier element is switched off too soon, the temperature of the solution drops to bulk temperature and, considering the high concentrations adjacent to the sensor surface, supersaturation is now created without any additional cooling. Instantaneous incrustation of the sensor surface is the result. The turbulence in the crystallizer, shown in Figure 5-19, is advantageous in this case, since incrustation fragments are transported from the sensor surface to the bulk and mixing is improved. Only settling crystals could prevent a complete cleaning of the sensor surface in both, beaker glasses and crystallizers.

These considerations lead to the following requirements during the three steps of a measurement:

step I – cooling
- solution at rest (no turbulence)
- almost crystal-free solution

step II – incrustation
- solution at rest (no turbulence)
- almost crystal-free solution

step III – heating and removal of incrustation
- mixed solution (turbulence, removal of incrustation, mixing with bulk)
- exchange of solution adjacent to sensor surface with solution from bulk
- almost crystal-free solution

These specifications demand a housing for the sensor with a crystal separation device. The first attempts resulted in a pump combined with a filter which provide the sensor housing with solution. The pump is switched off during step I and II, thus leading to a solution at rest in the sensor housing. Switching on the pump in step III provides an exchange of the solution and the flushing of the sensor surface. The filter prevents crystals from entering the sensor housing. Unfortunately, the filter might be blocked during batch crystallization and an additional installation of moving parts (pump) in the crystallizer should be avoided in order to ensure an easy operation.

Hydrocyclones are an alternative since they are simple, but reliable separation devices. Experiments have shown that a hydrocyclone with a cut size of 20 µm fulfilled the requirements. The pump which is necessary to operate the hydrocyclone raised the problem of the undesired additional installation of an apparatus with moving parts

again. Considering measurements in industrial crystallizers with high suspension densities, the possibility of blinding of the hydrocyclone is also very high.
The solution for these problems is a sensor housing combined with a jet pump and a sedimentation tube as a particle separation device, as is shown in Figure 5-20 and Figure 5-21.

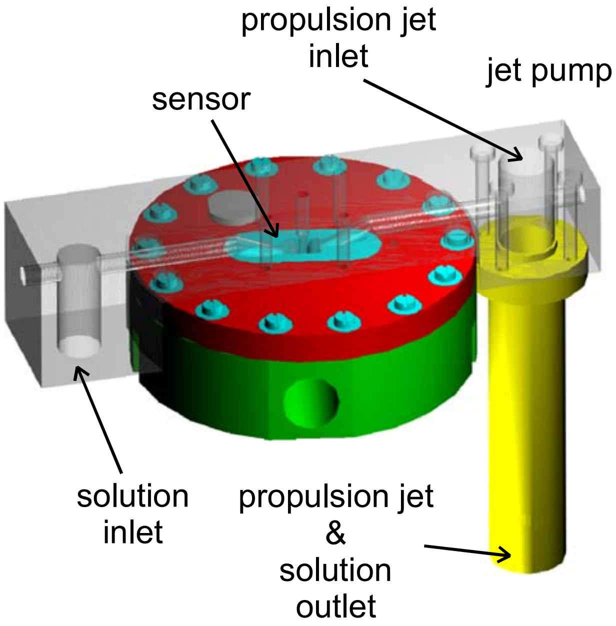

Figure 5-20: CAD sketch of jet pump attached to sensor

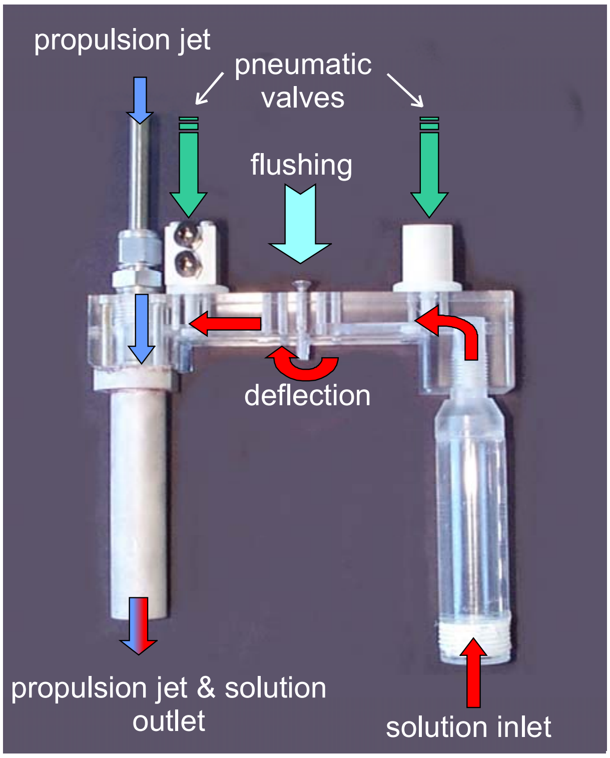

Figure 5-21: Sensor housing with jet pump

The jet pump is advantageous since it has no moving parts. In order to generate the transport of fluid it is necessary to employ a propulsion jet, which can be taken from flushing pipelines in the crystallizer or directly from the solution, which can be circulated by a pump installed outside the crystallizer. Due to the low pressure which is generated by the jet pump the solution is sucked into the housing and flows through it. A deflection positioned above the active sensor surface guarantees that the flow of solution is directed towards the sensor surface. After rinsing the active sensor surface the solution is mixed with the propulsion jet in the jet pump and leaves the housing at the outlet. Pneumatic valves at both ends of the channel, which runs over the sensor surface, are closed during step I and II of each measurement, thus ensuring a solution at rest. For a removal of the incrustation and an exchange of solution in step III the valves are opened and new solution from the bulk is sucked in. Above the deflection a connector for an additional flushing line of pure solvent or undersaturated solution is installed. This installation is able to wash away hardly removable incrustations by using high pressure. With the help of this housing, the turbulence in the crystallizer and the suspended crystals do not affect the measurement signals. In Figure 5-22 the housing with the jet pump and the sedimentation tube attached to the sensor can be seen.

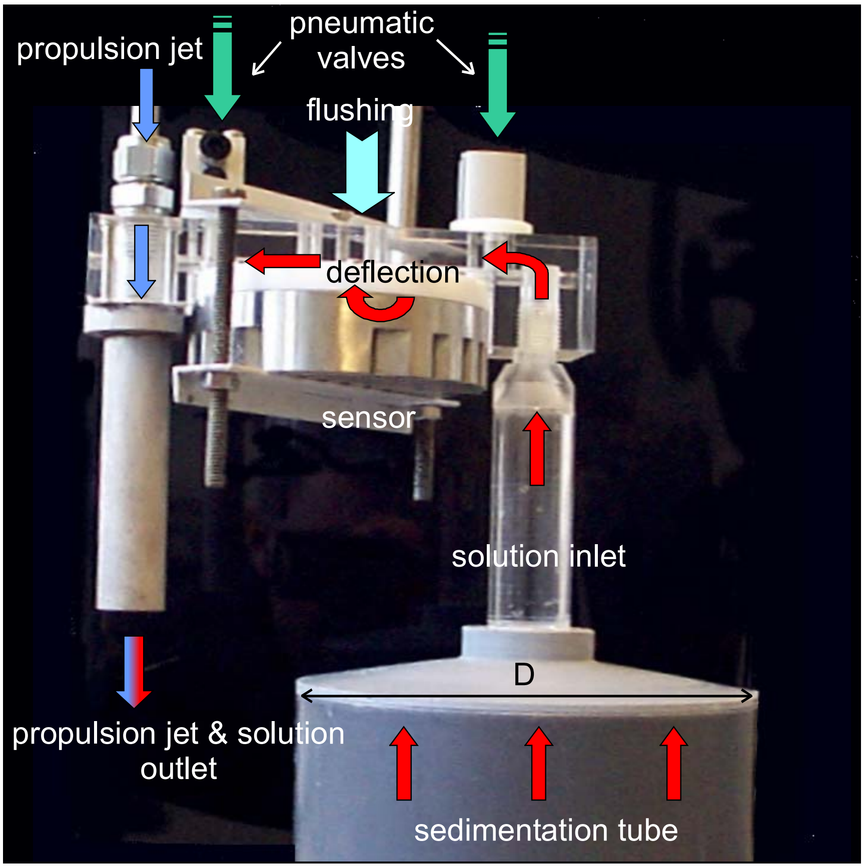

Figure 5-22: Sensor with housing, jet pump and sedimentation tube

The layout of the sedimentation tube, i. e. the required diameter D, can be estimated by the settling velocity of a single particle according to Stokes:

$$D = 2\sqrt{\frac{18\,\dot{V}\,\eta_{sol}}{\pi\, d_{sep}^{2}\, g\left(\rho_{C} - \rho_{sol}\right)}} \qquad (5\text{-}6)$$

Where d_{sep} is the cut size and g is the gravitational acceleration. The difference of the densities of crystal ρ_C and solution ρ_{sol} requires an individual layout for each substance. Since the measurements conducted with a hydrocyclone with a cut size of 20 µm showed good results, the same cut size was chosen for the layout of the sedimentation tube.

The jet pump was operated by a flexible tube pump installed outside the crystallizer. The propulsion jet was created by circulating process solution of the crystallizer with the flexible tube pump. The volumetric delivery of the jet pump was determined by experiments as the difference in the volumetric delivery of jet pump & flexible tube pump versus flexible tube pump. Figure 5-23 shows the volume flow rate plotted versus revolutions per minute of the flexible tube pump (Verder Peristaltic 2005).

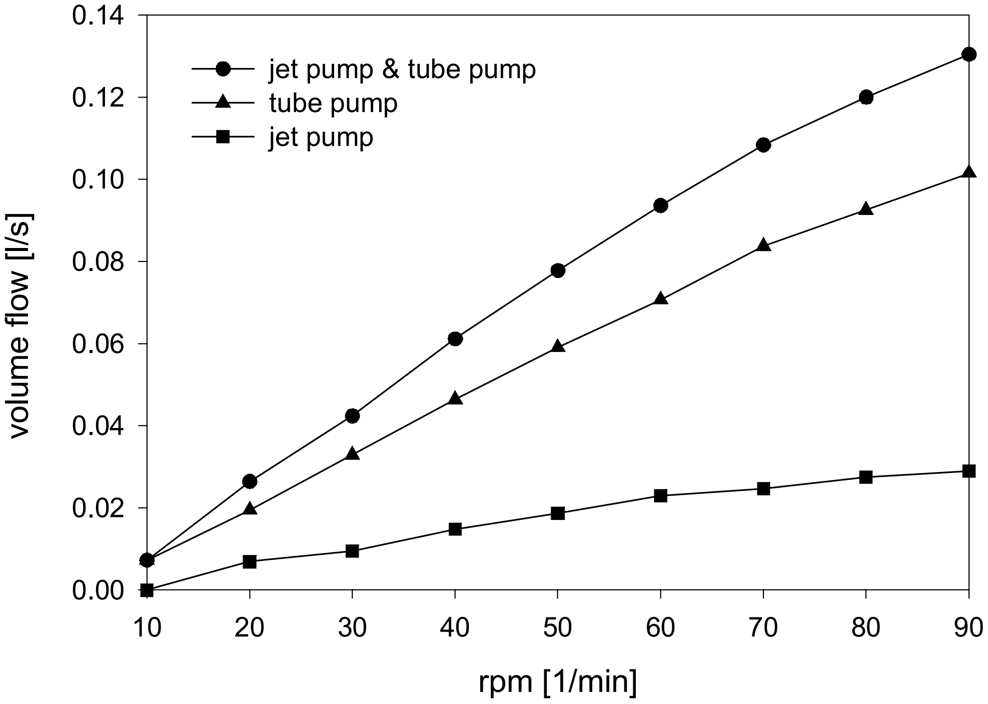

Figure 5-23: Volume flow of jet and tube pump as a function of revolutions per minute of tube pump

According to equation (5-6) the diameter D of the sedimentation tube is inversely proportional to the root of the density difference ($\rho_C - \rho_{sol}$) or $D \sim (\rho_C - \rho_{sol})^{-1/2}$ and can become large for small density differences.

6 Experiments

In this chapter the experimental results will be shown. In order to understand the functioning of the sensor, it is necessary to describe the way how supersaturation is derived from the measurement signals.

First of all, the behaviour of the measurement signals during cooling or heating of the sensor surface will be explained. Following, the results of experiments conducted in beaker glasses will help to demonstrate the operation principle and capabilities of the new sensor. The monitoring of supersaturation during a batch cooling crystallization will reveal the applicability of the sensor. The huge amount of measurement data, which were created during the development and test phase, would surely go beyond the scope of this thesis and will therefore be shortened to a description of the experiments with one inorganic (potassium nitrate - water) and one organic (adipic acid - water) system.

6.1 Measurement Signals

As mentioned in the previous chapter, the cooling of the sensor is provided by a peltier element. Therefore, the subcooling of the sensor surface can be adjusted by the amperage of the direct current. In general, the cooling can be realized with a step function (see Figure 6-1) or a constant cooling rate (see Figure 6-2), which means a constant increase of the amperage until the final value of the amperage is reached. Every measurement consists of pre-measurement, measurement and post-measurement phase. During the pre- and post-measurement phases, measurement signals are recorded, as well, but the peltier element is switched off. The recorded signals are used as reference signals to compare the initial start conditions for each measurement and to check whether the incrustation was completely removed at the end of the previous measurement sequence. In addition malfunctions of the sensor can easily be detected with the help of these reference signals. In Figure 6-1 and Figure 6-2 schematic courses of the current during a measurement sequence are shown. The “positive” or “negative” values of the amperage indicate the direction of the direct current, i. e. a negative value (-) represents cooling whereas a positive value (+) stands for heating of the sensor surface. In order to remove the incrustation from the sensor a heating of the sensor surface is implemented at the end of the measurement phase in both cases. This heating is controlled by an amperage step function.

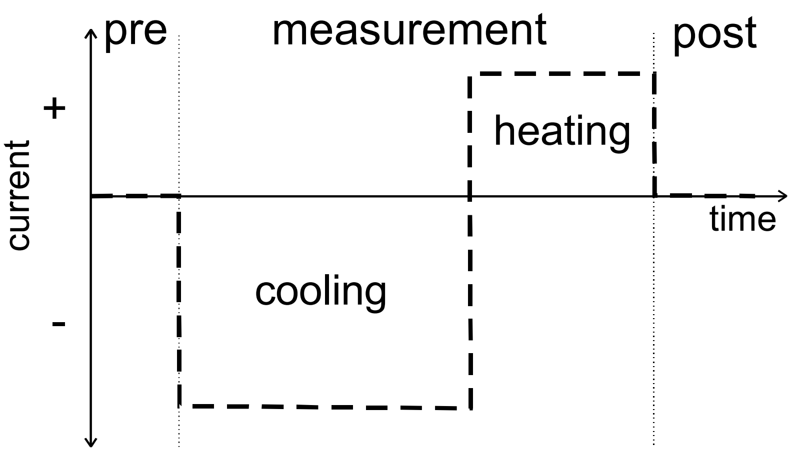

Figure 6-1: Qualitative step function of current

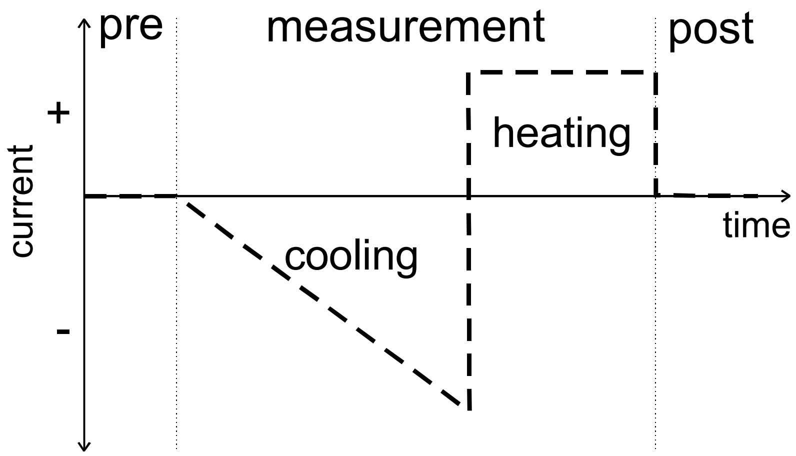

Figure 6-2: Qualitative function of current in case of a linear cooling rate

Nevertheless, most experiments were performed with a manual heating of the sensor. As a consequence the measurement phase consisted only of a cooling phase as shown in Figure 6-3.

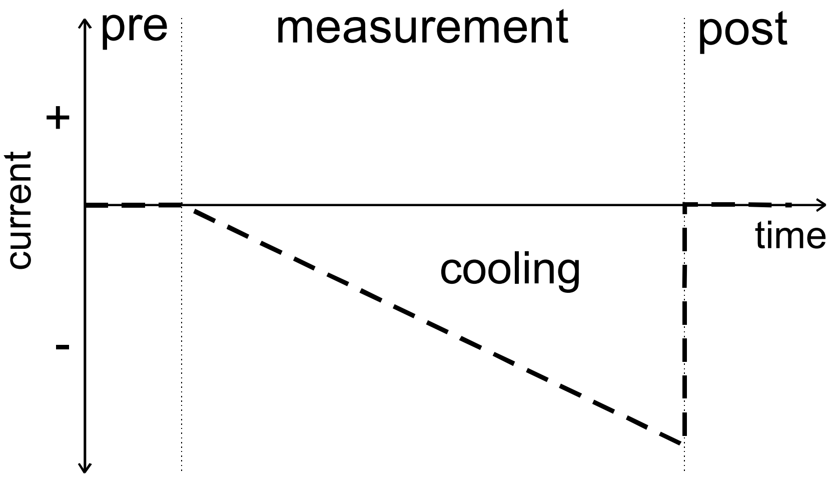

Figure 6-3: Qualitative function of current (linear cooling rate) used for experiments

First experiments have shown that the generation of the supersaturation ΔC_{Sensor} with a step function makes it nearly impossible to detect differences of supersaturation ΔC_{Proc} in solutions. The immediate and steep increase of supersaturation dominates the crystallization on the sensor surface and diminishes the influence of the supersaturation of the solution ΔC_{Proc}. Only a linear cooling rate is able to take into account the influence of ΔC_{Proc} during the measurements.

To demonstrate the cooling power of the peltier element the temperature measured with the gold resistance thermometer on the sensor chip and the amperage of the peltier element are shown in Figure 6-4. The measurement was conducted in deionized water. The depicted temperature is not the temperature on the sensor surface since the gold resistance thermometer is also passivated with a SiC-layer. It can be seen that during the pre-measurement phase, where no current is applied to the peltier element, the temperature remains constant. At the beginning of the cooling, the decrease of the temperature is almost linear and corresponds to the amperage of the direct current, whereas at the end the decrease is reduced by Joules heat (energy dissipation). The heat exchange between "warm" and "cold" side of the peltier element is the reason for the quick increase of the temperature in the post-measurement phase, when the current is switched off.

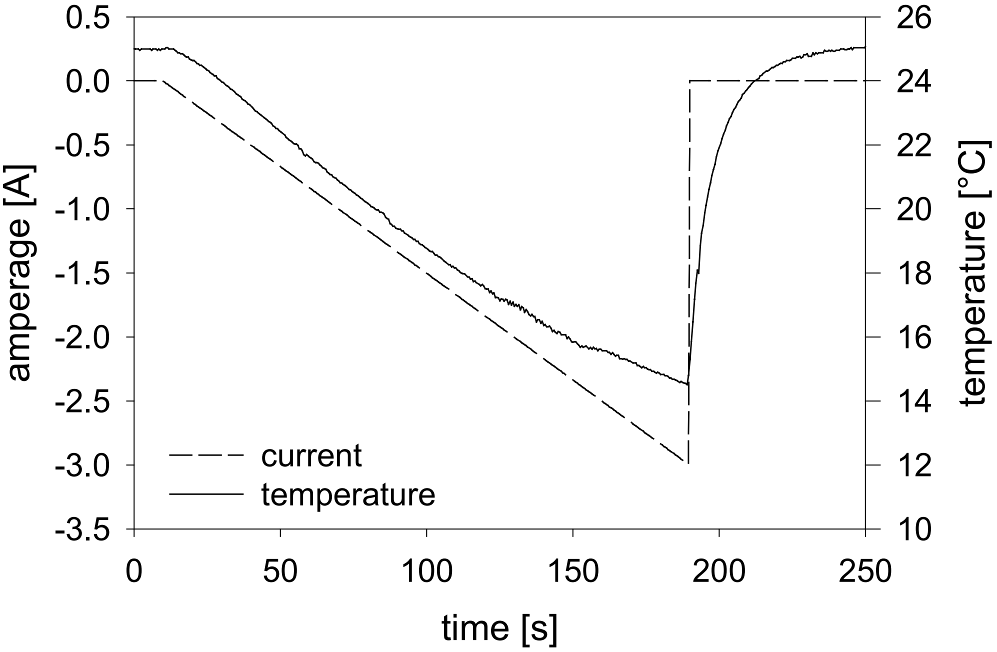

Figure 6-4: Current and temperature of the gold resistance thermometer versus time in deionized water (25°C)

The SAW-sensor is able to sense changes in the mechanical properties of the solution adjacent to the sensor surface according to (5-5). The cooling of the sensor causes an increase of the density and viscosity of the solution. Thus, the frequency of the surface acoustic waves is reduced and the attenuation is increased. A typical measurement signal of the SAW-sensor in deionized water with a temperature of 25°C are depicted in Figure 6-5.

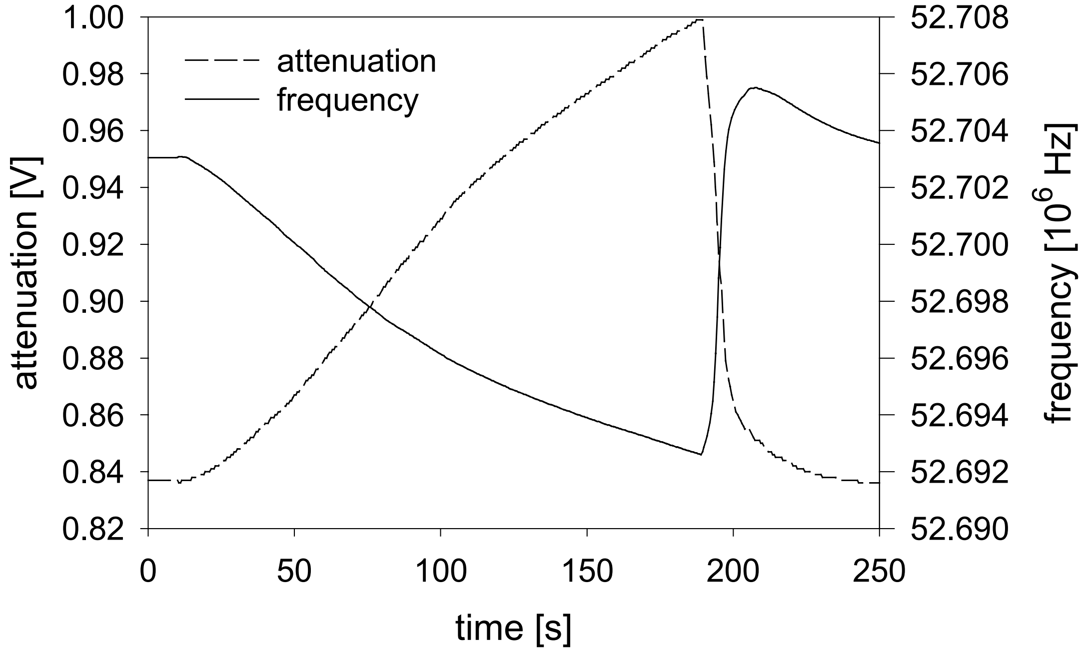

Figure 6-5: Attenuation and frequency of the SAW-sensor during cooling in deionized water at 25°C

The function describing the direct current in Figure 6-5 is the same as plotted in Figure 6-4.

Another important aspect is the dependency of the behaviour of the SAW signals on solution temperature. A solution temperature below 50°C leads to a decrease of the frequency during cooling of the sensor surface, whereas temperatures above 50°C cause an increase of the frequency. Considering heating of the sensor, the behaviour is vice versa. In Figure 6-6 the normalized change of frequency Δf for different temperatures of deionized water in combination with the corresponding function of the current can be seen. This temperature dependent behaviour must be taken into account during the evaluation of the measurement signals.

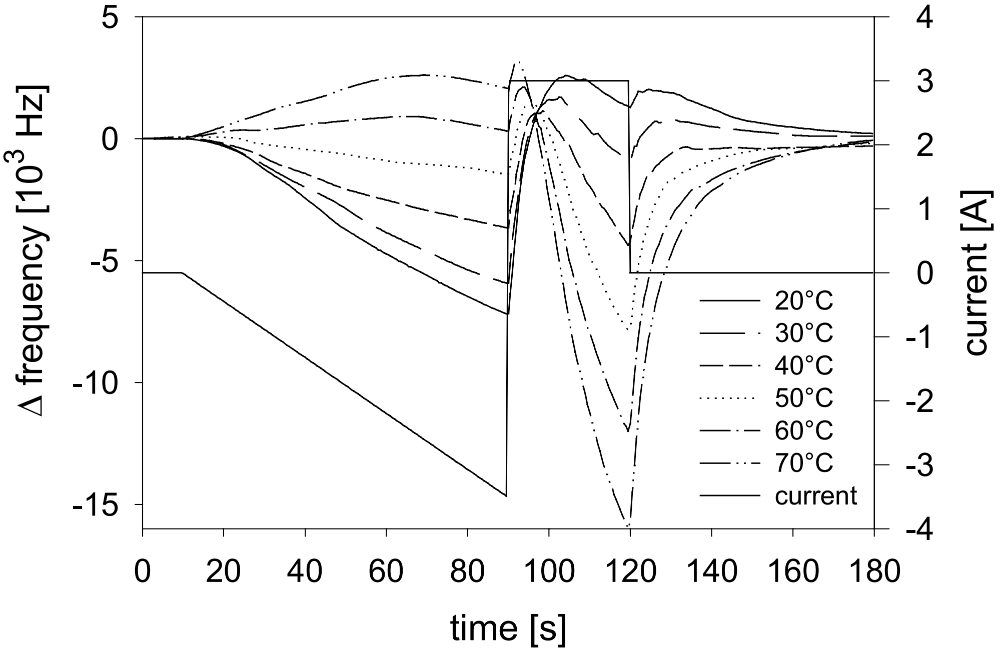

Figure 6-6: Frequency difference of the SAW-sensor in deionized water during cooling (-) and heating (+) at different solution temperatures

The measurement signals of the IDT-sensor are dependent on the electric properties of the solution. Considering the high frequency of the alternating current (~ 52 MHz), the temperature dependent velocity of the solvated ions in the solution can be neglected. Therefore almost no temperature dependence of the measurement signals (absolute value and phase) is expected. But a closer look at Figure 6-7 reveals an unexpected influence of the solution temperature adjacent to the sensor surface on phase and absolute value. This dependency is due to a change of density during the cooling period, which leads to higher ion concentration, thus affecting the electric properties. The appropriate function of the direct current of the peltier element is displayed in Figure 6-4.

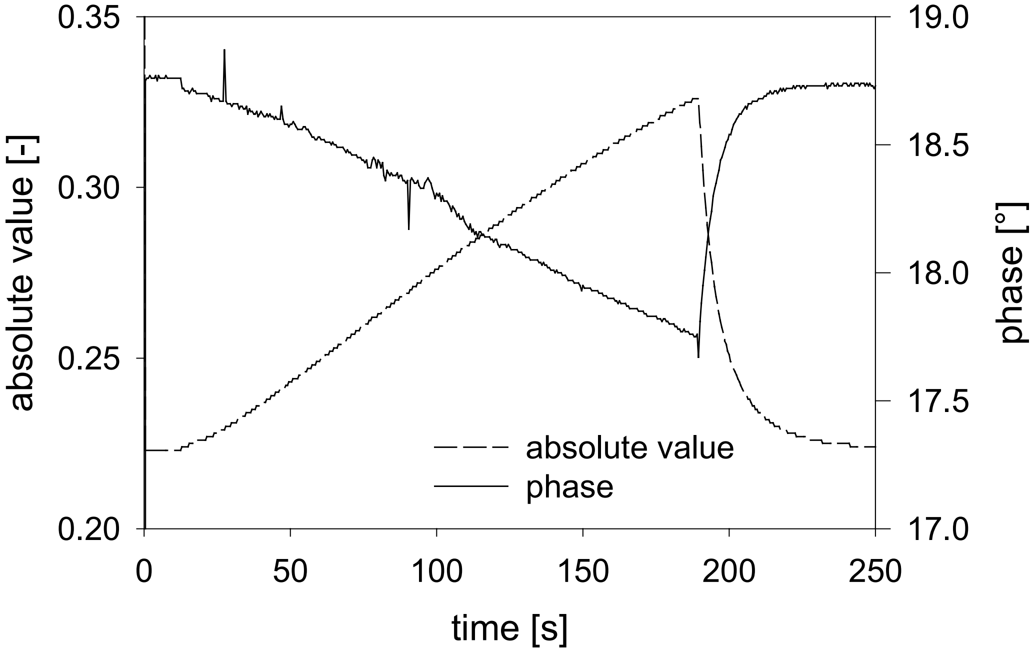

Figure 6-7: Phase and absolute value of the IDT-sensor during cooling in deionized water at 25°C

6.2 Beaker Glass Experiments

The experiments described in this chapter were conducted with a sensor according to chapter 5.2.4. Despite the purpose of the sensor to measure supersaturation in industrial crystallizers, the first tests were conducted in undersaturated solutions in beaker glasses. To verify the operation and the reproducibility of the sensor, constant test conditions have to be provided. In the case of supersaturated solutions it would be very difficult to provide for each measurement exact the same level of supersaturation, since these solutions are unstable and try to reach equilibrium by crystallization, thus leading to a shift of the saturation temperature. The major difference between measurements in undersaturated and supersaturated solutions is the higher cooling power, or in case of a constant cooling rate, a longer time period until the required start of incrustation on the sensor surface. The choice of measuring solutions in beaker glasses is furthermore justified since the problems arising from turbulence, which were explained in the previous chapter, can then be avoided.

The experimental setup is displayed in Figure 6-8. A beaker glass is kept at constant temperature by a water bath, with water, that is circulated through a cryostat. The beaker glass is filled with undersaturated potassium nitrate (KNO_3) solution and the sensor is positioned in the center of the beaker glass with an upward orientated sensor surface. The measurement signals are recorded by a PC.

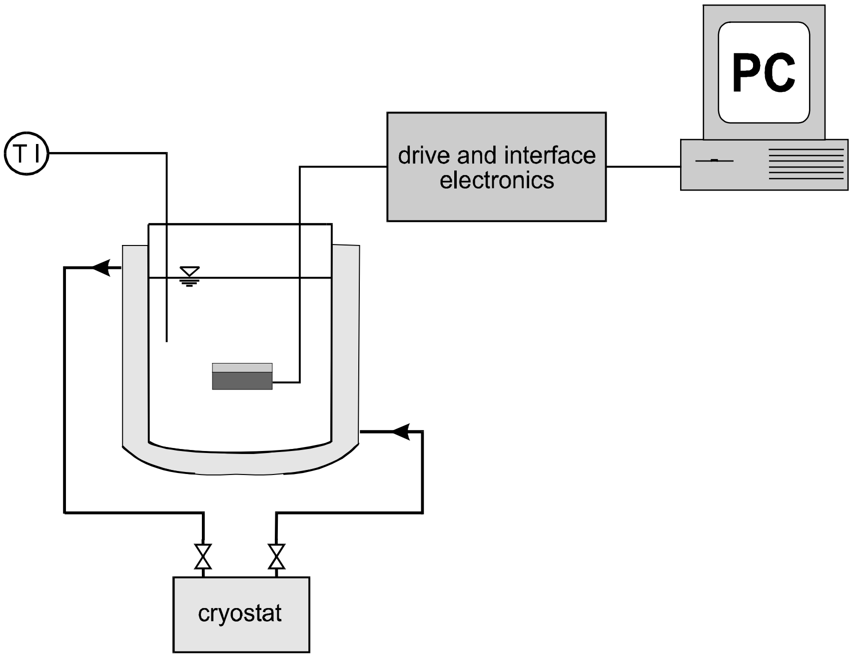

Figure 6-8: Experimental setup with beaker glass

In the first experiments potassium nitrate solutions with various degrees of undersaturation were prepared. Expressing the concentration in an subcooling with respect to the saturation temperature T^* and keeping these solutions at a constant temperature of 20°C, solutions with different levels of subcoolings are obtained. The subcooling of these solutions ΔT_{sol} and the corresponding undersaturation ΔC can be calculated according to equations (2-22) and (2-23). Table 6-1 gives an overview of the prepared potassium nitrate solutions.

Table 6-1: Prepared potassium nitrate solutions at 20°C

KNO3 concentration [mol/l]	undersaturation ΔC [mol/l]	saturation temperature T* [°C]	subcooling ΔT_{sol} [°C]
2.65	-0.09	19	-1
2.47	-0.27	17	-3
2.39	-0.35	16	-4
2.31	-0.43	15	-5

As mentioned in chapter 5.2 four different measurement signals (phase, absolute value, attenuation, and frequency) are recorded. Since the evaluation of the measurement data is similar in the case of all four signals, only the evaluation of the frequency will be discussed.

The dependency of the change of the frequency Δf has already been given by equation (5-5). The function of the amperage representing the cooling of the sensor in the following experiments is shown in Figure 6-9. The resulting temperature reduction on the sensor surface was recorded by the gold resistance thermometer on the sensor chip. Note that the temperature in Figure 6-9 is not the temperature on the sensor surface, since the gold resistance thermometer is positioned on the sensor chip and is passivated with a SiC-layer. Therefore, the temperature on the cold side of the sensor chip is measured. Due to the thermal resistance of the SiC-layer with a thickness of approximately 500 nm above the thermometer the temperature on the sensor surface is higher (temperatures below 0°C were not reached).

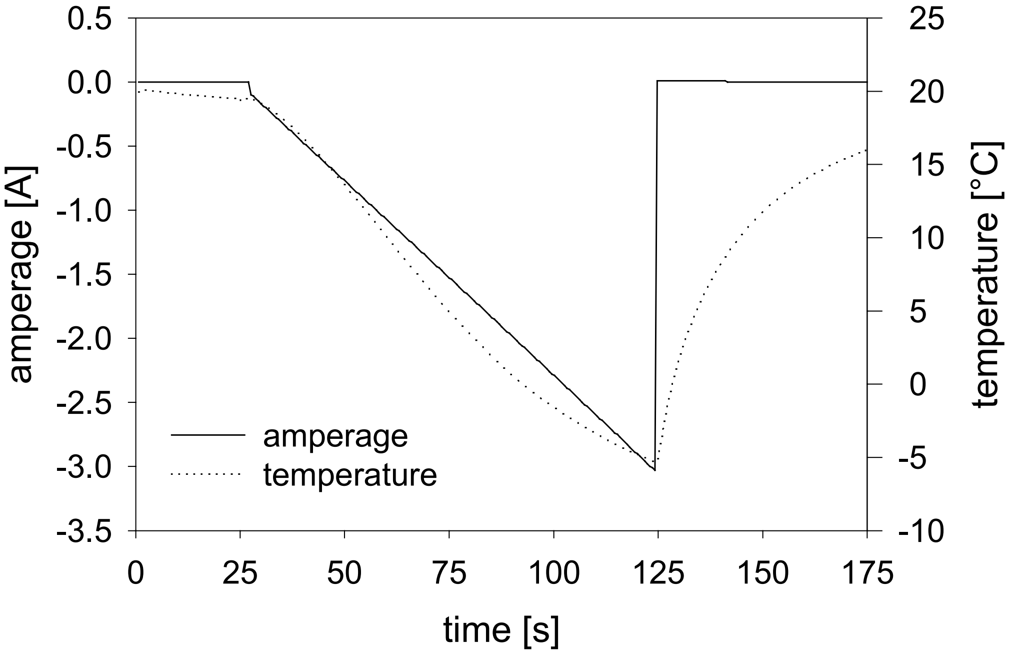

Figure 6-9: Function of amperage and resulting temperature on the sensor chip in KNO_3 solutions at 20°C; the mean cooling rate is 0.25 K / s = 900 K / h

In Figure 6-10 the change of frequency Δf in the different KNO_3 solutions is plotted versus time. Again a normalization of the frequency change has been made, because the different concentrations of potassium nitrate solutions (see Table 6-1) lead to different mechanical properties causing a shift in the starting frequency. Further on, the moving average (10 periods) was calculated to smooth the measurement signals.

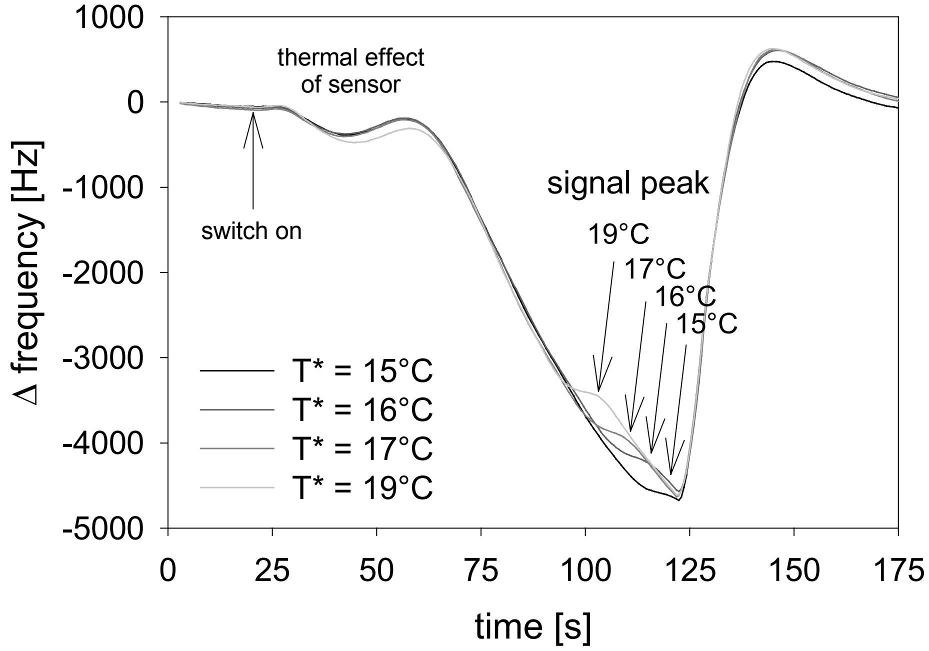

Figure 6-10: Change of frequency Δf (moving average) in different KNO_3 solutions at 20°C

In the beginning during the pre-measurement phase (0 s – 20 s), while the peltier element is not activated, reference signals are recorded. This can be seen by an almost constant frequency during the first twenty seconds. By switching on the peltier element after 20 s, the temperature starts to decrease (see Figure 6-9). This leads to a change in density ρ and viscosity η of the solution adjacent to the sensor surface and as a consequence the frequency alters.

The first local minimum (~ 40 s) and maximum (~ 60 s) of the frequency are due to a thermal effect of the sensor chip setup. In a later version of the sensor this thermal effect has been eliminated. After deactivating the peltier element after 125 s, the temperature and the frequency increase rapidly as a result of heat exchange between the warm and the cold side of the peltier element. Taking a closer look at the course of the frequency between 100 s and 120 s it can be seen that the solution with the highest concentration (T* = 19°C), respectively with the lowest undersaturation (ΔT = -1K) deviates first from the normal course. This phenomenon is linked to the starting point of the incrustation of the sensor surface. It is obvious that for the highest concentration the smallest subcooling or cooling power is needed in order to induce incrustation. Next, the solution with second highest concentration (T* = 17°C) starts to crystallize followed by the third (T* = 16°C) and finally the least (T* = 15°C) highest concentration. In Figure 6-11 the measurements are demonstrated schematically in the solubility diagram.

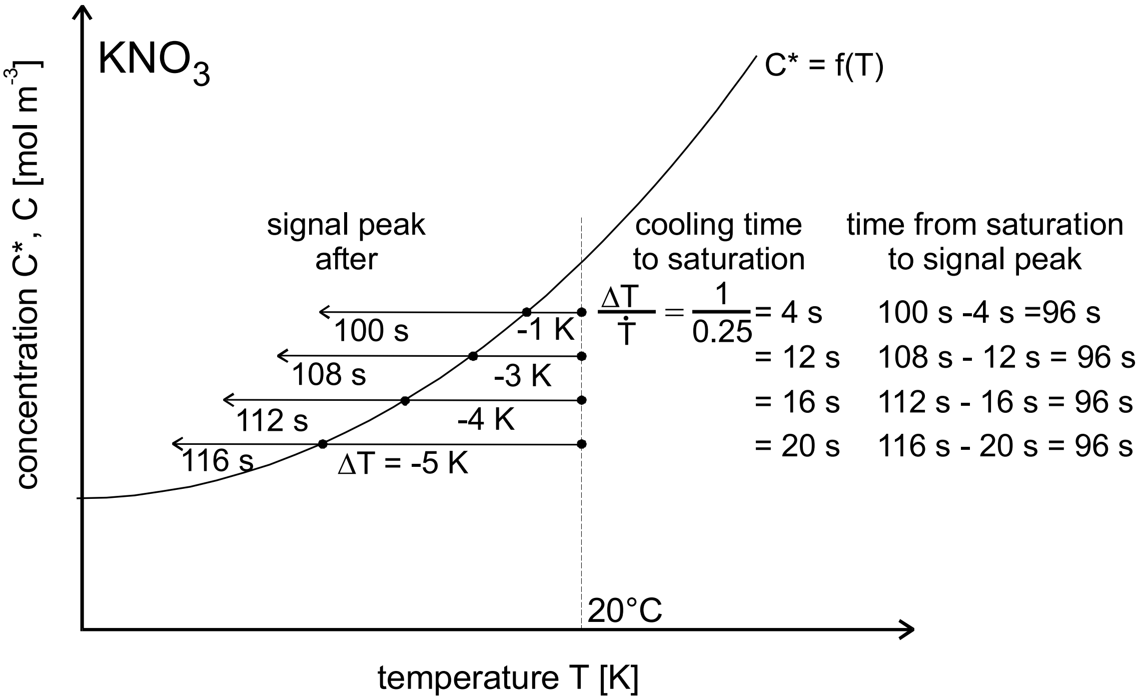

Figure 6-11: Measurements conducted in beaker glasses with KNO_3 schematically shown in the solubility plot

As can be seen from the diagram, the time elapsed from the saturation point at T* to the signal peak is always approximately 96 s.

To obtain the relevant measurement signals more clearly, the derivation of the frequency with respect to time has been calculated and plotted versus time (see Figure 6-12).

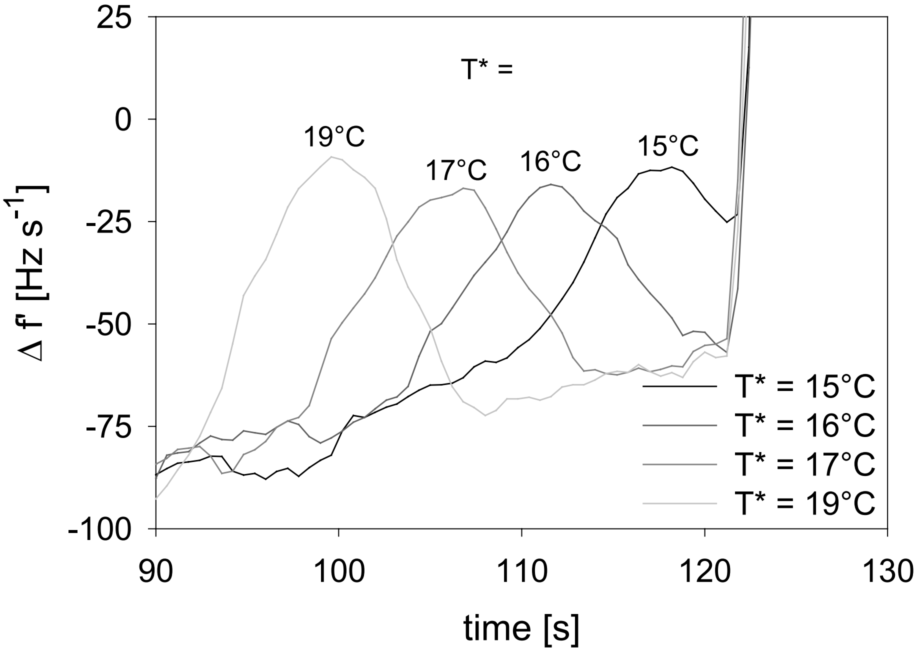

Figure 6-12:Derivation with respect to time of the frequency plotted versus time

Here, only the relevant interval of time (90 s – 130 s) is displayed. The obtained signal peaks are now more significant than those shown in Figure 6-10. If now these derivations are plotted versus the temperature of the peltier element, Figure 6-13 is obtained.

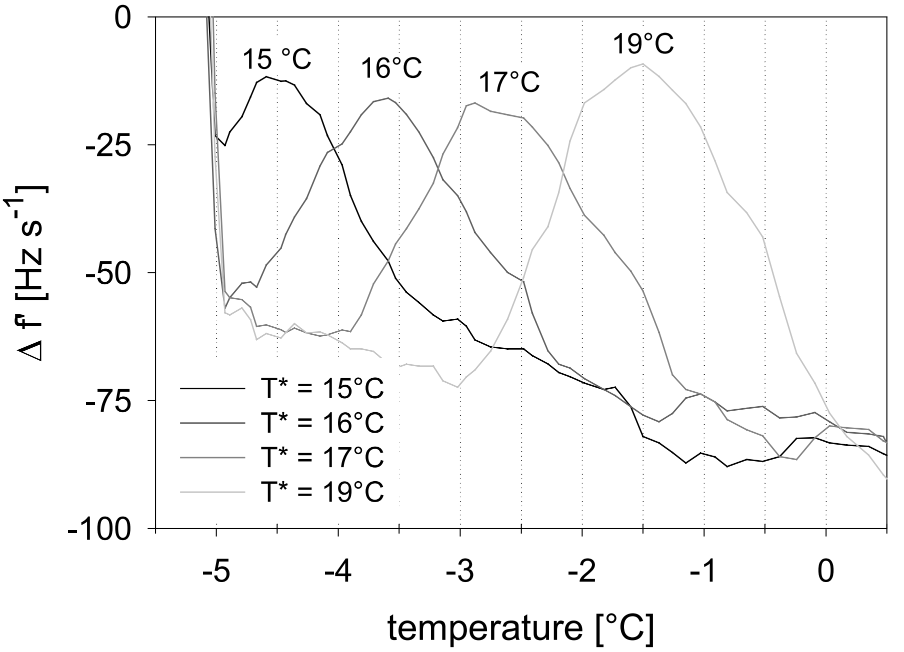

Figure 6-13: Derivation with respect to time of the frequency plotted versus temperature of the sensor chip

In Figure 6-13 only the section with the significant signal peaks (90 s – 130 s) is considered. For the highest saturation temperature (T* = 19°C) the smallest subcooling is required to induce crystallization on the sensor surface. Therefore, the peak of the curve with the highest concentration appears at the highest temperature (~ -1.5°C), followed by the peak representing the second highest concentration, respectively the second lowest undersaturation, and the peak of the curve with the lowest concentration (highest undersaturation) at the lowest temperature (~ -4.5°C).

It is remarkable that the difference of the saturation temperature (see Table 6-1) of the four solutions nearly equals the temperature difference of the required subcoolings between the signal peaks in Figure 6-13.

These experiments have proven the functioning of the new measurement method. The working of the sensor was demonstrated and the procedure of the evaluation of the measurement signals has been explained. The course of the measurement signals is dependent on:

- cooling rate of the sensor
- level of solution temperature
- crystallization on the sensor surface (incrustation)
- system (solute – solvent)

This means that conducting measurements in a different solute – solvent system can lead to different courses of the measurement signals due to different chemical, mechanical and electrical properties and behaviour. This must be taken into account when measurement signals of a different system are evaluated.

The four recorded measurement signals (phase angle, absolute value, frequency, and attenuation) show different sensitivities in detecting the starting of the incrustation. The signal that shows the highest sensitivity and the level of sensitivity are determined by the properties of the system. An a-priori criteria in order to determine the best measurement signal and the sensitivity according to the properties of the current system could not yet be found.

6.3 Crystallizer Experiments

In order to test the sensor under “real” conditions, the experimental setup had to be modified, which means that the beaker glass was substituted by a 60 l cooling-crystallizer. The whole experimental setup is shown schematically in Figure 6-14.

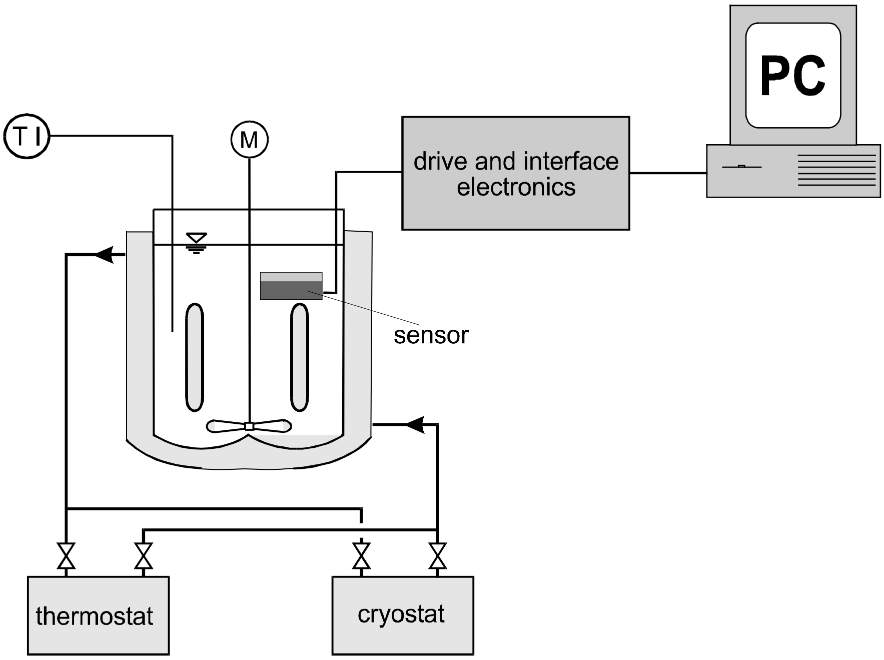

Figure 6-14: Experimental setup with 60 l cooling crystallizer

The temperature of the crystallizer is controlled by a cooling jacket, which is connected to a thermostat and a cryostat. Dependent on whether cooling or heating is required, the closed loop was switched to the thermostat or cryostat by magnetic valves. This separation between cooling or heating cycle proved to be useful, since a quicker change between cooling or heating was achieved as in the case when the heating and cooling was realized by one cryostat. In order to conduct measurements in crystallizers, certain modifications of the sensor setup had to be done. The experiments with KNO_3 described above were conducted in crystal-free solutions at rest in beaker glasses. However, switching from experiments in beaker glasses to experiments in crystallizers would mean introducing stirrer induced fluid flow and suspended crystals which can settle on the sensor surface. The fluid flow influences the temperature field on the sensor surface drastically. Therefore, the cooling of the sensor surface is not reproducible anymore, because of the mixing of the solution. As a consequence, the reproducibility of each measurement would be deteriorated tremendously. Furthermore, the settling of crystals on the sensor surface would cause an interference of the measurement signals of the IDT and SAW. Consequently certain requirements regarding the measurement conditions had to be fulfilled. In order to meet these demands a housing of the sensor and a particle separation device have been constructed. This housing has already been explained in chapter 5.2.4. During the first experiments a draft tube was installed inside the crystallizer. After the introduction of the sensor housing the tube had to be removed in order to provide enough space for the housing. The necessity of the sensor housing is demonstrated in Figure 6-15.

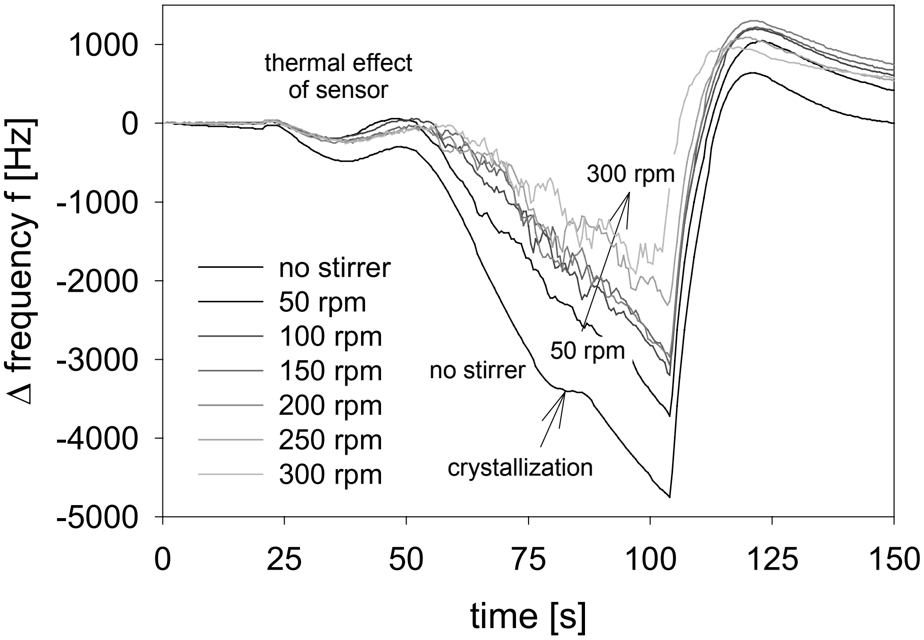

Figure 6-15:Measurements in undersaturated KNO_3-solution (ΔT = -1K) at 20°C without and with stirrer

All measurements depicted in Figure 6-15 were conducted without sensor housing at constant conditions except the revolutions per minute of the stirrer. In case of no fluid flow (no stirrer) the course of frequency is as expected according to the experiments in beaker glasses (see previous chapter). The starting of the crystallization on the sensor surface is detected by the shift of the frequency at about 80 s. During the other measurements in Figure 6-15 the stirrer was operated at different revolutions per minute (50 rpm – 300 rpm). In the beginning of each measurement (pre-measurement phase) the signals remain constant as the peltier element is not switched on. With increasing subcooling a noise in the signals can be observed. The higher the revolutions per minute of the stirrer (indicated by the arrow form 50 rpm to 300 rpm in Figure 6-15) and the higher the subcooling, the more intense the noise. The reason for the noisy signals can be related to temperature gradients or fluctuations resulting in density and viscosity fluctuations. Although the stirrer is already operated during the pre-measurement phase, no noise can be observed. No fluctuations of temperature of the solution adjacent to the sensor surface are expected here, because no cooling or heating is applied in the pre-measurement phase. Therefore, the solution adjacent to the sensor surface and the solution of the bulk have the same temperature, density and viscosity. In the further course of the measurements (cooling) the temperature gradient between the solution adjacent to the sensor surface and the bulk increases. The stirrer causes an exchange of cooled fluid (sensor surface) with solution from the bulk, this leads to fluctuations of temperature, density and viscosity on the sensor surface, resulting in noisy signals. This noise makes it nearly impossible to identify the starting of crystallization in the course of the measurement signal. In addition the incrustation of the sensor surface would be dependent on the degree of mixing, since the exchange of cooled and bulk solution affects the generation of the supersaturation ΔC_{sensor}. The use of the described housing eliminates these problems.

To prove the applicability for organic systems, adipic acid, an industrial large tonnage product, was chosen for the experiments in the 60 l crystallizer. A closer look at the comparison of the solubility curves of potassium nitrate and adipic acid in Figure 6-16 reveals that in order to generate incrustation on the sensor surface by cooling, the crystallizer should be operated at temperatures above 40°C, since at lower solution temperatures the slope of the solubility curve of adipic acid is very low.

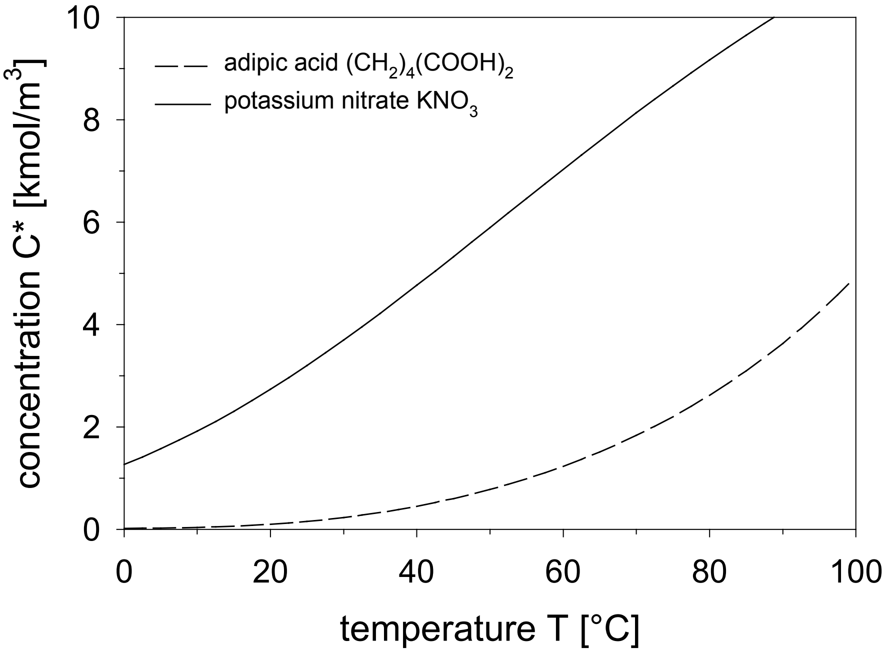

Figure 6-16: Solubility curve of potassium nitrate and adipic acid

As explained in chapter 5.2.2 the SAW sensor detects changes of the physical properties of the medium (solution) adjacent to the sensor surface. A comparison between the two systems KNO_3 - H_2O and $(CH_2)_4(COOH)_2$ - H_2O reveals that the detection of the starting of incrustation of adipic acid with the SAW sensor is more difficult than in case of potassium nitrate. Relevant data of the two systems can be found in Table 6-2.

Table 6-2: Data of potassium nitrate and adipic acid

	potassium nitrate KNO_3	adipic acid $(CH_2)_4(COOH)_2$
ρ_C [kg m^{-3}]	2110	1360
ρ_{sol} (saturated) [kg m^{-3}]	1168 (at 25°C)	1019 (at 50°C)
${dC^*}/{dT}$ [mol l^{-1} K^{-1}]	0.10 (at 25°C)	0.04 (at 50°C)
$\tilde{M}$ [kg mol^{-1}]	0.10110	0.14614

The ratio of the difference of solution and crystal densities can be calculated according to equation (6-1).

$$\frac{\Delta\rho_{\text{pot.nitrate}}}{\Delta\rho_{\text{adipic acid}}} = \frac{\rho_{\text{C,pot.nitrate}} - \rho_{\text{sol,pot.nitrate}}}{\rho_{\text{C,adipic acid}} - \rho_{\text{sol,adipic acid}}} = 2.76 \qquad (6\text{-}1)$$

Assuming total desupersaturation and in case of same subcooling of the sensor, the ratio of deposited crystal mass of both systems is given by equation (6-2).

$$\frac{\Delta m_{\text{pot.nitrate}}}{\Delta m_{\text{adipic acid}}} = \frac{\left({dC^*}/{dT}\right)_{\text{pot.nitrate}} \cdot \tilde{M}_{\text{pot.nitrate}}}{\left({dC^*}/{dT}\right)_{\text{adipic acid}} \cdot \tilde{M}_{\text{adipic acid}}} = 1.73 \qquad (6\text{-}2)$$

Considering this comparison, it is obvious that in case of adipic acid a lower signal level of the SAW sensor is obtained. The deposited crystal mass of potassium nitrate is almost twice as high as the crystal mass of adipic acid and the difference of solution and crystal densities is nearly three times higher for potassium nitrate.

Therefore, the phase angle, a measurement signal of the IDT sensor, was chosen for the evaluation. All experiments described in the following were conducted with constant settings:

- pre-measurement 10 s
- measurement 120 s
- linear cooling rate 0 – 2500 mA ($\dot{T}$ is approximately $\dot{T} = 0.15$ K / s)
- post-measurement 10 s
- manual heating
- flushing with bulk solution 60 s (water jet pump)

In Figure 6-17, the normalized phase angle is plotted versus measurement time. To achieve higher resolution only the relevant range is displayed in the diagram. The measurement phase after 60 s as well as the pre-, and the post-measurement phase are not depicted. The starting of incrustation on the sensor surface is detected by the maximum of the phase angle.

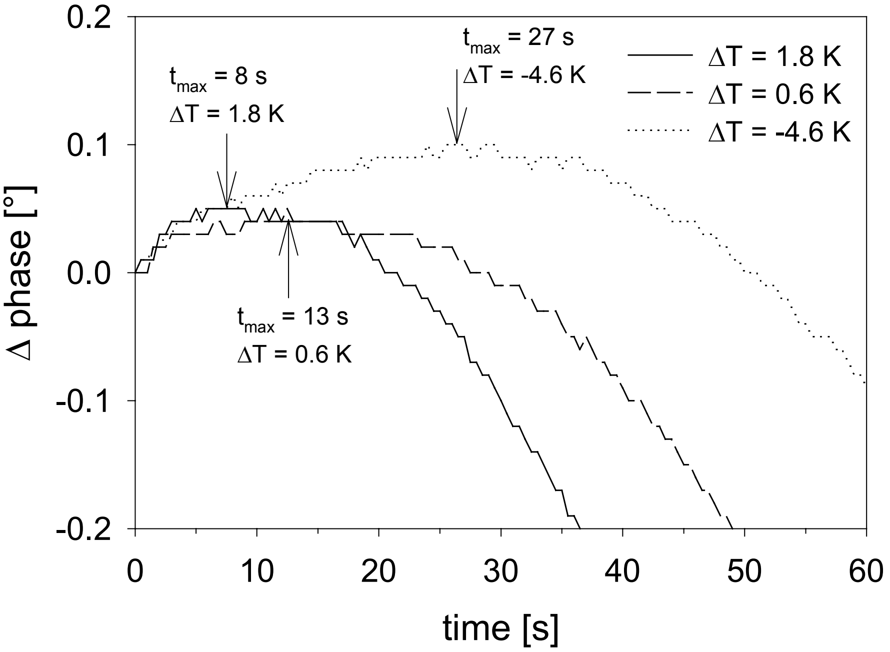

Figure 6-17: Difference of phase angle versus time for adipic acid solutions with different super- and undersaturations

It can be seen, that in case of the highest supersaturation (ΔT = 1.8 K) the maximum of the phase angle appears after 8 s of cooling. Less supersaturation (ΔT = 0.6 K) requires more cooling power, resulting in the longer cooling time of 13 s. In an undersaturated solution (ΔT = -4.6 K) the maximum is observed after 27 s cooling time.

Two batch cooling crystallizations of adipic acid with different cooling rates, 2 K/h and 5 K/h, were conducted in the 60 l crystallizer. The housing of the sensor enabled the measurement in the presence of a stirrer and suspended crystals. The solution was saturated at 43 °C. Although the crystallizer was designed as a closed system, evaporation of the solvent could not be prevented completely, therefore a shift of the saturation temperature T* to about 43.5 K took place during the experiments.

In Figure 6-18 the temperature of the solution and the time t_{max}, which has elapsed between the start of the cooling and the detection of incrustation on the sensor surface (maximum in the course of the phase angle), are plotted versus batch time.

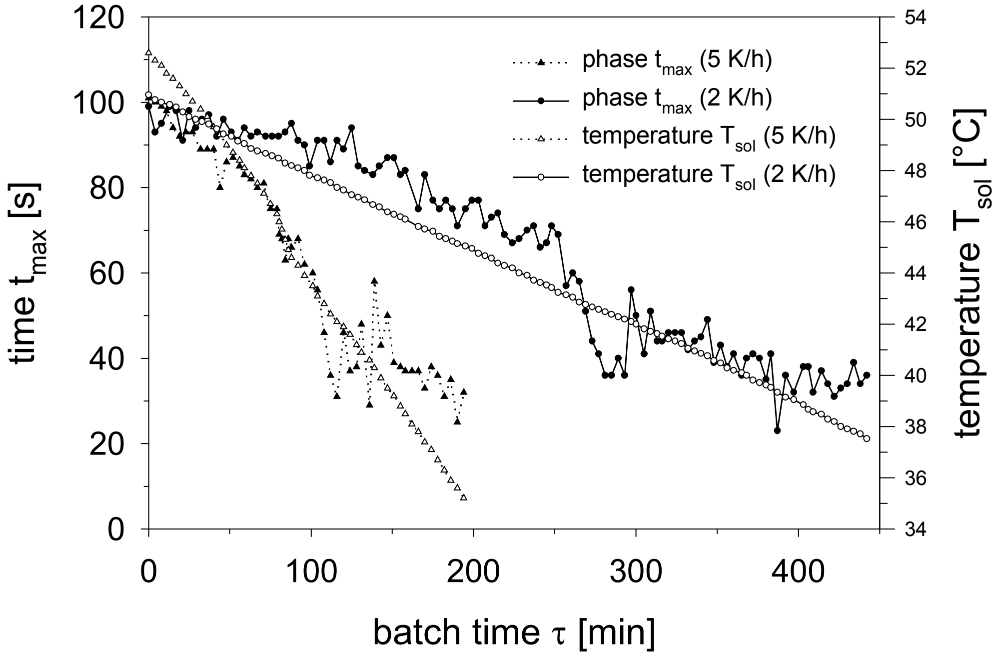

Figure 6-18: Solution temperature and time t_{max} of batch crystallizations of adipic acid with a cooling rate of 2 K / h and 5 K / h versus batch time

The linear cooling rate of both crystallizations processes can be derived from the slope of the corresponding temperature plot in Figure 6-18. At the beginning of the batch process at a solution temperature of 52°C, when the solution is extremely undersaturated ($T^* \approx 43°C$), high values for t_{max} are obtained, since a high cooling power is needed to generate the supersaturation required for the incrustation of the sensor surface. Reaching lower solution temperatures ($T_{sol} < 43°C$) results in a supersaturated solution which can be realized by the smaller values of t_{max}.

Figure 6-20 shows the required subcooling ΔT_{sensor} for an incrustation on the sensor surface plotted versus temperature of the solution. The level of the subcooling can be calculated by multiplying the cooling rate of the sensor, $\dot{T}_{sensor}$, with the time t_{max}, which has elapsed between the start of each measurement and the detection of incrustation by the IDT sensor (here: phase angle)

$$\Delta T_{sensor} = \dot{T}_{sensor} \cdot t_{max} \qquad (6\text{-}3)$$

The cooling rate $\dot{T}_{sensor}$ is approximately $\dot{T}_{sensor} = 0.15\,K/s$. In Figure 6-19 the first measurement point for the cooling rate $\dot{T}_{crystallizer}$ of $\dot{T}_{crystallizer} = 2\,K/h$ is shown.

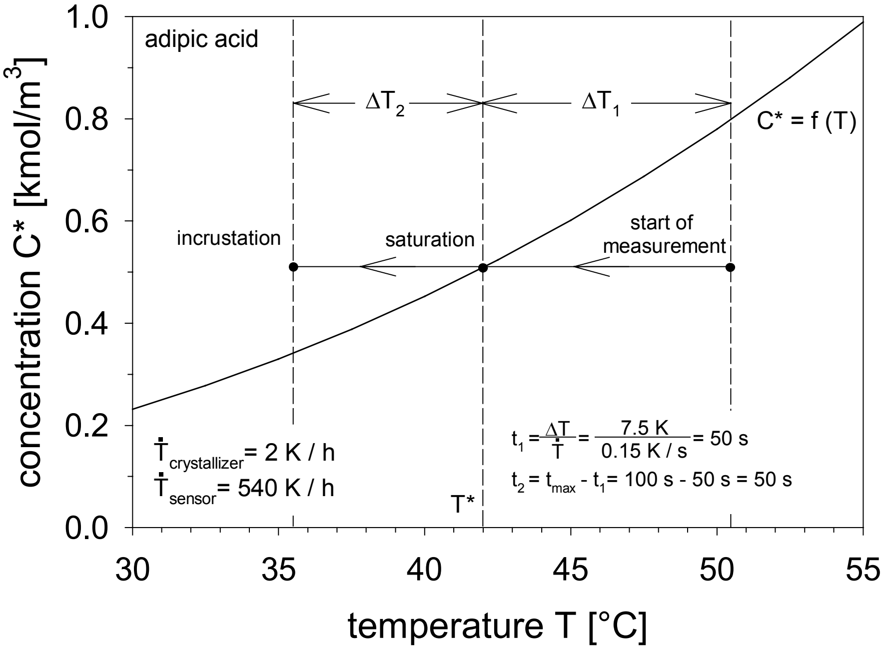

Figure 6-19: Measurement procedure of the first measurement point (2 K/h) shown in the solubility plot of adipic acid

The time elapsed for cooling of the undersaturated solution to saturation is approximately $t_1 = 50$ s and the time from saturation to incrustation is $t_2 = 50$ s.

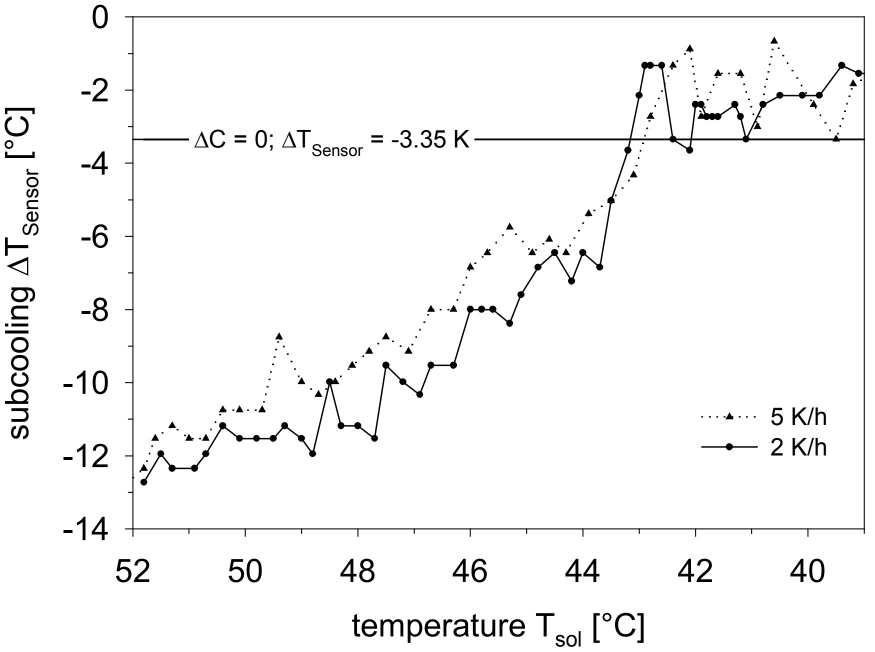

Figure 6-20: Subcooling of the sensor ΔT_{sensor} for two batch crystallizations of adipic acid (2 K/h and 5 K/h) versus temperature of the solution T_{sol}

In case of a saturated solution ($\Delta C = 0$) an average subcooling $\Delta T_{sensor,saturated} = -3.35$ K was needed in order to obtain an incrustation on the sensor surface. As a consequence a measured subcooling below the value for a saturated solution ($\Delta T_{sensor} < -3.35$ K) indicates an undersaturated solution, whereas, requiring a subcooling of less than -3.35 K ($\Delta T_{sensor} > -3.35$ K) stands for a supersaturated solution. This "borderline" at -3.35 K is drawn as a solid line in Figure 6-20 and represents saturated solution with undersaturated solution below and supersaturated solution above that line.
The actual level of subcooling of the solution ΔT_{sol} is then given by:

$$\Delta T_{sol} = \Delta T_{sensor} - \Delta T_{sensor,saturated} \tag{6-4}$$

In Figure 6-21 a comparison of the calculated subcooling ΔT_{sol} of both experiments is made. The saturated state is now given by $\Delta T_{sol} = 0$°C. The diagram shows that in case of the higher cooling rate a higher supersaturation, especially at the beginning of the crystallization, is achieved. This corresponds to the theory, that for higher cooling rates higher metastable zone widths are obtained [Mers98].

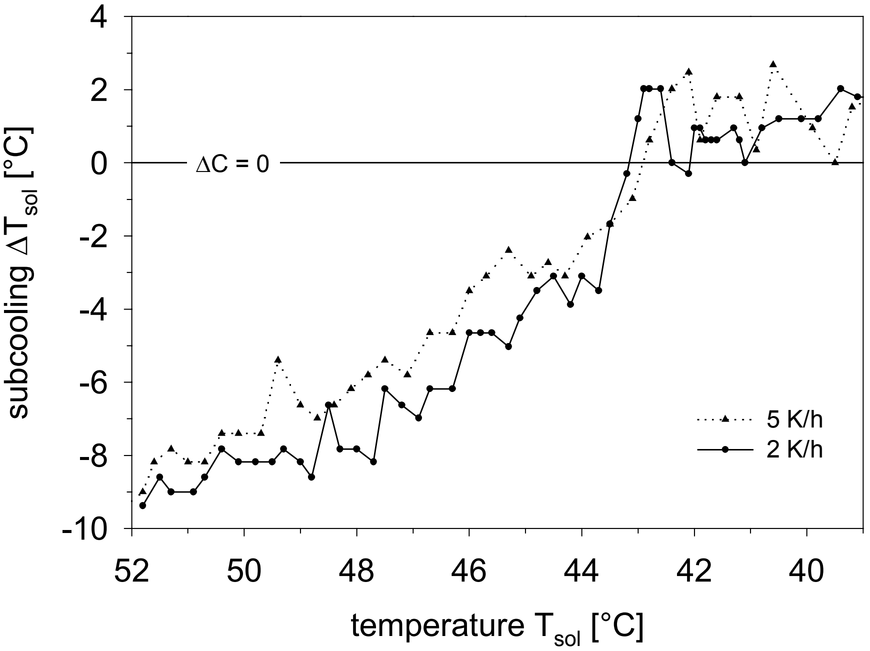

Figure 6-21: Subcooling ΔT_{sol} of the solution for two batch crystallizations of adipic acid (2 K/h and 5 K/h) versus temperature of the solution T_{sol}

Due to the limited space in the 60 l crystallizer the diameter D of the sedimentation tube had to be reduced from the original size of 0.23 m to 0.14 m. As a consequence the cut size d_{sep} of the sedimentation tube is shifted from 20 µm to 35 µm. A reduction of the volume flow in order to keep the cut size at 20 µm was not possible, since a volumetric flow of less than the current value of $6.4 \cdot 10^{-6}$ m^3 s^{-1} could not provide an efficient flushing of the sensor housing. This degradation of the cut size is a reason for the fluctuations of the measured supersaturation in Figure 6-21 caused by alternating crystal masses that are sucked into the measurement chamber and influence the crystallization of the sensor surface.

The results of the monitored batch cooling crystallizations of adipic acid demonstrated the high potential and applicability of the system. The major advantage of this sensor lies in the direct measurement of the driving force (and not of a concentration) of crystallization including every influence caused by impurities or other process disturbances. Of course, some further research has to be done until reliable measurements can be conducted in industrial crystallizers. Therefore a further improvement of the housing, which is necessary for measurements in industrial crystallizers, has to be realized.

6.4 Further Experiments with other Systems

Considering the way how the additional measurement supersaturation is generated by the sensor, the estimation of the possible field of application seems to be quite easy. If the supersaturation ΔC_{sensor} is established by cooling, systems with a positive slope $d C^* / d T$ seem to be suitable for that kind of supersaturation measurement.

Unfortunately, it is obvious that also other system properties (e. g. diffusivity, viscosity and absolute solubility), width of the metastable zone and the interactions crystal – sensor surface also play an important role in the determination of the applicability of the sensor for a certain system. Therefore it is necessary to conduct further experiments with different systems in order to determine the potential field of application. The chosen organic and inorganic systems are listed in Table 6-3, detailed system properties can be found in appendix 11.3.

Table 6-3: Systems for further experiments (see also appendix 11.3)

system	C^* [mol/l]	$d C^* / d T$ [mol / (1 K)]	$d \ln C^* / d \ln T$ [-]
adipic acid $(CH_2)_4(COOH)_2$	0.60	0.082	17.27
ammonium chloride NH_4Cl	5.82	0.049	2.48
ammonium nitrate NH_4NO_3	11.87	0.115	2.88
ammonium sulphate $(NH_4)_2SO_4$	4.04	0.009	0.70
maleic acid $C_2H_2(COOH)_2$	4.64	0.073	4.67
potassium bromide KBr	4.54	0.029	1.87
potassium dichromate $K_2Cr_2O_7$	0.48	0.019	11.42
potassium iodide KJ	6.05	0.022	1.08
potassium nitrate KNO_3	3.20	0.096	8.97
potassium sulphate K_2SO_4	0.66	0.010	4.37
sodium chloride NaCl	5.27	0.002	0.09
sodium nitrate $NaNO_3$	7.63	0.046	1.81
succinic acid $(CH_2)_2(COOH)_2$	0.68	0.034	15.07
urea $(NH_2)_2CO$	10.49	0.113	3.20

The experiments were conducted in beaker glasses in the same way as it is described in chapter 6.2 dealing with the experiments with potassium nitrate. This means that each measurement was made in an undersaturated solution. Amperages of 2000 mA and 3000 mA and measurement times ranging from 60 s to 300 s were chosen, thus resulting in different cooling rates.

In order to determine the exact subcooling of the sensor surface a NiCr – Ni thermoelement (ALMEMO T 430-2L), especially designed for the measurement of surface temperatures, was used. Figure 6-22 shows exemplarily the measured subcooling for a linear increase of the amperage from 0 mA up to 2000 mA and 3000 mA in the cases of 60 s and 180 s measurement time and cooling phase respectively. The pre- and post-measurement phase were not considered in this plot.

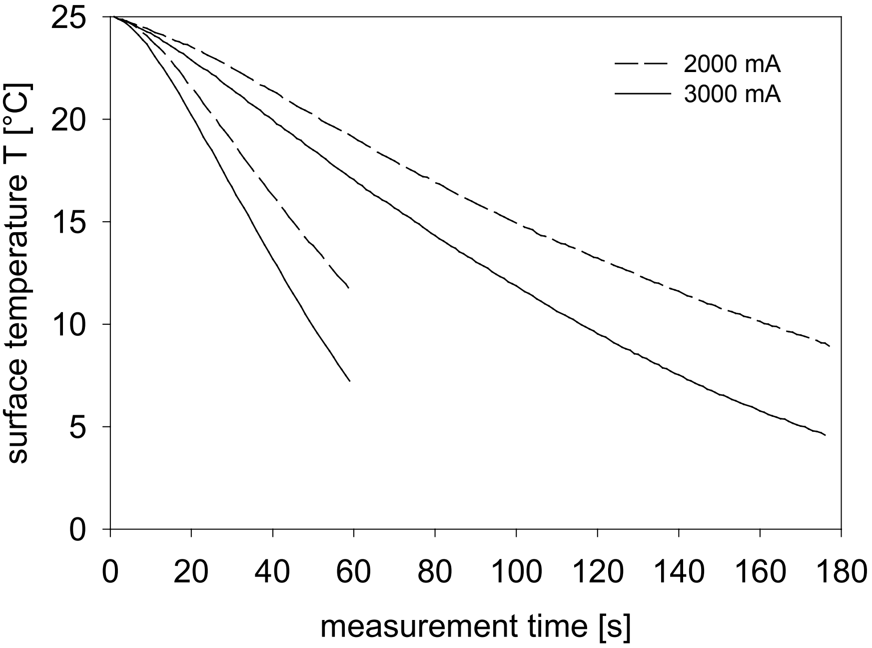

Figure 6-22: Measured subcooling of the sensor surface for 2000 mA and 3000 mA amperage and measurement times of 60 s and 180 s

As can be seen, the course of the subcooling in the case of 60 s measurement time is almost linear for both amperages, whereas the course of the subcooling for the higher measurement time of 180 s experiences a deviation from linearity due to Joules heat loss leading to a slight warm-up of the sensor setup. According to the settings of amperage and measurement time, different cooling rates were obtained. The average measured cooling rate for each combination of amperage and measurement time can be taken from Table 6-4.

Table 6-4: Average cooling rates measured for different amperages and measurement times

amperage [mA]	time [s]	cooling rate [K / s]	cooling rate [K / h]
2000	60	0.224	805.7
2000	120	0.129	463.8
2000	180	0.089	321.3
2000	240	0.068	245.0
2000	300	0.059	211.6
3000	60	0.296	1065.6
3000	120	0.171	614.9
3000	180	0.111	400.6
3000	240	0.077	278.0
3000	300	0.066	238.4

At first glance the obtained cooling rates seem to be very high compared to cooling rates relevant for industrial cooling crystallizers, which are normally in the range of 0.5 – 10 K / h. But it should be taken into account that these extremely high cooling rates are required to induce an incrustation of the sensor surface in an adequate measurement time.

The evaluation of the measurement data has been conducted in a similar way as explained in chapter 6.2. As in the case of potassium nitrate, deviations from the expected or normal (temperature dependent) course of the frequency, phase angle or attenuation indicate the start of the deposition of solid matter which finally leads to an incrustation of the sensor surface. To verify that these deviations can not be attributed to a thermal effect of the current system during the measurement (cooling) phase, the experiment was repeated at the same solution temperature and with the same parameter settings (amperage, measurement time), but with different concentrations (saturation temperatures). If a lower concentration causes a shift of the deviation to a later point of time and a higher concentration leads to an earlier deviation, this deviation is due to the start of crystallization on the sensor surface. If the deviation is still observed at the same time, it is caused by a thermal effect of the current system, which can not be related to crystallization. Depending on the system this deviation can be observed in form of a minimum, maximum or noise in the course of the particular measurement signal. Up to now it is not possible to predict the kind of deviation according to the system properties.

The exact results of the experiments can be seen in appendix 11.4. The saturation temperature T* and the corresponding concentration C* can be found in the first line of each table. All experiments were made with undersaturated solutions, which means that the solution temperature T_{sol} was higher than saturation temperature T*. The times t_{signal} that elapsed from the point of reaching saturation temperature and obtaining the deviation from the normal course of the measurement signal are listed in the tables of appendix 11.4. Figure 6-23 might help to understand the definition of the time t_{signal}. The corresponding subcooling ΔT_{signal} and relative supersaturation σ_{signal} are also given in appendix 11.4.

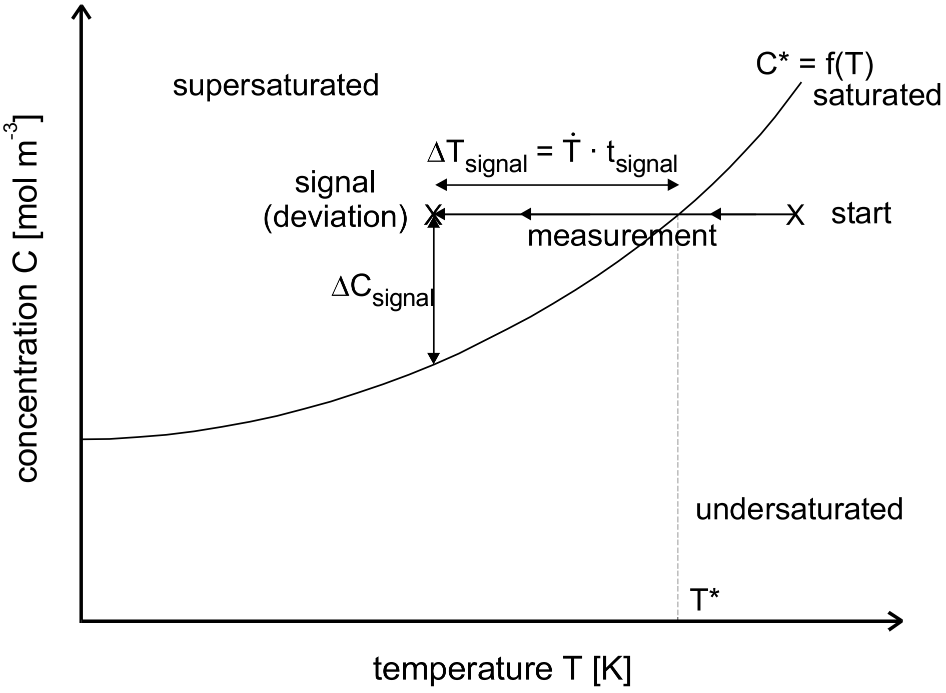

Figure 6-23: Definition of t_{signal}, ΔT_{signal} and ΔC_{signal}

Considering the results in appendix 11.4, the systems can be classified in four categories:

category A: visual observation of the incrustation is possible
good and easy feasibility of the evaluation of the measurement data
category B: no visual observation of the incrustation is possible
good and easy feasibility of the evaluation of the measurement data
category C: no visual observation of the incrustation is possible
evaluation of the measurement data is only in some cases possible
category D: no visual observation of the incrustation is possible
evaluation of the measurement data is not possible

Putting the systems according to the results of the experiments in the above described categories Table 6-5 is obtained.

Table 6-5: Systems categorized according to the results of the experiments (see appendix 11.4)

category	system	C* [mol/l]	d C* / d T [mol / (l K)]	d ln C* / d ln T [-]
A	adipic acid $(CH_2)_4(COOH)_2$	0.60	0.082	17.27
A	potassium dichromate $K_2Cr_2O_7$	0.48	0.019	11.42
A	potassium nitrate KNO_3	3.20	0.096	8.97
B	ammonium chloride NH_4Cl	5.82	0.049	2.48
B	ammonium nitrate NH_4NO_3	11.87	0.115	2.88
B	potassium bromide KBr	4.54	0.029	1.87
B	succinic acid $(CH_2)_2(COOH)_2$	0.68	0.034	15.07
C	maleic acid $C_2H_2(COOH)_2$	4.64	0.073	4.67
C	urea $(NH_2)_2CO$	10.49	0.113	3.20
D	ammonium sulphate $(NH_4)_2SO_4$	4.04	0.009	0.70
D	potassium iodide KJ	6.05	0.022	1.08
D	potassium sulphate K_2SO_4	0.66	0.010	4.37
D	sodium chloride NaCl	5.27	0.002	0.09
D	sodium nitrate $NaNO_3$	7.63	0.046	1.81

It should be mentioned that these measurements are not measurements of the metastable zone width in the classical understanding, since the results are only valid for heterogeneous nucleation on a SiC surface. The obtained extreme high values for the metastable zone width for heterogeneous nucleation on a SiC surface (see appendix 11.4) are caused by the chosen cooling rates $\dot{T}$ (see Table 6-4). These very high cooling rates lack any technical relevance regarding crystallization, thus making it nearly impossible to use existing descriptions of crystallization kinetics, since those were verified with experimental data of ‘normal’ cooling parameters. Therefore it is not possible to describe the obtained experimental results in appendix 11.4 with a model.

A closer look at Table 6-5 reveals, that it is not possible to estimate the applicability of the sensor for a certain system considering solubility C*, slope of the solubility curve d C* / d T, and the solubility parameter d ln C* / d ln T.

7 Theoretical Approach

7.1 Model of Metastability

In order to estimate the applicability of the sensor for a system, it is necessary to simulate the incrustation process of the sensor surface.

Starting each measurement in an undersaturated solution and cooling down the solution adjacent to the sensor surface until an incrustation is obtained, postulates primary, heterogeneous nucleation as the only possible nucleation mechanism. Schuberts model [Schu98] for the calculation of the heterogeneous nucleation rate B_{het} assumes a flat or platelike foreign particle (see Figure 2-8). This shape of the foreign particle corresponds to the geometry of the sensor surface, therefore equation (2-36) was used for the determination of B_{het}. The nuclei are regarded as spherical segments on the foreign (sensor) surface, like it is shown in Figure 7-1.

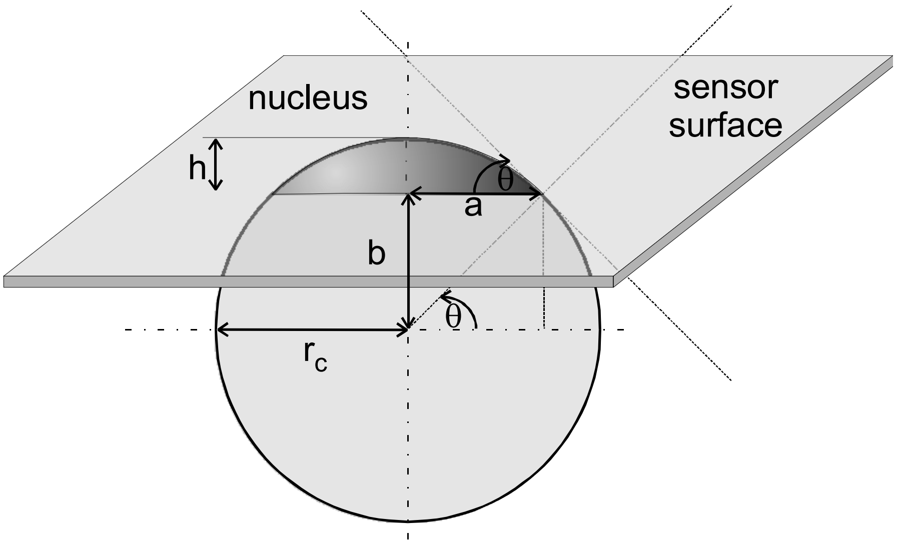

Figure 7-1: Nucleus on the sensor surface

The volume of the nucleus (spherical segment) V_n can be calculated with the following equation:

$$V_n = \frac{1}{3}\pi h^2 (3 r_c - h) \qquad (7\text{-}1)$$

with r_c as the radius of the critical nucleus and the height h given by

$$h = (1 - \sin\theta) r_c \qquad (7\text{-}2)$$

For the contact angle θ of the nucleus, which normally lies in the range of 40° - 53° [Mers2001], a value of 45° was assumed for all systems.
The subsequent growth of the nuclei is calculated with equation (2-69), which takes the diffusion and integration step into account. The assumed shape of the crystals is similar to their nuclei, thus remaining spherical segments. Figure 7-2 depicts the enlargement of the radius of the crystal $r_{C,1}$ to the size $r_{C,2}$, respectively the height $h_{C,1}$ to $h_{C,2}$, according to the mean face growth rate $\overline{v}$.

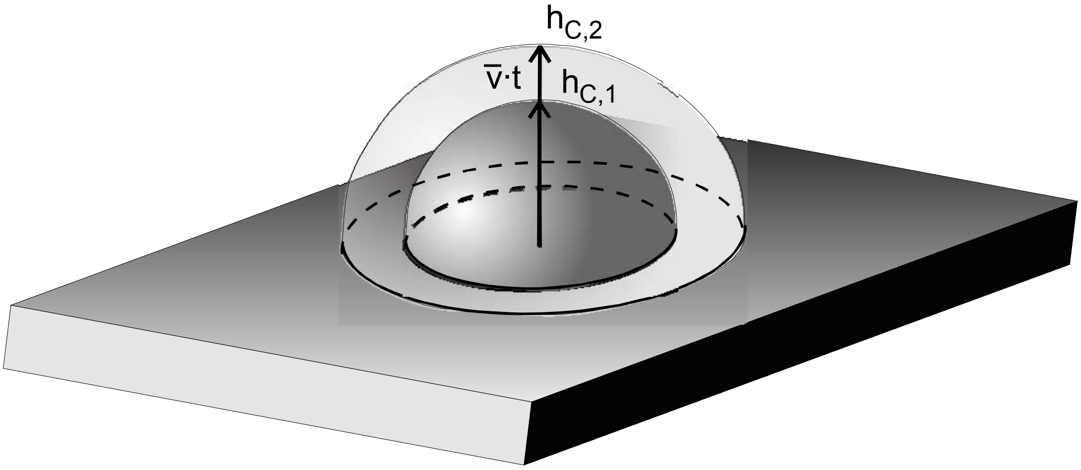

Figure 7-2: Growth of the crystals on the sensor surface

The increase of the radius of the crystal r_C is given by

$$\frac{d r_C}{d t} = \overline{v} \qquad (7\text{-}3)$$

Each calculation starts at saturated, but crystal-free, state.
In Figure 7-3 and Figure 7-4 the results of the calculations for potassium nitrate, KNO_3, for a cooling rate of 0.171 K / s are shown.

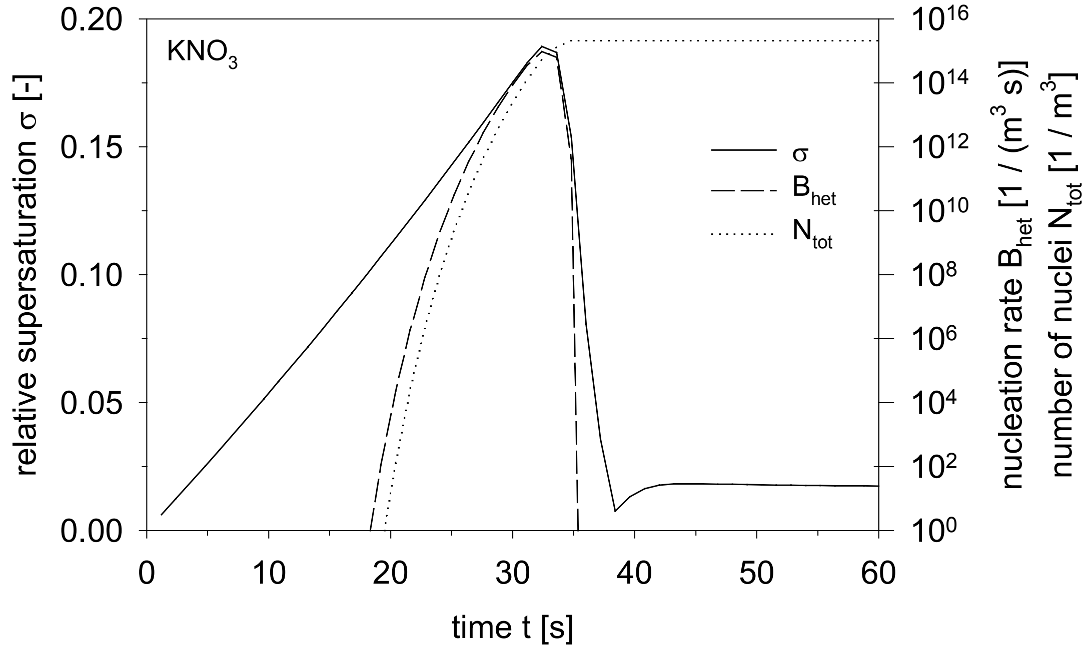

Figure 7-3: *Calculated relative supersaturation σ, nucleation rate B_{het} and total number of nuclei N_{tot} of KNO_3 (valid for: $a_{for} = 10^5\ m^{-1}$; $He_{ad} = 10^{-9}$; $T = 298\ K$; $K = 0.414$; $k_d = 10^{-4}\ m\ s^{-1}$; cooling rate = 0.171 K / s)*

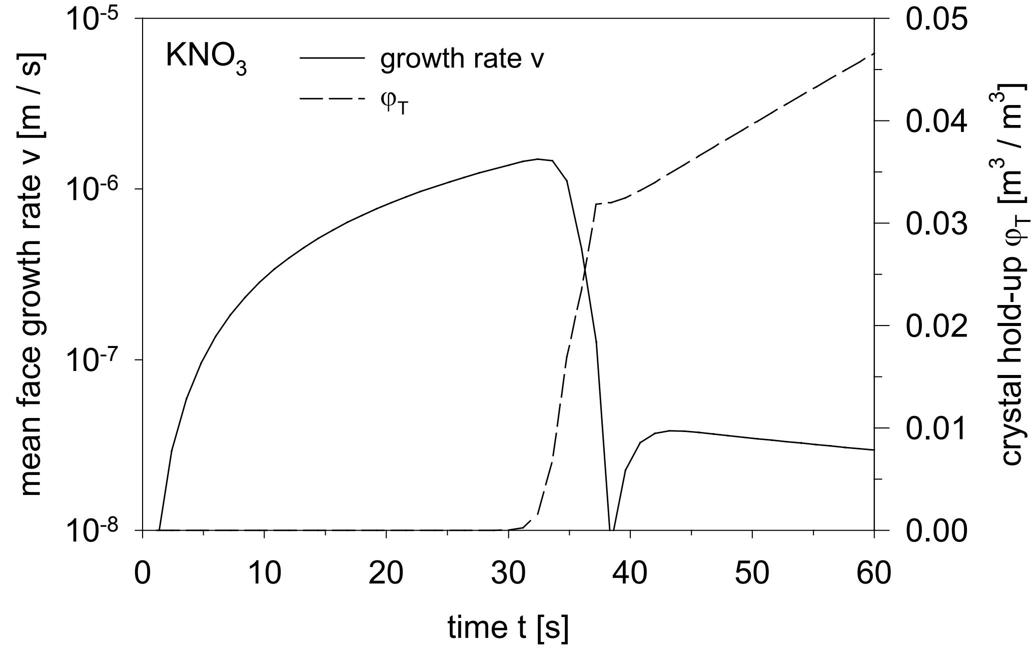

Figure 7-4: *Calculated growth rate* v *and volumetric crystal hold-up φ_T of KNO_3 (valid for: $a_{for} = 10^5\ m^{-1}$; $He_{ad} = 10^{-9}$; $T = 298\ K$; $K = 0.414$; $k_d = 10^{-4}\ m\ s^{-1}$; cooling rate = 0.171 K / s)*

Leaving the metastable zone, thus entering the labile zone, results in spontaneous nucleation. Therefore it is reasonable to define the metastable zone width by exceeding a certain nucleation rate or by reaching the maximum nucleation rate at the supersaturation σ_{met}. Considering the small amount of crystal mass generated only by nucleation, it is even nowadays very difficult to detect the nuclei shower immediately. As a consequence the nuclei have to grow until a detectable size L_{det} with a certain suspension density m_T or volumetric crystal hold-up φ_T is reached [Mers98].
Thus, the calculation of the heterogeneous nucleation rates B_{het}, especially the maximum nucleation rates, for each system indicates the applicability of the sensor for each system. Figure 7-5 depicts the course of the heterogeneous nucleation rates calculated for the systems listed in Table 6-5 according to the predescribed model.

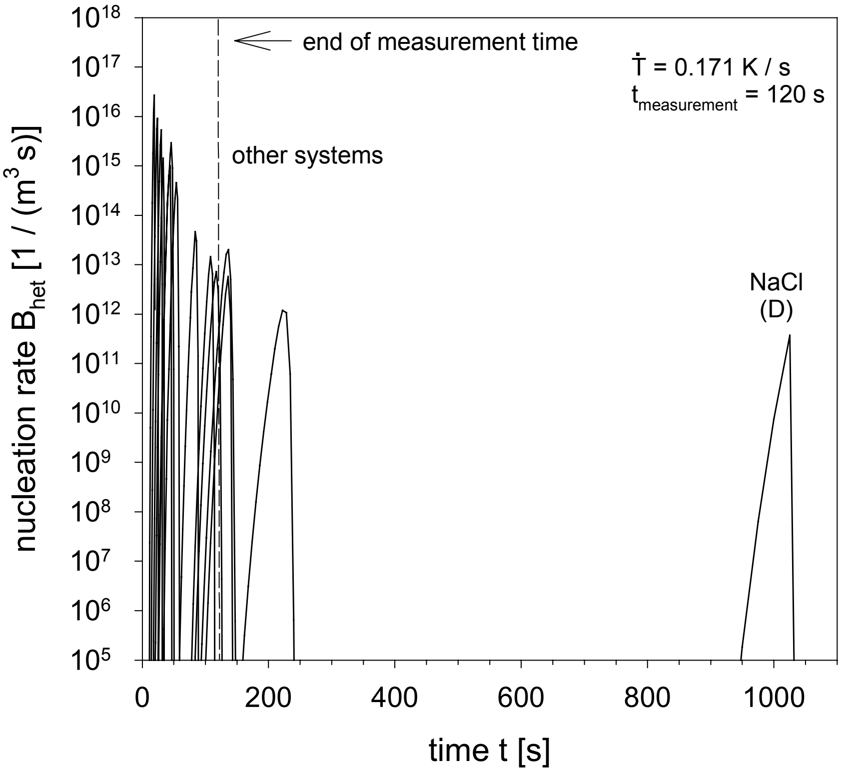

Figure 7-5: Calculated nucleation rates B_{het} (valid for: $a_{for} = 10^5$ m^{-1}; $He_{ad} = 10^{-9}$; $T = 298$ K; $K = 0.414$; $k_d = 10^{-4}$ $m\ s^{-1}$; cooling rate = 0.171 K / s)

The chosen cooling rate $\dot{T} = 0.171$ K / s corresponds to a measurement time $t_{measurement} = 120$ s and a linear increase of the amperage up to 2000 mA, see Table 6-4. The end of the measurement time is indicated by the dashed line. The maximum nucleation rate of sodium chloride is observed at ca. 1000 s, which drastically exceeds the measurement time. This can be explained by the flat solubility curve of NaCl, showing almost no temperature dependence of the solubility. The letter in brackets represents the category in which the systems were classified according to the results of the experiments in appendix 11.4, see Table 6-5. Omitting sodium chloride in Figure 7-5 leads to Figure 7-6.

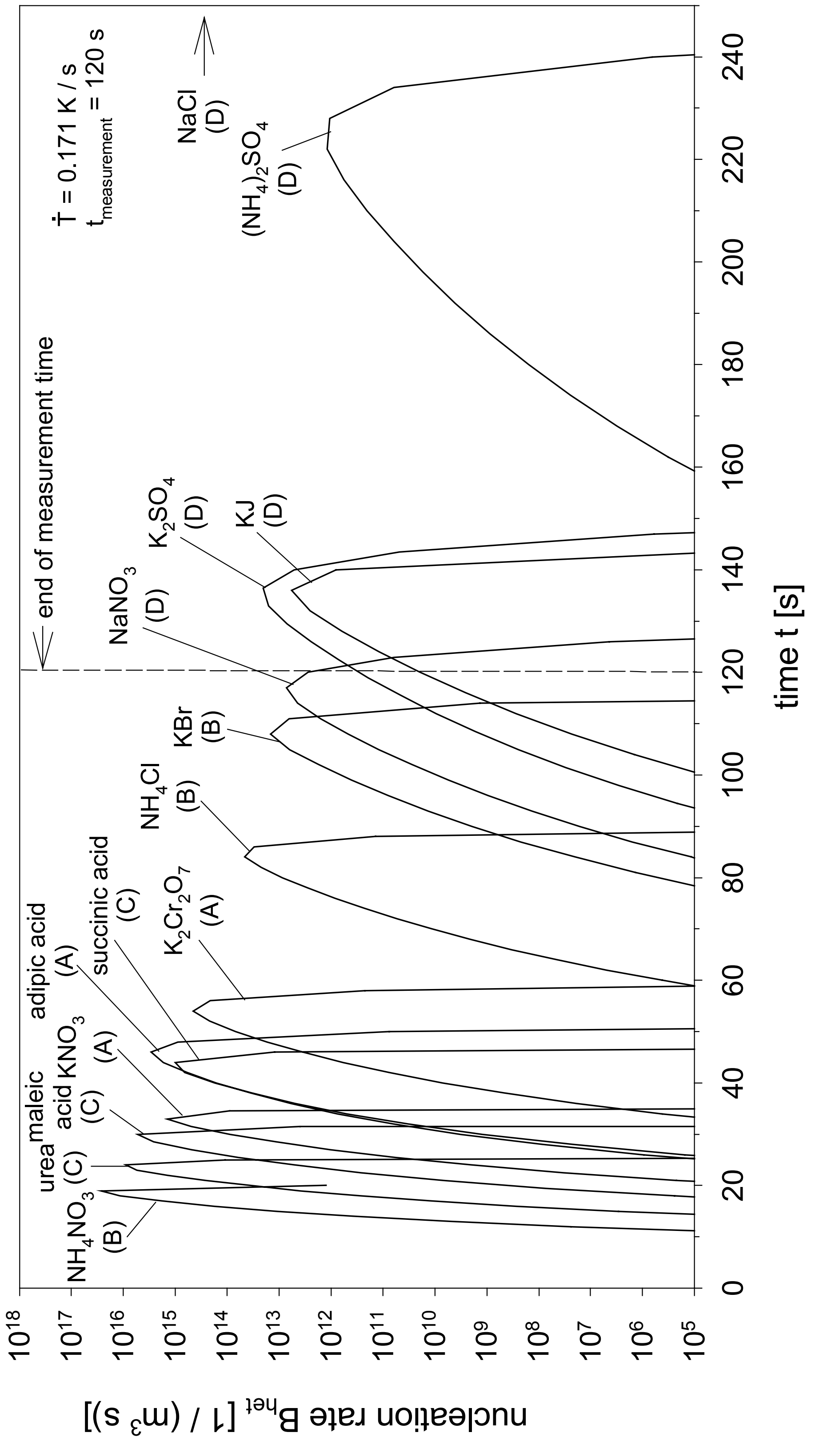

Figure 7-6: Calculated nucleation rates B_{het} (valid for: $a_{for} = 10^5\ m^{-1}$; $He_{ad} = 10^{-9}$; $T = 298\ K$; $K = 0.414$; $k_d = 10^{-4}\ m\ s^{-1}$; cooling rate = 0.171 K / s) without NaCl

The maximum nucleation rates of all systems (except $NaNO_3$) with the rating “D” can be found beyond the dashed line, which indicates the end of the measurement. Although the maximum nucleation rate B_{het} of sodium nitrate, $NaNO_3$, lies within the measurement time, an evaluation of the experimental data was not possible. This can be explained by the occurrence of the maximum nucleation rate almost at the end of the measurement time, which means that the emerged nuclei do not have enough time to grow to a detectable size L_{det} for the sensor.

All systems of the categories A, B and C experience the maximum nucleation rate before the measurement time has elapsed. Additional calculations for a cooling rate $\dot{T}$ of 0.066 K / s (300 s, 3000 mA) can be found in appendix 11.5.

It has to be mentioned, that this model lacks the consideration of the interactions of the particular solute – solvent system and the sensor surface. The contact angle of the nuclei θ, which was kept constant for all systems in the calculations, varies according to the interactions, thus promoting or impeding nucleation. Unfortunately, up to now it is not possible to measure the contact angle θ of nuclei. To show the difference of the interactions between each system and the sensor surface, the contact angle of the saturated solution on the sensor surface was measured (Dataphysics – Contact angle System OCA). The results can be seen in Table 7-1.

Table 7-1: Contact angles of the saturated solution on the sensor surface

system	contact angle θ [°]	relative contact angle [-]
adipic acid $(CH_2)_4(COOH)_2$	17.8	1.0
ammonium chloride NH_4Cl	29.1	1.7
ammonium sulphate $(NH_4)_2SO_4$	30.1	1.7
maleic acid $C_2H_2(COOH)_2$	21.7	1.2
potassium dichromate $K_2Cr_2O_7$	17.9	1.0
potassium iodide KJ	22.3	1.3
potassium nitrate KNO_3	27.6	1.6
potassium sulphate K_2SO_4	26.0	1.5
sodium chloride NaCl	25.3	1.4
sodium nitrate $NaNO_3$	32.7	1.9
succinic acid $(CH_2)_2(COOH)_2$	14.4	0.8
urea $(NH_2)_2CO$	15.6	0.9
water H_2O	17.5	1.0

In the right hand column the relative contact angle based on the contact angle of the pure solvent (H_2O) can be found. The small absolute values of all contact angles, especially of water, can be explained by a hydrophilic treatment of the sensor surface.

Nevertheless, it is not possible to estimate the contact angle θ of a nuclei on the basis of the measured contact angles of the pure solution. The overriding of the influence of the interactions between the system and the sensor surface may be the reason why the maxima of the nucleation rates do not appear in the order corresponding with their categories (A, B and C).

With the assumption, that the metastable zone width is exceeded when the maximum nucleation rate occurs, it is possible to estimate the metastable zone width of primary heterogeneous nucleation. Since this model of metastability does not take the specific interactions of the current system and the SiC-surface of the sensor into account, it could also be used to estimate the incrustation behaviour of a crystallizer. Primary heterogeneous nucleation is the responsible nucleation mechanism for incrustations on crystallizer installations (e. g. stirrer) or heat exchange surfaces. These incrustations lead to a reduction of the heat exchange caused by an increasing thermal resistance, thus reducing the operating time of a crystallizer due to longer cleaning intervals. To avoid these undesired incrustations, the relative supersaturation σ_{met} at which the maximum nucleation rate B_{het} occurs should not be exceeded.

In Figure 7-7 the relative supersaturation σ_{met} of the systems in Appendix 11.3 obtained for calculations with cooling rates of 0.171 K / s and 0.066 K / s are plotted versus the dimensionless solubility C^* / C_C. It can be seen, that with an increasing dimensionless solubility the metastable zone width declines.

For reasons of comparison lines valid for different values of the parameter $\frac{d \ln C^*}{d \ln T} \cdot \frac{\dot{T}}{T}$ are also drawn in this figure. As can be seen the metastable supersaturation σ_{met} is approximately by a factor 2 ÷ 5 greater for the cooling rates 0.066 K / s and 0.17 K / s than for the highest cooling rate of 5 K / h = 0.00139 K / s applied for the data of Figure 4-5.

Since the cooling rates applied by the sensor are extremely high and therefore not relevant for the operation of cooling crystallizers, also calculations for typical operational cooling rates of 2 K / h, 3 K / h, and 5 K / h have been made. The results of the calculations are listed in Table 11-9 in Appendix 11.6.

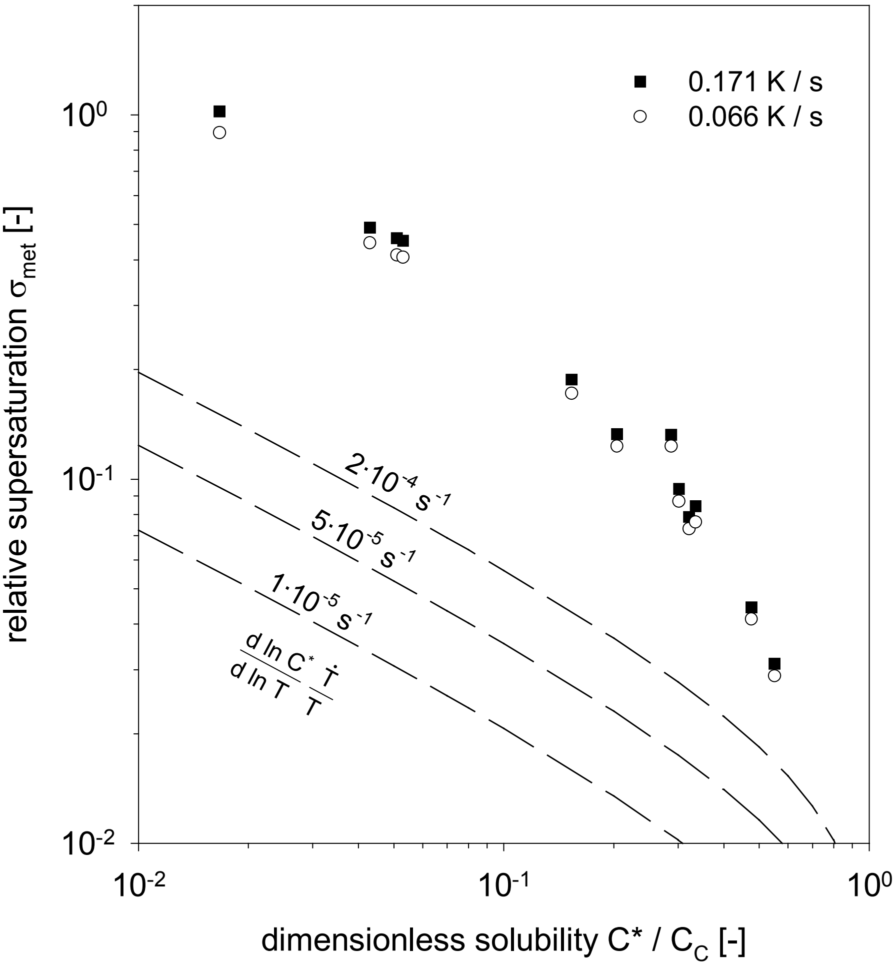

Figure 7-7: Relative supersaturation σ_{met} plotted versus dimensionless solubility C^* / C_C (calculated for: $a_{for} = 10^5$ m^{-1}; $He_{ad} = 10^{-9}$; $T = 298$ K; $K = 0.414$; $k_d = 10^{-4}$ m s^{-1}); (The dashed lines are the same as in Figure 4-5, however, $\sigma_{met} = 2\ \sigma_{opt}$ is plotted against the ratio C^* / C_C)

In Figure 7-8 and Figure 7-9 the obtained metastable zone widths, expressed in σ_{met}, for all systems are plotted versus the cooling rate. The lower the cooling rate, the smaller is the metastable supersaturation σ_{met}. This behaviour coincides with the model proposed by Mersmann [Mers98], see chapter 4.2.

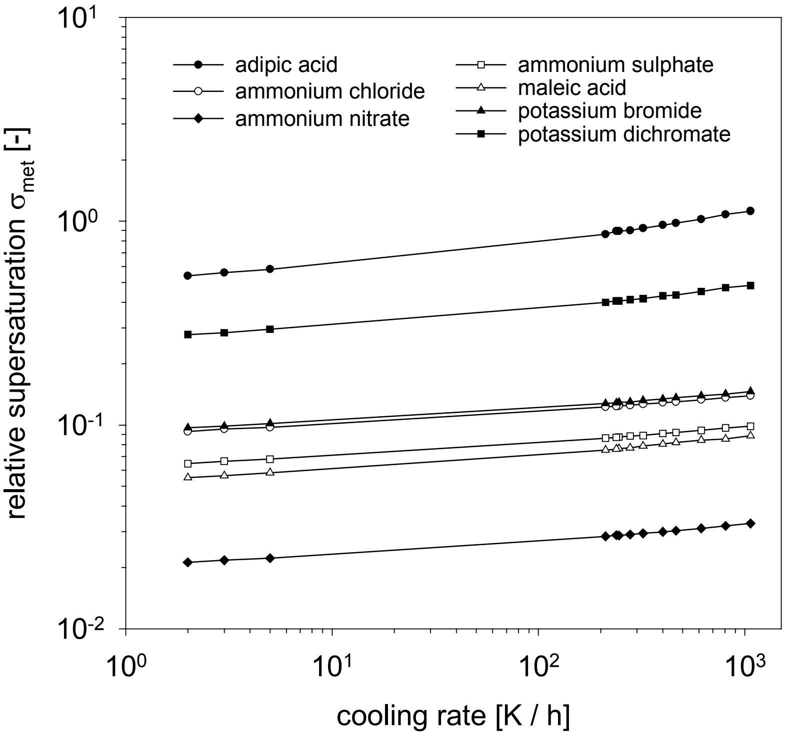

Figure 7-8: Relative supersaturation σ_{met} of organic and inorganic systems plotted versus cooling rate (calculated for: $a_{for} = 10^5\ m^{-1}$; $He_{ad} = 10^{-9}$; $T = 298\ K$; $K = 0.414$; $k_d = 10^{-4}\ m\ s^{-1}$)

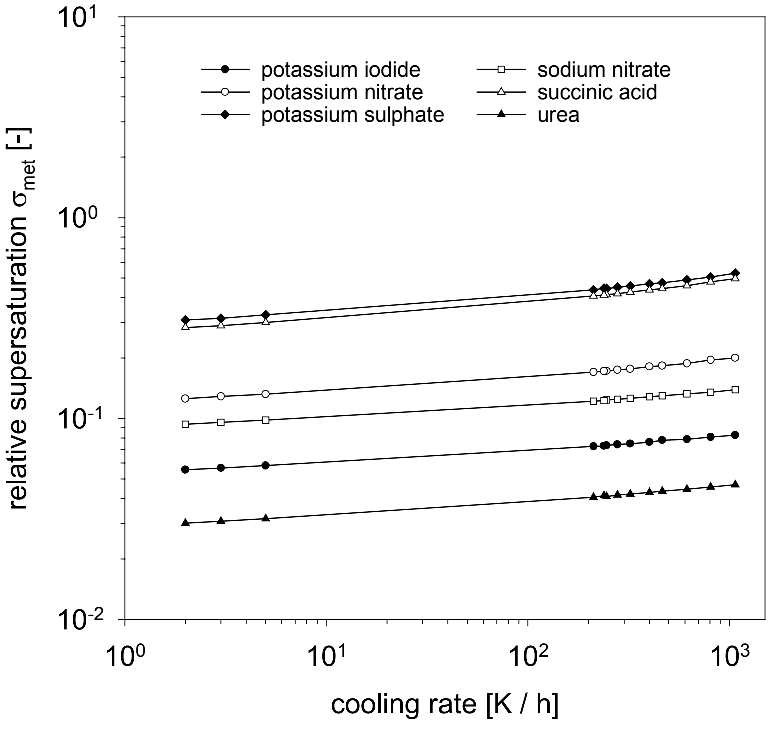

Figure 7-9: Relative supersaturation σ_{met} of organic and inorganic systems plotted versus cooling rate (calculated for: $a_{for} = 10^5\ m^{-1}$; $He_{ad} = 10^{-9}$; $T = 298\ K$; $K = 0.414$; $k_d = 10^{-4}\ m\ s^{-1}$)

The cooling rate of a crystallizer should now be adjusted according to these results, which means that subcoolings ΔT_{met} corresponding to σ_{met} should be avoided in order to reduce incrustation on installations. To ensure minimum incrustation with respect to an economic batch time, the optimal supersaturation σ_{opt} with respect to avoiding incrustation can be estimated to be half σ_{met} ($\sigma_{opt} = 0.5 \cdot \sigma_{met}$). In addition, this optimal supersaturation σ_{opt} is important for each starting up of a crystallizer with crystal-free or unseeded solution, as heterogeneous nucleation is the relevant nucleation mechanism for the case of crystal-free solutions.

During the crystallization process, when already the first crystals have been generated or seed crystals have been added, secondary nucleation is the dominant mechanism. As a consequence the model must be adjusted with equation (2-44). It is obvious, that the values for σ_{met} delivered by the "new" model of metastability according to secondary nucleation are smaller than those for heterogeneous nucleation. Therefore σ_{opt} based on surface nucleation is smaller.

7.2 Simplified Criteria for the Estimation of the Field of Application

The model in chapter 7.1 represents a good possibility for the estimation of the potential field of application based on system properties. Nevertheless, these numerical calculations can only be solved by numerical software packages or by manual programming. Therefore, the estimation based on the model of metastability is too time-consuming. In the next step a simplified and easy manageable criteria for the estimation of the field of application will be introduced.

One possibility of an easy and quick check of the applicability of the sensor for a system is the solubility parameter $\frac{d \ln C^*}{d \ln T}$ and the efficiency $E_{CE} = \frac{m_{T,C} / Q_C}{m_{T,E} / Q_E}$ (see equation (4-8)), which have been calculated for each system in Table 7-2. All systems with a

$$\frac{d \ln C^*}{d \ln T} \geq 1.9 \quad \text{or} \quad \frac{m_{T,C} / Q_C}{m_{T,E} / Q_E} \geq 1.9$$

are in the categories A, B or C and are therefore suitable for the new measurement method. A possible reason for the only exception of this estimation, potassium sulphate, is the high metastable zone width of that system, which is indicated by the high value of t_{det} in Table 7-4. This simple estimation is only based on "thermic" system properties, i. e. the slope of the solubility curve.

Since nucleation and growth, which are relevant for the incrustation of the sensor surface, are “kinetic” variables of each system, a combination of “thermic” and “kinetic” properties allow a better estimation of the applicability. Therefore the product of the diffusion coefficient D_{AB}, as the “kinetic” parameter, and the dimensionless solubility $\frac{d\ln C^*}{d\ln T}$ or the efficiency E_{CE}, as the “thermic” parameter, have been calculated (see Table 7-2). Unfortunately, potassium sulphate still does not fit that criteria, but for all other systems with

$$\frac{d\ln C^*}{d\ln T}\cdot D_{AB} \geq 10^{-9} \quad \text{or} \quad \frac{m_{T,C}/Q_C}{m_{T,E}/Q_E}\cdot D_{AB} \geq 2\cdot 10^{-9}$$

the measurement of supersaturation with the new sensor is possible. It has to be mentioned, that the sequence of the systems ranked by the product of “kinetic” and “thermic” properties corresponds better to the sequence of the categories, since urea and maleic acid (both category C) are now the last “measurable” systems in Table 7-2. The cells with systems belonging to category D have been marked with grey colour. The mismatching of potassium sulphate in this estimation, demands another criteria for the application.

The model of metastability in chapter 7.1 considers simultaneous nucleation and growth according to the supersaturation based on the mass balance. Figure 7-10 shows this model schematically.

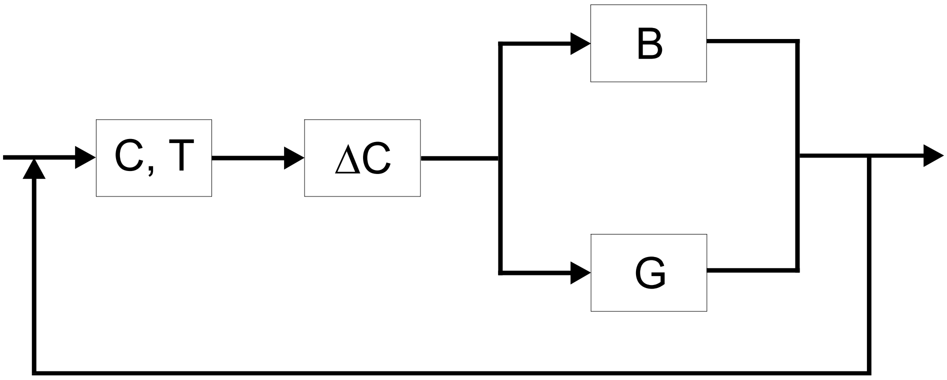

Figure 7-10:Scheme of the model of metastability in chapter 7.1

Table 7-2: Estimation of the application according to "thermic" and "kinetic" parameters

ranked by d ln C* / d ln T			ranked by d ln C*/ d ln T · D_{AB}			ranked by efficiency E_{CE}			ranked by efficiency E_{CE} · D_{AB}		
system	category	d ln C*/ d ln T [-]	system	category	$_{AB}$ $[m^2 / s]$	system	category	efficiency E_{CE} [-]	system	category	$_{CE}$ $_{AB}$ $[m^2 / s]$
adipic acid $(CH_2)_4(COOH)_2$	A	25.4	adipic acid $(CH_2)_4(COOH)_2$	A	1.82E-08	adipic acid $(CH_2)_4(COOH)_2$	A	28.3	adipic acid $(CH_2)_4(COOH)_2$	A	2.03E-08
succinic acid $(CH_2)_2(COOH)_2$	B	15.1	succinic acid $(CH_2)_2(COOH)_2$	B	1.11E-08	succinic acid $(CH_2)_2(COOH)_2$	B	25.9	succinic acid $(CH_2)_2(COOH)_2$	B	1.90E-08
potassium dichromate $K_2Cr_2O_7$	A	11.4	potassium nitrate KNO_3	A	8.36E-09	potassium dichromate $K_2Cr_2O_7$	A	17.5	potassium dichromate $K_2Cr_2O_7$	A	1.24E-08
potassium nitrate KNO_3	A	9.0	potassium dichromate $K_2Cr_2O_7$	A	8.07E-09	potassium nitrate KNO_3	A	11.9	potassium nitrate KNO_3	A	1.11E-08
maleic acid $C_2H_2(COOH)_2$	C	4.7	potassium sulphate K_2SO_4	D	3.44E-09	potassium sulphate K_2SO_4	D	7.0	potassium sulphate K_2SO_4	D	5.51E-09
potassium sulphate K_2SO_4	D	4.4	ammonium nitrate NH_4NO_3	B	2.96E-09	maleic acid $C_2H_2(COOH)_2$	C	5.9	ammonium chloride NH_4Cl	B	3.87E-09
urea $(NH_2)_2CO$	C	3.2	ammonium chloride NH_4Cl	B	2.57E-09	urea $(NH_2)_2CO$	C	4.4	ammonium nitrate NH_4NO_3	B	2.75E-09
ammonium nitrate NH_4NO_3	B	2.9	potassium bromide KBr	B	1.97E-09	ammonium chloride NH_4Cl	B	3.7	urea $(NH_2)_2CO$	C	2.33E-09
ammonium chloride NH_4Cl	B	2.5	urea $(NH_2)_2CO$	C	1.70E-09	ammonium nitrate NH_4NO_3	B	2.7	maleic acid $C_2H_2(COOH)_2$	C	2.06E-09
potassium bromide KBr	B	1.9	maleic acid $C_2H_2(COOH)_2$	C	1.64E-09	potassium bromide KBr	B	1.9	potassium bromide KBr	B	2.02E-09
sodium nitrate $NaNO_3$	D	1.8	potassium iodide KJ	D	9.45E-10	sodium nitrate $NaNO_3$	D	1.8	sodium nitrate $NaNO_3$	D	7.47E-10
potassium iodide KJ	D	1.1	sodium nitrate $NaNO_3$	D	7.44E-10	ammonium sulphate $(NH_4)_2SO_4$	D	0.9	potassium iodide KJ	D	6.34E-10
ammonium sulphate $(NH_4)_2SO_4$	D	0.7	ammonium sulphate $(NH_4)_2SO_4$	D	2.20E-10	potassium iodide KJ	D	0.7	ammonium sulphate $(NH_4)_2SO_4$	D	2.82E-10
sodium chloride NaCl	D	0.1	sodium chloride NaCl	D	5.72E-11	sodium chloride NaCl	D	0.2	sodium chloride NaCl	D	1.29E-10

The simplified criteria are based on parallel nucleation and growth and do not take the mass balance into account, as shown in Figure 7-11.

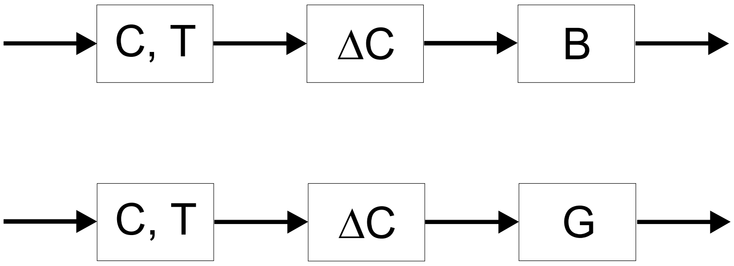

Figure 7-11: Scheme of the simplified criteria

The heterogeneous nucleation rate, B_{het}, is calculated with Schuberts model (see equation (2-36)), which was also used in the model of metastability. In contrast to chapter 7.1, the relative supersaturation σ required for obtaining a defined nucleation rate is determined, neglecting the mass balance.

The maximum heterogeneous nucleation rates in Figure 7-5 vary between 10^{12} m^{-3} s^{-1} and 10^{16} m^{-3} s^{-1} depending on the material properties. As a consequence a nucleation rate of 10^{10} m^{-3} s^{-1} is reached by every system. Considering the steep slopes of the nucleation rates plotted versus time in Figure 7-5, the point of time of the occurrence of the maximum heterogeneous nucleation rate of each system does not vary much from the time when a nucleation rate of 10^{10} m^{-3} s^{-1} is reached. Thus, the necessary relative supersaturation σ, required for a nucleation rate B_{het} 10^{10} m^{-3} s^{-1}, is calculated without consideration of the mass balance. The results are shown in Table 7-3.

Table 7-3: Relative supersaturation σ, subcooling ΔT and corresponding cooling times (for different cooling rates) necessary for obtaining a heterogeneous nucleation rate of 10^{10} m^{-3} s^{-1} (valid for: $a_{for} = 10^5$ m^{-1}; $He_{ad} = 10^{-9}$; $T = 298$ K; $K = 0.414$; $\theta = 45°$)

system	category	σ [-]	Δ T [K]	cooling time [s] (cooling rate: 0.296 K / s)	cooling time [s] (cooling rate: 0.171 K / s)	cooling time [s] (cooling rate: 0.111 K / s)	cooling time [s] (cooling rate: 0.077 K / s)	cooling time [s] (cooling rate: 0.066 K / s)
adipic acid	A	0.28	2.03	6.9	11.9	18.3	26.4	30.8
maleic acid	C	0.06	3.83	12.9	22.4	34.5	49.7	58.0
potassium nitrate	A	0.14	4.63	15.6	27.0	41.7	60.1	70.1
succinic acid	B	0.32	6.28	21.2	36.7	56.6	81.6	95.2
potassium dichromate	A	0.31	8.20	27.7	47.9	73.9	106.5	124.2
ammonium chloride	B	0.10	12.58	42.5	73.6	113.3	163.4	190.6
urea	C	0.15	13.74	46.4	80.3	123.8	178.4	208.1
potassium iodide	D	0.06	17.20	58.1	100.6	154.9	223.3	260.5
potassium sulphate	D	0.35	23.91	80.8	139.8	215.4	310.5	362.3
sodium nitrate	D	0.17	28.33	95.7	165.7	255.2	367.9	429.3
sodium chloride	D	0.15	477.18	1612.1	2790.5	4298.9	6197.1	7230.0

The growth step is calculated with the simplified model for the estimation of the metastable zone width of Mersmann [Mers98], where the growth of a crystal to a detectable size L_{det} is calculated according to the current cooling rate and system properties, see equation (4-9). The obtained supersaturation σ_{met} and the corresponding point of time when the crystals have grown to a detectable size L_{det} of 10^{-5} m can be seen in Table 7-4. The calculations have been made for the cooling rates resulting from the combination of an amperage of 3000 mA and measurement times ranging from 60 s to 300 s. The systems in Table 7-4 are ranked by the time t_{det}, which is calculated from the subcooling ΔT_{met} corresponding to σ_{met} and the current cooling rate. It can be seen, that the systems of category D show the highest values of t_{det}.

A combination of the two separate steps, nucleation and growth, leads to Table 7-5, where the sum of the cooling time (see Table 7-3) and the time t_{det} (see Table 7-4) is shown. The grey cells indicate, that the obtained time exceeds the measurement time corresponding to the particular cooling rate, as a consequence these systems are not suited for the supersaturation sensor. Considering the categories (A – D) in which the systems have been classified, this method predicts very well the applicability of the sensor for a certain system. In addition, the calculations for potassium sulphate do now fit the experimental observations.

Table 7-4: Metastable zone widths calculated according to equation (4-8) (valid for $L_{det} = 10^{-5}$ m)

$L_{det} = 10^{-5}$ m		cooling rate: 0.296 K / s		cooling rate: 0.171 K / s		cooling rate: 0.111 K / s		cooling rate: 0.077 K / s		cooling rate: 0.066 K / s	
		settings: 3000 mA; 60 s		settings: 3000 mA; 120 s		settings: 3000 mA; 180 s		settings: 3000 mA; 240 s		settings: 3000 mA; 300 s	
system	category	σ_{met} [-]	t_{det} [s]	σ_{met} [-]	t_{det} [s]	σ_{met} [-]	t_{det} [s]	σ_{met} [-]	t_{det} [s]	σ_{met} [-]	t_{det} [s]
adipic acid $(CH_2)_4(COOH)_2$	A	0.690	4.4	0.574	6.4	0.498	8.5	0.441	10.8	0.419	12.0
ammonium nitrate NH_4NO_3	B	0.030	10.5	0.025	15.1	0.022	20.1	0.019	25.7	0.018	28.5
potassium bromide KBr	B	0.211	11.3	0.175	16.3	0.152	21.8	0.135	27.8	0.128	30.7
potassium nitrate KNO_3	A	0.118	13.2	0.098	19.0	0.085	25.3	0.075	32.3	0.071	35.8
urea $(NH_2)_2CO$	C	0.044	14.0	0.037	20.2	0.032	26.8	0.028	34.2	0.027	37.9
maleic acid $C_2H_2(COOH)_2$	C	0.081	17.4	0.067	25.2	0.058	33.5	0.052	42.7	0.049	47.3
succinic acid $(CH_2)_2(COOH)_2$	B	0.303	20.2	0.252	29.2	0.218	38.8	0.193	49.5	0.184	54.9
ammonium chloride NH_4Cl	B	0.060	24.2	0.050	34.9	0.043	46.4	0.038	59.2	0.036	65.6
potassium dichromate $K_2Cr_2O_7$	A	0.285	25.1	0.237	36.3	0.206	48.3	0.182	61.6	0.173	68.2
sodium nitrate $NaNO_3$	D	0.058	32.4	0.049	46.7	0.042	62.1	0.037	79.3	0.035	87.8
potassium iodide KJ	D	0.036	34.0	0.030	49.0	0.026	65.2	0.023	83.2	0.022	92.2
potassium sulphate K_2SO_4	D	0.212	48.8	0.176	70.4	0.153	93.7	0.135	119.5	0.128	132.5
ammonium sulphate $(NH_4)_2SO_4$	D	0.048	69.8	0.040	100.7	0.035	133.9	0.031	170.9	0.029	189.3
sodium chloride NaCl	D	0.029	313.5	0.024	452.4	0.021	601.9	0.018	768.0	0.018	850.9

Table 7-5: Times calculated for consecutive nucleation and growth to a detectable size L_{det}

system	category	time [s] (cooling rate: 0.296 K / s)	time [s] (cooling rate: 0.171 K / s)	time [s] (cooling rate: 0.111 K / s)	time [s] (cooling rate: 0.077 K / s)	time [s] (cooling rate: 0.066 K / s)
adipic acid	A	11.3	18.3	26.8	37.2	42.8
potassium nitrate	A	28.8	46.1	67.0	92.4	105.9
maleic acid	C	30.4	47.6	68.0	92.4	105.4
succinic acid	B	41.4	65.9	95.4	131.1	150.1
potassium dichromate	A	52.8	84.2	122.1	168.0	192.4
urea	C	60.4	100.5	150.6	212.6	246.1
ammonium chloride	B	66.7	108.4	159.7	222.6	256.2
potassium iodide	D	92.1	149.6	220.1	306.6	352.8
sodium nitrate	D	128.1	212.4	317.4	447.2	517.1
potassium sulphate	D	129.6	210.2	309.1	430.1	494.7
sodium chloride	D	1925.6	3242.9	4900.8	6965.1	8080.9

8 Conclusion

In this work the combination of a new measurement technique and an innovative measurement principle was introduced. Thus, showing the long way from an idea to an implementation.

A survey and brief discussion of the current supersaturation measurement techniques and crystallizer control strategies showed their weaknesses and the lack of a sensor capable of direct measuring of supersaturation. As a consequence there is an urgent demand for a measurement method, that is able to indicate the influence of impurities or other process disturbances by incorporating the current crystallization in its measurement method. The idea of implementing two detection devices in the new sensor concept proved to be useful, since the experimental results have shown, that the measurement of mechanical properties with the SAW or of electrical properties with the IDT showed different sensitivity depending on the current system. Unfortunately, it was not possible to estimate which sensor, IDT or SAW, is suitable for a certain system according to known system properties.

The capability of the new sensor in measuring directly the driving force of a cooling crystallization from solution, the supersaturation, was demonstrated in various experiments in laboratory and pilot plant scale. The preconditions of a crystal-free solution at rest during each measurement and of a subsequent exchange of the solution adjacent to the sensor surface, including the removal of the incrustation, after each measurement showed the complexity of a crystallization process in general. The multitude of process parameters influencing a crystallization made it necessary to design a sensor housing to provide the required conditions for each measurement in order to guarantee evaluable and reproducible measurement data. The solution of the problems obtained by switching from beaker glasses to crystallizers during the experimental phase was very crucial and still offers some potential of further improvement to enable highly reliable measurements in industrial vessels.

Possibilities of a-priori estimations of the applicability of the sensor for the control of a crystallization process have been found. These criteria are based on material properties and differ in accuracy corresponding to the required effort. They allow an easy assessment of the possible field of application considering the prevalent systems in industry.

A specific border line between systems being suitable or non-suitable for this sensor can not be drawn according to a single specific material property. As shown, only an individual evaluation based on a combination of “thermic” and “kinetic” properties or coefficients of each system is able to give sufficient information about the applicability.

The way of generating the additional supersaturation in order to induce a quick incrustation on the sensor surface and the results of the a-priori criteria have shown the limit of this new supersaturation sensor. Generally speaking, this sensor is capable of measuring supersaturation for systems with positive temperature dependent solubility.

To make the high potential of this supersaturation measurement method accessible for other - up to now not suitable - systems or in other words, to broaden the range of suitable systems, it is necessary to adapt or change the way of generating the additional measurement supersaturation according to the current process. This means that other ways of supersaturation generation, like removal of solvent by evaporation or membrane-pervaporation or drowning-out, must be realized, thus enabling the measurement of supersaturation in solutions of systems with flat solubility curves.

9 Notation

A	area, surface area	m^2
a	surface area per unit volume	$m^2\ m^{-3}$
a_i	activity of component i	-
B	volumetric nucleation rate	$m^{-3}\ s^{-1}$
B_0	nucleation rate based on volume suspension ($L \rightarrow 0$)	$m^{-3}\ s^{-1}$
B_{agg}	agglomeration based birth rate	$m^{-4}\ s^{-1}$
C	molar concentration	$mol\ m^{-3}$
ΔC	supersaturation ($\Delta C = C - C^*$)	$mol\ m^{-3}$
c	concentration	$kg\ m^{-3}$
c_i	molarity / molar concentration of substance i	
c_p	specific heat capacity	$J\ kg^{-1}\ K^{-1}$
D	diameter	m
D_{AB}	diffusion coefficient	$m^2\ s^{-1}$
D_{agg}	agglomeration based death rate	$m^{-4}\ s^{-1}$
d	diameter	m
E	efficiency factor	-
E_{CE}	efficiency cooling-evaporation	-
f	factor	-
f	frequency	Hz
f_i	activity coefficient	$m^3\ mol^{-1}$
G	Gibbs free energy	$J\ mol^{-1}$, J/molecule
G	linear crystal growth rate	$m\ s^{-1}$
g	gravitational acceleration (= $9.81\ m\ s^{-2}$)	$m\ s^{-2}$
He_{ad}	Henry coefficient	-
H_V	Vickers Hardness	$J\ m^{-3}$
ΔH^*_{CL}	enthalpy of crystallization	$J\ mol^{-1}$
h	heat transfer coefficient	$W\ m^{-2}\ K^{-1}$
h	height	m
h	specific enthalpy	$J\ kg^{-1}$
I	current	A
K	factor	-
K_r	factor	-
K_x	dissociation constant based on concentration	$mol\ m^{-3}$
k	Boltzmann constant (= $1.381 \cdot 10^{-23}\ J\ K^{-1}$)	$J\ K^{-1}$
k_d	mass transfer coefficient	$m\ s^{-1}$
k_g'	growth rate constant	$m\ s^{-1}$
k_r	growth rate integration constant	var.
L	length	m

$\Delta\dot{L}^0$	evaporated solvent mass rate	$kg\ s^{-1}$
M	mass	kg
$\tilde{M}$	molar mass	$kg\ mol^{-1}$
m	factor	-
m	mass per volume solution	$kg\ m^{-3}{}_{sol}$
m°	mass per volume solvent	$kg\ m^{-3}{}_{solv}$
$\dot{m}$	mass flux density	$kg\ m^{-2}\ s^{-1}$
m_T	suspension density, total crystal mass per unit volume	$kg\ m^{-3}$
N	number of particles	-
n	population density per unit volume	m^{-4}
n	exponent	-
N_A	Avogadro's number ($= 6.023 \cdot 10^{23}\ mol^{-1}$)	mol^{-1}
Ne	Newton Number	-
N_V	pumping capacity	-
n_i	amount of substance	mol
$\dot{P}_{cool}$	cooling parameter	s^{-1}
$\dot{P}_{evap}$	evaporation parameter	s^{-1}
Q	quantity of heat	J
$Q_i(L)$	cumulative undersize distribution factor	-
$q_i(L)$	undersize distribution factor	m^{-1}
R	resistance	Ω
$\mathfrak{R}$	ideal gas constant (8.314 J/(mol K))	$J\ mol^{-1}\ K^{-1}$
r	radius	m
r	order of the integration process	var.
S	supersaturation ratio ($S = C/C^*$)	-
S_a	supersaturation ratio ($S_a = a_i/a_i^*$)	-
Sh	Sherwood number	-
s	impeller or stirrer speed, rate of rotation	s^{-1}
T	temperature	K
$\dot{T}$	cooling rate	$K\ s^{-1}$
t	time	s
U	circumference	m
U	voltage	V
u_{tip}	stirrer tip speed	$m\ s^{-1}$
V	volume	m^3
$\dot{V}$	volumetric flow rate	$m^3\ s^{-1}$
v	velocity	$m\ s^{-1}$
$\bar{v}$	mean growth rate of a face	$m\ s^{-1}$
VR	volume reduction coefficient	-
W	mass ratio of two substances	$kg\ kg^{-1}{}_{solv}$
W	work	J

w	velocity	$\mathrm{m\ s^{-1}}$
w	thickness	m
w	mass fraction of substance	$\mathrm{kg\ kg^{-1}{}_{sol}}$
X	mass ratio of solute and solvent	$\mathrm{kg\ kg^{-1}}$
X	reactive part of impedance	Ω
x	ratio of the sizes of foreign particle to critical nucleus	-
x_i	mole ratio of substance i	$\mathrm{mol\ mol^{-1}}$
Z	imbalance factor	-
Z	impedance	Ω

Greek Symbols

$\gamma_\pm$	average activity coefficient	-
$\bar{\varepsilon}$	mean specific power input	$\mathrm{W\ kg^{-1}}$
Γ	fracture resistance	$\mathrm{J\ m^{-2}}$
ϑ	temperature	°C
α	degree of dissociation	-
α	volume shape factor	-
α	efficiency factor	-
β	surface area shape factor	-
β	agglomeration kernel	$\mathrm{m^3\ s^{-1}}$
β_{coll}	collision kernel	$\mathrm{m^3\ s^{-1}}$
ε	local specific power input	$\mathrm{W\ kg^{-1}}$
ε	specific inductive capacity	-
γ_{CL}	interfacial tension	$\mathrm{J\ m^{-2}}$
γ_i	activity coefficient	-
η	dynamic viscosity	Pa s
η_f	target efficiency	-
η_{geo}	target efficiency	-
η_w	target efficiency	-
φ	volumetric crystal hold-up	$\mathrm{m^3\ m^{-3}}$
φ	phase shift	°
φ_i	current phase angle	°
φ_u	voltage phase angle	°
κ	electric conductance	$\mathrm{S\ m^{-1}}$
λ	crystal size	m
μ	chemical potential	$\mathrm{J\ mol^{-1}}$
μ	shear modulus	Pa
ν	stoichiometric coefficient, number of ions	-
θ	contact angle	°

ρ	density	kg m^{-3}
σ	relative supersaturation ($\sigma = C/C^*$)	-
τ	relaxation time, residence time	s

Superscripts

*	equilibrium

Subscripts

0	standard state
50	median value
a	attrition
B	batch
B + S	birth and spread
BCF	Burton – Cabrera – Frank
C	crystal, cooling
c	critical, contact
col	collision
cool	cooling, coolant
det	detectable
dis	dissociated
E	evaporation
eff	effective
F	fluid
for	foreign
g	growth
geo	geometrical
het	heterogeneous
hom	homogeneous
i	component i of mixture
I	interface value
ind	induction
L	liquid
LV	liquid – vapour
m	molar-value, molecular
max	maximum value
meas	measurement
met	metastable
min	minimum value
mix	mixture
n	nucleation, nucleus

opt	optimal
p	particle
par	parent
PN	polynuclear
proc	process
r	relaxation
S	solid, seed
s	surface
sec	secondary
sensor	sensor
sep	cutsize
sol	solution
solv	solvent
start	starting point of incrustation
surf	surface
susp	suspension
T	total, cut size
tot	total
V	evaporation
α	initial
ω	final

10 References

[Abra75] Abrahamson, J., *Collision Rates of Small Particles in a Vigorously Turbulent Fluid*, Chem. Eng. Sci., 30: 1371 – 1379 (1975)

[Alte09] Altenkirch, E., *Über den Nutzeffekt der Theromsäule*, Physikalische Zeitschrift, 16: 560 – 568 (1909)

[Aust85] Austmeyer, K., Frankenfeld, T., Die radiometrisch erfaßte Dichte als Meßgröße für den Kochprozeß, Zuckerindustrie, 110 (2): 122 – 130 (1985)

[Benn69] Bennema, P., *The importance of surface diffusion for crystal growth from solution*, J. Cryst. Growth, 5: 29 (1969)

[Benn73] Bennema, P., Boon, J., van Leeuwen, C., Gilmer, G. H., *Confrontation of the BCF theory and computer simulation experiments with measured (R, σ) curves*, Krist. Tech., 8: 659 (1973)

[Benn76] Bennema, P., *Theory and experiment for crystal growth from solution: Implications for industrial crystallization*, in Industrial Crystallization (ed. by J. W. Mullin), Plenum Press, New York (1976)

[Brau02] Braun, B., *Agglomeration in Aqueous Solutions during Precipitation*, Thesis, TU München (to be published)

[Burt51] Burton, W. K., Cabrera, N., Frank, F. C., *The growth of crystals and the equilibrium structure of their surface*, Phil. Trans. Roy. Soc. London, 243: 299 (1951)

[Camp43] Camp, T.R., Stein, P.C., *Velocity Gradients and Internal Work in Fluid Motion*, J. Boston Society Civil Engin., 30: 219 - 237 (1943)

[Chia96] Chianese, A., Sangl, R., Mersmann, A., *On the size distribution of fragments generated by crystal collisions*, Chem. Eng. Comm., 146: 1-12 (1996)

[Dave00] Davey, R., Garside, J., Form Molecules to Crystallizers, Oxford University Press Inc., New York (2000)

[Denk70] Denk, E. G., *Fundamental studies in secondary nucleation*, Thesis, Tufts University, Medford (1970)

[Dirk91] Dirksen, J. A., Ring, T. A., *Fundamentals of Crystallizationkinetic effects on particle size distribution and morphology*, Cvhem. Eng. Sci., 46:;2389 (1991)

[Dirk91] Dirksen, J. A., Ring, T. A., *Fundamentals of crystallization: Kinetic effects on particle size distributions and morpholgy*, Chem. Eng. Sci., 46 (10): 2389 (1991)

[Drob93] Drobe, H., Leidl, A., Rost, M., Ruge, I., *Acoustic sensors based on surface-localized HPSWs for measurements in liquids*, Sensors and Actuators A, 37 – 38: 141 – 148 (1993)

[Dunu97] Dunuwila, D.D., Berglund, K.A., ATR FTIR spectroscopy for in situ measurement of supersaturation, Journal of Crystal Growth, 179: 185 – 193 (1997)

[Eek95a] Eek, R.A., Control and dynamic modelling of industrial suspension crystallizers, Thesis, TU Delft (1995)

[Eek95b] Eek, R.A., Dijkstra, S., Design and experimental evaluation of a state estimator for a crystallization process, Ind. Eng. Chem. Res., 34: 567 – 574 (1995)

[Ehre97] Ehrenberg, J., Kessler, K., Anwendung der Hochfrequenzmesstechnik zur Bestimmung des Trockensubstanzgehalts in Lösung und Suspensionen sowie zur Regelung von Verdampfungskristallisation, Werkstoffe und Korrosion, 122 (2): 100 – 107 (1997)

[Eins22] Einstein, A., *Untersuchungen über die Theorie der Brownschen Bewegung*, Ed. R. Fürth, Leipzig (1922)

[Fevo96a] Fevotte, G., Klein, J.P., A new policy for the estimation of the course of supersaturation in batch crystallization, The Canadian Journal of Chemical Engineering, 74: 372 – 384 (1996)

[Fevo96b] Fevotte, G., Klein, J.P., Calorimetric methods for the study of batch crystallization processes: Some key results, Trans. Institution of Chemical Engineers, 74: 791 – 796 (1996)

[Fran49] Frank, F. C., *The influence of dislocations on crystal growth*, Disc. Faraday Soc., 5: 48 (1949)

[Fuch89] Fuchs, N., *Über die Stabilität und Aufladung der Aerosole*, Z. Physik, 89: 736 – 743 (1989)

[Gahn97] Gahn, C., *Die Festigkeit von Kristallen und ihr Einfluß auf die Kinetik in Suspensionskristallisatoren*, Thesis, TU München (1997)

[Gers98] Gerstlauer, A., Mann, M., Gilles, E.D., Gahn, C., Mersmann, A., Development, analysis and simulation of a population model for a continuous crystallizer including nucleation ,growth and attrition (1998)

[Gold54] Goldsmid, H. J., Douglas, R. W., *The use of semiconductors in thermoelectric refrigeration*, British Journal of applied Physics, 5: 386 – 390 (1954)

[Gutw91] Gutwald, T., Über die Bestimmung kinetischer Parameter bei der diskontinuierlichen Kristallisation aus Lösungen, Thesis, TU München (1991)

[Gutw94] Gutwald, T., Mersmann, A., Evaluation of kinetic parameters of crystallization from batch and continuos experiments, Separ. Technol., 4: 2 (1994)

[Hart86a] Hartel, R. W., Gottung, B. E., Randolph, A. D., Drach, G. W., *Mechanisms and kinetic modeling of calcium oxalate crystal aggregation in a urinelike liquor - Part I: Mechanisms*, AIChE Journal, 32: 1176 – 85 (1986)

[Hart86b] Hartel, R. W., Randolph, A. D., *Mechanisms and Kinetic Modeling of calcium oxalate crystal aggregation in a urinelike liquor - Part II: Kinetic modeling*, AIChE Journal, 32: 1186-95 (1986)

[Heds94] Hedström, L., *Secondary nucleation of pentaerythritol and citric acid monohydrate*, Thesis, TH Stockholm (1994)

[Heij92] Van der Heijden, A. E. D. M., *Secondary nucleation and crystallization kinetics*, Thesis, Nijwegen (1992)

[Helt77] Helt, J.E., Larson, M.A., Effects of temperature on the crystallization of potassium nitrate by direct measurement of supersaturation, AIChE Journal, 23 (6): 822 – 830 (1977)

[Hemp87] Hempelmann, R., Austmeyer, K., Zur Kalibirierung der radiometrisch arbeitenden Dichtemeßeinrichtung für den Kochprozeß, Zuckerindustrie, 112 (8): 695 – 698 (1987)

[Heye01] Heyer, C., *Production of nano-sized particles by drowning-out precipitation*, Thesis, TU München (2001)

[Hill66] Hilling, W. B., *A derivation of classical two-dimensional nucleation kinetics associated crystal growth laws*, Acta Met., 14: 1868 (1966)

[Hloz92] Hlozny, L., Sato, A., Kubota, N., On-line measurement of supersaturation during batch cooling crystallization of ammonium alum, Journal of Chemical Engineering of Japan, 25 (5): 604 – 606 (1992)

[Hofm91] Hofmann, G., *Verfahren zur Kristallisation*, Die Praxis der Kristallisation, Haus der Technik, Essen (1991)

[Isra91] Israelachvili, J., *Intermolecular & Surface Forces*, 2nd ed.,Academic Press, London (1991)

[Jone73] Jones, A.G., Optimal operation of a batch cooling crystallizer, Chemical Engineering Science, 29: 1075 – 1087 (1973)

[Jone74] Jones, A.G., Mullin, J.W., Programmed cooling crystallization of potassium sulphate solutions, Chemical Engineering Science, 29: 105 – 118 (1974)

[Just53] Justi, E., *Elektrothermische Kühlung*, Kältetechnik, 6: 150 – 157 (1953)

[Juza77] Juzaszek, P., Larson, M.A., AIChe J., 23: 460 (1977)

[Kara] Karakaya, C., Stepanski, M., Ulrich, J., A on-line in-situ measuring technique for the determination of crystal growth rates by measuring time related changes in crystal size distribution

[Kind83] Kind, M., Mersmann, A., *Methoden zur Berechnung der homogenen Keimbildung aus wässrigen Lösungen*, Chem.-Ing.-Tech., 55: 720-721 (1983)

[Kind89] Kind, M. H., *Über die Übersättigung während der Kornkristallisation*, Thesis, TU München (1989)

[Krui97] Kruis, F.E., Kusters, K.A., *The Collision Rate of Particles in Turbulent Flow*, Chem. Eng. Comm., 158: 201 – 230 (1997)

[Kubo72] Kuboi, R., Komasawa, I., Otake, T., *Behavior of Dispersed Particles in Turbulent Liquid Flow*, J. Chem. Eng. Japan, 5: 349 – 355 (1972)

[Leid97] Leidl, A., Oberlack, I., Schaber, U., Mader, B., Drost, S., *Surface acoustic wave devices and applications in liquid sensing*, Smart Mater. Struct., 6: 680 – 688 (1997)

[Leid98] Leidl, A., *Oberflächenwellenbauelemente als Sensoren für Flüssigkeiten und Beschichtungen*, Thesis, Universität der Bundeswehr München (1998)

[Marc88] Marchal, P., David, R., Klein, J. P., Villermaux, J., *Crystallization and precipitation engineering - I An efficient method for solving population balance in crystallization with agglomeration*, Chemical Engineering Science, 59-67 (1988)

[Mayr88] Mayrhofer, B., Nývlt, J., Programmed Cooling of Batch Crystallizers, Chemical Engineering and Processing, 24: 217 – 220 (1988)

[Mers00] Mersmann, A., Löffelmann, M., *The optimal supersaturation: Crystallization and precipitation*, Chemical Engineering Technology, 23: 11 – 15 (2000)

[Mers01] Mersmann, A., *Crystallization Technology Handbook* (ed. by A. Mersmann), Marcel Dekker Inc., New York (2001)

[Mers90] Mersmann, A., *Calculation of interfacial tensions*, J. Cryst. Growth, 102: 841 (1990)

[Mers95] Mersmann, A., *General prediction of statistically mean growth rates of a crystal collective*, J. Cryst. Growth, 141: 181-195 (1995)

[Mers96] Mersmann, A., *Supersaturation and Nucleation*, 13th Symposium on Industrial Crystallization, Toulouse (1996)

[Mers98] Mersmann, A., Bartosch, K., *How to predict the metastable zone width*, J. Cryst. Growth, 183: 240 – 250 (1998)

[Mess72] Messing, T., Übersättigungsbestimmungen als wichtige Problemlösung bei der Massenkristallisation, Verfahrenstechnik, 6 (3): 106-108 (1972)

[Mier07] Miers, H. A., Isaac, F., *The spontaneous crystallization of binary mixtures*, Proc. of the Royal the Society , A79: 322 – 351 (1907)

[Müll63] Müller, H., *Bemessung und Aufbau von Peltieraggregaten*, Kältetechnik, 15, 5: 137 – 143 (1963)

[Mull70] Mullin, J. W., Chakraborty, M., Mehta, K., *Nucleation and growth of ammonium sulphate crystals*, Journal of Applied Chemistry, 20: 367 – 371 (1970)

[Mull71] Mullin, J.W., Nyvlt, J., Programmed cooling of batch crystallizers, Chemical Engineering Science, 26: 369 – 377 (1971)

[Mull79] Mullin, J. W., Jancic, S. J., *Interpretation of metastable zone widths*, Trans IChemE , 57: 188 – 193 (1979)

[Müll91] Müller, R., *Bauelemente der Halbleiter-Elektronik*, Springer, Berlin (1991)

[Mull93] Mullin, J.W., *Crystallization*, Butterworth-Heinemann Ltd., Oxford (1993)

[Mumt00] Mumtaz, H. S., Hounslow, M. J., *Aggregation during precipitation from solution: An experimental investigation using Poiseuille flow*, Chemical Engineering Science, 55: 5671-5681 (2000)

[Mumt97] Mumtaz, H. S., Hounslow, M. J., Seaton, N. A., Paterson, W. R., *Orthokinetic aggregation during precipitation*, TransIChemE, 75: 152-159 (1997)

[Neum92] Neumann, D., *Peltier-Kälteaggregate in der Praxis*, product description of Neumann Peltier-Technik, Munich (1992)

[Niel81] Nielsen, A. E., *Theory of electrolyte crystal growth*, Pure & Appl. Chem., 53: 2025 (1981)

[Niels81] Nielsen, A. E., *Pure Appl. Chem.*, 53: 2025 (1981)

[Nyvl70] Nyvlt, J., Rychly, R., Gottfried J., Wurzelova, J., *Metastable zone widths of some aqueous solutions*, J. Cryst. Growth, 6: 151 – 162 (1970)

[Ohar73] Ohara, M., Reid, R. C., *Modelling crystal growth rates from solutions*, Englewood, Cliffs, Prentice Hall (1973)

[Omar99a] Omar, W., Strege, C., Ulrich, J., *Bestimmung der Breite des metastabilen Bereichs von realen Lösungen mittels der Ultraschallmesstechnik zur online Prozessregelung bei Kristallisationen*, Chemische Technik, 51(5): 286 – 290 (1999)

[Omar99b] Omar, W., *Zur Bestimmung von Kristallisationskinetiken auch unter der Einwirkung von Additiven mittels Ultraschallmesstechnik*, Thesis, Bremen (1999)

[Ostw97] Ostwald, W., *Studien über die Umwandlung und Bildung fester Körper*, Zeitschrift für Physikalische Chemie, 22: 289 – 330 (1897)

[Pate95] *Patent specification DE 43 45 163 C 2*, Deutsches Patentamt (1995)

[Pate95a] *Patent specification DE 43 40 383 C 2*, Deutsches Patentamt (1995)

[Pohl87] Pohlisch, R.J., *Einfluß von mechanischer Beeinflussung und Abrieb auf die Korngrössenverteilung in Kühlungskristallisatoren*, Thesis, TU München (1987)

[Rand88] Randolph, A. D., Larson, M. A., *Theory of Particulate Processes*, 2nd ed., Academic Press, San Diego (1988)

[Raul00] Rauls, M., Bartosch, K., Kind, M., Kuch, St., Lacmann, R., Mersmann, A., *The Influence of Impuruities on Crystallization Kinetics – A Case Study on the Crystallization of Ammonium Sulfate*, J. Cryst. Growth 213, 116 – 128 (2000)

[Raul90] Rauls, M., Beckmann, W., *On the Relation between Dissolution and Growth of Crystals*, Proc. of the 11th Symposium on Industrial Crystallization (ed. by Mersmann), Garmisch-Partenkirchen (1990)

[Redm95] Redman, T.P., Rohani, S., Strathdee, G., *On-line control of supersaturation in a continuos cooling KCl crystallizer*, The Canadian Journal of Chemical Engineering, 73: 725 – 732 (1995)

[Rieb90] Riebel, U., Kofler, V., Löffler, F., *Ein Verfahren zur Kontrolle der Übersättigung bei der Suspensionskristallisation*, Chemie Ingenieur Technik, 62 (7): 553 – 554 (1990)

[Robi55] Robinson, R.A., Stokes, R.H., *Electrolyte Solutions*, Butterworth, London (1955)

[Roha86] Rohani, S., *Dynamic study and control of crystal size distribution (CSD) in KCI crystallizers*, The Canadian Journal of Chemical Engineering, 64: 112 – 118 (1986)

[Roha87] Rohani, S., Paine, K., *Measurement of solid concentration of a soluble compound in a saturated slurry*, The Canadian Journal of Chemical Engineering, 65: 163-165 (1987)

[Roha90] Rohani, S., Tavare, N.S., Garside, J., *Control of crystal size distribution in a batch cooling crystallizer*, The Canadian Journal of Chemical Engineering, 68: 260 – 267 (1990)

[Rous82] Rousseau, R.W., Howell, T.R., *Comparison of simulated crystal size distribution control systems based on nuclei density and supersaturation*, Ind. Eng. Chem. Process Des. Dev., 21 (4): 606 – 610 (1982)

[Saff56] Saffman, P.G., Turner, J.S., *On the Collision of Drops in Turbulent Clouds*, J. Fluid Mechanics, 1: 16 – 30 (1956)

[Sage62] Sagel, K., *Halbleitermaterialien für die thermoelektrische Kühlung und Stromerzeugung*, Metall, 16, 2: 87 – 96 (1962)

[Sang91] Sangl, R., *Mechanischer Abrieb von Kristallen als Beitrag zur sekundären Keimbildung*, Thesis, TU München (1991)

[Schu98] Schubert, H., *Keimbildung bei der Kristallisation schwerlöslicher Feststoffe*, Thesis, TU München (1998)

[Seife76] Seifert, D., *Der metastabile Bereich bei der Kornkristallisation*, Verfahrenstechnik, 10: 518 – 520 (1976)

[Smol17] Smoluchowski, M., *Versuch einer mathematischen Theorie der Koagulationskinetk kolloider Lösungen*, Z. physikal. Chemie, 92: 129 – 168 (1917)

[Suzu90] Suzuki, M., *Adsorption Engineering*, Chemical Engineering Monographs, 25, Elsevier, Amsterdam (1990)

[Tava95] Tavare, N. S., *Industrial Crystallization*, Plenum Press, New York (1995)

[Verv48] Vervey, E.J., Oberbeek, J. T. G., *Theory of the Stability of Lyophobic Colloids*, Elsevier, Amsterdam (1948)

[Volm26] Volmer, M., Weber, A., *Keimbildung in übersättigten Lösungen*, Z. Phys. Chem., 119: 277-301 (1926)

[Volm39] Volmer, M., *Kinetik der Phasenbildung*, Steinkopf, Dresden (1939)

[Wang89] Wang, Z.K., Zeng, Q.S., Qian, R.Y., *Precise Determination of supersaturation by temperature float method*, AIChE Journal, 35 (4): 679 – 682 (1989)

[Wang92] Wang, S., *Größenabhängige Wachstumsdispersion von Abriebsteilchen und die Relevanz zur effektiven sekundären Keimbildung*, Thesis, TU München (1992)

[Youn55] Young, T., *Miscellanous Works* (ed. by G. Peacock), J. Murray, London (1855)

[Yu75] Yu, K.M., Douglas, J.M., *Self-generated oscillations in continuous crystallizers*, AIChE Journal, 21 (5): 917 – 924 (1975)

[Zach95] Zacher, U., *Die Kristallwachstumsdispersion in einem kontinuierlichen Suspensionskristallisator*, Thesis, TU München (1995)

[Zeld42] Zeldovich, J., *Ќ Теории Образованя Новой Фазы Кавитация*, J. exp. theor. Physics (USSR), 12: 525 (1942)

[Zeve98] Zevenbergen, M.J.G., *An on-line evolving estimator for batch crystallization processes*, Thesis, TU Delft (1998)

11 Appendix

11.1 Comparison of the Dependence of the pre-exponential Factor on Supersaturation S

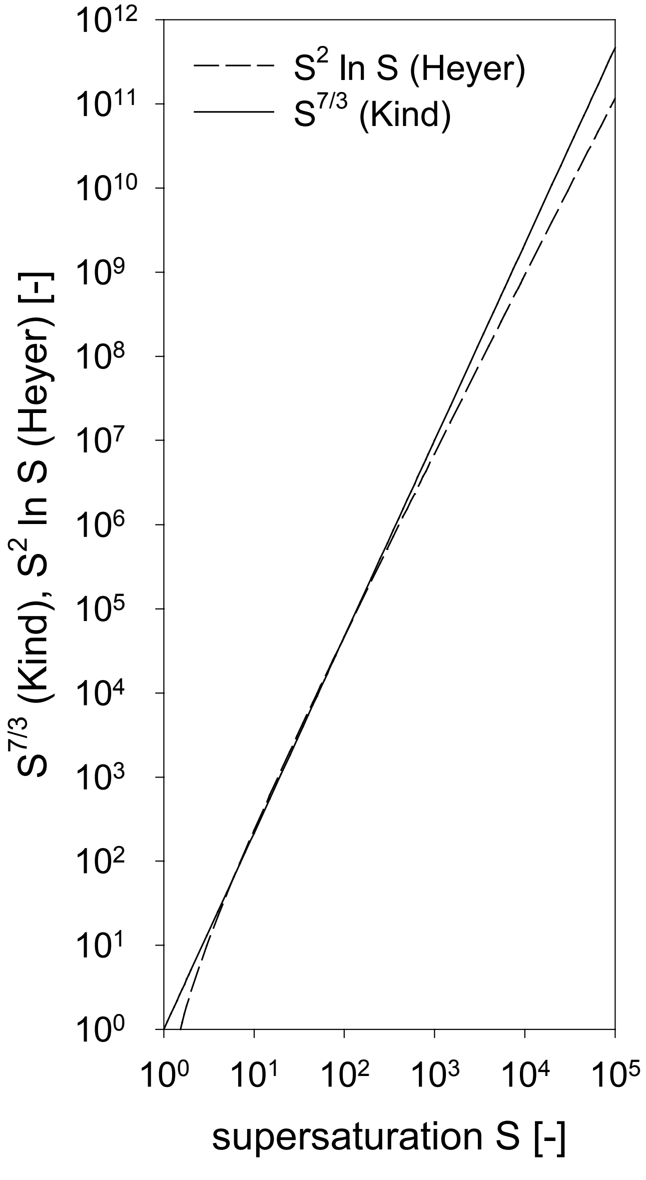

Figure 11-1: $S^{7/3}$ *and* $S^2 \cdot \ln S$ *calculated for* $1 < S < 10^5$

11.2 Conversion of the Rate B_{het} of heterogeneous Nucleation into the Rate B_{hom} of homogeneous Nucleation for the Models of Schubert and Heyer

In the special case of homogeneous nucleation the following assumptions are valid:

- $\theta = 180°$; $\sin\theta = 0$; $\cos\theta = -1$
- $f = 1$ (see equation (2-32))
- $a_{for} \cdot d_m = 1$
- $He_{ad} = 1$
- $x \to 0$
- $m = 1$

The rate of heterogeneous nucleation B_{het} suggested by Schubert (equation (2-36)) can be converted into the rate of homogeneous nucleation B_{hom} (equation (2-28)) as follows:

$$B_{het} = \frac{1}{2\pi} \underbrace{a_{for}\, d_m}_{=1} \underbrace{He_{ad}}_{=1} \left(C\, N_A\right)^{7/3} \sqrt{\frac{\gamma_{CL}}{kT}} \frac{1}{C_C\, N_A} \tag{2-36}$$

$$\left[\underbrace{\frac{D_{surf} \sin\theta}{r_c} \left(He_{ad}\, d_m\right)^{3/2} \left(C\, N_A\right)^{1/6}}_{=0} + \frac{3}{2}\pi D_{AB} \underbrace{\left(1 - \cos\theta\right)}_{=2} \right]$$

$$\cdot \exp\left[-\underbrace{f}_{=1} \frac{16}{3}\pi \left(\frac{\gamma_{CL}}{kT}\right)^3 \left(\frac{1}{C_C\, N_A}\right)^2 \frac{1}{\left(\nu \ln S\right)^2} \right] =$$

$$= 1.5\, D_{AB} \left(C\, N_A\right)^{7/3} \sqrt{\frac{\gamma_{CL}}{kT}} \frac{1}{C_C\, N_A} \tag{2-28}$$

$$\cdot \exp\left[-\frac{16}{3}\pi \left(\frac{\gamma_{CL}}{kT}\right)^3 \left(\frac{1}{C_C\, N_A}\right)^2 \frac{1}{\left(\nu \ln S\right)^2} \right] = B_{hom}$$

Whereas B_{het} calculated with the model proposed by Heyer (equation (2-39)) equals 0 for the assumptions made for homogeneous nucleation:

$$
\begin{aligned}
B_{het} = {} & 2\underbrace{a_{for}\, d_m}_{=1}\underbrace{He_{ad}}_{=1}\left(C\, N_A\right)\sqrt{\frac{\gamma_{CL}}{\underbrace{f}_{=1}\, k\, T}}\,\frac{1}{\left(C_C\, N_A\right)L_c} \\
& \left[\underbrace{\frac{x\ \sin\theta}{m}\frac{D_{surf}}{2\,\pi}\left(He_{ad}\, d_m C\, N_A\right)^{3/2}}_{=0} + D_{AB} C\, N_A \underbrace{\left(1-\frac{1-x\cos\theta}{m}\right)}_{=0}\right] \\
& \cdot\exp\left[-\underbrace{f}_{=1}\frac{16}{3}\pi\left(\frac{\gamma_{CL}}{k\, T}\right)^3\left(\frac{1}{C_C\, N_A}\right)^2\frac{1}{\left(\nu\ln S\right)^2}\right] = \\
= {} & 0
\end{aligned}
\tag{2-39}
$$

11.3 System properties

Table 11-1: System properties

system	C* [mol/l]	d C* / d T [mol / (1 K)]	d ln C* / d ln T [-]	d ln C* / d (1/T) [K]	w* [kg_{anh} / kg_{sol}]	W* [kg_{anh} / kg_{solv}]	m* [kg_{anh} / m^3_{sol}]	m°* [kg_{anh} / m^3_{solv}]	ρ_{sol} [kg/m^3]	η [10^{-3} · Pa s]	D_{AB} [10^{-10} · m^2/s]
adipic acid $(CH_2)_4(COOH)_2$	0.60	0.082	17.27	-5494.15	0.09	0.09	87.93	94.66	1014.16	1.08	7.18
ammonium chloride NH_4Cl	5.82	0.049	2.48	-740.62	0.28	0.39	311.51	391.34	1105.23	1.09	10.34
ammonium nitrate NH_4NO_3	11.87	0.115	2.88	-859.55	0.68	2.12	950.41	2116.52	1398.16		10.26
ammonium sulphate $(NH_4)_2SO_4$	4.04	0.009	0.70	-207.23	0.43	0.77	533.34	763.55	1229.85	2.76	3.17
maleic acid $C_2H_2(COOH)_2$	4.64	0.073	4.67	-1391.31	0.45	0.81	539.07	810.67	1202.13	2.52	3.52
potassium bromide KBr	4.54	0.029	1.87	-558.23	0.40	0.68	543.42	677.24	1343.51		10.50
potassium dichromate $K_2Cr_2O_7$	0.48	0.019	11.42	-3403.58	0.13	0.15	142.58	150.56	1086.86	1.09	7.07
potassium iodide KJ	6.05	0.022	1.08	-320.54	0.60	1.48	1003.73	1479.12	1680.39	1.11	8.84
potassium nitrate KNO_3	3.20	0.096	8.97	-2675.48	0.28	0.38	323.71	382.37	1167.87	1.09	9.31
potassium sulphate K_2SO_4	0.66	0.010	4.37	-1301.53	0.11	0.12	114.42	119.56	1068.70	1.16	7.89
sodium chloride NaCl	5.27	0.002	0.09	-27.63	0.26	0.36	307.82	358.90	1163.05	1.99	6.18
sodium nitrate $NaNO_3$	7.63	0.046	1.81	-540.81	0.48	0.91	648.28	909.53	1359.01	2.68	4.11
succinic acid $(CH_2)_2(COOH)_2$	0.68	0.034	15.07	-4492.85	0.08	0.08	80.15	84.46	1026.45	1.19	7.34
urea $(NH_2)_2CO$	10.49	0.113	3.20	-953.89	0.55	1.21	629.80	1202.00	1152.26	1.95	5.30

The viscosities were measured with a rheometer (Bohlin Instruments CVO 120) and the diffusion coefficients D_{AB} were calculated according to equation (2-29).

11.4 Experimental results

Table 11-2: Experimental results of adipic acid

adipic acid $(CH_2)_4(COOH)_2$			T* = 50°C		C*= 779.65 mol/m³				category A		
measurement time [s]	amperage [mA]	cooling rate [K/s]	phase			attenuation			frequency		
			min	max	noise	min	max	noise	min	max	noise
t_{signal} [s]											
300	-3000	0.066		132				211			177
240	-3000	0.077		122				165			158
180	-3000	0.111		87				138			136
120	-3000	0.171		68							99
60	-3000	0.296									
300	-2000	0.059		175				229			234
240	-2000	0.068		153				171			190
180	-2000	0.089		126				137			
120	-2000	0.129									
60	-2000	0.224									
ΔT_{signal} [K]											
300	-3000	0.066		8.72				13.92			11.65
240	-3000	0.077		9.43				12.74			12.18
180	-3000	0.111		9.68				15.27			15.08
120	-3000	0.171		11.71							16.96
60	-3000	0.296									
300	-2000	0.059		10.30				13.49			13.78
240	-2000	0.068		10.40				11.60			12.94
180	-2000	0.089		11.18				12.16			
120	-2000	0.129									
60	-2000	0.224									
σ_{signal} [-]											
300	-3000	0.066		1.18				1.89			1.58
240	-3000	0.077		1.28				1.73			1.65
180	-3000	0.111		1.31				2.07			2.05
120	-3000	0.171		1.59							2.30
60	-3000	0.296									
300	-2000	0.059		1.40				1.83			1.87
240	-2000	0.068		1.41				1.57			1.76
180	-2000	0.089		1.52				1.65			
120	-2000	0.129									
60	-2000	0.224									

Table 11-3: Experimental results of ammonium chloride

ammonium chloride NH_4Cl			T* = 25°C		C*= 5823.59 mol/m³					category B	
measurement time [s]	amperage [mA]	cooling rate [K/s]	phase			attenuation			frequency		
			min	max	noise	min	max	noise	min	max	noise
t_{signal} [s]											
300	-3000	0.066			67	51					
240	-3000	0.077			43	40					
180	-3000	0.111			61	40					
120	-3000	0.171			53						
60	-3000	0.296			23						
300	-2000	0.059			89						
240	-2000	0.068			76						
180	-2000	0.089			56						
120	-2000	0.129			55						
60	-2000	0.224			37						
ΔT_{signal} [K]											
300	-3000	0.066			4.43	3.39					
240	-3000	0.077			3.32	3.12					
180	-3000	0.111			6.80	4.46					
120	-3000	0.171			9.14						
60	-3000	0.296			6.79						
300	-2000	0.059			5.23						
240	-2000	0.068			5.19						
180	-2000	0.089			4.98						
120	-2000	0.129			7.14						
60	-2000	0.224			8.27						
σ_{signal} [-]											
300	-3000	0.066			0.04	0.03					
240	-3000	0.077			0.03	0.03					
180	-3000	0.111			0.06	0.04					
120	-3000	0.171			0.08						
60	-3000	0.296			0.06						
300	-2000	0.059			0.04						
240	-2000	0.068			0.04						
180	-2000	0.089			0.04						
120	-2000	0.129			0.06						
60	-2000	0.224			0.07						

Table 11-4: Experimental results of maleic acid

maleic acid $C_2H_2(COOH)_2$			T* = 25°C			C*= 4644.35 mol/m³			category C		
measurement time [s]	amperage [mA]	cooling rate [K/s]	phase			attenuation			frequency		
			min	max	noise	min	max	noise	min	max	noise
t_{signal} [s]											
300	-3000	0.066						256		257	
240	-3000	0.077						208		212	
180	-3000	0.111									
120	-3000	0.171									
60	-3000	0.296									
300	-2000	0.059									
240	-2000	0.068									
180	-2000	0.089									
120	-2000	0.129									
60	-2000	0.224									
ΔT_{signal} [K]											
300	-3000	0.066						16.90		16.96	
240	-3000	0.077						16.02		16.32	
180	-3000	0.111									
120	-3000	0.171									
60	-3000	0.296									
300	-2000	0.059									
240	-2000	0.068									
180	-2000	0.089									
120	-2000	0.129									
60	-2000	0.224									
σ_{signal} [-]											
300	-3000	0.066						0.26		0.27	
240	-3000	0.077						0.25		0.26	
180	-3000	0.111									
120	-3000	0.171									
60	-3000	0.296									
300	-2000	0.059									
240	-2000	0.068									
180	-2000	0.089									
120	-2000	0.129									
60	-2000	0.224									

Table 11-5: Experimental results of potassium dichromate

potassium dicromate K2Cr2O7			T* = 25°C		C*= 484.65 mol/m³				category A		
measurement time	amperage	cooling rate	phase			attenuation			frequency		
[s]	[mA]	[K/s]	min	max	noise	min	max	noise	min	max	noise
t_{signal} [s]											
300	-3000	0.066		98			203		222		
240	-3000	0.077		100			183		203		
180	-3000	0.111		141			115				
120	-3000	0.171		92							
60	-3000	0.296									
300	-2000	0.059		236			235				
240	-2000	0.068		178							
180	-2000	0.089		128							
120	-2000	0.129		70							
60	-2000	0.224									
ΔT_{signal} [K]											
300	-3000	0.066		6.50			13.43		14.65		
240	-3000	0.077		7.70			14.09		15.63		
180	-3000	0.111		15.61			12.78				
120	-3000	0.171		15.74							
60	-3000	0.296									
300	-2000	0.059		13.90			13.87				
240	-2000	0.068		12.09							
180	-2000	0.089		11.36							
120	-2000	0.129		9.05							
60	-2000	0.224									
σ_{signal} [-]											
300	-3000	0.066		0.25			0.51		0.56		
240	-3000	0.077		0.29			0.54		0.60		
180	-3000	0.111		0.60			0.49				
120	-3000	0.171		0.60							
60	-3000	0.296									
300	-2000	0.059		0.53			0.53				
240	-2000	0.068		0.46							
180	-2000	0.089		0.43							
120	-2000	0.129		0.35							
60	-2000	0.224									

Table 11-6: Experimental results of potassium nitrate

potassium nitrate KNO_3			T* = 25°C			C*= 3201.74 mol/m³			category A		
measurement time [s]	amperage [mA]	cooling rate [K/s]	phase			attenuation			frequency		
			min	max	noise	min	max	noise	min	max	noise
t_{signal} [s]											
300	-3000	0.066			123	140	126		122	134	
240	-3000	0.077			106	131	120		119	131	
180	-3000	0.111			79	112	102		102	111	
120	-3000	0.171			64	83	66		78	81	
60	-3000	0.296			39	50	49		49	50	
300	-2000	0.059			154	193	186		181	193	
240	-2000	0.068			123	166	158		156	166	
180	-2000	0.089			100	137	126		125	137	
120	-2000	0.129			84				105	106	
60	-2000	0.224			49						
ΔT_{signal} [K]											
300	-3000	0.066			8.11	9.23	8.31		8.07	8.81	
240	-3000	0.077			8.14	10.06	9.24		9.19	10.06	
180	-3000	0.111			8.79	12.46	11.31		11.35	12.35	
120	-3000	0.171			10.94	14.13	11.28		13.39	13.79	
60	-3000	0.296			11.63	14.69	14.39		14.49	14.88	
300	-2000	0.059			9.06	11.38	10.97		10.67	11.37	
240	-2000	0.068			8.35	11.28	10.73		10.57	11.30	
180	-2000	0.089			8.90	12.16	11.23		11.14	12.21	
120	-2000	0.129			10.85				13.60	13.73	
60	-2000	0.224			11.00						
σ_{signal} [-]											
300	-3000	0.066			0.24	0.28	0.25		0.24	0.27	
240	-3000	0.077			0.24	0.30	0.28		0.28	0.30	
180	-3000	0.111			0.26	0.37	0.34		0.34	0.37	
120	-3000	0.171			0.33	0.43	0.34		0.40	0.41	
60	-3000	0.296			0.35	0.44	0.43		0.44	0.45	
300	-2000	0.059			0.27	0.34	0.33		0.32	0.34	
240	-2000	0.068			0.25	0.34	0.32		0.32	0.34	
180	-2000	0.089			0.27	0.37	0.34		0.34	0.37	
120	-2000	0.129			0.33				0.41	0.41	
60	-2000	0.224			0.33						

Table 11-7: Experimental results of succinic acid

succinic acid $(CH_2)_2(COOH)_2$			T* = 25°C		C*= 678.72 mol/m³					category B	
measurement time	amperage	cooling rate	phase			attenuation			frequency		
[s]	[mA]	[K/s]	min	max	noise	min	max	noise	min	max	noise
t_{signal} [s]											
300	-3000	0.066			98			85	95	124	
240	-3000	0.077			79			78	100	135	
180	-3000	0.111			73			74	88	143	
120	-3000	0.171						66	85		
60	-3000	0.296									
300	-2000	0.059							235		
240	-2000	0.068							202		
180	-2000	0.089									
120	-2000	0.129									
60	-2000	0.224									
ΔT_{signal} [K]											
300	-3000	0.066			6.48			5.60	6.24	8.20	
240	-3000	0.077			6.11			5.98	7.70	10.37	
180	-3000	0.111			8.06			8.17	9.73	15.83	
120	-3000	0.171						11.22	14.59		
60	-3000	0.296									
300	-2000	0.059							13.87		
240	-2000	0.068							13.74		
180	-2000	0.089									
120	-2000	0.129									
60	-2000	0.224									
σ_{signal} [-]											
300	-3000	0.066			0.33			0.28	0.32	0.41	
240	-3000	0.077			0.31			0.30	0.39	0.52	
180	-3000	0.111			0.41			0.41	0.49	0.80	
120	-3000	0.171						0.57	0.74		
60	-3000	0.296									
300	-2000	0.059							0.70		
240	-2000	0.068							0.69		
180	-2000	0.089									
120	-2000	0.129									
60	-2000	0.224									

Table 11-8: Experimental results of urea

urea $(NH_2)_2CO$				T* = 25°C			C*= 10486.20 mol/m³			category C	
measurement time [s]	amperage [mA]	cooling rate [K/s]	phase			attenuation			frequency		
			min	max	noise	min	max	noise	min	max	noise
					t_{signal} [s]						
300	-3000	0.066			224			218			229
240	-3000	0.077						190			
180	-3000	0.111									
120	-3000	0.171									
60	-3000	0.296									
300	-2000	0.059									
240	-2000	0.068									
180	-2000	0.089									
120	-2000	0.129									
60	-2000	0.224									
					ΔT_{signal} [K]						
300	-3000	0.066			14.81			14.39			15.11
240	-3000	0.077						14.63			
180	-3000	0.111									
120	-3000	0.171									
60	-3000	0.296									
300	-2000	0.059									
240	-2000	0.068									
180	-2000	0.089									
120	-2000	0.129									
60	-2000	0.224									
					σ_{signal} [-]						
300	-3000	0.066			0.16			0.15			0.16
240	-3000	0.077						0.16			
180	-3000	0.111									
120	-3000	0.171									
60	-3000	0.296									
300	-2000	0.059									
240	-2000	0.068									
180	-2000	0.089									
120	-2000	0.129									
60	-2000	0.224									

11.5 Calculated heterogeneous nucleation rates B_{het}

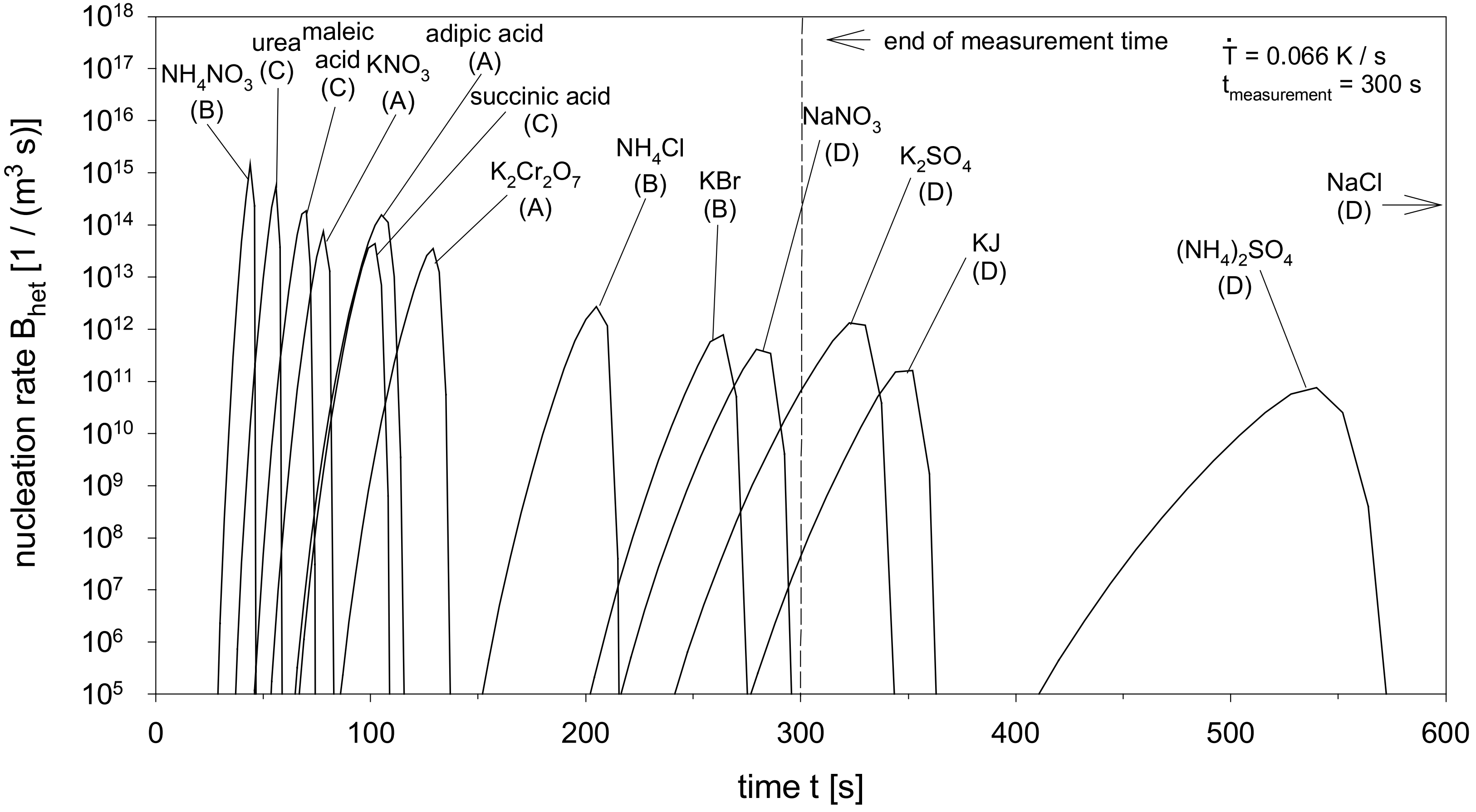

Figure 11-2: Calculated nucleation rates B_{het} (valid for: $a_{for} = 10^5$ m^{-1}; $He_{ad} = 10^{-9}$; T = 298 K; K = 0.414; $k_d = 10^{-4}$ m s^{-1}; cooling rate = 0.066 K / s) without NaCl

11.6 Calculation of σ_{met} for primary heterogeneous nucleation

Table 11-9: Relative supersaturation σ_{met} of organic and inorganic systems calculated for different cooling rates (calculated for: $a_{for} = 10^5\ m^{-1}$; $He_{ad} = 10^{-9}$; $T = 298\ K$; $K = 0.414$; $k_d = 10^{-4}\ m\ s^{-1}$)

cooling rate [K / s]	0.296	0.224	0.171	0.129	0.111	0.089	0.077	0.068	0.066	0.059	1.389E-03	8.333E-04	5.556E-04	C^* / C_C [-]
cooling rate [K / h]	1065.6	805.7	614.9	463.8	400.6	321.3	278.0	245.0	238.4	211.6	5.0	3.0	2.0	
adipic acid $(CH_2)_4(COOH)_2$	1.1209	1.0788	1.0222	0.9802	0.9575	0.9245	0.9007	0.8933	0.8940	0.8632	0.5812	0.5587	0.5396	0.017
ammonium chloride NH_4Cl	0.1393	0.1361	0.1330	0.1299	0.1287	0.1265	0.1248	0.1239	0.1233	0.1224	0.0972	0.0955	0.0930	0.204
ammonium nitrate NH_4NO_3	0.0329	0.0320	0.0311	0.0303	0.0299	0.0294	0.0290	0.0287	0.0288	0.0284	0.0222	0.0217	0.0212	0.551
ammonium sulphate $(NH_4)_2SO_4$	0.0986	0.0968	0.0941	0.0919	0.0909	0.0888	0.0883	0.0874	0.0870	0.0862	0.0679	0.0664	0.0646	0.301
maleic acid $C_2H_2(COOH)_2$	0.0885	0.0855	0.0843	0.0820	0.0807	0.0789	0.0773	0.0766	0.0763	0.0754	0.0583	0.0564	0.0552	0.335
potassium bromide KBr	0.1461	0.1419	0.1391	0.1361	0.1341	0.1320	0.1298	0.1295	0.1286	0.1276	0.1017	0.0987	0.0969	0.020
potassium dichromate $K_2Cr_2O_7$	0.4834	0.4725	0.4518	0.4345	0.4305	0.4172	0.4122	0.4061	0.4070	0.3994	0.2953	0.2839	0.2781	0.053
potassium iodide KJ	0.0825	0.0809	0.0788	0.0781	0.0764	0.0749	0.0743	0.0735	0.0731	0.0726	0.0583	0.0567	0.0555	0.321
potassium nitrate KNO_3	0.2001	0.1956	0.1877	0.1832	0.1815	0.1766	0.1747	0.1724	0.1720	0.1701	0.1319	0.1288	0.1255	0.153
potassium sulphate K_2SO_4	0.5285	0.5061	0.4903	0.4747	0.4682	0.4576	0.4507	0.4440	0.4449	0.4370	0.3282	0.3157	0.3100	0.043
sodium nitrate $NaNO_3$	0.1393	0.1351	0.1325	0.1298	0.1281	0.1261	0.1244	0.1236	0.1231	0.1222	0.0981	0.0956	0.0937	0.287
succinic acid $(CH_2)_2(COOH)_2$	0.4967	0.4792	0.4588	0.4437	0.4374	0.4260	0.4188	0.4141	0.4122	0.4079	0.3000	0.2899	0.2837	0.051
urea $(NH_2)_2CO$	0.0468	0.0456	0.0445	0.0435	0.0429	0.0420	0.0416	0.0409	0.0413	0.0405	0.0317	0.0308	0.0301	0.476

11.7 Further possibilities for improvement and additional sensor concepts

11.7.1 Design improvement of the existing sensor

One key issue for every measurement is a crystal-free or nearly crystal-free solution. Therefore a housing including a particle separation device (housing with water-jet pump and sedimentation tube) was constructed. The disadvantage of this solution is due to the system properties which decide on the design of the sedimentation tube. This tube becomes large in the case of small density differences. Another possibility for particle separation is shown in Figure 11-3.

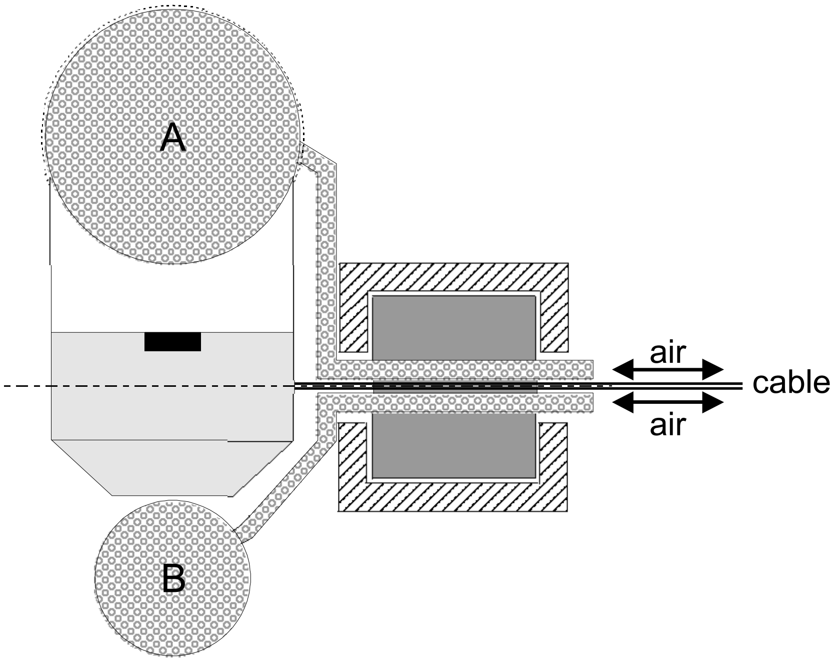

Figure 11-3: Pivoted sensor with balloons during the measurement phase

Figure 11-3 shows the position of the sensor during the measurement phase. Balloon A is inflated, thus closing the measurement chamber. After the measurement, balloon A is discharged and balloon B is inflated. This leads to a 180° rotation of the sensor device, which is shown in Figure 11-4.

The sensor will now be heated in order to remove the incrustation which was generated during the last measurement. Because of the turbulence in the crystallizer the solution in the measurement chamber is replaced by fresh solution from the bulk phase. Due to the downwards orientated sensor surface crystals are prevented from depositing on the sensor and the volume close to the sensor surface becomes nearly crystal-free.

After a while balloon A will be inflated slowly whereas balloon B will be discharged. The measurement chamber will be closed again by balloon A and the sensor will turn

180° until the sensor surface is upwards orientated, which is also a prerequisite for each measurement.

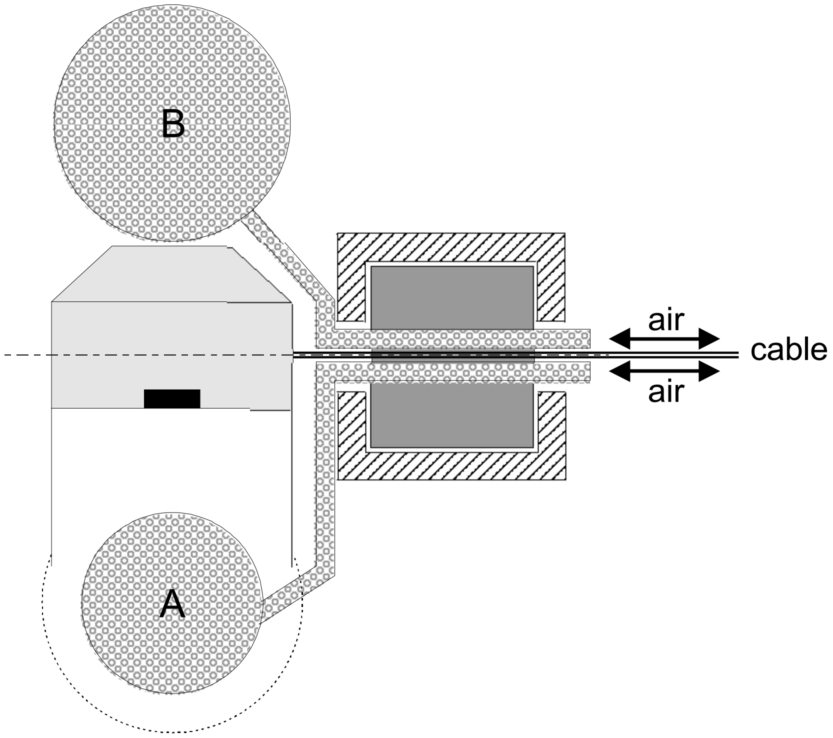

Figure 11-4: Pivoted sensor with balloons during the cleaning phase

11.7.2 Sensor for systems with flat solubility curves

The additional supersaturation ΔC_{sensor} that is generated by cooling with a peltier element is necessary to obtain an incrustation on the sensor surface in an adequate time. In case of systems with non-temperature dependent solubility $\left(\frac{dC^*}{dT}\right) \approx 0$ no relevant supersaturation can be obtained by cooling. For these systems it is useful to apply removal of solvent as supersaturation generation method. This can be realized by pervaporation with a membrane (e.g. tube module). Reversed osmosis is another possibility.

Figure 11-5 shows a possible solution with a tube module. The suspension flows through the tube module with a well defined volume flow $\dot{V}_{susp}$ and the solvent is removed with a constant pervaporation rate $\dot{V}_{perv}$.

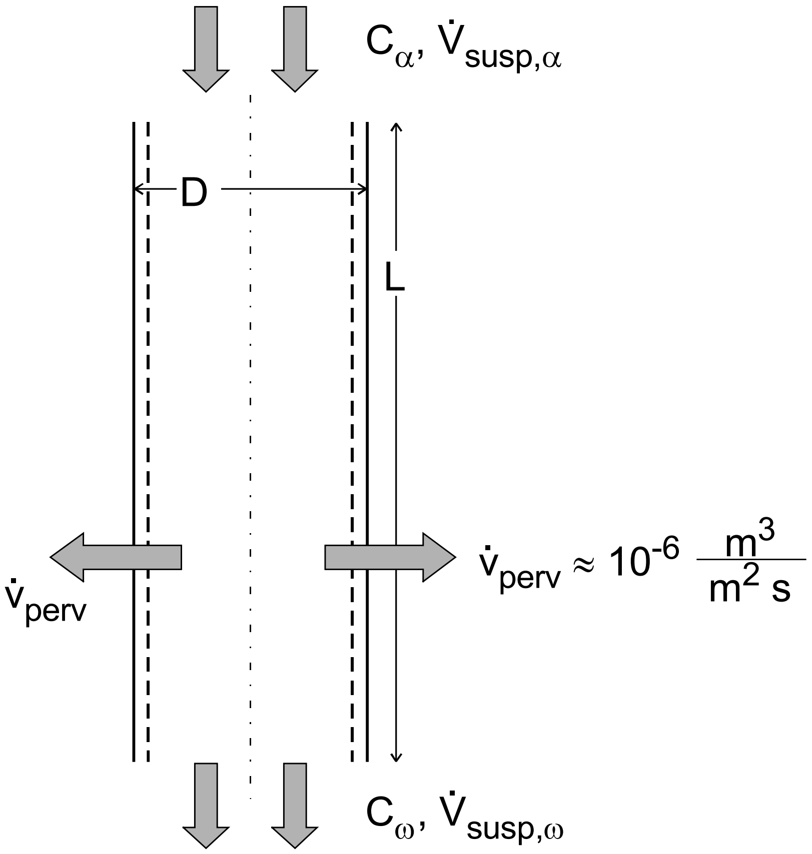

Figure 11-5: Pervaporation with a tube module

This leads to an increase of supersaturation in the solution flowing through the tube module. Pervaporation causes an additional cooling of the solution which leads in case of $\left(\frac{dC^*}{dT}\right) > 0$ to an additional generation of supersaturation. The supersaturation will be increased until the metastable supersaturation σ_{met} is reached and spontaneous nucleation starts. The shower of nuclei can now be detected with optical methods or ultrasonic.

In order to obtain the metastable supersaturation σ_{met} without cooling it is necessary to adjust the volume flow according to Equation (11-1) (valid for L/D = const. and $\dot{V}_{perv}$= const.).

$$\dot{V}_{sus} = 4\frac{L}{D}\dot{V}_{perv}\frac{1+\sigma_{met}}{(1-f)\sigma_{met}} \qquad (11\text{-}1)$$

The factor f is the process supersaturation, σ_{proc}, referring to σ_{met}:

$$f = \frac{\sigma_{\mathrm{proc}}}{\sigma_{\mathrm{met}}} \qquad (11\text{-}2)$$

Here the factor f is in the range of 0.3 – 0.5. The additional cooling ΔT caused by pervaporation increases the prevailing process supersaturation σ_{proc} with the additional supersaturation $\sigma_{\mathrm{add},\Delta T}$ and depends on the heat of evaporation of the solvent, Δh_{LG}:

$$\sigma_{\mathrm{add},\Delta T} = 4 \frac{L}{D} \frac{1}{C^*} \left(\frac{dC^*}{dT} \right) \frac{\rho_{\mathrm{solv}} \cdot \Delta h_{LG}}{\rho_{\mathrm{sus}} \cdot c_{p,\mathrm{sus}}} \frac{\dot{V}_{\mathrm{perv}}}{\dot{V}_{\mathrm{sus}}} \qquad (11\text{-}3)$$

If the existing sensor setup (IDT and SAW) should be used for systems with $\left(\frac{dC^*}{dT} \right) \approx 0$, the two following ideas seem to be feasible.

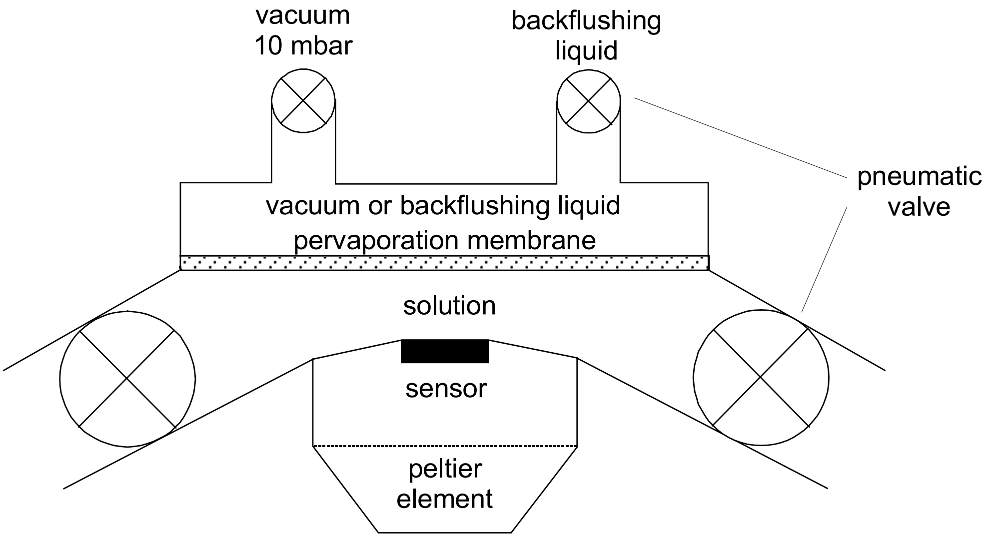

Figure 11-6: Existing sensor setup in combination with pervaporation opposite the sensor surface as supersaturation generation method

In Figure 11-6 a pervaporation membrane is positioned opposite the sensor surface. The solution flows across the sensor surface and is at rest when the valves at the end of the measurement chamber are closed. The constant increase of supersaturation leads to nucleation which can be measured with the sensor by a change of the physical properties of the solution. This arrangement can have the drawback that a solution with a high density close to the membrane surfaces causes a natural convection flow.

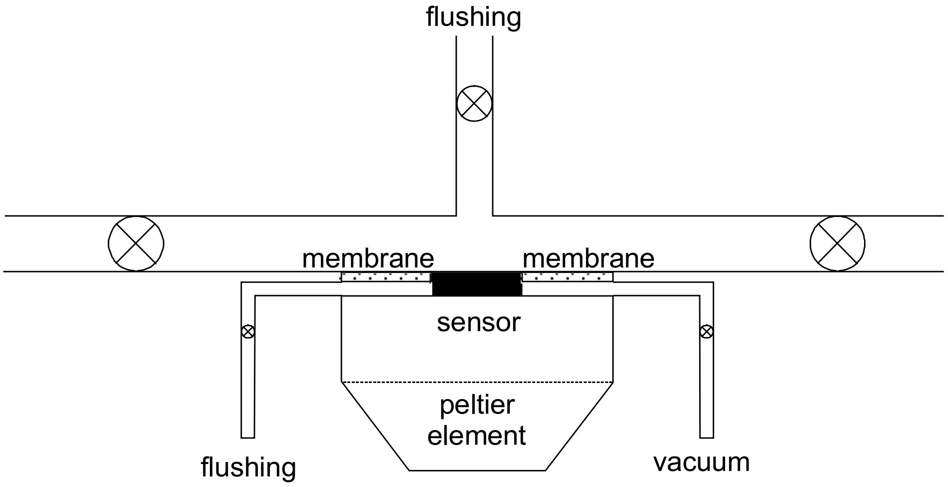

Figure 11-7: Existing sensor setup in combination with pervaporation adjacent the sensor surface as supersaturation generation method

In case of Figure 11-7 the membrane is adjacent to the sensor surface and the measurement procedure is similar to Figure 11-6.

11.7.3 Equilibrium state sensor

11.7.3.1 Systems with (d C* / d T) > 0

The following type of sensor is applicable for continuously operated crystallizers, since it is necessary to keep the temperature of the solution T_{sol} constant. In the case of batch cooling crystallizers it is necessary to measure exactly the process temperature, T_{proc}, in the vicinity of the sensor.
Figure 11-8 explains the measurement procedure schematically.

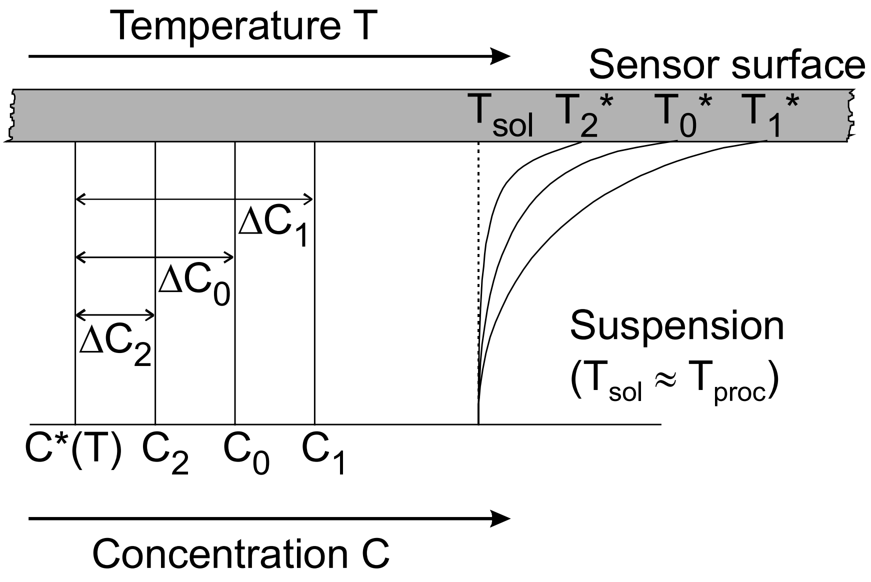

Figure 11-8: Equilibrium state measurement method for systems with (dC/dT) > 0*

The major difference between the equilibrium state sensor and the other sensors is that the first prevents incrustation on the sensor surface. Instead of promoting incrustation only the starting point of the incrustation is detected.

The sensor surface will be kept at the equilibrium temperature T_0^* which corresponds to the concentration C_0 of the solution in the crystallizer. The solution has the constant temperature T_{sol}. In case of $T_0 < T_0^*$ and starting incrustation on the sensor surface, the sensor surface has to be heated in order to prevent further incrustation. Whereas in the case of $T_0 > T_0^*$ the surface can be cooled until the starting of incrustation is detected. The start of the crystallization on the sensor surface and the dissolution of the crystal layer will be detected by a sensor, e. g. by use of optical detection methods as shown in Figure 11-9.

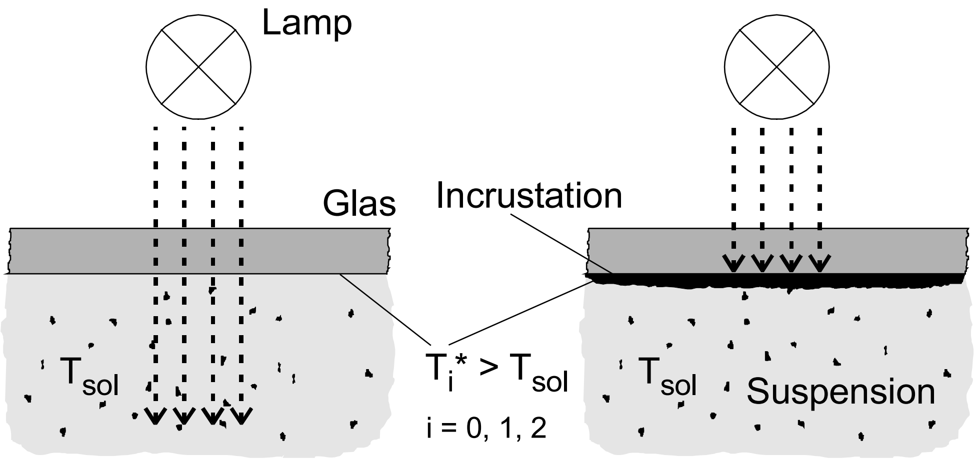

Figure 11-9: Optical detection of the incrustation

The supersaturation ΔC_0 can be calculated by

$$\Delta C_0 = \frac{d\,C^*}{d\,T}\left(T_0^* - T_{sol}\right) \tag{11-4}$$

with d C* / d T as the slope of the solubility curve. The temperature of the solution T_{sol} and the temperature of the sensor surface T_0^* (minimum temperature without incrustation of the sensor surface) will be measured.

If the supersaturation rises from ΔC_0 up to ΔC_1 and the temperature T_{sol} is still constant, the sensor surface temperature has to be increased from T_0^* to T_1^* in order to prevent incrustation. The prevailing supersaturation ΔC_1 is given by equation (11-5).

$$\Delta C_1 = \frac{d\,C^*}{d\,T}\left(T_1^* - T_{sol}\right) \tag{11-5}$$

In case of a supersaturation ΔC_2 which is lower than the initial supersaturation ΔC_0 and the same temperature T_{sol}, the sensor surface temperature T_0^* must be reduced to T_2^* in order to obtain the minimum surface temperature without inducing incrustation. The supersaturation ΔC_2 can be calculated according to equation (11-6).

$$\Delta C_2 = \frac{d\,C^*}{d\,T}\left(T_2^* - T_{sol}\right) \tag{11-6}$$

The calculations of the equations (11-4) - (11-6) are schematically shown in Figure 11-10.

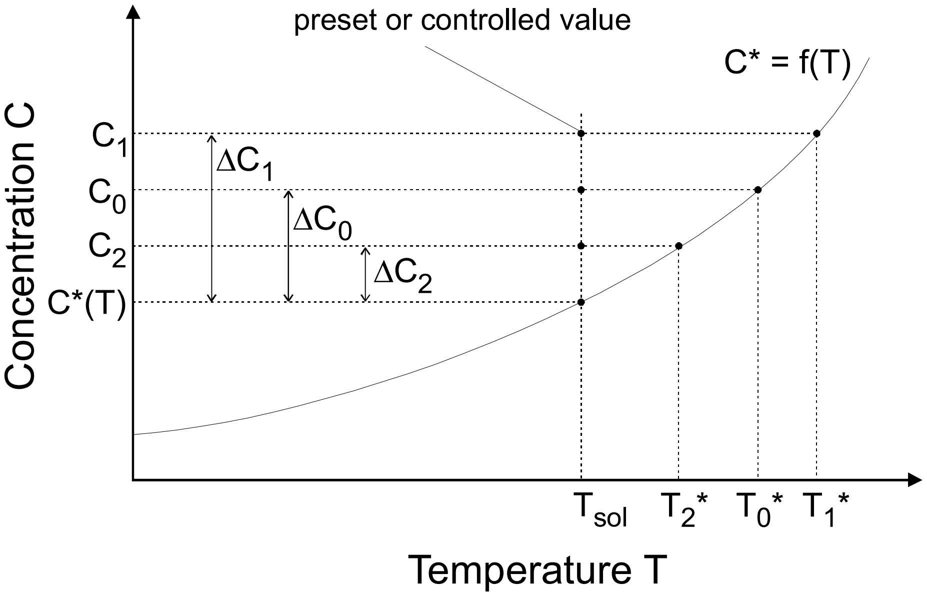

Figure 11-10: Schematic solubility plot

11.7.3.2 Systems with (d C* / d T) < 0

The temperature of the solution T_{sol} is either constant or measured and the solution has the supersaturation $\Delta C_0 = C_0 - C^*(T_{sol})$. The sensor surface is kept at the equilibrium temperature T_0^* by cooling. The temperature T_0^* corresponds to the concentration C_0 of the solution in the crystallizer (see Figure 11-11 and Figure 11-12).

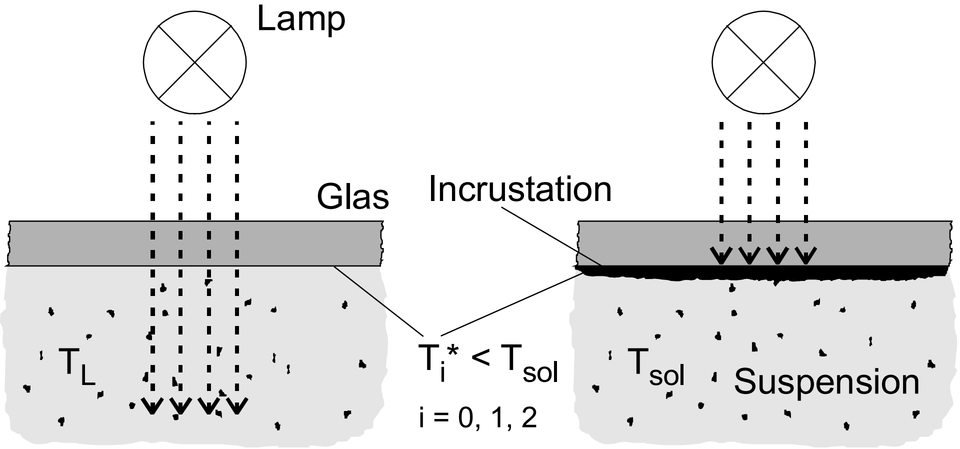

Figure 11-11: Optical detection of the incrustation

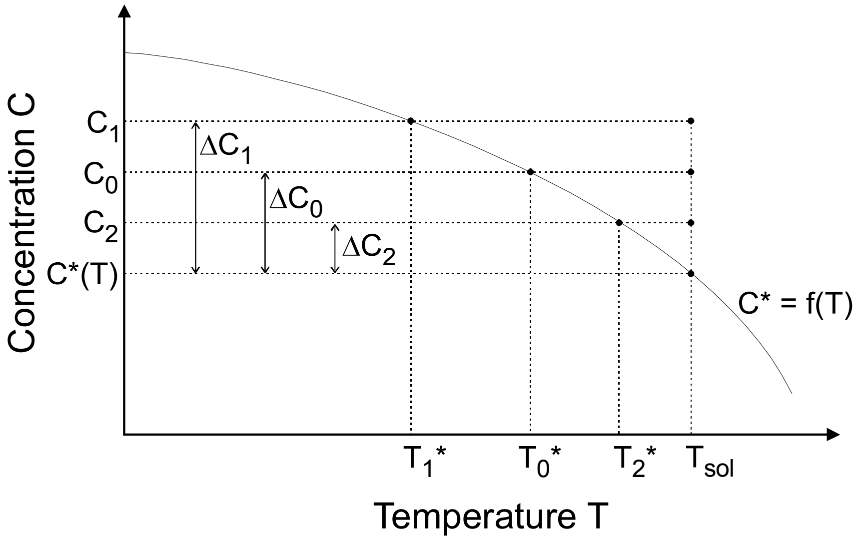

Figure 11-12: Schematic solubility plot

In case of $T_0 > T_0^*$ and starting incrustation on the sensor surface, the sensor surface has to be cooled in order to keep the temperature T_0^* constant. If $T_0 < T_0^*$ and the last fragment of incrustation has been dissolved, the surface can be heated until the starting of incrustation is detected. The onset of incrustation and the total dissolution of the incrustation can be detected optically, as shown in Figure 11-11.

The supersaturation can be calculated with equation (11-7).

$$\Delta C_0 = \frac{d\,C^*}{d\,T}\left(T_0^* - T_{sol}\right) \qquad (11\text{-}7)$$

with d C* / d T as the negative slope of the solubility curve in Figure 11-12. The temperature of the solution T_{sol} and the temperature of the sensor surface T_0^* (maximum temperature without incrustation of the sensor surface) will be measured.
In case of a higher supersaturation $\Delta C_1 > \Delta C_0$ or a lower supersaturation $\Delta C_2 < \Delta C_0$ the temperature of the sensor surface has to be reduced or increased respectively in order to prevent incrustation and to keep the surface at the maximum temperature without incrustation on the sensor surface (see Figure 11-13).

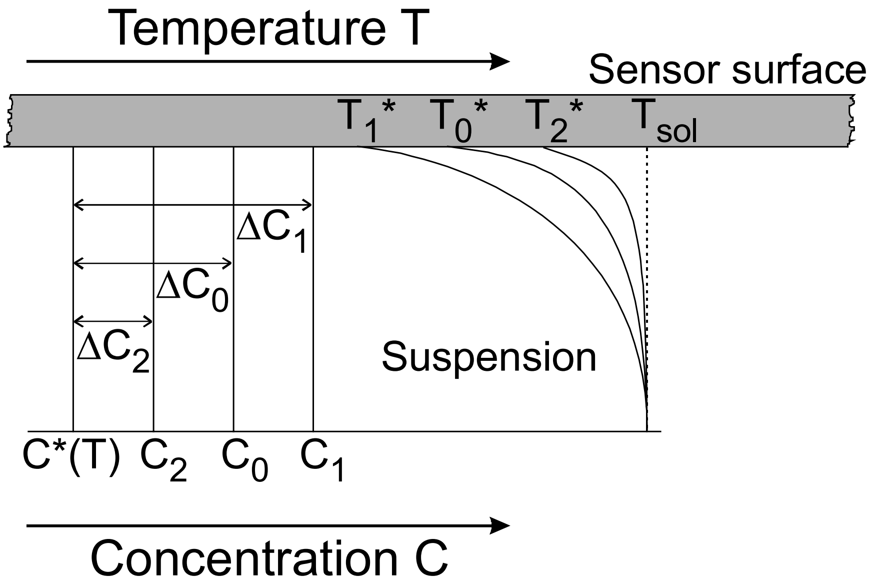

Figure 11-13: Equilibrium state measurement method for systems with (dC/dT) < 0*

11.7.3.3 Systems with (d C* / d T) ≈ 0

For systems with an almost flat solubility curve a change of temperature would hardly cause a shift of supersaturation. Therefore a change of the supersaturation can only be achieved by change of concentration of the solution by adding or removing solvent. This can be accomplished by solvent in the liquid or vapour state.

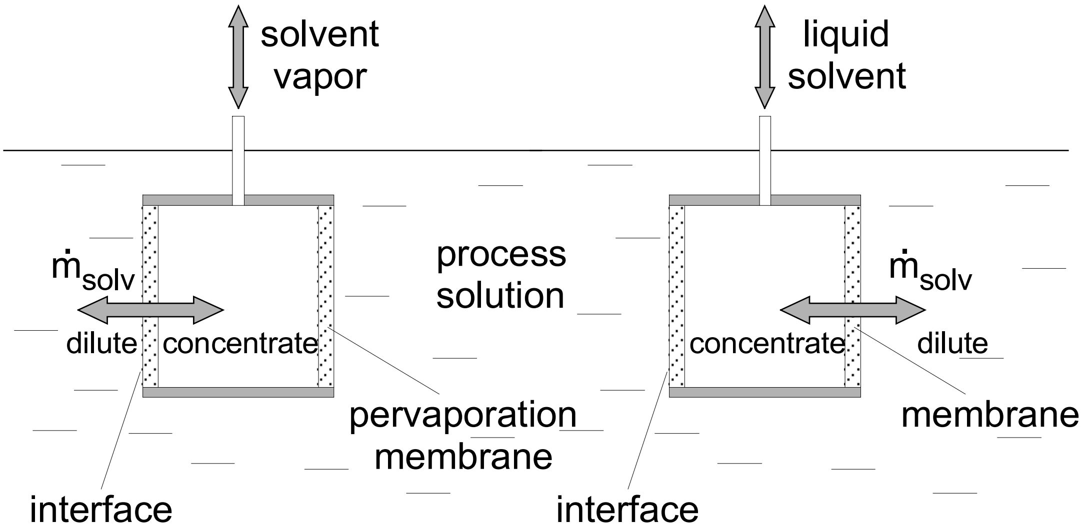

Figure 11-14: Dilution or concentration of the solution with a membrane

If the solution is in contact with a membrane, as shown in Figure 11-14, the supersaturation of the solution adjacent to the membrane can be changed by dilution or concentration. This is realised by changing the pressure of the pure solvent in the membrane module. A higher pressure in the membrane module causes a dilution of the solution, whereas a pressure lower than the pressure of the solution leads to an increase of concentration of the solution outside the membrane module. This is explained by Figure 11-15.

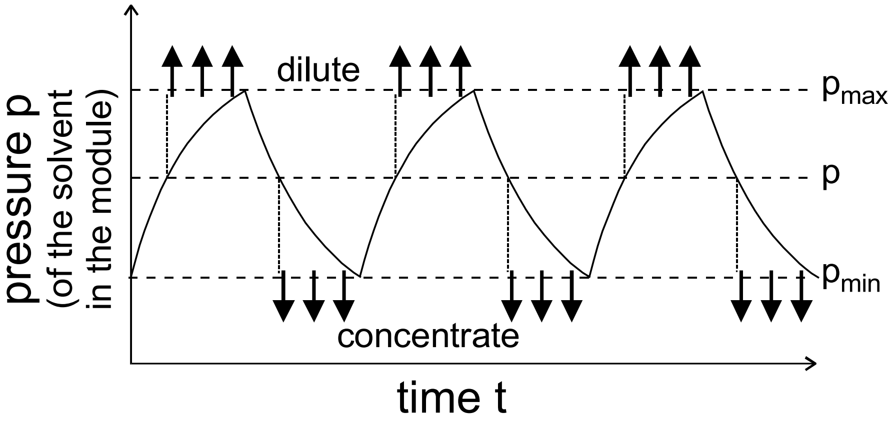

Figure 11-15: Alternating pressure in the membrane module leads to a dilution or increase of concentration of the solution outside the membrane module

At the beginning the pressure in the module will be reduced, thus leading to an increase of concentration and of supersaturation in the solution outside the module close to its surface. If the beginning of crystallization on the membrane surface is detected, the pressure inside the module will be increased in order to dissolve the crystals on the membrane outside the module. By this means the pressure in the module will start to oscillate keeping the pressure at the minimum level without incrustation on the membrane (see Figure 11-15). By measuring the pressure inside the module the supersaturation can be evaluated with the help of calibration curves, see Figure 11-16 and Figure 11-17.

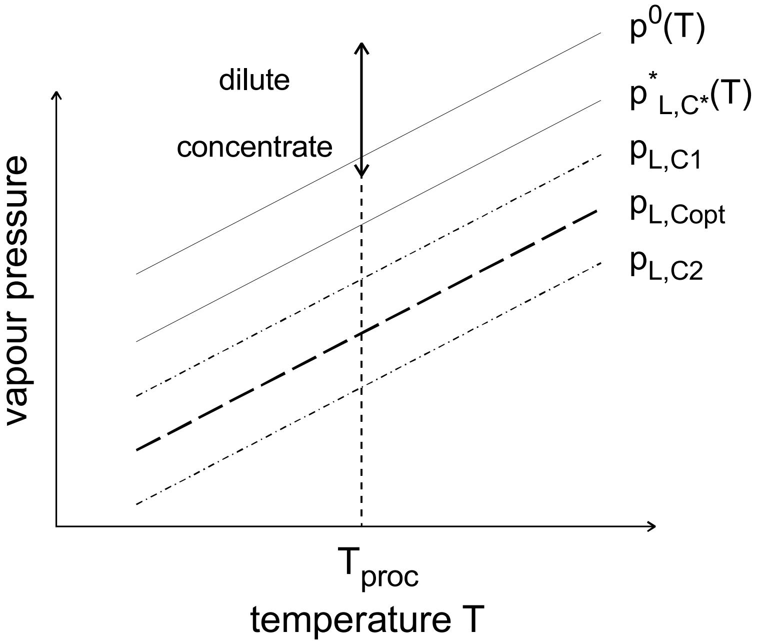

Figure 11-16: Vapour pressure calibration curves

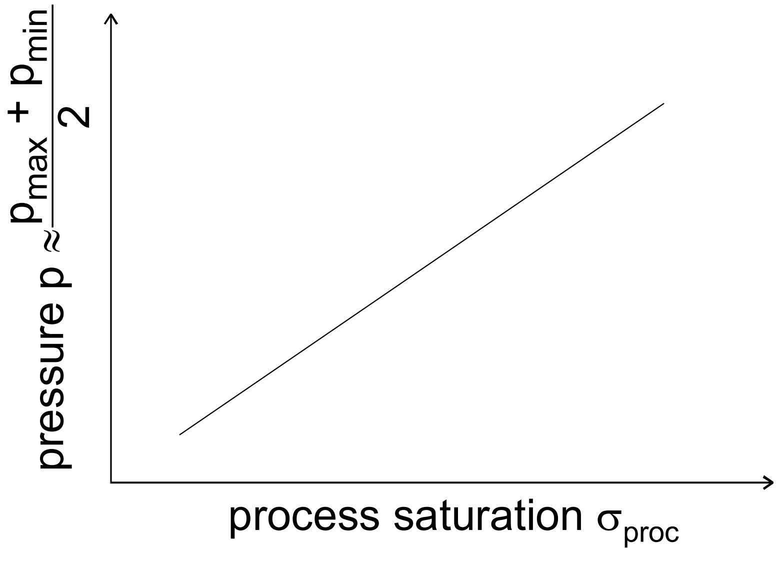

Figure 11-17: Relationship between the solvent pressure p and the process supersaturation

11.7.3.4 Addition of a solvent – antisolvent mixture of constant or oscillating concentration

The addition of the solvent through a membrane leads to a fast dissolution of the incrustation, however, the subsequent incrustation step can be slow because the process supersaturation is usually low. This incrustation can be enhanced by the addition of an antisolvent (for instance an organic solvent in the case of aqueous systems) which results in a fast increase of the supersaturation close to the membrane surface. The inner volume of the membrane module (see Figure 11-18) is fed by a solvent – antisolvent mixture of constant or oscillating concentration C_{mix}.

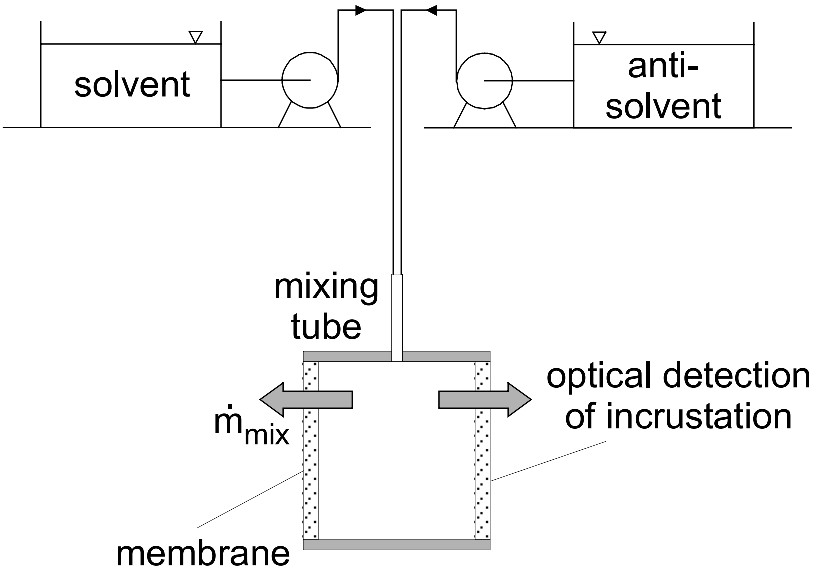

Figure 11-18: Membrane module with metering pumps

The feeding is accomplished by two metering pumps. The solvent is charged by the first pump and the antisolvent is pressurized by the second one. The two pumps can be operated with constant or oscillating speed. In the latter case the concentration of the solvent – antisolvent mixture (after mixing in a blending tube) is oscillating, and the frequency and period of this oscillation depend on the speed changes of the metering pumps (see Figure 11-19).

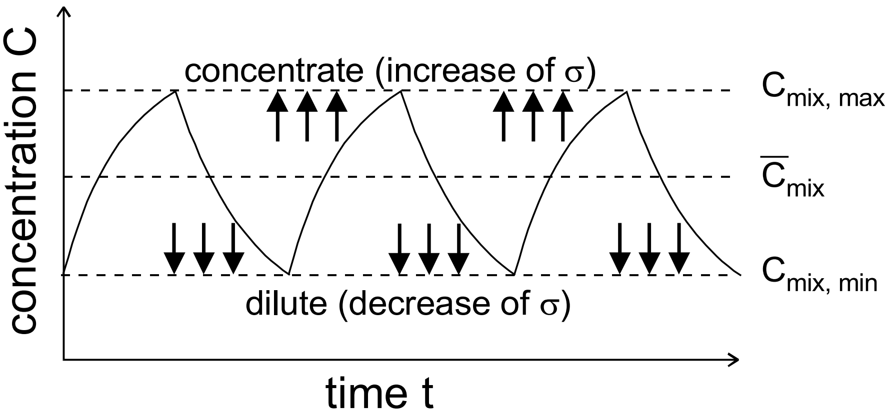

Figure 11-19: Oscillating solvent – antisolvent concentration versus time

The passage of this solvent – antisolvent mixture with the concentration C_{mix} leads to an oscillating supersaturation close to the outer membrane surface, and this results in an oscillating incrustation and dissolution. The two pump streams and their concentrations are chosen in such a way that no permanent incrustation of the outer membrane surface takes place. The mean solvent – antisolvent concentration C_{mix} is a function of the process supersaturation, σ_{proc}, which can be determined after calibration. A calibration diagram C_{mix} versus σ_{proc} is shown in Figure 11-20.

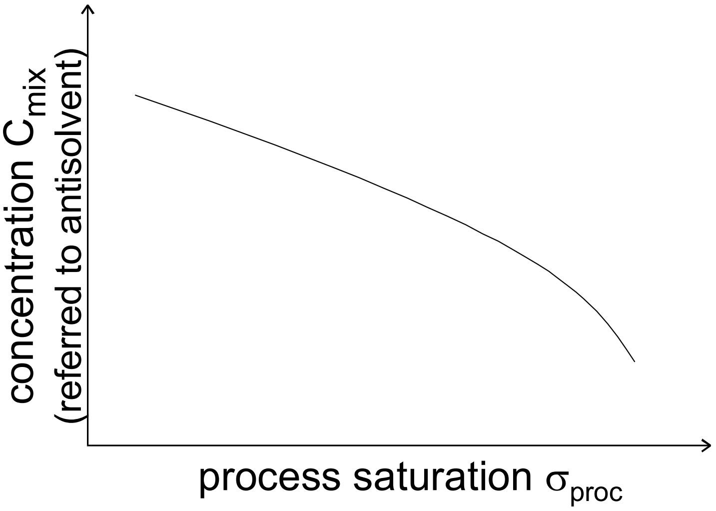

Figure 11-20: Calibration diagram (schematically)